The Quest for the Rare Decay $K^+ \rightarrow \pi^+ \nu \bar{\nu}$

by

Benji Bengal Lewis

B.S., Physics, Western Carolina University, 1998
B.S., Mathematics, Western Carolina University, 1998

DISSERTATION

Submitted in Partial Fulfillment of the
Requirements for the Degree of

Doctor of Philosophy
Physics

The University of New Mexico
Albuquerque, New Mexico

December, 2007

Dedication

To Mom and Laura.

Acknowledgments

Many thanks go out to those who helped, encouraged, and supported me though out my life. I appreciate all the support given by my very large family, especially my Mom, brother, and sister. To Pappaw who hounded me about graduation by asking me “When are you going to get those papers (diploma)?”, ”here are those papers!”

To all of my friends from back home, Albuquerque, Long Island, and the ones that I haven’t met yet, ”thanks.” I appreciate Shannon’s unwavering attitude of “do whatever you gotta do to finish your degree.” I always got a kick out of how Bird made me into a side-show attraction by asking me say the title of my dissertation to people we just met, just to blow their minds. It was always funny to see the expressions on their faces (and Bird’s) when they heard the title; in the final version I shortened it, but I’m sure it will still turn some heads. I learned a great deal about science and politics during many conversations with Paul Kingsberry. Whether it was to solve homework problems or to drink a beer, my fellow students at the physics department were always helpful and fun.

Of all my great teachers, my high school math teachers had the largest impact on the course of my life. Although I didn’t fully comprehend what I was doing in Mrs. Painter’s class, I excelled next to the classmates that I had always thought were smarter than myself. At the end of my freshman year, I went to her desk for sophomore class placement thinking I would be in geometry; geometry was the next class you were suppose to take. When I took the signature slip to her she asked “Is this the class you want to take?” I didn’t understand what she meant and asked her “What do you think?” Without any words or additional comments she placed a red ‘H’, for honors, next to Geometry, signed the slip, and handed it back to me. One of my proudest moments. Without this moment, I would have probably dropped out of college early to start an internet company. After making millions, I would have retired in the Caribbean sipping Piña Coladas on the beach. Thank you, Mrs. Painter for saving me from that boring life. In honors geometry, Mrs. Woodard showed me that math can be fun and I began to enjoy it. After two years with Mrs. Herren, I continued to excel, but everything started to make sense. She made me believe I could actually create a future around math. I consider myself very lucky to have been taught by these teachers at Smoky Mountain High School. I would also like to acknowledge Mr. Mike Pendergast, my *World History* and *Medieval History* teacher, as arguably the best teacher I ever had as a student. I just wish I could have appreciated history back when there was less of it.

I would like to thank all of my WCU math teachers, especially Prof. Marshall, Dr. Klerlein, Dr. Norgaard, Dr. Williford, and Dr. Sportsman. They inspired me to explore difficult problems.

Undoubtedly, Professor Ted Moody was the reason I became a physicist. After a year with Prof. Moody, I changed my major to Physics; my original intention was to teach high school math. He made physics fun and for reasons beyond me I was able to answer most of the trick questions he asked the class. Dr. Kurt Vandervoort, a.k.a. Dr. V, was a great mentor. He introduced me to experimental physics and I've hardly looked back. I learned a great deal, under Dr. V's tutelage, implementing my idea to measure quantized conductance in nano-wires formed in a liquid metal. Thanks to Dr. Heckert for allowing me to point toward the stars as the Astronomy TA. Dr. Liming was always insightful as Brian and I spent fruitless hours trying to find holes in special relativity (still looking).

My two summers in the National Science Foundation's *Research Experience for Undergraduates* program solidified my experimental nature and my love of the outdoors. Thanks goes to Dr. Panitz for pushing me to think on my feet, by asking me questions as a Drill Sergeant would ask a private to do push-ups. Luckily, I was able to work out most of the questions before I had to do any push-ups. I appreciate Dr. Dunlap, one great and witty guy, for taking me on some wonderful outdoor trips across New Mexico. It was great riding in an inconspicuous white run-downed van across New Mexico with a bunch of physicists which will get you locked-up these days. Thank you Dr. Wolfe for getting me into the particle physics group at UNM. No one can ask for a better advisor as I had in Bernd Bassalleck. Thanks Bernd for all of your support through my graduate work.

I'm glad that I chose E949 for my graduate work. Being a relatively small experiment, for particle physics, I was able to be a part of almost every aspect of the experiment. From helping construct part of the Range Stack to sweating my ass off in the middle of the summer while installing the RS modules by crawling into the beamline (just big enough for an expendable grad student) where the UTC would soon be resting. Collecting data during those late night shifts, getting blisters from trimming cables by blindly reaching thru a nest of cables for hours and hours, calibrating the Range Stack PMT's, doing archaeology by reading Fortran code that was decades old, writing reconstruction code from scratch, … kept my "fun" calendar booked solid!

I would like to thank the entire E949 collaboration, especially Jim Frank, Steve Kettell, Milan Diwan, Bipul Bhuyan, and Laurie Littenberg. They all made my stay at BNL pleasant and memorable. I appreciate Ilektra, Joss, Tetsuro, Dima, Tetsuro, and Kentaro for being in the trenches with me. I really appreciated George Redlinger's patience with putting up with my constant stream of questions. Without David Jaffe's tenacious attitude of "better is the enemy of the good" the analysis would have ground to a halt long ago. Thanks for keeping it going. I also appreciate all the hands-on training from the E949 technicians, especially Joe, Bill, Artie, and Neil.

I'm very happy that I chose E949 for more that just the science I've learned working on the E949 experiment. Without choosing E949, I would have never met some of the greatest people I've ever known. I'm very fortunate that I became close friends with Neil and his family. Neil's son Matthew with his inquisitive nature is already a scientist at heart. Neil and his family have had a extremely positive impact on my life and my gratitude goes out to all of them for all that they have done for me. Without moving to Long Island, a necessity for E949 work, I would probably never have met Laura, who I love more than any experiment can measure.

Experiment E949, it was a blast while it lasted. Thanks for bringing me to BNL, LI, NY to meet the wonderful people who changed my life. Viva 949!

How often have I said to you that when you have eliminated the impossible,
whatever remains, however improbable, must be the truth?

Sherlock Holmes to Watson
The Sign of Four

The Quest for the Rare Decay $K^+ \rightarrow \pi^+ \nu \bar{\nu}$

by

Benji Bengal Lewis

ABSTRACT OF DISSERTATION

Submitted in Partial Fulfillment of the
Requirements for the Degree of

Doctor of Philosophy
Physics

The University of New Mexico
Albuquerque, New Mexico

December, 2007

The Quest for the
Rare Decay $K^+ \to \pi^+\nu\bar{\nu}$

by

Benji Bengal Lewis

B.S., Physics, Western Carolina University, 1998
B.S., Mathematics, Western Carolina University, 1998

Ph.D., Physics, University of New Mexico, 2008

Abstract

Experiment E949 at Brookhaven National Laboratory studied the rare decay $K^+ \to \pi^+\nu\bar{\nu}$ and other processes with an exposure of 1.77×10^{12} K^+'s. The data were analyzed using a blind analysis technique, yielding one candidate event upon a background of 0.30 ± 0.03 events in the PNN1 region (211 MeV/c $\leq P_{\pi^+} \leq$ 229 MeV/c). Analysis to ultimately measure $\mathcal{B}(K^+ \to \pi^+\nu\bar{\nu})$ at lower (PNN2) momentum region (140 MeV/c $\leq P_{\pi^+} \leq$ 195 MeV/c) with larger signal-to-background, compared previous measurements in this momentum region, was accomplished. In the signal region, the single-event sensitivity (SES^{-1}) of 0.417×10^{-9} and a total expected background of $1.069 \pm 0.222^{+0.31}_{-0.26}$ were measured. A tight signal region was also devised with a SES^{-1} of 1.28×10^{-9} and expected background of $0.193 \pm 0.086^{+0.17}_{-0.07}$.

Contents

List of Figures

List of Tables

Glossary

θ	Polar angle of charged track determined by UTC.
etot	Kinetic energy of charged track.
ptot	Momentum of charged track at decay point.
rtot	Range of charged track from decay point to the stopping counter.
t_{RS}	Time of the charged track in the Range Stack. Often referred to as charged-track time.
t_{K}	Energy-weighted time of all K^+ fiber hits in the Target (K^+ time).
t_π	Energy-weighted time of all π^+ fiber hits in the Target (π^+ time).
etg	Total π^+ energy contained within the TG. Does not include energy found by CCD fitting, except those found *a priori* during PASS2 *swathccd* reconstruction.
rtg	Range of the π^+ with the TG as measured from the decay vertex to the inner surface of the IC. The curve employed in the measurement is the extrapolated UTC track and there is a θ correction applied.

AD	Active Degrader
ADC	Analog-to-Digital Converter
AGS	Alternating Gradient Synchrotron
B4	B4 Hodoscope
BeO	Beryllium-oxide
BNL	Brookhaven National Laboratory
BR	Branching Ratio
BV	Barrel Veto
BVL	Barrel Veto Liner
BW, BWPC	Beam Wire proportional chambers
BW1	Upstream beam wire proportional chamber
BW2	Downstream beam wire proportional chamber
CO	Collar
CCD	Charged-Couple Device
CEX	Charged Exchange
$\check{C}_K$	Kaon Čerenkov
CKM	Cabibbo-Kobayashi-Maskawa
CP	Charge-Parity
$\check{C}_\pi$	Pion Čerenkov
CsI	Cesium-iodine

ct	Charged track
DAQ	Data Acquisition
DIF	Decay-in-Flight
DSPV	Downstream Photon-Veto
EC	End Caps
EC1	End-Cap 1, Upstream EC
EC2	End-Cap 2, Downstream EC
FCNC	Flavor-Changing Neutral Current
FERA	Fast Encoding and Readout ADC
FWHM	Full-Width at Half Maximum
GWS	Glashow-Weinberg-Salam
IC	I-counter
ID	Inactive degrader
K_{e4}	$K^+ \rightarrow \pi^+\pi^-e^+\nu$
$K_{\mu 2}$	$K^+ \rightarrow \mu^+\nu$
$K_{\mu 2\gamma}$	$K^+ \rightarrow \mu^+\nu\gamma$
$K_{\pi 2}$	$K^+ \rightarrow \pi^+\pi^0$
$K_{\pi 2\gamma}$	$K^+ \rightarrow \pi^+\pi^0\gamma$
LED	Light-Emitting diode
LESBIII	Low-Energy Separated Beamline III

μCO,MC	Microcollar
NNLO	Next-to-next-to Leading Order
P	Parity
PAW	Physics Analysis Workstation
PID	Particle Identification
PMT	Photo-Multiplier Tube
PV	Photon Veto
QCD	Quantum Chromodynamics
RS	Range Stack
RSMON	RS Monitoring System
RSSC	Range-Stack Straw Chambers
RV	Ring Veto
SES	Single-Event Sensitivity
SM	Standard Model
$T\bullet 2$	RS Layer 1+Layer2 hit
TD	Transient Digitizers
TDC	Time-to-Digital Converter
TG	Target
UMC	E949 Monte Carlo
UPV	Upstream Photon Veto

UTC	Ultra-Thin (Drift) Chamber
VC	V-counter, Veto-counter
WLS	Wavelength-Shifting
X_0	Radiation Lengths
Active Degrader	Beam and Photon detector.
AGS	A particle accelerator located at BNL.
ADC	Analog-to-Digital Converter is an electronic device capable of digitizing an electronic signal. ADCs employed by E949 are listed in Table C.1
B4 Hodoscope	Plastic-scintillator detector located upstream of the Target used in particle identification.
Barrel Veto	A barrel shaped photon detector composed of four layers and 48 sectors of lead-scintillator sandwich.
Barrel Veto Liner	An additional layer (added during E949 upgrade), interior to the BV, of photon lead-scintillator detector.
Beam	A fast moving mixture of K^+ and π^+ particles that are produced by the AGS.
Beamline	A volume, $\sim$ 12 cm wide, where the beam particles travel.
BW chambers	Beam wire chambers are detectors capable of detecting incoming charged beam particles.
Beryllium-oxide	Beryllium-oxide was used in the Inactive Degrader due to high density and low atomic number causing less multiple scattering.

Box	The multidimensional parameter space which defines the signal region. Box may also be used to describe a confided kinematic region such as the kinematic box or energy box.
BNL	Brookhaven National Laboratory is an United States national laboratory located on Long Island in New York, see www.bnl.gov.
Branching Ratio	The fraction of particles which decay by an individual decay mode with respect to the total number of particles which decay.
CCD	Charged-Couple Device is an device capable of registering and storing electronic signals over time. As denoted in Table C.1, E949's CCDs had 500 MHz sampling with 256 ns depth.
Collar	A beamline photon detector.
Cut	Requirements on data which if not satisfied will remove an event from further consideration.
Decay-in-Flight	A term describing when a particle decays before coming to rest.
Delayed Coincidence	Requirement in which K^+ decay products are detected later than the stopped K^+ entered the detector.
Downstream	Describes z-axis position along the path of the beam, as if the K^+ beam is a stream of water; downstream points in the positive z-direction.
E787	Predecessor experiment to experiment E949.

E949	An experiment to measure $\mathcal{B}(K^+ \rightarrow \pi^+\nu\bar{\nu})$ which collected data from 2001 to 2002
Edge fibers	Scintillating fibers located in the TG periphery.
End Cap	Detects photons close to the beam line (large θ).
Event	A single datum in the analysis in which all relevant detector information was stored.
FCNC	Flavor-Changing Neutral Current is a weak-interaction process which changes the flavor of a fermion without altering the electric charge.
Hextant	A group of four adjacent sectors in the RS. There are six hextants grouped by sectors (1-4, 5-8, 9-12, 13-16, 17-20, 21-24).
I-counter	Scintillator detector surrounding Target. Used in trigger to determine if an outgoing track exists.
Inactive Degrader	An block of BeO located directly upstream of the AD used to slow beam K^+'s.
Kaon Čerenkov	A detector which identifies K^+'s entering the E949 detector by Čerenkov light emitted by when the particle traverses a radiator. It is contained within the same structure as the Kaon Čerenkov.
KB	The number of K^+'s entering the detector.
KB_{live}	The number of K^+'s that decay in the Target while the E949 is available to register a trigger (i.e. the detector is live).

Kink	A kink refers to an abnormal bend in the charged-track trajectory, in the $x - y$ plane, due to a scatter. A kinked event can differ from an event which produces the background associated with TG-scatters due to the Target's $x - y$ resolution (and lack of z resolution).
Layer	Refers to the radial segmentation of a detector, usually in reference to the RS's 19 layers or the BV's 4 layers.
LESB III	A Low-Energy Separated Beamline at the AGS, see Appendix A, which produces a very pure and intense K^+ beam.
Microcollar	A photon detector located between of the downstream Collar and downstream end of the Target
Mix,Mixing	Common description of one elementary particles transforming into another particle.
Muon Band	A correlated kinematic region of range and momentum which is consistent with a μ^+ track, see Fig. 3.3, due mostly to radiative muon decays.
ntuple	Data file employed by Physics Analysis Workstation (PAW) software.
Offline	The time period after a triggered event has been stored.
Online	The time period after a K^+ has entered the detector and before a decision has occurred whether to select the event for further analysis.
$\pi\nu\bar{\nu}(1)$	PNN1 trigger, see Section 2.12.

$\pi\nu\bar{\nu}(2)$	PNN2 trigger, see Section 2.12.
PASS0	The initial stage of data storage.
PASS1	The first stage of data reduction using a set of cuts with the same name.
PASS2	The second stage of data reduction using a set of cuts with the same name.
Photo-Multiplier Tube	A device which converts light into an electronic signal.
Photon Veto	E949 is composed of many photon detectors, commonly referred to as photon veto, since the sole purpose of photon detectors is to veto (or reject) events with photons in the decay. Also, describes the composite set of photon cuts.
Pion Beam	π^+'s which exist in the K$^+$ particle beam.
Pion Čerenkov	A detector which identifies π^+'s entering the E949 detector by Čerenkov light emitted by when the particle traverses a radiator. It is contained within the same structure as the Kaon Čerenkov.
Pion Band	A correlated kinematic region of range and momentum which is consistent with a π^+ track, see Fig. 3.3.
PNN1	The momentum region 211 MeV/c $\leq P_{\pi^+} \leq$ 229 MeV/c and the experiment to measure $\mathcal{B}(K^+ \to \pi^+\nu\bar{\nu})$ within this region.
PNN2	The momentum region 140 MeV/c $\leq P_{\pi^+} \leq$ 195 MeV/c and the experiment to measure $\mathcal{B}(K^+ \to \pi^+\nu\bar{\nu})$ within this region.

Range	Distance traveled by the charged track in plastic scintillator.
Range Stack	A segmented (19 layers, 24 sectors) charged-track scintillator detector which is equipted with TDCs, TDs, and ADCs.
Run	A block of events segmented during data collection which occurred during the same period of time.
Sector	Azimuthal segmentation of the RS, BVL, or BV, such that sector 1 is located at $\phi = 0^\circ$ and increases with increasing ϕ (as looking upstream).
Stopping Counter	RS counter in which the charged track comes to rest.
Swath	The area surrounding the UTC track extrapolated into the TG. This area (swath) is employed by the reconstruction algorithm *swathccd*.
swathccd	Reconstruction algorithm for the Target.
T•2	Trigger condition requiring RS-layers 1 and 2 within the same sector. Used to determine charged track in fiducial region.
T-counter	RS-layer 1 which defines the fiducial region within the Range Stack.
Target	Detector composed of small scintillating fibers whose main purpose is to observe decay of the K$^+$.
TD cuts	Cuts employing the RS TDs to find the $\pi^+ \rightarrow \mu^+ \rightarrow e^+$ decay chain.

TDC	Time-to-Digital Converter is an electronic device capable of converting electronic pulses into digitized time values. The TDCs employed by E949 are listed in Table C.1.
Transient Digitizers	A waveform digitizer. As denoted in Table C.1, E949's TDs had 500 MHz sampling for 2 μs depth.
Upstream	Describes z-axis position along the path of the beam. As if the K^+ beam is a stream of water. Upstream of a given point is in the negative z-axis direction.
UTC	The Ultra-Thin Chamber is E949's drift chamber which determines the precise trajectory of a charged particle particle.
UPV	The Upstream Photon Veto is located between the $\check{\mathrm{C}}_K$ detector and BW1. This detector made of plastic scintillator and copper sheets was used to detect extra beam particles at decay time.
V(eto)-counter	Ring of plastic scintillator surrounding Target downstream of fiducial region.
Wavelength Shifting	Material in which scintillating light shifts to a longer wavelength allowing for greater propagation through the material to a detector such as a PMT.

Chapter 1

Theory

Up and down quarks comprise the nucleus of elements of the universe. Matter, not antimatter, fills the universe. If everything is symmetrical, then the universe should be made of equal parts of matter and antimatter. These two statements imply that there must be something that is not symmetrical within physics to allow matter to dominate the universe. As will be shown, the decay $K^+ \to \pi^+ \nu \bar{\nu}$ can explain, at least in part, the reason why the universe is made of matter.

1.1 Standard Model

The Standard Model of particle physics (SM) [1] is an amalgam of theory and experiments which was built upon by experiments pushing theory [2] and theory pushing experiments [3, 4]. Matter within the SM is built of three generations of quarks and three generations of leptons and their partner neutrinos, as seen in Table 1.1. The SM successfully describes the electromagnetic, weak, and strong interactions between elementary particles (see Table 1.2).

The interaction between quarks, strong force, is explained by Quantum Chromo-

	Quarks			Leptons		
Generation	Flavor	Mass ($\frac{\mathrm{GeV}}{\mathrm{c}^2}$)	Electric Charge	Flavor	Mass ($\frac{\mathrm{GeV}}{\mathrm{c}^2}$)	Electric Charge
I	(u) Up	0.003	2/3	(ν_e) electron neutrino	$< 3. \times 10^{-9}$	0
I	(d) Down	0.006	-1/3	(e) electron	0.000511	-1
II	(c) Charm	1.3	2/3	(ν_μ) muon neutrino	< 0.00019	0
II	(s) Strange	0.1	-1/3	(μ) muon	0.1057	-1
III	(t) Top	174.3	2/3	(ν_τ) tau neutrino	< 0.0182	0
III	(b) Bottom	4.3	-1/3	(τ) tau	1.777	-1

Table 1.1: SM fermions ($\frac{1}{2}$ spin particles). The three generation of quarks (I, II, III) are displayed in progressively darker rows. The electric charge is reported in units of the charge of the proton. [5]

Interaction	Weak	Electromagnetic	Strong
Acts on	Flavor	Electric Charge	Color Charge
Experienced by	Quarks,Leptons	Electrically charged	Quarks, Gluons
Mediating by	W^+, W^-, Z^0	γ	Gluons

Table 1.2: Forces within the Standard Model.

dynamics (QCD). QCD, a gauge theory, contains eight vector gauge bosons called gluons. The electroweak interaction, the unification of electromagnetic and weak forces, can be explained by the Glashow-Weinberg-Salam (GWS) gauge theory. The force carriers in GWS theory are γ (electromagnetic), $W^{\pm}$ (weak), and Z^0 (weak).

Unlike the strong and electromagnetic interactions, which conserves particle flavor, the weak interaction allows particle flavor to change (e.g. $c \rightarrow d$). The decay process $K^+ \rightarrow \pi^+\nu\bar{\nu}$ obviously is manifested via the weak force. This is apparent when one observes the constituent quarks of K$^+$ and π^+. K$^+$ has u and $\bar{s}$ quarks and the π^+ has u and $\bar{d}$ quarks. Hence, investigation into the weak interaction is required to further understand the decay $K^+ \rightarrow \pi^+\nu\bar{\nu}$.

1.2 Weak Interaction

It has been evident from as early as 1956 that the weak interaction differs from the other SM forces in the non-conservation of parity P, as it is a vector-axial ($V - A$) interaction. However, the combination of charge conjugation and parity (CP) was thought to be conserved until the astonishing result of experiment E-0181 at Brookhaven Nation Laboratory (BNL) in 1964 [2] showed CP violation in the neutral Kaon system. Since the discovery of CP violation, an elegant explanation has been incorporated in the SM, where CP violation arises naturally from the existence of three families of quarks that interchange or mix with each other through weak interactions.

The Kobayashi-Maskawa (KM) theory [6] explains the fashion in which the weak interaction changes quark flavor by introducing a quark mixing matrix, called the Cabibbo-Kobayashi-Maskawa (CKM) matrix. The CKM matrix is a 3×3 unitary matrix that quantifies the amount of mixing that occur between quark flavors. In this case, mixing refers to one quark transforming into another quark. The CKM matrix does not effect the strong and electromagnetic interactions allowing particle flavor conservation within these forces.

The weak interaction is mediated by the W^+, W^- and the Z^0 bosons. In the charged-current processes (via W^+ or W^-), one quark can transform into another quark of the same family with a different electric charge (e.g. $d \to u + W^-$), and one lepton can transform into the respective neutrino (e.g. $e^- \to \nu_e + W^-$) and vice versa. The charged-current weak interaction allows transformation of quarks between different generations (e.g. $s \to u+W^-$), with the strength of the interaction depending on the parameters of the CKM matrix V_{CKM}, as shown in Eq. (1.1).

$$\begin{pmatrix} d' \\ s' \\ b' \end{pmatrix} = V \begin{pmatrix} d \\ s \\ b \end{pmatrix} = \begin{pmatrix} V_{ud} & V_{us} & V_{ub} \\ V_{cd} & V_{cs} & V_{cb} \\ V_{td} & V_{ts} & V_{tb} \end{pmatrix} \begin{pmatrix} d \\ s \\ b \end{pmatrix} \tag{1.1}$$

The CKM matrix, V_{CKM}, connects the weak eigenstates d', s', b' to their mass eigenstates d, s, b. Thus the quark that couples to the weak-interaction charged bosons is a linear combination of the free (mass) eigenstates making it possible to change quark flavor through a weak interaction. Introduction of an imaginary phase in the CKM matrix allows for CP violation to proceed naturally within the SM. Since neutrinos have been found to possess mass [7], an analogous CKM-like structure has gained a foothold in the leptonic sector, described by the 3×3 Maki-Nakagawa-Sakata (MNS) matrix [8].

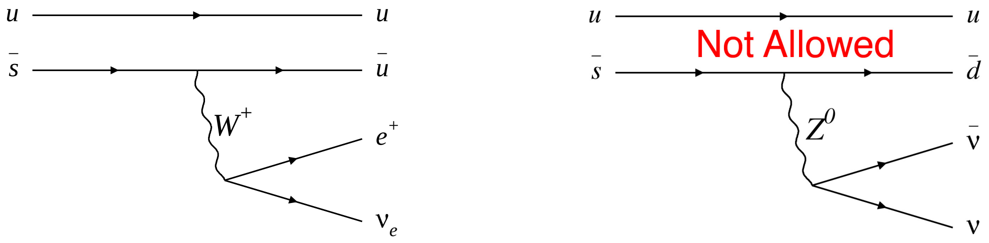

Figure 1.1: The tree level Feynman diagram for the decay $K^+ \rightarrow \pi^0 e^+ \nu_e$ is allowed via the SM weak-interaction (left). The tree level Feynman diagram for the $K^+ \rightarrow \pi^+ \nu\bar{\nu}$ decay which is not allowed in the SM (right).

A quark cannot transform into another quark with the same charge by an exchange of a Z^0 (e.g. $s \nrightarrow d + Z^0$), as shown in Fig. 1.1. The flavor-changing neutral-current (FCNC) processes are forbidden at first order (see Fig. 1.1) and suppressed at the one-loop level due to the Glashow-Iliopoulos-Maiani (GIM) mechanism [9]. In $s \nrightarrow d + Z^0$ the weak eigenstates, d' and s', not the mass eigenstates, d and s, participate in the weak interaction. Their relation is written as

$$\begin{pmatrix} d' \\ s' \end{pmatrix} = \begin{pmatrix} \cos\theta_c & \sin\theta_c \\ -\sin\theta_c & \cos\theta_c \end{pmatrix} \begin{pmatrix} d \\ s \end{pmatrix} \tag{1.2}$$

such that θ_c is the Cabibbo angle [10]. The neutral current J^0 is expressed by Eq. (1.3).

$$\begin{aligned} J^0 &= \bar{u}u + \bar{c}c + \bar{d'}d' + \bar{s}'s' \\ &= \bar{u}u + \bar{c}c + (\bar{d}d + \bar{s}s)\cos^2\theta_c + (\bar{d}d + \bar{s}s)\sin^2\theta_c \quad : \text{(flavor conserving term)} \\ &\quad +(\bar{d}s + \bar{s}d - \bar{d}s - \bar{s}d)\sin\theta_c\cos\theta_c \quad : \text{(flavor changing term)} \\ &= \bar{u}u + \bar{c}c + \bar{d}d + \bar{s}s. \end{aligned} \tag{1.3}$$

The term that accounts for the FCNC processes vanishes, and therefore the absence of first order FCNC processes is explained by this description. The GIM cancellation can also work at 1-loop diagrams (see Fig. 1.5), where the initial-to-final quark transitions are effectively the FCNC processes, if the quarks in the intermediate state (e.g. the u and c quarks in the $K^0 - \overline{K^0}$ mixing) have the same mass. Since the quark masses depend on the quark flavors, this cancellation is not perfect, and thus the FCNC processes are allowed as rare decays at higher orders.

The unitary CKM matrix has four independent parameters, which in leading order of the Wolfenstein parameterization [11] are A, λ, ρ and η. In terms of these parameters, the CKM matrix can be written as

$$\begin{pmatrix} V_{ud} & V_{us} & V_{ub} \\ V_{cd} & V_{cs} & V_{cb} \\ V_{td} & V_{ts} & V_{tb} \end{pmatrix} \simeq \begin{pmatrix} 1-\lambda^2/2 & \lambda & A\lambda^3(\rho - i\eta) \\ -\lambda & 1-\lambda^2/2 & A\lambda^2 \\ A\lambda^3(1-\rho-i\eta) & -A\lambda^2 & 1 \end{pmatrix} \tag{1.4}$$

where $\lambda = \sin\theta_c = 0.22$, θ_c is the Cabibbo angle. The parameter η describes CP violation in the SM; a non-zero value of this parameter breaks the CP invariance for weak interactions.

Within the SM, the values of the CKM matrix elements are not defined by first principles. Therefore, the CKM matrix can only be determined experimentally.

Eq. (1.5) list the magnitudes at the 90% confidence level interval [5].

$$\begin{pmatrix} |V_{ud}| & |V_{us}| & |V_{ub}| \\ |V_{cd}| & |V_{cs}| & |V_{cb}| \\ |V_{td}| & |V_{ts}| & |V_{tb}| \end{pmatrix} \simeq \begin{pmatrix} [0.9736, 0.9741] & [0.2262, 0.2282] & [0.0039, 0.0041] \\ [0.2261, 0.2281] & [0.9727, 0.9732] & [0.0414, 0.0423] \\ [0.0075, 0.0085] & [0.0409, 0.0417] & [0.9991, 0.9991] \end{pmatrix} \tag{1.5}$$

These values can either be determined directly from tree-level decays (e.g. the simplest, neutron beta decay or $B \rightarrow \pi l \nu$) or (particularly those involving couplings to the top quark) indirectly from flavor-changing second-order weak processes that involve the up-type quarks in an internal loop (e.g. $K^+ \rightarrow \pi^+ \nu \bar{\nu}$, see Section 1.2.1).

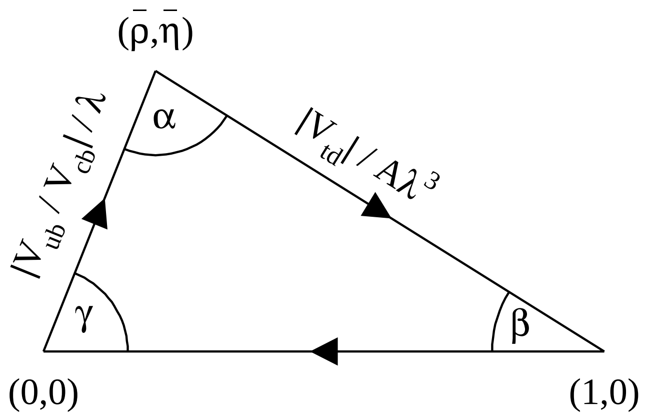

Figure 1.2: Unitarity triangle in the $\rho - \eta$ plane. Two sides of the triangle can be expressed by the CKM matrix elements $|V_{td}|/A\lambda^3$ and $|V_{ub}/V_{cb}|/\lambda$, respectively, where A and λ are parameters in the Wolfenstein parameterization.

The unitarity property, $V^\dagger V = 1$, of the CKM matrix can be summarized in nine conditions. The six conditions for the off-diagonal terms can be represented geometrically as six (unitarity) triangles with equal area, see Fig. 1.2. The condition of interest for the decay $K^+ \rightarrow \pi^+ \nu \bar{\nu}$, involving the CKM element $|V_{td}|$, is

$$V_{ub}^* V_{ud} + V_{cb}^* V_{cd} + V_{tb}^* V_{td} \simeq V_{ub}^* - \lambda V_{cb}^* + V_{td} = 0, \tag{1.6}$$

where the approximations $V_{ud} \simeq V_{tb}^* \simeq 1$ and $V_{cd} \simeq -\lambda$ have been made. This equation can is represented graphically in Fig. 1.2, where both sides of the equation have been divided by λV_{cb}^*. The apex of the triangle in the $\rho - \eta$ plane is given by two improved Wolfenstein parameters, $\bar{\rho}$ and $\bar{\eta}$, where $\bar{\rho} = \rho(1 - \lambda^2/2)$ and $\bar{\eta} = \eta(1 - \lambda^2/2)$. The values of $\bar{\rho}$ and $\bar{\eta}$ are established from several measurements of B meson decays performed by the Bell and BaBar experimental groups, as well as measurements of the indirect CP violation parameter from $K^0 - \overline{K^0}$ mixing, ϵ_K, as shown in Fig. 1.3 [12]. These many measurements of $\bar{\rho}$ and $\bar{\eta}$ statistically agree [5,12] allowing the parameters to be constrained.

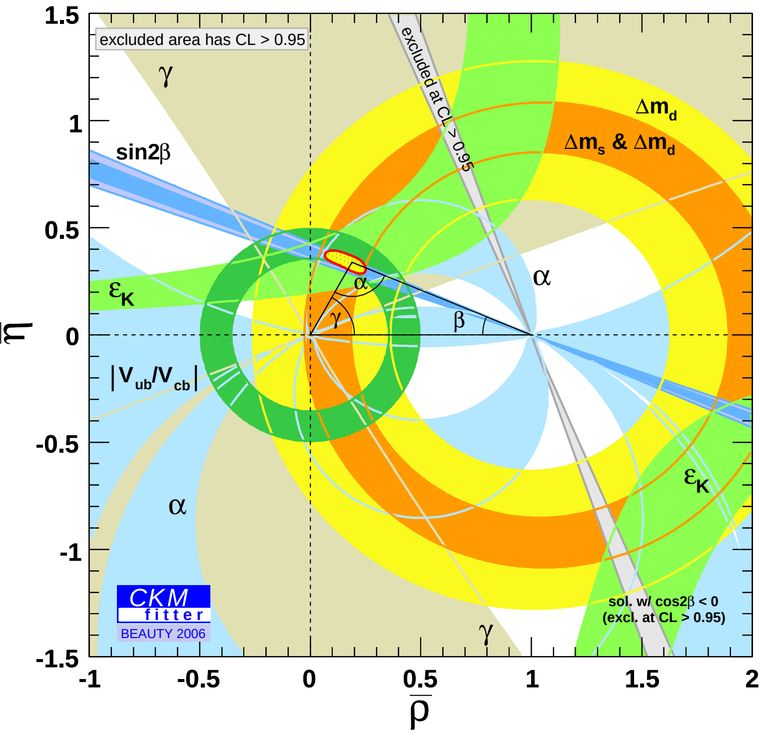

Figure 1.3: The global CKM fit results for the unitarity triangle, using the latest B and K measurements [12]. The results of constraints from the following measurements can be seen: the green annular area comes from the rates of tree-level semileptonic B decays, the orange and yellow ones from B meson oscillation parameters, the blue wedge around angle β, as well as the light blue and brown constraints in the other angles, from CP asymmetries in the rates of hadronic B decays, and the light green hyperbola from indirect CP violation in $K^0 - \overline{K^0}$ mixing.

One method in searching for non-SM physics can be achieved by over-constraining the $\rho - \eta$ apex by many independent measurements. As indicated in Fig. 1.4, determining the $\rho - \eta$ apex independently from B decay and kaon decays can be accomplished by: (1) Measurements of the angle β from $\mathcal{B}(K_L^0 \to \pi^0 \nu\bar{\nu})/\mathcal{B}(K^+ \to \pi^+ \nu\bar{\nu})$ and $B_d^0 \to J/\psi K_s^0$. (2) Comparing $|V_{td}|$ from a $\mathcal{B}(K^+ \to \pi^+ \nu\bar{\nu})$ measurement and mixing frequencies for B_s and B_d mesons from ratio of mass differences $\Delta M_{B_s}/\Delta M_{B_d}$. Any significant disagreement between measurements could only be explained by what is commonly called "new physics." A precise value of $|V_{td}|$ from measuring $\mathcal{B}(K^+ \to \pi^+ \nu\bar{\nu})$, as discussed in the following section, will allow an additional independent constraint on the $\rho - \eta$ apex.

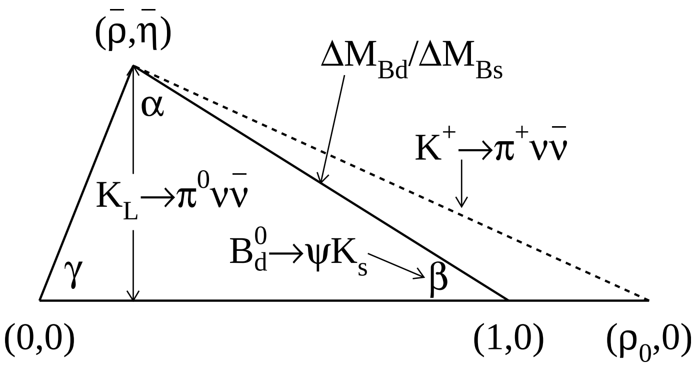

Figure 1.4: Unitarity triangle determined by B and K decays.

CP violation within the SM is not sufficient to explain the observed matter-antimatter asymmetry of the Universe. An especially powerful probe for such new physics is the comparison of the results from B-meson and kaon decays with small theoretical ambiguities. The CKM phase, η, is the only source of CP violation within the current construction of the SM, so precise measurements of all the CKM matrix elements are crucial to either further support SM validity or to discover a SM frailty.

1.2.1 $K^+ \to \pi^+ \nu\bar{\nu}$ Decay

The motivation to measure $\mathcal{B}(K^+ \to \pi^+ \nu\bar{\nu})$ allows an otherwise previously imprecise CKM-matrix element, $|V_{td}|$, to be accurately determined while also probing for non-

SM physics. The decay $K^+ \to \pi^+ \nu\bar{\nu}$ is a FCNC process, prohibited at tree level (see Fig. 1.1). As seen in the Feynman diagrams in Fig. 1.5, $K^+ \to \pi^+ \nu\bar{\nu}$ is allowed as a second-order process.

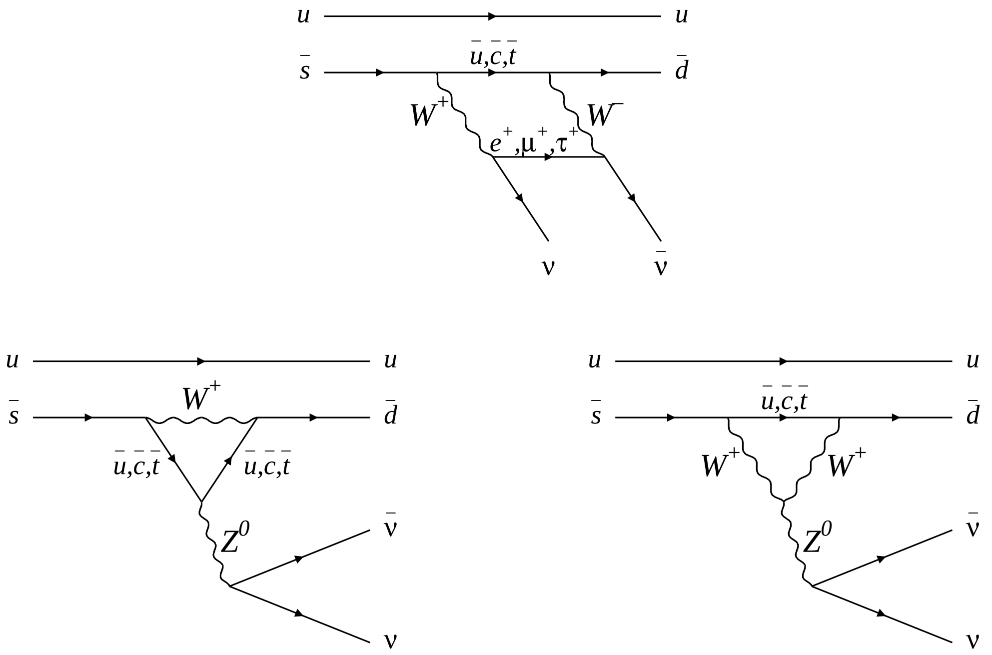

Figure 1.5: Second-order weak processes that contribute to $K^+ \to \pi^+ \nu\bar{\nu}$: the "box" diagram (upper) and two "Z-penguin" diagrams (bottom).

Taking into account only the $\overline{s} \to (\overline{u}, \overline{c}, \overline{t}) \to \overline{d}$ part of the box diagram, the part of the weak-interaction amplitude for this process directly involving quarks is represented as

$$\mathcal{M} \sim \overline{s} \left(\sum_{i=u,c,t} V_{is}^* V_{id} (\gamma^\mu P_L \frac{\not{p} + m_i}{p^2 - m_i^2} \gamma^\nu P_L) \right) d \tag{1.7}$$

where V_{ij}'s are the CKM matrix elements, the γ's are the Dirac matrices, $P_{L/R} = \frac{1 \mp \gamma^5}{2}$ is the left/right-handed projection operator, p is the momentum transfer, and m_i's are the quark masses. The term in the inner parenthesis can be written as

$$\gamma^\mu P_L \frac{\not{p} + m_i}{p^2 - m_i^2} \gamma^\nu P_L = \frac{1}{p^2 - m_i^2} (\gamma^\mu P_L \not{p} P_R \gamma^\nu + m_i \gamma^\mu P_L P_R \gamma^\nu) \tag{1.8}$$

where the relation $\gamma^\nu P_L = P_R \gamma^\nu$ has been used. The second term vanishes because $P_L P_R = 0$, therefore equation 1.7 can be written as

$$\mathcal{M} \sim \bar{s} \left(\sum_{i=u,c,t} \frac{V_{is}^* V_{id}}{p^2 - m_i^2} \gamma^\mu P_L \not{p} \gamma^\nu \right) d \tag{1.9}$$

The smaller the difference in the quark masses the smaller $\mathcal{M}$. If the quark masses are equal, then $\mathcal{M}$ vanishes and this rare K^+ decay becomes the nonexistent K^+ decay. However, the breaking of flavor symmetry, which results in the different quark masses, allows this decay to proceed at a very small rate. Since the mass of the top quark is so much larger than the charm and up quarks (see Table 1.1), $\mathcal{B}(K^+ \to \pi^+ \nu\bar{\nu})$ is very sensitive to the mixing of the top to down quark, i.e. CKM element V_{td}.

The branching ratio (BR) for $K^+ \to \pi^+ \nu\bar{\nu}$ ($\mathcal{B}(K^+ \to \pi^+ \nu\bar{\nu})$) is theoretically calculated by following the convention in [13] and [14]. The effective Hamiltonian in the SM can be written as

$$\mathcal{H}_{eff}^{SM} = \frac{G_F}{\sqrt{2}} \frac{\alpha}{2\pi \sin^2 \Theta_W} \sum_{l=e,\mu,\tau} (V_{cs}^* V_{cd} X^l(x_c) + V_{ts}^* V_{td} X(x_t)) (\bar{s}d)_{V-A} (\bar{\nu}_l \nu_l)_{V-A}, \tag{1.10}$$

where $X(x_j)$ are functions of $x_j \equiv m_j^2/M_W^2$ summarizing the top and charm quark contributions in the loop, including QCD corrections at the next-to-next-to-leading-order (NNLO) level. Using the unitarity of the CKM matrix, the up-quark term vanishes. The dependence on the charged-lepton mass in the loop is negligible for the top-quark contribution. However, the dependence on the τ lepton in the charm-quark contribution is not negligible. Therefore, the perturbative charm contribution is described in terms of the parameter $P_c(X)$ as shown in Eq. (1.11).

$$P_c(X) \equiv \frac{1}{\lambda^4} (\frac{2}{3} X^e + \frac{1}{3} X^\tau) = 0.375 \pm 0.009_{theory} \pm 0.031_{m_c} \pm 0.009_{\alpha_s} \tag{1.11}$$

where $\lambda = \sin\theta_c = 0.2248$ has been used. The errors in (1.11) correspond to the uncertainty in the charm mass, m_c, and the coupling constant, $\alpha_s(M_Z^2)$.

As can be seen from Eq. (1.11), the charm-mass contribution dominates the theoretical uncertainty. Although, this contribution has recently been drastically reduced, to the same order as the other contributions, by recent NNLO calculations described in [14].

The theoretical uncertainty in the dominant contribution for the top quark is very small and is essentially determined by the experimental error on the top-quark mass, m_t. With the top-quark mass $m_t = (162.3 \pm 2.2)$ GeV/c^2 [14],

$$X(x_t) = 1.464 \pm 0.025 \tag{1.12}$$

is obtained and contributes about 4% to the BR uncertainty.

The hadronic part of the $K^+ \to \pi^+\nu\bar{\nu}$ amplitude can be factored out using the tree level $K^+ \to \pi^0 e^+\nu$ decay, whose BR is well known and which is the isospin-rotated $K^+ \to \pi^+\nu\bar{\nu}$ one:

$$< \pi^+|\mathcal{M}|K^+ >= \sqrt{2} < \pi^0|\mathcal{M}|K^+ > \tag{1.13}$$

With these definitions $\mathcal{B}(K^+ \to \pi^+\nu\bar{\nu})$ can be written as

$$\kappa_+ \left[\left(\frac{\mathrm{Im}(\lambda_t)}{\lambda^5} X(x_t) \right)^2 + \left(\frac{\mathrm{Re}(\lambda_c)}{\lambda} (P_c(X) + \delta P_{c.u}) + \frac{\mathrm{Re}(\lambda_t)}{\lambda^5} X(x_t) \right)^2 \right] \tag{1.14}$$

where

$$\kappa_+ = r_+ \frac{3\alpha^2 \mathcal{B}(K^+ \to \pi^0 e^+ \nu)}{2\pi^2 \sin^4\theta_W} \lambda^8 = (5.04 \pm 0.17) \times 10^{-11} \left[\frac{\lambda}{0.2248} \right]^8 \tag{1.15}$$

$\delta P_{c.u} = 0.04 \pm 0.02$ is the long-distance contribution calculated in [15], $\lambda_j \equiv V_{js}^* V_{jd}$ are from the CKM matrix elements. Re and Im are real and imaginary terms, such that $\mathrm{Re}(a+bi) = a$ and $\mathrm{Im}(a+bi) = b$. r_+ ($= 0.901$) represents isospin breaking corrections in relating $K^+ \to \pi^+\nu\bar{\nu}$ to the well-measured leading decay $K^+ \to \pi^0 e^+\nu$ [16]. The values in Eq. (1.16) are employed to determine the result in Eq. (1.15) [17].

$$\sin^2\theta_W = 0.231, \qquad \alpha = \frac{1}{127.9}, \qquad \mathcal{B}(K^+ \to \pi^0 e^+ \nu) = (4.98 \pm 0.07) \times 10^{-2}. \tag{1.16}$$

Eq. (1.14) describes an ellipse in the $\bar{\rho}-\bar{\eta}$ plane with a small eccentricity, that is to say

$$(\sigma\bar{\eta})^2+(\bar{\rho}-\bar{\rho}_0)^2=\frac{\sigma\mathcal{B}(K^+\to\pi^+\nu\bar{\nu})}{\bar{\kappa}_+|V_{cb}|^4X^2(x_t)}, \tag{1.17}$$

where

$$\bar{\rho}_0\equiv 1+\frac{\lambda^4P_c(X)}{|V_{cb}|^2X(x_t)}, \sigma\equiv\left(1-\frac{\lambda^2}{2}\right)^{-2}, \bar{\kappa}_+\equiv\frac{\kappa_+}{\lambda^8}=(7.64\pm0.09)\times10^{-6}. \tag{1.18}$$

Using (1.14) and the NNLO calculations in [14] for $P_c(X)$, $\mathcal{B}(K^+\to\pi^+\nu\bar{\nu})$ is predicted to be

$$\mathcal{B}(K^+\to\pi^+\nu\bar{\nu})=(8.0\pm1.1)\times10^{-11} \tag{1.19}$$

within the SM. The uncertainty of 14% in (1.19) is dominated by the uncertainty of the charm-quark mass.

The measurement of $\mathcal{B}(K^+\to\pi^+\nu\bar{\nu})$ is regarded to be one of the cleanest ways to extract $|V_{td}|$ for the following reasons:

- Long-distance contributions to the BR are negligible (at most 10^{-13}) [18, 19].
- The uncertainty from the hadronic matrix element has been removed by using $\mathcal{B}(K^+\to\pi^0e^+\nu)$.
- The remaining theoretical uncertainties (7%) are relatively small and reliable as compared with the errors in other K and B decays.

1.3 Beyond the Standard Model

Since $K^+\to\pi^+\nu\bar{\nu}$ is a second order process, a precise measurement of the branching ratio can investigate whether there are non-SM effects involved in this decay mode. A possible discrepancy between the measured branching ratio and the SM prediction would indicate the existence of new physics beyond the SM. The first measurements of $\mathcal{B}(K^+ \to \pi^+\nu\bar{\nu})$ put limits in fourth-generation theories, SUSY and fifth-force theories [18]. The B sector measurements of the CKM elements are now precise enough to determine ρ and η so that independent measurements of K decays could determine if any non-SM physics exist, as shown in Fig. 1.6.

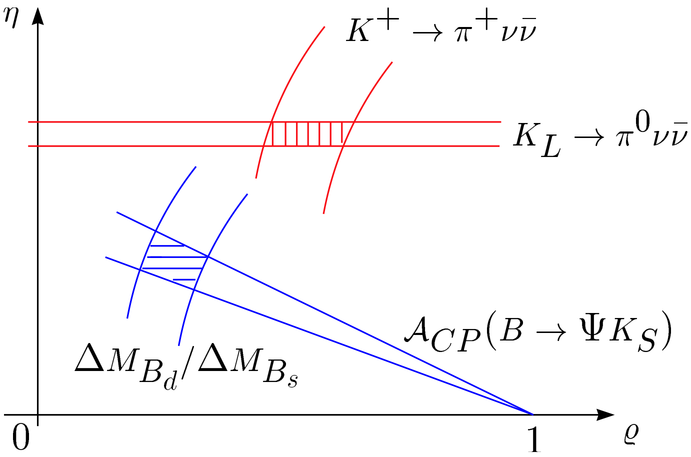

Figure 1.6: Schematic determination of the unitarity triangle apex (ρ,η) from the B system (blue horizontal hatches) and from the $K \to \pi\nu\bar{\nu}$ decays (red vertical hatches). The K$^+$ measurements can be performed with small theoretical uncertainties, therefore any discrepancy between the K$^+$ and B determinations, as illustrated in this hypothetical example [20], would indicate new physics.

The information that is currently being used to constrain the unitarity triangle is obtained only from the charged-current processes (i.e. tree-level amplitudes) and the $\Delta S, \Delta B = 2$ loop-induced processes. For example, determinations of ρ and η can be obtained from the $B_d^0 - \bar{B}_d^0$ mixing and the CP asymmetry in $B_d^0 \to J/\psi K_s^0$, both of which are mediated by $\Delta B = 2$ loop-induced processes. On the contrary, $K^+ \to \pi^+\nu\bar{\nu}$ and $K_L^0 \to \pi^0\nu\bar{\nu}$ are mediated via the $\Delta S = 1$ FCNC transition. New physics may therefore be seen in a discrepancy between K and B decays [20].

Several SM extensions to new physics would affect $\mathcal{B}(K^+ \to \pi^+\nu\bar{\nu})$. In the Minimal Flavor Violation (MFV) model, $\mathcal{B}(K^+ \to \pi^+\nu\bar{\nu})$ is allowed to be as large as 1.9×10^{-10} [21]. In this model, the origin of CP violation and quark mixing comes from the CKM matrix as in the SM, and from process-independent universal master functions, which are real and which in the SM reduce to the Inami-Lim functions [22].

In the "Enhanced Z^0 Penguin" model [23], where a new imaginary phase is introduced, $\mathcal{B}(K^+ \to \pi^+ \nu\bar{\nu})$ is expected to be almost the same as the SM prediction. However, the $K_L^0 \to \pi^0 \nu\bar{\nu}$ branching ratio is predicted to be $(3.1 \pm 0.1) \times 10^{-10}$, which is 10-times larger than the SM prediction, and is close to the Grossman-Nir limit, $\mathcal{B}(K_L^0 \to \pi^0 \nu\bar{\nu})/\mathcal{B}(K^+ \to \pi^+ \nu\overline{\nu}) < 4.4$ [24]. Another interesting prediction derived from this model is that the value of $\sin 2\beta$ obtained from $K \to \pi\nu\bar{\nu}$ is not equal to that obtained from $B_d^0 \to J/\psi K_s^0$.

Since a detection of the $K^+ \to \pi^+ \nu\bar{\nu}$ decay in practice detects the transition $K^+ \to \pi^+ + \text{nothing}$, limits can be set for the $K^+ \to \pi^+ X^0$, where X^0 is a massless weakly interacting particle such as a familon [18]. Such a limit from the E949 measurements currently exists at $\mathcal{B}(K^+ \to \pi^+ X^0) < 0.73 \times 10^{-10}$ [25].

Additionally, the lower π^+-momentum phase-space studied in this thesis, is also sensitive to a different shape of the π^+ spectrum, resulting from scalar or tensor interactions as opposed to the SM vector spectrum. Therefore, extra information in addition to just the value of the BR can be extracted from such a measurement.

Chapter 2

The Experiment

The quest to discover the $K^+ \to \pi^+\nu\bar{\nu}$ decay began over thirty years ago leading to the discovery of the decay at BNL twenty-five years later; this quest is summarized in Fig. 2.1.. The search for $K^+ \to \pi^+\nu\bar{\nu}$ at BNL began in 1983 as experiment E787 began to take shape. Experiment E787, collecting data from 1988 until 1991, improved the upper-limit on the BR of $K^+ \to \pi^+\nu\bar{\nu}$ by two orders of magnitude [26–28]. After detector upgrades in 1992 and 1993 [29], E787 obtained data in 1995, 1996, and 1997 yielding two events [30–32]. Further upgrades and a name change to E949 yielded another event in 2002. These three events were observed within the "PNN1" signal region, nominally 211 MeV/c $\leq P_{\pi^+} \leq$ 229 MeV/c (see Fig. 2.2), resulting in a combined branching-ratio measurement of $(1.47^{+1.30}_{-0.89}) \times 10^{-10}$ [25]. Although the measured BR is consistent with the SM prediction, Eq. (1.19), the central value is twice the predicted value leading to speculation of possible new physics.

Additional efforts were done during E787 to measure $\mathcal{B}(K^+ \to \pi^+\nu\bar{\nu})$ within the "PNN2" momentum region, 140 MeV/c $\leq P_{\pi^+} \leq$ 195 MeV/c, obtaining an upper limit of 2.2×10^{-9} [33–35]. The PNN2 region has significantly more background than the PNN1 region. Thus, PNN2 results have a smaller impact upon a combined BR

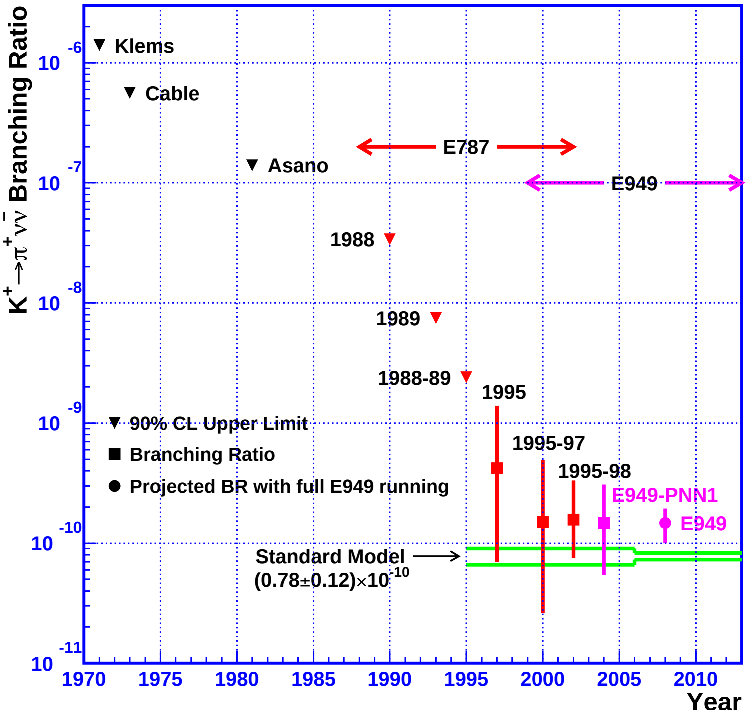

Figure 2.1: History of the search for $K^+ \to \pi^+\nu\bar{\nu}$. The vertical axis is $\mathcal{B}(K^+ \to \pi^+\nu\bar{\nu})$ and the horizontal axis is the publication year. The projected E949 value assumes that the central value of the branching ratio remained what the combined E787 and E949 results had found, $(1.47^{+1.30}_{-0.89}) \times 10^{-10}$ [25]. The error bars show the 68% CL intervals.

measurement.

2.1 Experimental Considerations

Constraints from theoretical expectations and detection limitations molded the implementation of the detectors for E949. Problems from a number of backgrounds are immediately illuminated when observing the rarity of the $K^+ \to \pi^+\nu\bar{\nu}$ decay as predicted by the SM, Eq. (1.19). Therefore, the emphasis on detector design is to detect background processes and remove them from consideration as early as possible.

The weakly-interacting nature of neutrinos[1] reduces the observable products of $K^+ \to \pi^+\nu\bar{\nu}$ to be a to be just a single π^+. For PNN2, a signal π^+ has a nominal momentum of 140 MeV/c $\leq P_{\pi^+} \leq$ 195 MeV/c. The necessity to have as many K$^+$ decays as possible by having a high-rate K$^+$ beam is obvious due to the rarity of $K^+ \to \pi^+\nu\bar{\nu}$. Considering the signature is a π^+, having a particle beam with a high K$^+$/π^+ ratio is desired to reduce backgrounds from π^+-beam particles being misidentified as a K$^+$-decay product.

An important experimental constraint, imposed by E787 and E949, was requiring the K$^+$ to be at rest when a decay occurs. This has the benefit of identifying the two largest K$^+$ branching-fractions, $K^+ \to \mu^+\nu$ and $K^+ \to \pi^+\pi^0$ with branching ratios of 0.63 and 0.21 respectively (see Table 2.1), by kinematics. As shown in Fig. 2.2, the charged product of these two-body decays have a specific momentum, which can be highly suppressed by precise kinematic measurements. To measure the momentum of the charged product a magnetic field and tracking system capable of detecting the charged particles track are required.

As seen in Table 2.1, or the more detailed Table 3.1, and Fig. 2.2, the momentum of many K$^+$ decays occur within the momentum of signal events, 140 MeV/c $\leq P_{\pi^+} \leq$ 195 MeV/c. Accurate and independent measurement of other kinematic quantities such as energy would aid in determination of the decay mode.

In addition to π^+'s, K$^+$ decays produce μ^+'s and e$^+$'s which could be difficult to discern from a signal π^+ solely by energy and momentum measurements. Therefore, independent particle identification (PID) techniques are necessary. One PID method involves measuring the distance traversed by the charged product in material (range). Since K$^+$'s, π^+'s, μ^+'s, and e$^+$'s have different dE/dX each particle will have a different range for a given energy or momentum. Another PID method includes

---

[1] Neutrinos can travel light-years through lead without interacting, which is the reason the current neutrino detectors [7] are so massive. Hence, the ability of any experiment in the conceivable future, outside a *Star Trek* episode, to detect a neutrino from a given 'event' is nonexistent.

Background	Branching Ratio
$K^+ \rightarrow \mu^+\nu$ ($K_{\mu 2}$)	0.6343
$K^+ \rightarrow \pi^+\pi^0$ ($K_{\pi 2}$)	0.2092
$K^+ \rightarrow \pi^+\pi^0\gamma$ ($K_{\pi 2\gamma}$)	0.000275
$K^+ \rightarrow \pi^0\mu^+\nu$ ($K_{\mu 3}$)	0.0332
$K^+ \rightarrow \mu^+\nu\gamma$ ($K_{\mu 2\gamma}$)	0.0062
$K^+ \rightarrow e^+\nu$ (K_{e4})	0.000041
Beam backgrounds	-
CEX: $K^+n \rightarrow K^0p$	$R_{K_L} = 2.8 \times 10^{-5}$
$K_L^0 \rightarrow \pi^+\mu^-\bar{\nu}$	0.1350
$K_L^0 \rightarrow \pi^+e^-\bar{\nu}$	0.1940

Table 2.1: Background processes to the decay $K^+ \rightarrow \pi^+\nu\bar{\nu}$ with their Branching Ratios [5]. CEX stands for Charge Exchange, and R_{K_L} is the K_L production rate as found in [36]. A more complete list of K$^+$ decays is in Table 3.1.

observing the decay chain $\pi^+ \rightarrow \mu^+\nu_\mu \rightarrow e^+\bar{\nu}_e\nu_\mu$ which occurs $\sim 100\%$ of the time [5].

A very powerful method of identifying decay modes includes the observation of photons. Since a π^0 decays into two photons 98.8% ($e^+e^-\gamma$ 1.2%) of the time and π^0 has a very short lifetime of 8.4×10^{-17} s [5], any K$^+$ decay with a π^0 product can be flagged by identifying photons in coincidence with the time of decay.

The following sections will detail how E949 employed the experimental constraints and ideas discussed in this section.

2.2 E949 Detector Overview

The E949 detector, as seen in Fig. 2.3, is composed of beam-line instrumentation, a K$^+$-decay region (Target), a drift chamber, plastic-scintillator charged-track detectors (Range Stack), and photon detectors. K$^+$ particles enter the detector via the Low-Energy Separated Beam-Line III (LESBIII) [37] at BNL's Alternating Gradient Synchrotron (AGS), see Appendix A for further information. LESBIII produced 2.2 s

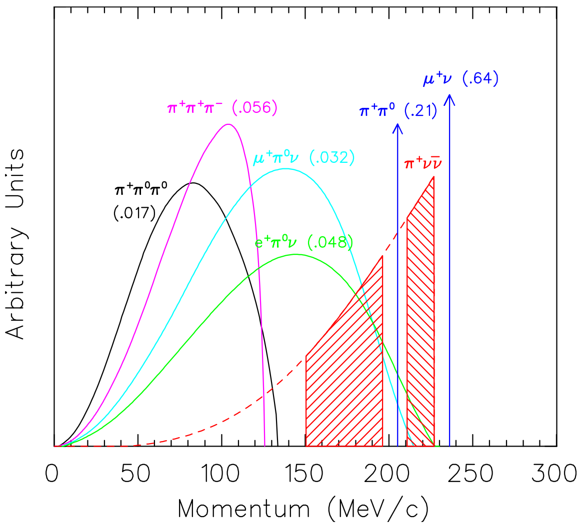

Figure 2.2: Spectra of the most common K$^+$ decay modes, along with the Standard Model spectrum for $K^+ \rightarrow \pi^+\nu\bar{\nu}$ (shown in red line). The branching ratios of the various decay modes are shown in parentheses.

long K$^+$ bunches, commonly referred to as spills, which arrive every 5.4 s. 3.5×10^6 K$^+$'s from each bunch enter the decay region; beamline running conditions for the E949 experiment are cataloged in [38].

A solenoid magnet that surrounds the detector region where the track of the charged particle will be observed creates a 1 T magnetic field pointing in the positive-z direction (downstream). The coordinate system (and origin) is defined by the center of the drift chamber; the x-y center of the decay-region detector is positioned to be near the origin. As observed in Fig. 2.3, the z-axis and y-axis are defined to be the horizontal and vertical directions, respectively. The K$^+$ beam travels in the positive-z direction.

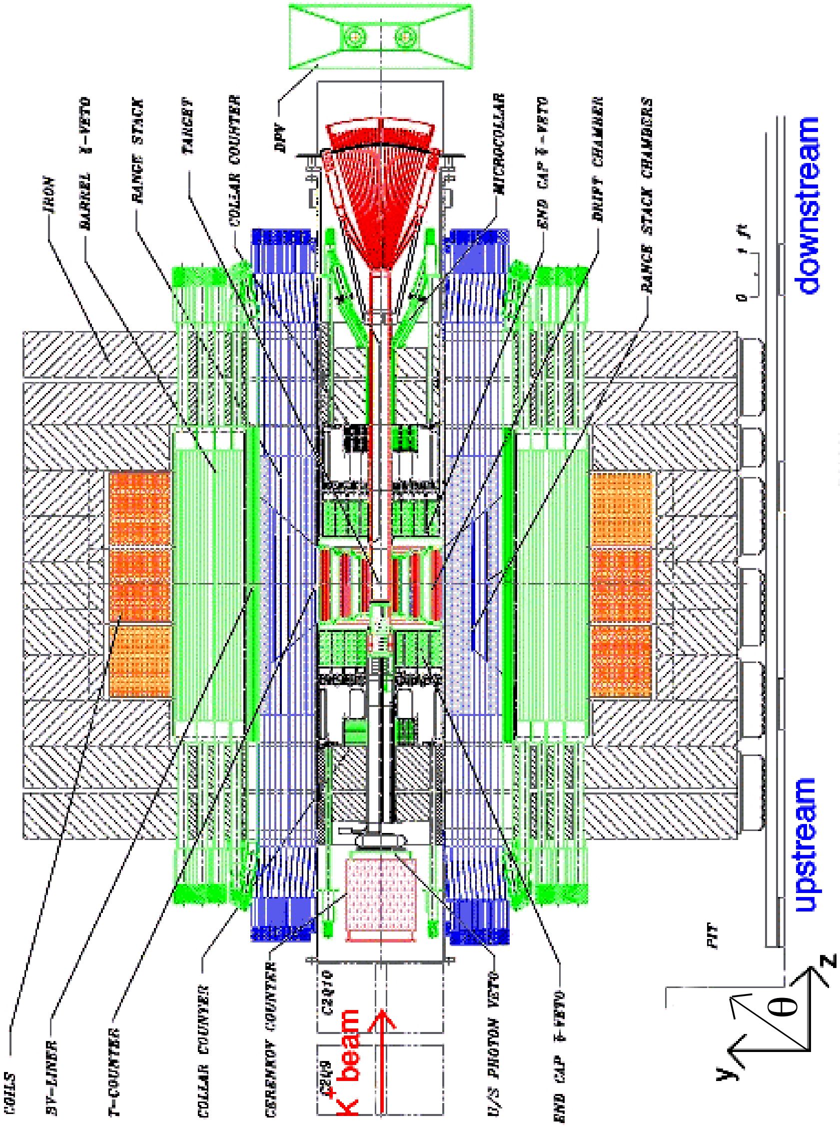

Figure 2.3: Side-view schematic of E949 detector.

A beam particle will traverse a large scintillation counter, a Čerenkov counter, Upstream Photon Veto, two beam wire proportional chambers, a passive BeO degrader, Active Degrader, and a beam hodoscope. The K^+ will come to rest in the decay-region detector. The charged product(s) will traverse the Target, Drift Chamber, and come to rest within the Range Stack. Any photons from the decay will be observed by one or a few of the numerous photon detectors.

The B0 counter is located upstream of the Čerenkov counter and counted all charged particles in the beam. B0 does not enter into the analysis and is mention here for completeness.

2.3 Čerenkov Counters

Since the beam intensity was very high and the beam contained pions with a ratio of $K^+ : \pi^+ = 3 : 1$[2], a single K^+ entering the decay region should be identified by the beam instrumentation. It has three roles: K^+ identification, slowing down the K^+, and the detection of extra beam particles if they exist at the K^+-beam time (time at which the K^+ entered the detector) or the K^+-decay time.

The K^+ beam from LESBIII first enters the Čerenkov counter located just downstream of the last quadrupole magnet (Q10) and 2 m upstream of the Target. A side view and cross section of the Čerenkov counter is shown in Fig. 2.4.

The refractive index (n) of the 2.5 cm thick acrylic radiator is 1.49, providing a threshold for Čerenkov radiation of $\beta_{\check{C}} = 1/n = 0.671$ and a threshold for total internal reflection of $\beta_{ref} = \sqrt{1/(n^2-1)} = 0.905$. K^+'s and π^+'s with a momentum of 710 MeV/c have $\beta_{K^+} = 0.82$ and $\beta_{\pi^+} = 0.98$, respectively; the Čerenkov light from K^+'s (π^+'s) was transmitted (reflected) at the downstream surface of the

---

[2] Initially K^+:π^+ = 4:1, however due to a AGS separator high-voltage problem the K^+:π^+ ratio became 3:1 and remained that for most of the data collection.

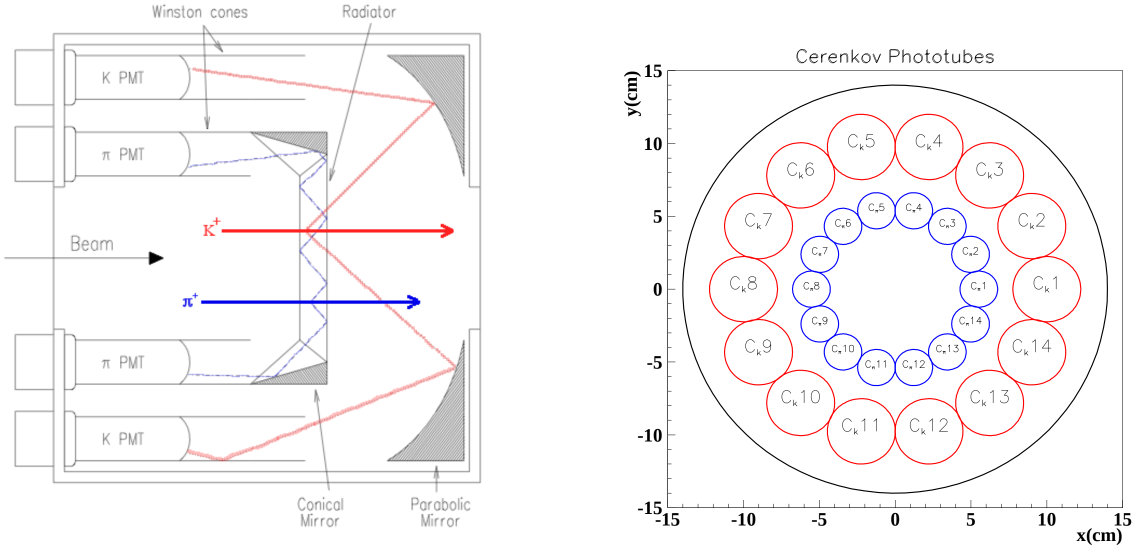

Figure 2.4: Schematic sideview of Čerenkov Counter (left) and endview of PMT configuration (right). The K$^+$, Čerenkov light from the K$^+$, and the K$^+$ PMTs are denoted in red while that of the π^+ is shown in blue.

Čerenkov radiator. The Čerenkov light from a K$^+$ within the radiator was reflected by a parabolic mirror to the outer ring of 14 photomultiplier tubes (PMT). The set of 14 PMTs are referred to as the K$^+$ Čerenkov counter (Č$_K$). However, the Čerenkov light from a π^+ was internally reflected within the radiator and directed to the inner ring of 14 PMTs (π^+ Čerenkov counter, Č$_\pi$). The PMT signals were split, with 90% fed to time-to-digital converters (TDCs) via discriminators and 10% fed into a ×10 amplifier and then to 500 MHz transient digitizers based on gallium-arsenide (GaAs) charge-coupled devices (CCDs) [39]. Every 2 ns pulse-height information was recorded in CCDs to reproduce the time development of the pulses and to detect two particles close in time to each other. The number of photoelectrons in all PMTs provided additional particle identification. At the trigger level the number of Čerenkov discriminator channels firing (typically 5) was used to identify K$^+$'s and π^+'s. Offline analysis treated all PMT hits coincident with each other as a cluster. Multiple incoming beam particles (additional K$^+$'s or π^+'s) may also be in coincidence with the K$^+$ initiating the Č$_K$ triggering condition. This extra particle can cause an additional cluster when passing through the Čerenkov counter. A K^+ was therefore identified by requiring that the $\check{C}_K$ had only one hit cluster. Pile-up signals may result from two close-in-time incoming particles firing the same PMTs. Since these pile-up signals may not be identified by the TDCs, pulse shapes were recorded by CCDs allowing offline discrimination of the two particles.

2.4 Upstream Photon Veto

Downstream of the Čerenkov counter there is the Upstream Photon Veto (UPV) detector (see Fig. 2.5). This is made of 12 layers of square sheets of plastic scintillator, 28.4 cm × 2 mm, alternating with square lead (or copper) sheets. The six most downstream lead sheets are 1 mm thick and the five most upstream sheets are 2 mm thick. The downstream-most layer of lead was replaced by 2.2 mm thick copper, which formed part of the box holding the layers together. The upstream side of the box is made by 3.175 mm thick aluminum. The detector has a 175 mm wide by 40 mm high slot in the center to allow the beam to pass through. UPV is divided horizontally in two modules with a PMT attached to each module. Each scintillator segment had 21 wavelength shifting (WLS) fibers embedded into grooves in the scintillator. As shown in Fig. 2.5, the fibers from each segment were bundled and attached to a PMT. The signals from each PMT were fed to a TDC, an ADC and a CCD.

Although the UPV was originally designed as a photon detector for the photons that travel in the upstream direction, the beam rate was too large and overwhelmed the UPV. Therefore time, energy and CCD pulse information from UPV was used to veto beam particles coincident with the K^+ decay time.

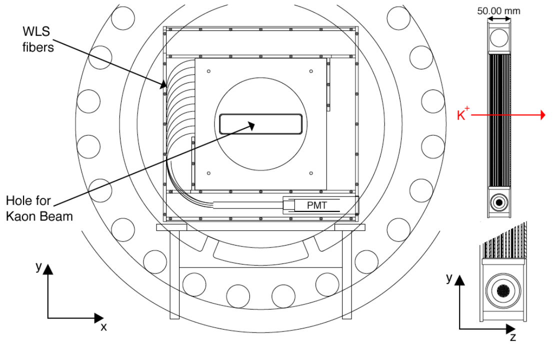

Figure 2.5: Upstream-Photon-Veto schematic as looking downstream. The bulk of the K^+ beam travels through the horizontal slot near the center. A cross-section is shown on the right and a enlarged cross-section to the bottom right.

2.5 Beam Wire Chambers

Two beam wire proportional chambers (BWPCs), filled with a mixture of Tetrafluoromethane (CF4) (80%) and Isobutane (20%), were located downstream of the UPV. BWPCs monitor the beam profile and is able to identify multiple incoming charged particles. Cross-sectional views of the BWPCs are shown in Fig. 2.6. The first chamber (BW1) consists of three planes (U, V, and X) of anode wires $\sim$ 20 cm long. The direction of the 0.012 mm diameter gold-plated tungsten wires in the X-plane is vertical and in the U- and V-planes are at ±45° to the vertical plane respectively. The BW1 has 72, 60 and 60 read-out channels for the X-, U- and V-planes, respectively, with a 2.54 mm wire spacing. The spatial resolution is 1.54 mm. The cathode foils are 0.025 mm thick aluminized mylar coated with carbon. The anode-cathode distance is 3.175 mm.

The second chamber (BW2) is located at 90 cm downstream of the BW1 and consists of three planes (U, V and X) of anode wires $\sim$ 10 cm long. Each plane has 24 read-out channels with a 2.40 mm wire spacing in the central region and eight channels with a 4.80 mm wire spacing in the peripheral region (19.2 mm on

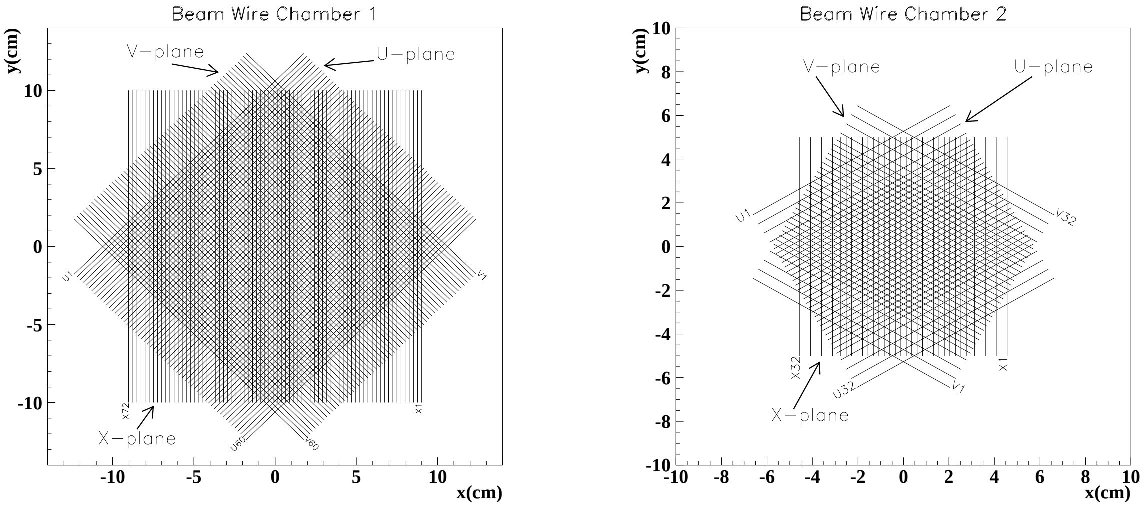

Figure 2.6: Cross-sectional views of the beam wire proportional chambers: the upstream BW1 (left) and the downstream BW2 (right). Only the first and last wire numbers of each plane are listed (others are omitted for picture clarity).

each end). The cathode foils are 0.008 mm single-side aluminized mylar coated with carbon. The anode-cathode distance is 1.5875 mm.

2.6 Degraders

An inactive cylindrical degrader (ID) is located downstream of BW2. The sole purpose of the ID is to slow down the K^+'s, so that they come to rest in the decay region. The thickness of the ID was determined such that a 710 MeV/c K^+ will come to reset in the middle of the E949 decay-region. The ID has two segments; the upstream segment is 111.1 mm of beryllium oxide (BeO) and downstream portion is 4.76 mm of Lucite. BeO, with high density and low atomic-number, allows a large degrading of the energy while minimizes multiple scattering

As shown in Fig. 2.7, the Active Degrader (AD), whose upstream face is adjacent to the downstream face of the ID, consists of 40 layers of 2 mm thick scintillator

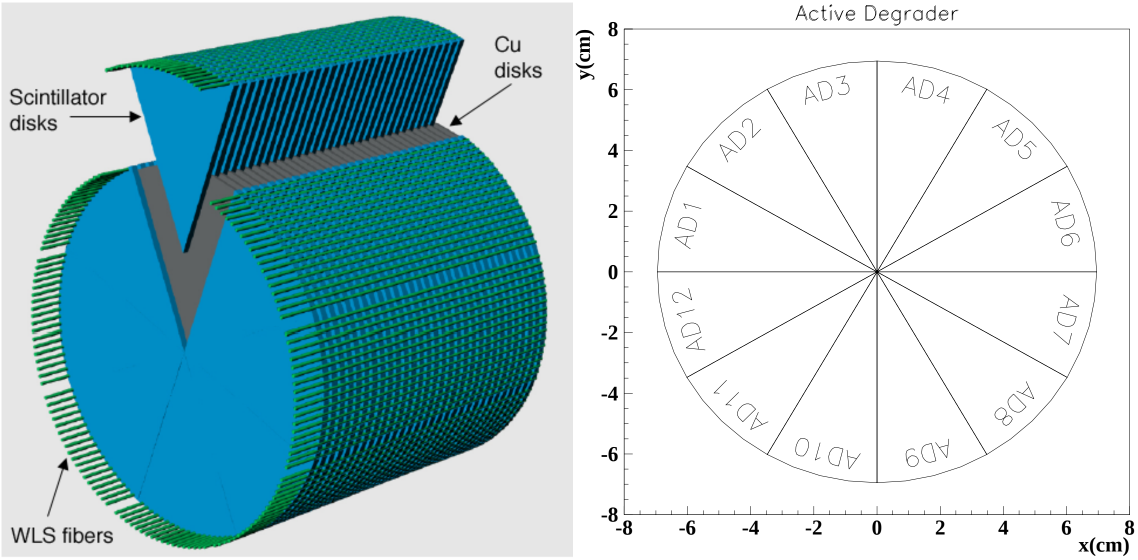

Figure 2.7: Schematic of Active Degrader (left) and cross section (right).

disks (139 mm in diameter) alternating with 2 mm thick copper disks (136 mm in diameter). The AD is split into 12 azimuthal segments. The scintillation light in each segment is sent to a single PMT through 14 wave length shifting (WLS) fibers running in grooves cut into the perimeter of the disks. The PMT outputs are fed to TDCs and CCDs. The signals from four PMTs are multiplexed and fed to a single analog-to-digital converter (ADC). Signals from sectors 1-4, 5-8, 9-12 are grouped together and feed to ADCs. Using this information, the AD has the ability to identify the beam particles and to detect activity coincident with K^+ decays, such as photons.

2.7 Beam Hodoscope

Downstream of the AD and just upstream decay-region detector is a Beam Hodoscope (B4). The B4, as shown in Fig. 2.8, measures the beam particle position which is matched to the target position information. The B4 also identifies the particle as a K^+ or π^+ by measuring the energy deposit, in effect measuring dE/dX.

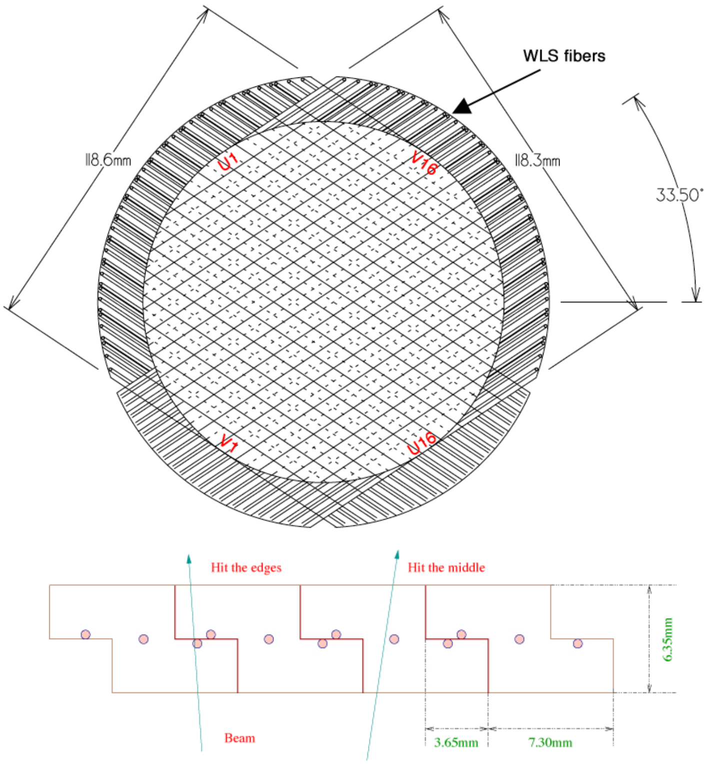

Figure 2.8: End view of the B4 Hodoscope (top). Downstream (upstream) segments have solid (dotted) outlines. Schematic cross section of the B4 Hodoscope (bottom) shows the approximate position of the three wavelength shifter fibers (small circles) in each segment. Arrows indicate difference situations of beam particles passing through the B4 Hodoscope.

The B4 Hodoscope consisted of two planes, U and V, each with a diameter of 119 mm and oriented at a 33.40° and 123.40° angle to the horizontal. Each plane had 16 scintillator segments with a 7.2 mm pitch. The cross section of each segment had a ‘Z-shape’, as shown in bottom of Fig. 2.8, with a 6.35-mm thick middle part and 3.175-mm thick edges. The z-shape reduced inactive regions and improved the spatial resolution.

Three WLS fibers are embedded in each segment and fed to a single PMT that was read out by TDCs, ADCs and CCDs. The CCD signals were fit with both single-pulse and double-pulse assumption to identify multiple incoming particles during a short time period and to detect pile-ups [40].

At the same z-position as the B4 Hodoscope, but at larger radius was a ring of scintillator, the ring veto (RV). The RV was designed to veto particles that passed through the dfperimeter of the B4 Hodoscope. The RV was composed of two 180° arcs of 3.27 mm thick scintillator with an inner diameter varying from 118.5 mm to 120 mm and an outer diameter of 145.5 mm. Each RV element was read out to a PMT and the signal was split three ways to ADCs, TDCs and CCDs [40]

2.8 K^+-Decay Region

After passing through all beam elements and being slowed down by the degraders, $\sim 3.9 \times 10^6$ K^+'s per spill enter the scintillating-fiber detector (Target, TG) located in the center of the spectrometer. Within the TG, the K^+ will lose more energy, come to rest, and eventually decay (or traverse radially outside the TG).

The TG consists of 413 5-mm square and 3.1-m long plastic scintillating fibers that are bundled to form a 12-cm diameter cylinder. Edge fibers, filling the gap between the TG and I-Counter, consist of 128 3.5-mm, 128 2.0-mm, and 64 1.0-mm square fibers. End and side views of the Target are shown in Fig. 2.9.

Each 5.0 mm fiber was connected to a PMT. However, the edge fibers are multiplexed into 16 groups such that each group was connected to a single PMT; each group was composed of eight 3.5 mm, eight 2.0 mm, and four 1.0 mm fibers. The PMTs are read out by ADCs, TDCs and CCDs. K^+'s, whose velocities are small, typically lose a large amount of energy (tens of MeV) in each fiber.

Since π^+'s from K^+ decays are minimum-ionizing particles in the TG, π^+'s loose ~ 1.25 MeV per fiber. Pattern recognition was performed, see Appendix B, using

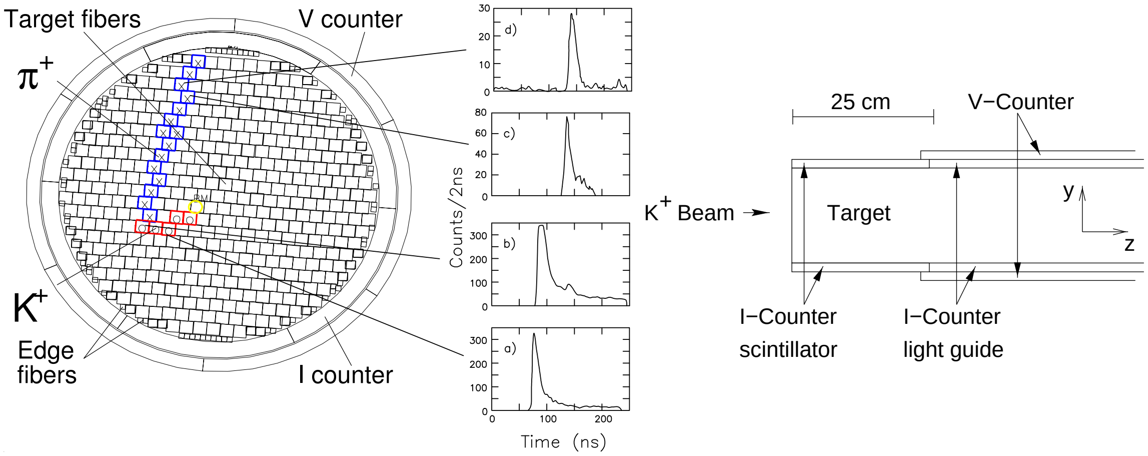

Figure 2.9: End (left) and side (right) views of the Target. The CCD pulse-shape information was used to find kaon and pion clusters, as shown in the left figure. The lower two plots ((a) and (b)), are CCD pulses for a kaon, and the upper two plots ((c) and (d)), are those for a pion. Two layers of six plastic scintillators, the I-Counter (IC) and V-Counter (VC), surround the Target.

all available information, to find fibers belonging to the K^+'s path and the π^+'s (or other charged product's) path. A double-pulse fit was performed on the CCD pulses from all hit fibers to identify energy deposit from the π^+ in fibers were the K^+ also deposited energy. This is especially useful in determining the decay-vertex (the fiber where the K^+ decay occurs) location. Accurate identification of the decay vertex gives a better estimate for the π^+ range. Measuring the energy of the second pulse, due to the π^+, yields a better estimate for the total energy of the π^+; without the double-pulse fit the energy from the π^+ would be lost within the K^+ energy loss within the TG. Each fiber had a thin layer of inactive cladding 0.009-cm thick which surrounded the fiber.

The fiducial region of the Target was restricted by two cylindrical rings of plastic-sintillator. Each ring was segmented into six elements that surround the Target (see Fig. 2.9). The inner-scintillator ring (I-Counter, IC) tags charged decay products before they enter the drift chamber; this was used by the trigger, see Section 2.12. The IC was 6.4 mm thick with an inner radius of 6.0 cm and extends 24 cm downstream from the upstream face of the Target. Each IC segment was instrumented with a PMT which was read out by an ADC, a TDC, and a 500 MHz transient digitizer (TD) based on flash ADC [41].

The outer ring of scintillator, called the V-Counter (VC), overlaps the downstream edge of the IC by 6 mm. The VC detects particles that decay downstream of the fiducial region of the TG. The VC is 5 mm thick, 1.96 m long. To prevent gaps each element was rotated 30° with respect to the IC elements. Each scintillator was instrumented with a PMT which was read out by an ADC and a TDC.

2.9 Tracking Chamber

The trajectory of the charged track was measured by a drift chamber, referred to as the “Ultra-Thin Chamber” (UTC) due to it’s low mass. The UTC was located 1.2 cm radially outside the IC. The 1 T magnetic field bends positively charged particles clockwise as seen looking upstream (see Fig. 2.3). The primary functions of the UTC are measuring the momentum of charged particles and providing a matching between the tracks in the Target and in the detector radially outside the UTC (Range Stack).

The UTC has a length of 51 cm and inner and outer radii of 7.85 cm and 43.31 cm respectively. It is composed of 12 layers of drift cells, grouped into three superlayers. As shown in Fig. 2.10, the inner superlayer has four layers of 48 cells, the middle superlayer has four layers of 96 cells, and the outer superlayer has four layers of 144 cells.

Each cell is composed of nine axially-strung wires. A single anode wire, made of gold-coated tungsten with a 20 μm diameter, is surrounded by eight cathode wires made of gold-coated aluminum with a 100 μm diameter, which are arranged in a square, see upper left of Fig. 2.10. Adjacent cells share the cathode wires at the boundaries. The cells in each layer are staggered by one-half cell with respect to the

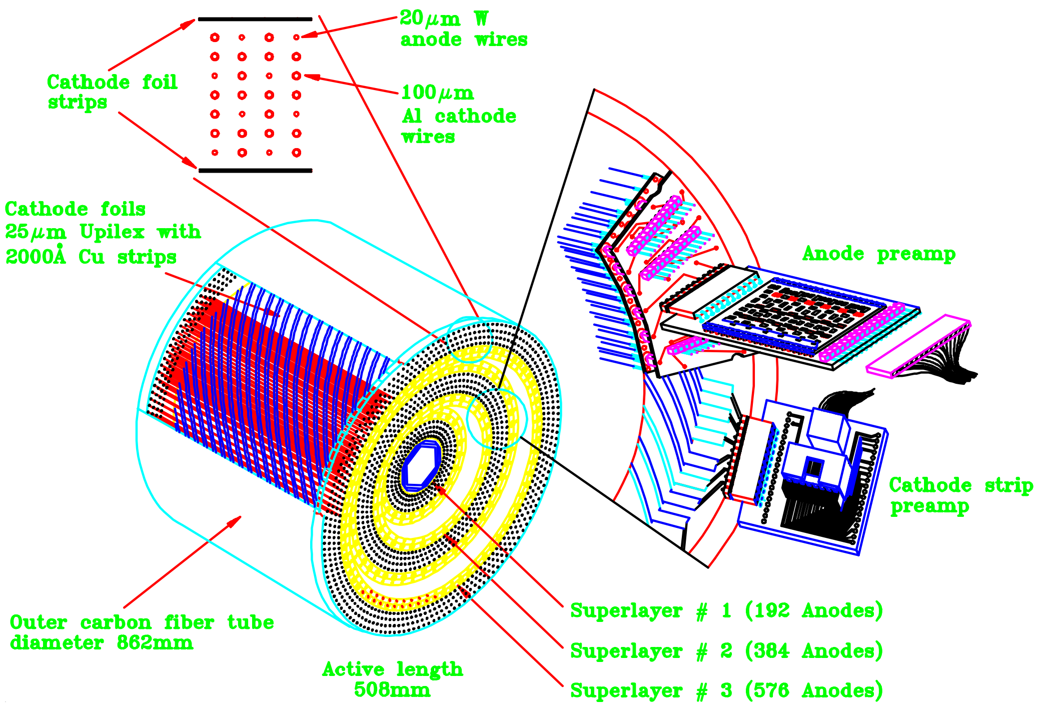

Figure 2.10: Schematic view of the Ultra-Thin Chamber.

neighboring layers, in order to resolve left-right ambiguity. The superlayers are filled with a gas mixture composed of argon (49.6%), ethane (49.6%) and ethanol (0.8%). The cathode wires are grounded and the anode wires are maintained at 2 kV (gain $= 8 \times 10^4$, drift velocity $= 5$ cm/μs). Each anode wire is instrumented with an ADC and a TDC. The drift time to the anode wires provides x-y positions for charged tracks.

Helical arrays of cathode strips are at the inner and outer surface of each superlayer; the pitch angle is 45° (see "Cathode foils" in Fig. 2.10). The strips, with a width of 7 mm, are made of 1200 Å thick copper coated with 300 Å thick nickel, and are mounted on a 25 μm thick Kapton® foil. The separation between the strips is 1 mm. The cathode foils have 48, 72, 108, 144, 180, and 216 strips from the inner to the outer layers, respectively; each strip is read out by an ADC and TDC. The z position of a charged track is measured from the energy-weighted mean of the cluster of hit strips. The resolution for a z-position measurement is about 1 mm.

There are two inactive regions filled with nitrogen gas between the three superlayers. The differential pressure in the five gas volumes supports the interior cathode foils; support tubes held the innermost and outermost foils. The total mass in the active region of the UTC, excluding the inner and outer support tubes and innermost and outermost foils, amounts to only 2×10^{-3} X_0 (radiation-lengths).

The momentum resolution ($\Delta P/P$) for the two body decays $K_{\pi 2}$ and $K_{\mu 2}$ is 1.1% and 1.3% [36], respectively. Further details regarding the UTC are available in [42].

2.10 Range Stack

A thick barrel of plastic scintillator (Range Stack, RS[3]), located $\sim$ 2 cm radially outside the UTC, is the region where the π^+ from a K^+ decay comes to rest. The primary functions of the Range Stack (RS) are energy and range measurements of charged particles and their identification. It is also used as a photon detector, with ~ 1 X_0. The RS extends radially from 45.08 cm to 84.67 cm. The RS is segmented radially into of 19 layers of plastic scintillators and azimuthally segmented into 24 sectors (see Fig. 2.11). Each of the 456 RS elements, are “light tight” and within each sector layers 2-5, 6-10, 11-14, 15-18, 19 are bound together with Kapton® tape into modules, such that there is minimal space between each element within a module. Each RS module is held in place by the “spider-web” detector superstructure, forming a gap between modules.

---

[3] RS is commonly abbreviated as ‘RD’ within E949 technical notes and analysis code.

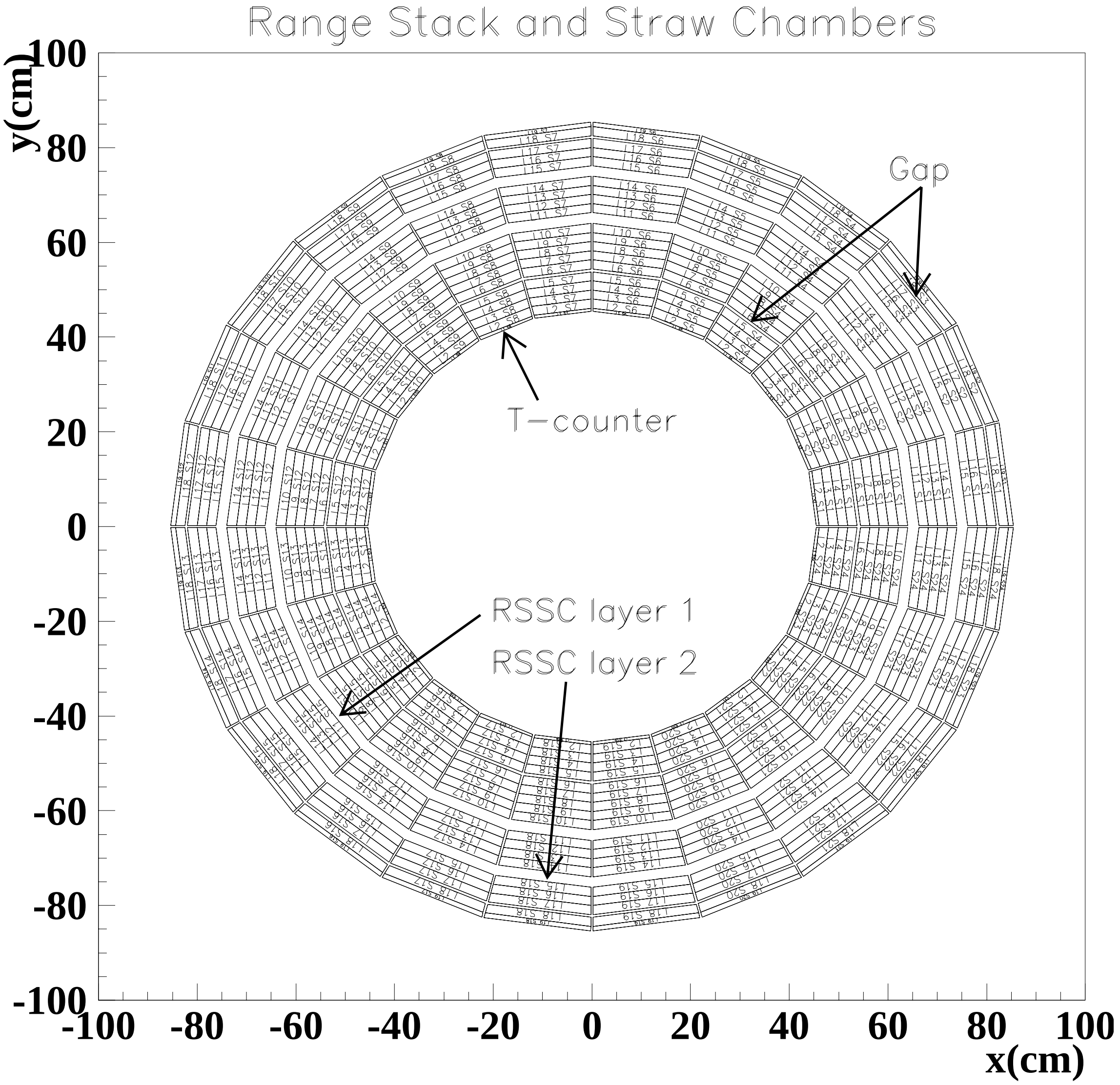

Figure 2.11: This end view of the Range Stack (looking upstream) shows the labeling scheme used during analysis, as looking upstream (e.g., layer 2 sector 14 is denoted "L2 S14"). The two layers of the Range-Stack Straw Chambers are located after RS-layers 10 and 14.

The scintillators of layers 2-18 have a thickness of 1.905 cm (3/4") and a length of 182 cm. Layer-19 scintillators, which were newly installed in the E949 upgrade, have a thickness of 1 cm. Layer 19 was mainly used to veto charged particles with long range by requiring that they do not reach the layer-19 scintillators. The scintillation light from elements in layers 2-19 is led by light guides to PMTs at both the upstream and downstream ends, see Fig. 2.12.

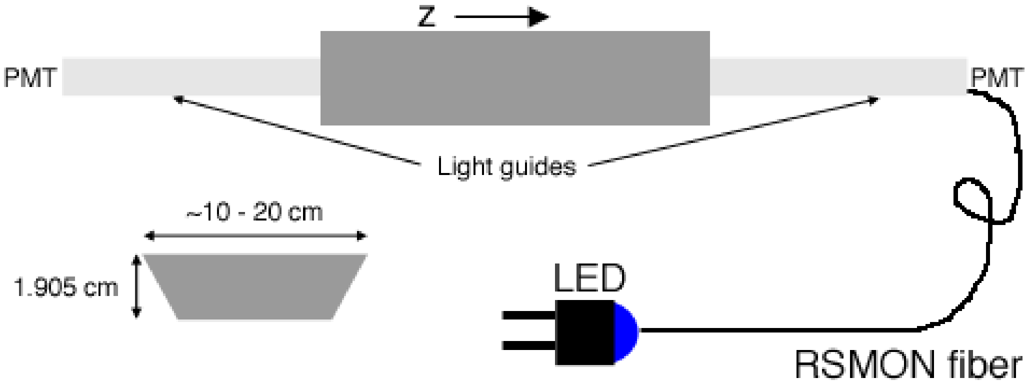

Figure 2.12: Single RS module. The top drawing shows geometrical construction of RS module (appropriate for BV and BVL as well). Left drawing indicates the cross-sectional shape of a RS element. Also shown is a conceptual drawing of the RSMON system.

The innermost RS counters are referred to as trigger counters (T-counters, T) because they serve a special purpose. The T-counters are constructed with a length of 52 cm to define the fiducial region to $\sim 2\pi$ sr. The reduced length insures that the charged track will come to rest inside RS. The thickness of the T-counters was constructed $\sim \frac{1}{3}$ smaller than other RS elements (0.635 cm) to reduce the chance a photon converts causing a trigger. The combination of reduced length and thickness allows a more efficient trigger, see Section 2.12. There are 17 wavelength shifting (WLS) fibers embedded within each T-counter element.

The first five layers, including the WLS-fiber T-counters, were replaced during the E949 upgrade to counteract efficiency loss from the aging E787 RS.

Every RS PMT is read out by an ADC and a TDC. The 24 sectors are grouped into six "hextants" of four sectors each (sectors 1-4, 5-8, 9-12, 13-16, 17-20, 21-24). Signals from four PMTs at the same end, same hextant and same layer are multiplexed and read out by a single TD (e.g., PMT signals from upstream-end layer 4, sector 1, 2, 3, and 4 are sent to one TD channel). The signals are demultiplexed in the offline event reconstruction by using TDC information in order to determine which counter the signal came from. The ADCs record charges in the $(-20., 85.)$ ns window about the T•2 time. The TDCs record the time of hits in the $(-0.5, 10)$ μs range. The TDs record pulse heights of PMT signals in 2 ns intervals (500 MHz sampling) between -0.5 to 2.0 μs to provide information on the time development of the pulses, see Fig. 2.13. This 500 MHz sampling provides detailed information about the pulse shapes, which enables the separation of two pulses as close as 5 ns in time, by performing an offline pulse fitting.

It was shown that TDCs could adequately find the electron [43]. Since the TD pulse-shape contains an abundance of information and TDCs are capable of e^+ finding, the TD timing gate was reduced to ultimately reduce detector dead-time. In addition, a much larger timing gate was feasible for TDCs, without affecting dead-time, which increases acceptance due to the possibility of finding e^+'s at later times. The TDs play an important role in the determination of whether an event satisfies the online trigger by flagging the $\pi^+ \to \mu^+$ decay, discussed further in Section 2.12. Since the TDC stores hit information in all RS counters, including both ends, the multiplexed TD pulse information can be reconstructed as occurring in a specific counter. This supplemental hit information creates better rejection of accidentals.

The time of a hit in a RS counter was obtained from the average of the upstream and downstream TDC times; the z position of the hit was obtained from the upstream-downstream time difference. The TDC time information from each hit was complemented with the corresponding TD information when available.

The π^+'s from the $K^+ \rightarrow \pi^+\nu\bar{\nu}$ decay in the PNN2 region, whose momentum is up to 199 MeV/c can traverse up to $\sim$ 28 cm of plastic scintillator. The total radial thickness of the RS and Target was 45 cm. Therefore all kinetic energy from PNN2 π^+'s can be deposited within the E949 detectors, coming to rest by the RS-layer 10. However, a μ^+ with 236 MeV/c (such as a μ^+ from $K_{\mu2}$ decays) can propagate $\sim$ 54.3 cm into plastic scintillator (possibly traversing the entire RS). Requiring charged tracks not exceeding RS-layer 12 suppresses $K_{\mu2}$ decays.

The μ^+'s from $K_{\mu2\gamma}$ decays could come to rest earlier in the RS. In addition, a π^+ can decay in flight and the resulting μ^+ may stop within the first twelve RS layers. For this reason, further identification of π^+ in the RS was performed by observing the $\pi^+ \rightarrow \mu^+ \rightarrow e^+$ decay sequence in the TDs and TDCs of the stopping counter, the counter where the π^+ comes to rest. Typical TD pulses in and around the stopping counter for a π^+ track are shown in Fig. 2.13.

The μ^+ from a $\pi^+ \rightarrow \mu^+\nu_\mu$ decay at rest has 4 MeV of kinetic energy. A 4 MeV μ^+ has an equivalent range in plastic scintillator of 1 mm; $\sim$ 1% will escape the stopping counter [44]. The e^+ from the $\mu^+ \rightarrow e^+\nu_e\bar{\nu}_\mu$ decay at rest has a kinetic energy of up to 52 MeV, so the e$^+$ can travel into neighboring counters of the stopping counter. The $\pi^+ \rightarrow \mu^+$ decay at rest, whose lifetime is 26 ns, is detected by using TD information of the stopping counter by performing double-pulse fitting, while the sequential $\mu^+ \rightarrow e^+$ decay, whose lifetime is 2.2 μs, is detected by using TDC information of the stopping counter as well as the neighboring counters by requiring that the times of the hits from the e$^+$ track are consistent with each other.

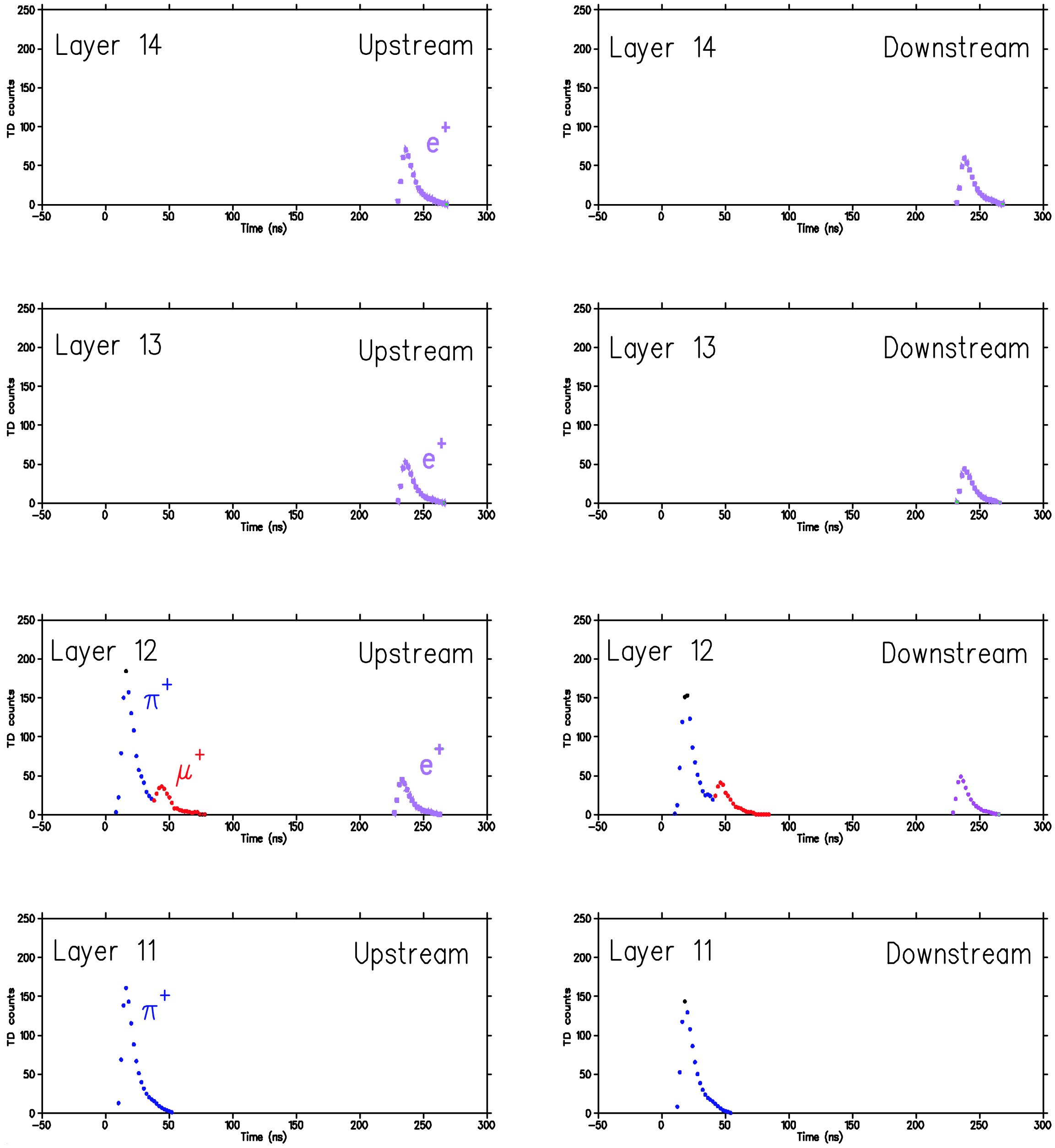

Figure 2.13: Pulses in and around the stopping counter as recorded by the TDs of the upstream and downstream ends. The $\pi^+ \to \mu^+ \to e^+$ decay sequence is recorded in the stopping counter (Layer 12 in this case). The μ^+ from the $\pi^+ \to \mu^+$ decay is contained in the stopping counter. The positron from the $\mu^+ \to e^+$ decay should also be found in the counters around the stopping counter (Layers 13 and 14 in this case).

2.10.1 Range-Stack Monitoring System

The increased beam rate in E949 and the aging E787 RS scintillator was expected to reduce the overall energy resolution. As detailed in [45], E949 implemented a monitoring system for the RS (RSMON) which greatly improved energy resolution in the RS. A temperature-controlled LED pulsed light into a bundle of thin fibers as shown in Fig. 2.12. The other end of each fiber was attached into the PMT-to-light-guide optical contact material, a “cookie”. The LED emitted light would be detected by the PMT on the opposite side of the RS element allowing a precise standard to calibrate the PMTs.

A rate dependence of the RS energy measurement was discovered. A method was devised to calibrate out the observed rate dependence. Using the RSMON system, a run-by-run and event-by-event energy calibration was performed. The run-by-run calibration, due to the average rate for a given run changed over the coarse of experiment, was incorporated to the previous method of calibrating by averaging over many runs. The rate within a spill changed, such that the rate was slower at the beginning and end of a spill, leading to the event-by-event calibration, based upon the time of the event within the spill.

2.10.2 Range-Stack Straw Chambers

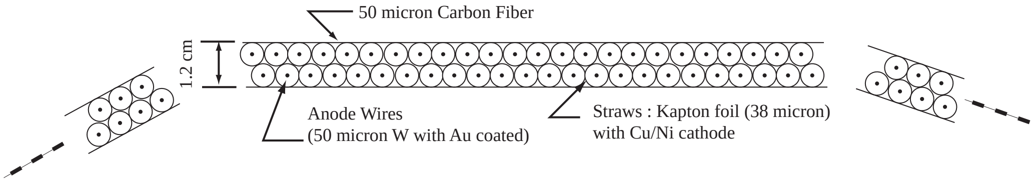

Figure 2.14: Schematic end view of the inner RSSC. The tubes run parallel to the beam direction. The outer RSSC has similar construction, but with 28 straws.

Range-Stack Straw Chambers (RSSCs) were located after layers 10 and 14 of the RS. The inner RSSCs consist of two layers of 24 straws per sector, as shown in Fig. 2.14, and the outer RSSC consists of two layers of 28 straws per sector. The RSSCs were used to assist in determining the charged particle's trajectory in the RS. Further details on the RSSCs is available in [46].

Energy, range and momentum measurements of charged tracks are crucial to distinguish the π^+'s in the signal region from backgrounds due to $K_{\pi 2}$ decays, which have monochromatic momenta of 205 MeV/c. Energy, range and momentum resolutions of 2.8%, 2.9% and 1.1% respectively are achieved for fully contained $K_{\pi 2}$ decays.

2.11 Photon Detectors

The detection of any activity coincident with the charged track is crucial for suppressing the $K^+ \rightarrow \pi^+ \nu \bar{\nu}$ backgrounds. Photons from $K_{\pi 2}$ and radiative K$^+$ decays are identified by photon detectors fully encompassing the fiducial region, which are shown in Fig. 2.15.

Detectors whose sole purpose is to detect photons are the Barrel Veto, the Barrel Veto Liner, the upstream and downstream End Caps, the upstream and downstream Collars, the downstream Microcollar. The multiple purpose detectors AD, Target, IC, VC, and RS also detect photons. As seen in Fig. 2.16, E949 has poor photon detection in the beam direction ($\cos(\theta) \sim 1$) and weak photon detection in the angle between the Barrel Veto Liner and the End Caps.

2.11.1 Barrel Veto

The Barrel Veto (BV), 1.9-m long, was located in the outermost barrel region with an inner radius of 94.5 cm and an outer radius of 145.3 cm. It surrounds two-thirds of

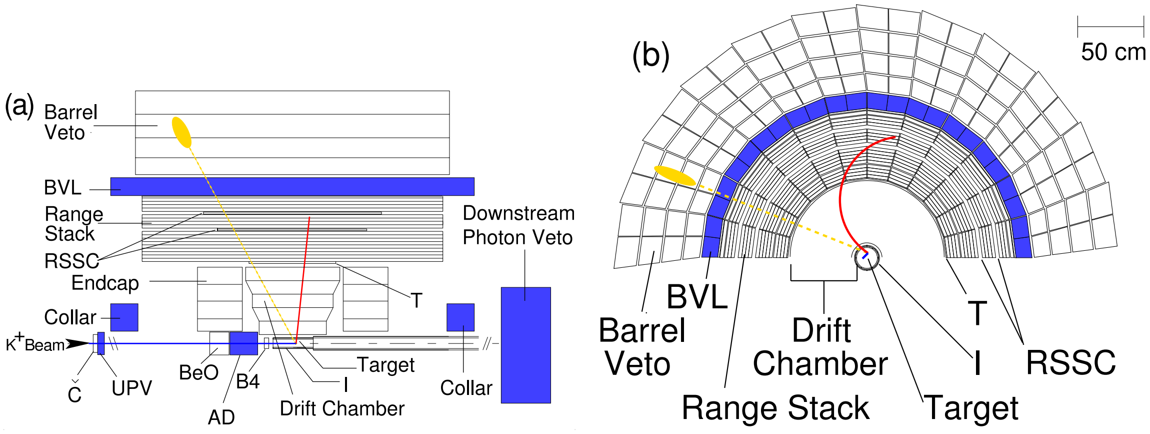

Figure 2.15: Schematic side (left) and end (right) views of the upper half of the E949 detector. Newly installed or upgraded photon detectors for E949 are in shaded blue.

the 4π sr solid angle. The BV consists of 48 azimuthal sectors and four radial layers (see Fig. 2.17). The radial modules consist of 16, 18, 20 and 21 layers of 1-mm thick lead and 5-mm thick plastic scintillator from inner to outer module, respectively. To avoid gaps in photon coverage, the boundaries between azimuthal segments are non-projective; that is, they do not point back to any part of the Target; otherwise a photon originating from a decay in the Target has a chance to avoid detection.

The BV has $\geq 14.3\ X_0$ in total. Each end of each module is read out by a PMT and the signals are recorded by an ADC and a TDC. The time resolution of individual BV counters, limited by TDC sampling time, is measured to be 1.0 ns. Approximately 30% of the photon energy absorbed by the BV is observed by the active scintillator. [48, 47].

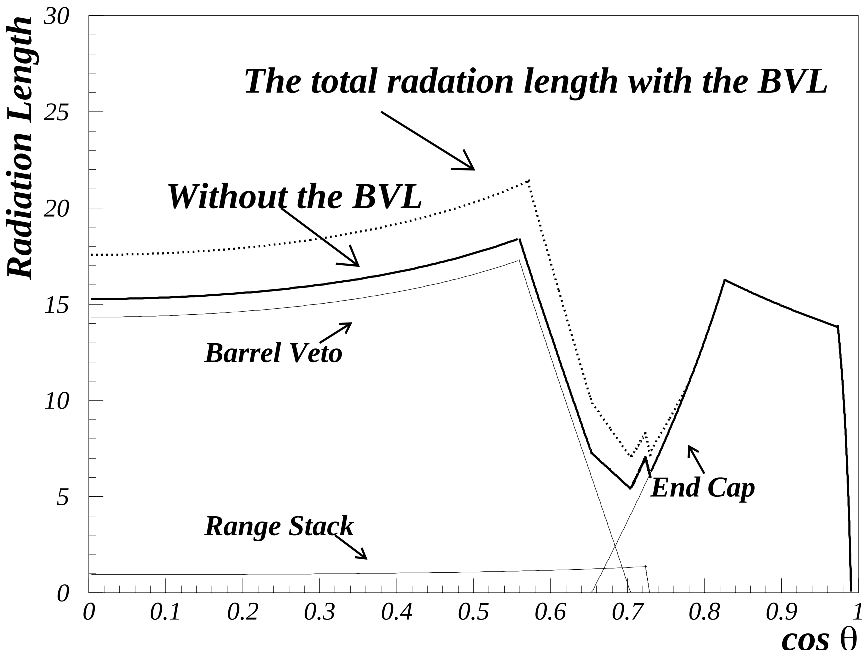

Figure 2.16: Radiation length versus polar angle for photon detectors.

2.11.2 Barrel Veto Liner

Newly installed for E949, the Barrel Veto Liner (BVL[4]) was located between the RS and BV. The BVL consists of 24 azimuthal modules, see Fig. 2.17, where each module is two BVL elements bound together by Kapton® tape. The inner surface of each module was attached to a new thinner RS-layer 19 before being placed in the spider-web support structure during the E949 upgrade; the BVL-RS-layer-19 module replaced E787's RS-layers 19-21. BVL elements have a thickness of 8.3 cm with 12 radial layers alternating between 1 mm thick lead and 5 mm thick plastic scintillator.

The BVL has 2.3 X_0 (when the photon hits perpendicularly). The 2.2 m length of each BVL active region was larger than that of the BV, so that the BVL adds active material to a region of the detector where the radiation length was relatively small (see Fig. 2.16). Each end of every module was read out by a PMT and the

---

[4] The Barrel Veto Liner is sometimes designated as 'BL' in analysis code and technical notes.

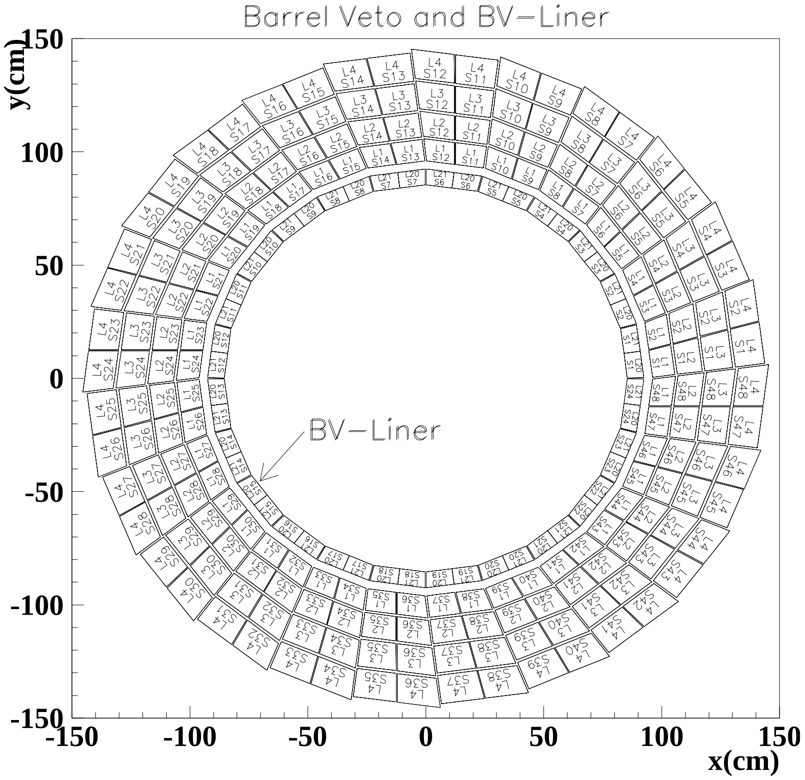

Figure 2.17: Barrel Veto and Barrel-Veto Liner. The layer and sector numbering are shown (e.g., Layer 1 Sector 1 is denoted as $^{S1}_{L1}$). Within a BVL sector, the layers are 20 and 21. This is due the BVL replacing RS-layers 20, 21 in the E949 upgrade.

signal was recorded by an ADC and a TDC. Groups of four adjacent sectors (eight modules) in each end are read by TDs; the grouped sectors are 1-4, 5-8, 9-12, 13-16, 17-20, 21-24. The time resolution of the individual BVL counters, limited by TDC sampling time, was measured to be 0.5 ns. Approximately 30% of the photon energy was absorbed by the BVL's active scintillator.

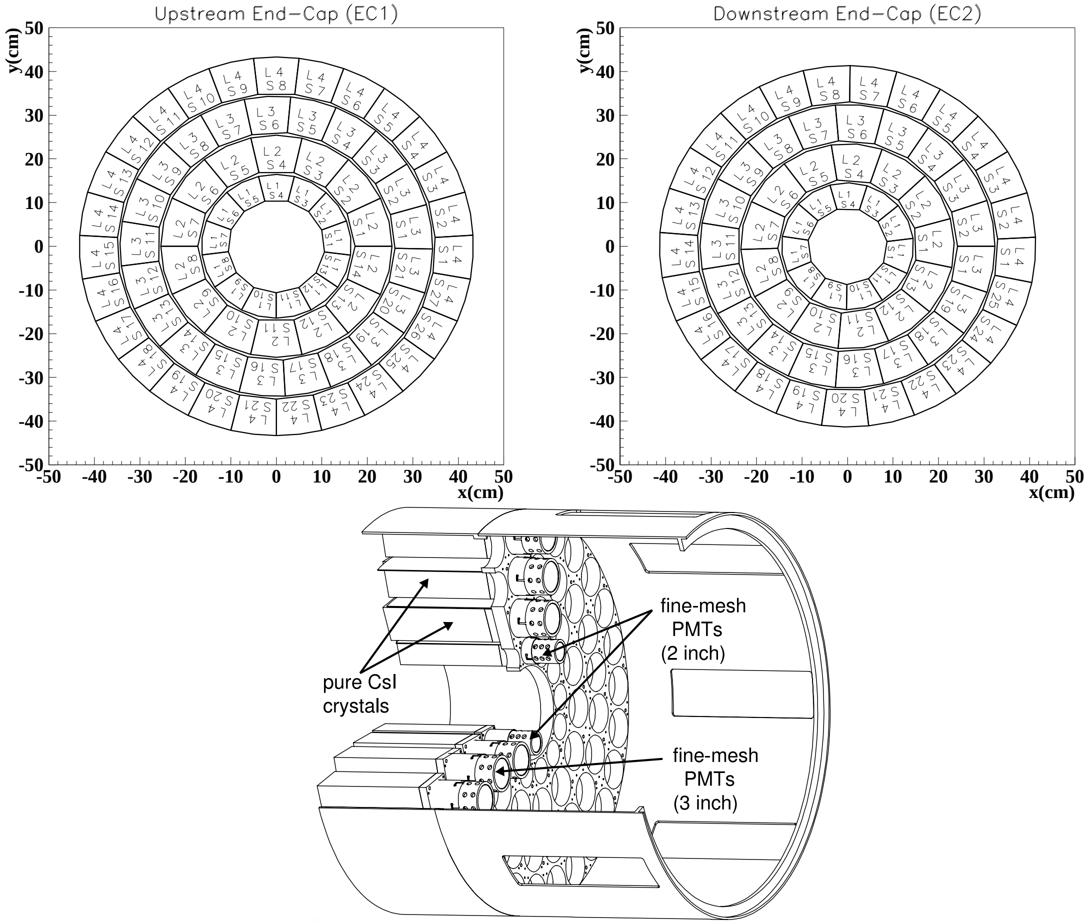

Figure 2.18: End view of the upstream End Cap (left) and downstream End Cap (right) includes the layer and sector numbering system used during the analysis. The bottom plot is a schematic of the EC assembly.

2.11.3 End Caps

The two End Cap (EC) photon detectors cover roughly one-third of the 4π sr photon coverage. As Fig. 2.18 shows, the upstream EC (EC1) detector consists of 75 undoped Cesium Iodide (CsI) crystals with pentagonal cross-sections, segmented in four rings (13, 14, 21 and 27 crystals from the inner to outer ring respectively). The downstream EC (EC2) detector consists of 68 crystals in four rings (11, 13, 19 and 25 crystals from the inner to outer ring respectively). Each crystal has a length of 25 cm (13.5 X_0 when hit perpendicularly, see Fig. 2.16). The ECs were designed to minimize photon escape via radial cracks by rotationally offsetting each layer with respect to the adjacent layers. Fine-mesh PMTs [49], which maintain high gains in strong magnetic fields, are attached directly to the crystals to achieve efficient light collection (see bottom of Fig. 2.18). Only the fast component of the CsI light output with a decay time of 30 ns at a wavelength of 305 nm is enhanced by ultraviolet transmitting optical filters attached to the PMT window; the slow component has a 680 ns decay time and contributes $\sim 20\%$ of the total light output [50]. The PMT signals are read out by ADCs, TDCs, and CCDs.

The ECs are exposed to a high counting-rate environment near the beam line, where beam particles cause many hits that are not coincident with K^+ decays. If an EC has an accidental hit occurring earlier than the photon hit, then a photon converting in the EC could be masked effectively blinding some electronics. A high rate of accidental hits will also lead to efficiency (signal acceptance) loss from vetoing events with no photon activity. Therefore, offline double-pulse finding in the pulse shapes are a necessity to help discern photon activity from beam activity.

2.11.4 Collar

The upstream and downstream Collar(CO) detectors, see Fig. 2.19, are located outside the ECs and around the beamline, so that they cover the region with small angles around the beam line. They are similar in construction and cross-sectional size, but the upstream CO is about half the thickness of the downstream one. Their x-y crossection is a ~ 50 cm by ~ 50 cm dodecagon with a 20.32 cm (16.43 cm for the downstream CO) hole in the middle, and they are segmented in 12 azimuthal sectors. The downstream CO consists of 25 layers of 5 mm thick scintillator alternating with 2 mm thick lead, with a total thickness of about 173.5 mm and about 9 X_0. The light from each sector is read out by bundles of WLS fibers glued in grooves in the scintillator, then fed to a PMT outside the magnetic field through a lucite lightguide. The upstream CO is read out directly with the lightguide, and has no fibers. The signals are recorded by TDCs and ADCs.

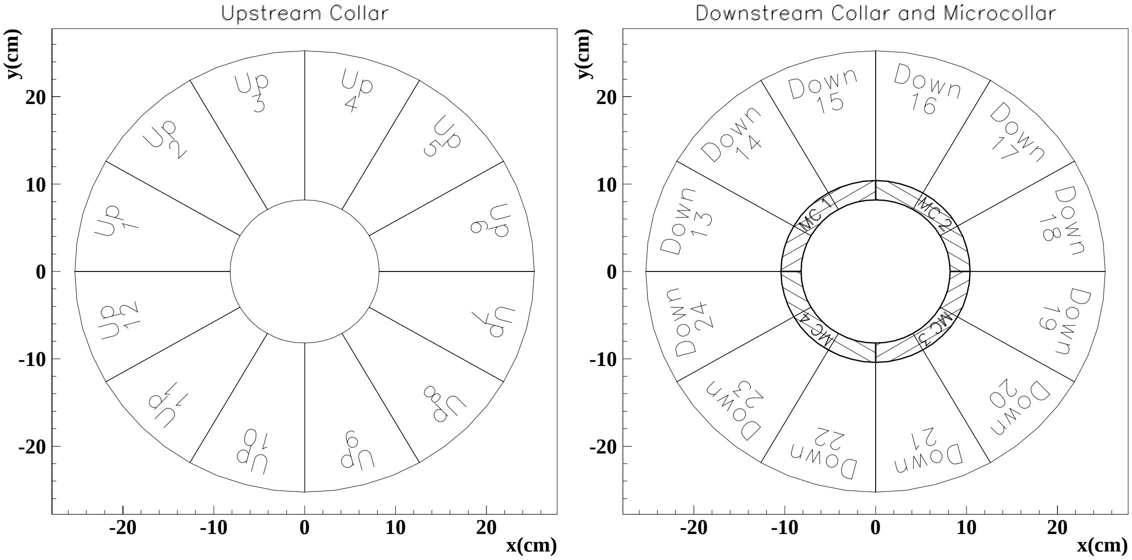

Figure 2.19: Collar and Microcollar. The element numbers are listed.

2.11.5 Microcollar

As seen in Fig. 2.3, the Microcollar (μCO[5]) surrounds the beamline directly downstream of the downstream Collar. The Microcollar was comprised of a 2.2 cm thick ring (7.8 cm inner radius) of plastic scintillator segmented into eight elements. Each element contains eight layers of 2 mm scintillating fibers (30, 31, . . . , 37 fibers in layer 1, 2,. . . , 8 respectively). Two adjacent elements were multiplexed and attached to a PMT. Between each layer of fibers are 53 cm long lead sheets; the inner-most and outer-most lead sheets are 16 mils and the others are 24 mils which created radial thickness of 1.63 cm of scintillator fibers and 0.39 cm of lead. This geometric

---

[5] The Microcollar is denoted as 'CM' within the analysis code.

arrangement of the μCO allows glancing photons to traverse a large distance of material (e.g., a photon with $\theta = 5^\circ$ will traverse ~ 7 mm ($> 1\ X_0$) in a single sheet of lead).

2.11.6 Downstream Photon Veto

The Downstream Photon Veto (DSPV), Fig. 2.20, located in the far downstream end of the detector after the TG PMTs (see Fig. 2.3), was a 700 mm by 700 mm square right on the beam path. It consists of 26 sheets of 10 mm thick scintillator alternating with 1.5 mm thick lead, with a total thickness of about 300 mm and 7.3 X_0. It was not optically segmented into modules, and was read out directly by four PMTs simultaneously, two on each side. The signal from each PMT was sent to TDCs and ADCs.

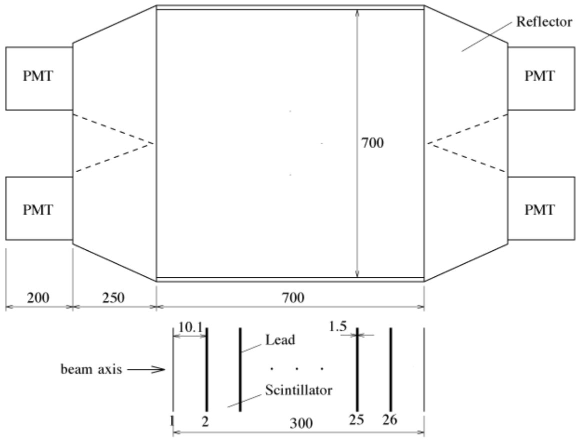

Figure 2.20: Schematic of the Downstream Photon Veto. Dimensions are in mm.

2.12 Triggers

The trigger selects signal-like events out of all K^+ decays to be recorded, based on logic pulses, ADC and TD information from the detector elements. 70-80 kB of data per event was digitized, and the digitized information of selected events was transfered from the electronics hut to the main computer for data taking.

The trigger was composed of a fast level-0 trigger, a level-1.1 trigger, and a level-1.2 trigger. The level-0 trigger makes a decision entirely with logic pulses from detectors. It has a rejection of 10^3 and introduces 38 ns of dead time for every coincident hit in the first two layers of the Range Stack (T•2). Dead time is the amount of time the detector is not able to trigger an event because it is busy processing a previously triggered event.

The level-1.1 and level-1.2 triggers involve partial processing of ADC and TD data and operate on only those events that pass the level-0 trigger. Level-1.1 trigger has a rejection of 12, after level-0, and introduces 10 to 20 μs of dead time per level-0 trigger. The level-1.2 trigger has a rejection of 2, after level-1.1, and introduces a dead time of up to 100 μs per level-1.1 trigger. The trigger to select $K^+ \rightarrow \pi^+\nu\bar{\nu}$ events has a rejection of 24000 and reduces the $\sim 2.6 \times 10^6$ K^+ decays per spill (while the detector is live) to about 100 events per spill.

Two $K^+ \rightarrow \pi^+\nu\bar{\nu}$ triggers are employed for the two kinematic regions of interest. For the PNN1 analysis, $\pi\nu\bar{\nu}(1)$ was used. For the PNN2 analysis, $\pi\nu\bar{\nu}(1)\ OR\ \pi\nu\bar{\nu}(2)$ was used. They consist of the following requirements:

$$\begin{aligned}\pi\nu\bar{\nu}(1) \quad \equiv \quad & \mathrm{KB} \cdot \mathrm{DC} \cdot \mathrm{IC} \cdot \mathrm{T} \bullet 2 \cdot (6_{ct} + 7_{ct}) \cdot \overline{19_{ct}} \cdot \overline{\mathrm{BV} + \mathrm{BVL} + \mathrm{EC}} \cdot \\ & (\mathrm{L0\_rr1(1)} \cdot US + \mathrm{L0\_rr1(2)} \cdot DS) \cdot \overline{\mathrm{L0\_zfrf}} \cdot \mathrm{HEX} \cdot \mathrm{L1.n}\end{aligned} \tag{2.1}$$

$$\begin{aligned}\pi\nu\bar{\nu}(2)_1 \quad \equiv \quad & \mathrm{KB}\cdot\mathrm{DC}\cdot\mathrm{IC}\cdot\mathrm{T}\bullet 2\cdot 3_{ct}\cdot 4_{ct}\cdot 5_{ct}\cdot 6_{ct}\cdot(\overline{13_{ct}+\cdots+18_{ct}})\cdot\overline{19}\cdot \\ & \overline{\mathrm{BV}+\mathrm{BVL}+\mathrm{EC}}\cdot \mathrm{L0\_rr2(1)}\cdot\mathrm{HEX}\cdot\mathrm{L1.n} \qquad (2.2)\end{aligned}$$

$$\begin{aligned}\pi\nu\bar{\nu}(2)_2 \quad \equiv \quad & \mathrm{KB}\cdot\mathrm{DC}\cdot\mathrm{IC}\cdot\mathrm{T}\bullet 2\cdot 3_{ct}\cdot 4_{ct}\cdot 5_{ct}\cdot 6_{ct}\cdot(\overline{13_{ct}+\cdots+18_{ct}})\cdot\overline{19}\cdot \\ & \overline{\mathrm{BV}+\mathrm{BVL}+\mathrm{EC}}\cdot \mathrm{L0\_rr2(1)}\cdot\mathrm{HEX}\cdot\mathrm{L1.n}\cdot(\mathrm{ps16}+\overline{C_\pi}) \qquad (2.3)\end{aligned}$$

where

- K^+ Stop Requirements:
  - KB : K^+ Beam requires a coincident hit in the Kaon Čerenkov Counter, the B4 Hodoscope, and an analog sum of the energy of the hit fibers in the Target of greater than or equal to 20 MeV. This requirement ensures that a K^+ enters the Target.
  - DC : Online delayed coincidence, in which the IC hit time was required to be at least 2 ns later than the time in the Kaon Čerenkov Counter. Requiring a delayed coincidence (of the entering K^+ to the outgoing charged track, π^+) ensures that a K^+ decays at rest.
- Fiducial Requirements on Charged Tracks:
  - IC : At least one hit in the I-Counter is required to be coincident with the T•2 time. This condition requires that a charged track from the Target enters the fiducial region of the detector.
  - T•2 : This condition requires that a charged track enters the fiducial region of the RS by requiring a coincidence hit in the first two layers (T-counter and layer 2) of the Range Stack in the same sector. Since the track curves, there is a small chance that the track will hit layer 2 in the adjacent sector leading to an efficiency loss in T•2 (see Fig. 2.21).

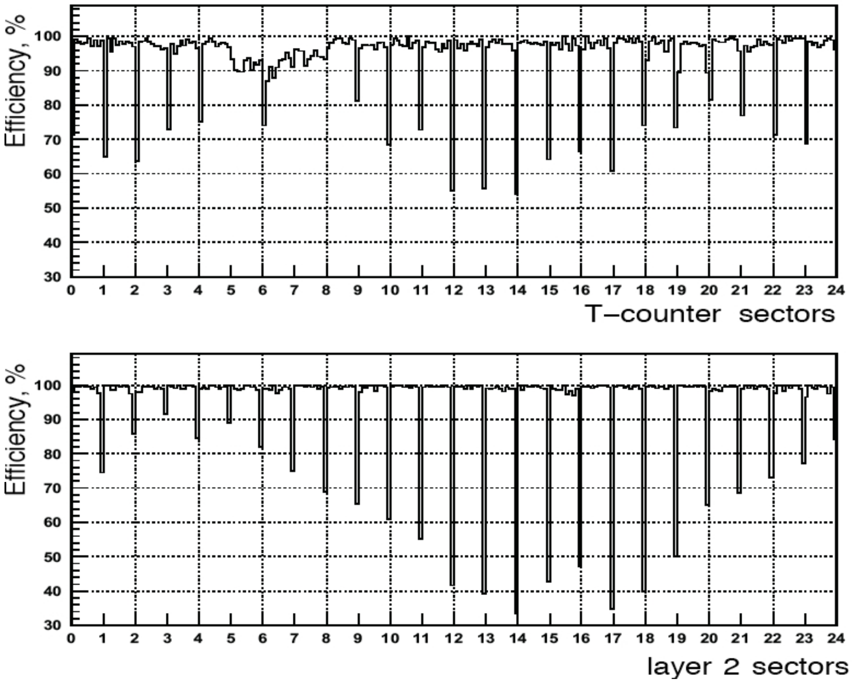

Figure 2.21: T•2 efficiency versus azimuthal angle (0=0° and 24=360° in units of RS-sector number. Tracks selected by UTC tracks with an IC hit and neighboring RS counters and assuming minimum ionizing particle. The downward spikes are from track which cross sectors between layers. The layer efficency loss at sector 6 is due to broken WLS fibers. [51].

  - $\overline{\mathrm{L0\_zfrf}}$: For $\pi\nu\bar{\nu}(1)$, extra fiducial requirements are imposed. A charged track is required to stop in the active region of the RS scintillators (not in the second RSSC). In such a case, μ^+'s from $K_{\mu 2}$ decays can fake π^+'s that come to rest in the RS-layer 14. Such a constraint was not needed for $\pi\nu\bar{\nu}(2)$, because $\pi\nu\bar{\nu}(2)$ pions are not allowed to reach RS-layer 13.

- Range Requirements on Charged Tracks:

  - $(6_{ct} + 7_{ct})$ or $3_{ct} \cdot 4_{ct} \cdot 5_{ct} \cdot 6_{ct}$: For $\pi\nu\bar{\nu}(1)$, a charged track (ct) must reach RS-layer 6 or 7. For $\pi\nu\bar{\nu}(2)$, a ct must reach layer 6 and have hits in all previous layers. The T•2 sector and two sectors clockwise from it are defined as the ct sectors. This condition removes short-range tracks from

3- and 4-body decays.

- $\overline{(13_{ct}+\cdots+18_{ct})}\cdot\overline{19}$: For $\pi\nu\bar{\nu}(2)$, a charged track is not allowed to reach RS-layers 13-19, whereas for $\pi\nu\bar{\nu}(1)$ this requirement only requires no activity in RS-layer 19. This condition removes μ^+ and other long tracks, and, for the case of $\pi\nu\bar{\nu}(2)$, it allows to collect more events in the kinematic region of interest.
- L0_rr2(i) : Refined-range requirement on a charged track. μ^+'s from $K_{\mu2}$ decays are suppressed by the $\overline{19_{ct}}$ requirement. However, some of the μ^+'s can still survive the requirement if their polar angle with respect to to beam direction was small and they stop near the end (in the z direction) of the RS scintillators. Events were rejected if the range calculated in the online trigger was too long. For $\pi\nu\bar{\nu}(1)$ and $\pi\nu\bar{\nu}(2)$ different "masks" are used, given their different range. The online range in the Target was obtained from the number of hit fibers, and the online range in the Range Stack was obtained from the stopping layer of the charged track and corrected for the polar angle. The polar angle was measured by the z positions at RS-layers 11, 12 and 13, which are obtained from the end-to-end time difference of both-end hits. The online stopping counter was found by the stopping-counter finder (SCF), which defines the outermost and most clockwise *ct* counter as the stopping counter.

- Online Photon Veto:
  - $\overline{\mathrm{BV}+\mathrm{BVL}+\mathrm{EC}}$: Online photon veto occurs in the BV, BVL and EC. Any photon hit which was coincident with T•2 and whose energy was above a threshold was not allowed. Each PMT signal from each end of the BV and BVL counters was discriminated by the threshold corresponding to 5 MeV. The mean time of the discriminated signals from both ends was given by digital mean-timers [52]. Events are rejected if the output signals of the mean timers are coincident with T•2. Each EC PMT signal

  was discriminated by the threshold corresponding to 20 MeV. Events are rejected if the output signals are coincident with T•2.

  - HEX : Only one RS hextant was allowed to have hits coincident with T•2, or two hextants if they are adjacent. This requirement rejects events with multiple tracks and events with photon activity in the RS.

- L1.1 : Level-1.1 trigger requires a signature of $\pi^+ \to \mu^+$ decay in the online stopping-counter. The pulse height (PH) and pulse area (PA) as recorded by the TDs in the stopping counter are compared. The decision was made by a control board with Application-Specific Integrated Circuits in each TD board. The ratio PH/PA would be smaller for double pulses than for a single pulse. Events were rejected if the PH/PA ratio was large.

- L1.2 : Level-1.2 trigger consists of three parts: (1) Events are rejected if coincident hits are detected in a RS counter near the stopping counter. This rejects events with μ^+'s that pass L1.1 due to accidental hits from the outside providing the double-pulse $\pi^+ \to \mu^+$ decay signature in the stopping counter. (2) Events are rejected if one of two adjacent hextant hits was not due to a charged track ("hextant afterburner"). This requirement removes those events that pass the HEX requirement because of accidental hits. (3) Events are rejected if the SCF assignments are not meaningful (e.g., SCF finds the stopping layer more than 19).

- Pion Čerenkov Veto

  - (ps16+$\overline{C_\pi}$) : When the beam separator broke down and the rate of beam pions was found to be too high for the $\pi\nu\bar{\nu}(2)$ trigger an online pion Čerenkov veto was imposed in the middle of the run, when the beam separator broke down and the rate of beam pions was found to be too high. This requirement was prescaled by 16 (i.e., The $\overline{C_\pi}$ condition was not applied in one every 16 events), in order to be able to measure its rejection and assess its effect. Due to an oversight, the ps16 condition was not saved causing issues with beam background measurement (see Section 4.3). Approximately 39.4% of all data was taken before the (ps16+ $\overline{C_\pi}$) was imposed.

In addition to the $\pi\nu\bar{\nu}$ trigger, various monitor triggers allowed events for use in data quality assessments, calibration of detector subsystems, and acceptance and background calculations. Monitor data used throughout the rest of this analysis use the following triggers:

- $K_{\pi 2}(1)$= $\mathrm{KB} \cdot \mathrm{T} \bullet 2 \cdot (6_{ct} + 7_{ct}) \cdot \overline{19_{ct}}$
- $K_{\pi 2}(2)$= $\mathrm{KB} \cdot \mathrm{DC} \cdot \mathrm{T} \bullet 2 \cdot \mathrm{IC} \cdot (6_{ct} + 7_{ct}) \cdot \overline{19_{ct}} \cdot \mathrm{HEX} \cdot \mathrm{L1.n}$
- $K_{\mu 2}(1)$= $\mathrm{KB} \cdot \mathrm{T} \bullet 2 \cdot (6_{ct} + 7_{ct}) \cdot (17_{ct} + 18_{ct} + 19_{ct})$
- $\pi_{scatter}$= $\pi B \cdot \overline{\mathrm{DC}} \cdot \mathrm{T} \bullet 2 \cdot \mathrm{IC} \cdot (6_{ct} + 7_{ct}) \cdot \overline{\mathrm{BV} + \mathrm{BVL} + \mathrm{EC}} \cdot \mathrm{HEX}$,

where πB requires that a π^+ enters the TG (via pion Čerenkov and B4 hits). Because each monitor trigger was highly prescaled, the number of monitor triggered events in each spill were at most 10. As the trigger names suggest, each monitor trigger attempts to record the respective decay mode or in the case of $\pi_{scatter}$ a beam-background process.

A complete list of all E949 triggers is available at [53]. Data was collected by triggering on a mix of all triggers of interest. The "standard mix" of triggers was changed as beam conditions and experimental needs evolved. Monitor data which was not collected as part of a standard mix was not considered for analysis measurements (e.g., special runs with using only $K_{\pi 2}(2)$ trigger, which were collected to calibrate and adjust RS-PMT gains, were not used for any acceptance measurements). E949 analysis only considers monitors, for a given run, in which we also have signal ($\pi\nu\bar{\nu}(1)$

or $\pi\nu\bar{\nu}(2)$) data. This constraint guarantees that experimental conditions are the same for all analyzed data.

2.13 Event Reconstruction

Reconstruction of each event requires determining (1) the trajectory of a charged track in the Target, UTC, and Range Stack, (2) the K^+ path and the decay vertex in the Target, (3) the beam particle hits in the beam instrumentation, (4) and the photon hits in the photon detectors. The event reconstruction in the x-y view is shown in Fig. 2.22.

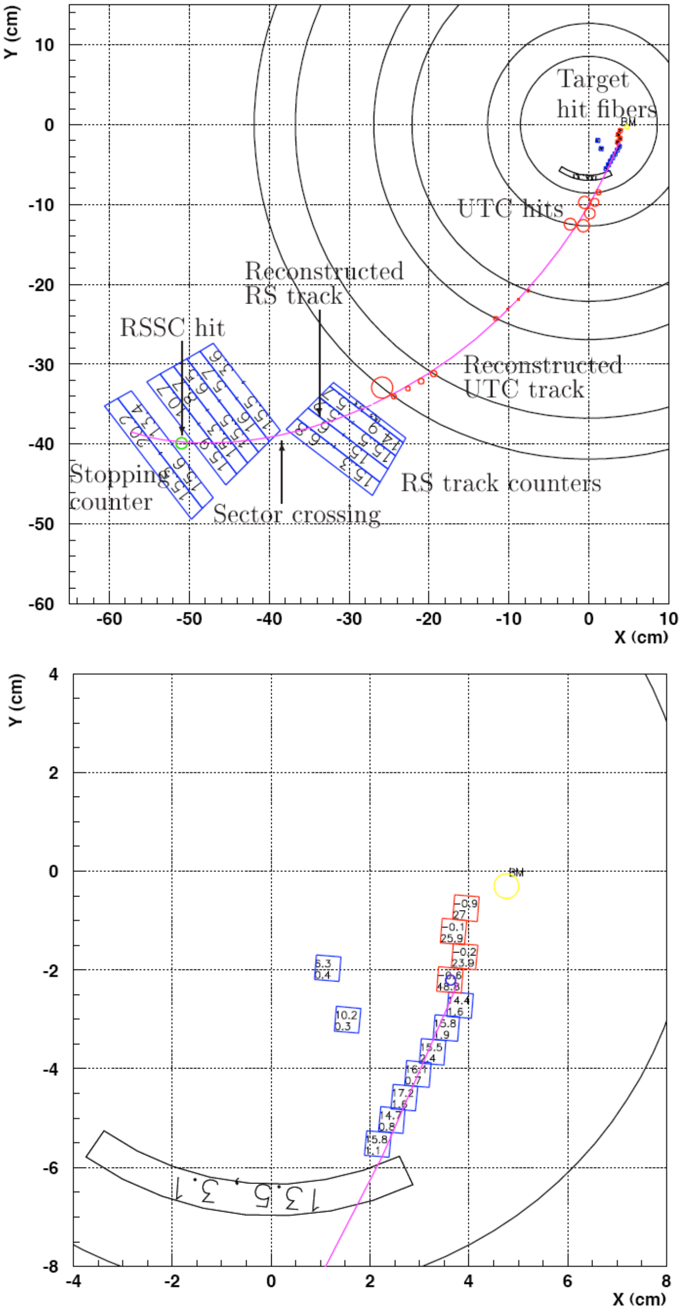

Figure 2.22: Reconstruction of an event in the x-y view: the reconstruction in the Target, UTC and Range Stack (top), and the reconstruction in the Target (bottom).

Charged-track reconstruction is performed twice for the Target, UTC and RS. The first step is to identify the Range Stack counters that have hits due to the track ("track counters"). First, a sector that has coincident TDC hits in the first two layers of the RS counters around the online T•2 timing is determined to be the offline T•2 sector. If the sector is not found, the online T•2 sector is used. The track counters are defined as the counters that have TDC hits coincident with the T•2 timing. The average time of the track counters is defined as the track time, t_{RS}. The outermost and most clockwise track counter is defined as the offline "stopping counter".

The UTC track is reconstructed by two separate fits: one in the x-y plane (perpendicular to the beam axis) and one in the r-z plane (formed by the radial and beam axes). In the x-y plane, a circle is fitted to the hit positions derived from the wire locations and drift distances. In the r-z plane, a straight line is fitted to the cathode strip hits. The polar angle of the charged track is evaluated from this r-z fitting.

In the first step of the target reconstruction, the times, energies and positions of the target fibers having CCD hits are examined, and they are categorized into "kaon", "pion", "opposite-side pion" and "gamma" fibers. The "kaon" fibers are determined as the ones that have energies larger than 4 MeV, times coincident with that of the B4 Hodoscope, and positions located outside a band ("swath") around the extrapolated UTC track. The average time of the kaon fibers is defined as the target kaon time, t_{K}, and their energy sum represents the target kaon energy. The kaon decay vertex is determined by the kaon fiber that is closest to the extrapolated UTC track and farthest from the x-y position of the B4 Hodoscope hit. The z position of the kaon decay vertex is obtained by extrapolating the UTC track to the decay vertex fiber. The "pion" and "opposite-side pion" fibers are selected by taking the fibers which have energies typically less than 1 MeV, times coincident with the track time, and positions inside the swath. The fibers on the side of the UTC track relative to the decay vertex are assigned to "pion" fibers, and the ones on the other side are assigned to “opposite-side pion” fibers. The opposite-side pion fibers could potentially be indicating additional charged particles. The average time of hits in the pion fibers is defined as the target pion time, t_π. The fibers that have times consistent with the track time and are not categorized as the kaon, pion or opposite-side pion fibers, are assigned to “gamma” fibers. Hits in the gamma fibers potentially originate from photons, secondary beam particles, or additional charged tracks from multiple-body decays.

In the RS stopping-counter, the $\pi^+ \rightarrow \mu^+$ decay signature is searched for via a pulse-fitting method. When a π^+ comes to rest in the RS, the stopping counter has the signature of double pulses due to the π^+ and the secondary μ^+. A χ^2 fit is performed on the TD output twice, with a single-pulse assumption and a double-pulse assumption, and sometimes three times, with a triple-pulse assumption, by varying the leading edges, heights and pedestals of template pulses that have been prepared for the individual counters and calibrated with $\pi_{scatter}$ monitor trigger data. A triple-pulse fitting is performed when more than two pulses are found, or the fitted second pulse does not look to be due to a μ^+ but an accidental, based on the double-pulse fit output. In this case, one of the three pulses is assigned to an accidental. The algorithm returns the fit qualities for both the single- and double-pulse assumptions (and triple-pulse assumption if the fit is performed) and the time and energy information of the pulses obtained by the fit. The TD pulse shapes in the examples of the double-pulse and triple-pulse fits are shown in Figures 2.23. More details can be found in [54].

After the pulse fitting is made, a second iteration of the track reconstruction is performed. The momentum in the UTC is calculated from the radius of the circle in the x-y fit and the polar angle in the r-z fit. The total momentum of the charged track, *ptot*, is obtained by correcting the momentum in the UTC by the target range, the I-Counter range and the amount of dead material in the inner wall of the UTC and the drift gas. After the UTC track determination is finished, a second iteration

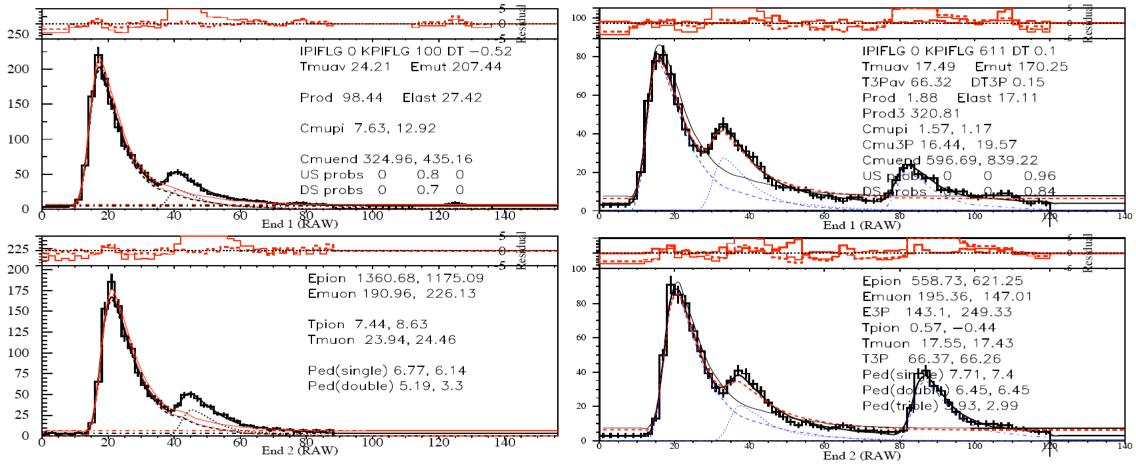

Figure 2.23: Double-pulse fit (left) to the TD pulse shape in the stopping counter for the upstream (top) and downstream (bottom) end. Triple-pulse fit to the TD pulse shape in the stopping counter for the upstream (top) and downstream (bottom) end.

of the target reconstruction is made. In this iteration, a double-pulse fit is performed on the CCD pulses of the kaon decay vertex fiber, in order to identify the $K^+ \to \pi^+$ decay pattern. The energy loss of the pion in the kaon decay vertex fiber, obtained from the second pulse found by the fit, is subtracted from the target kaon energy and is added to the target pion energy only when there is a high probability of a double-pulse and the delayed coincidence is greater than 15 ns; otherwise the π^+ energy is not changed. Two examples of such a fit are shown in Fig. 2.24 and Fig. 2.25. In the second example, the energy of the second pulse is higher than expected from just a decay pion heading directly towards the detector acceptance. This case is discussed in the next section.

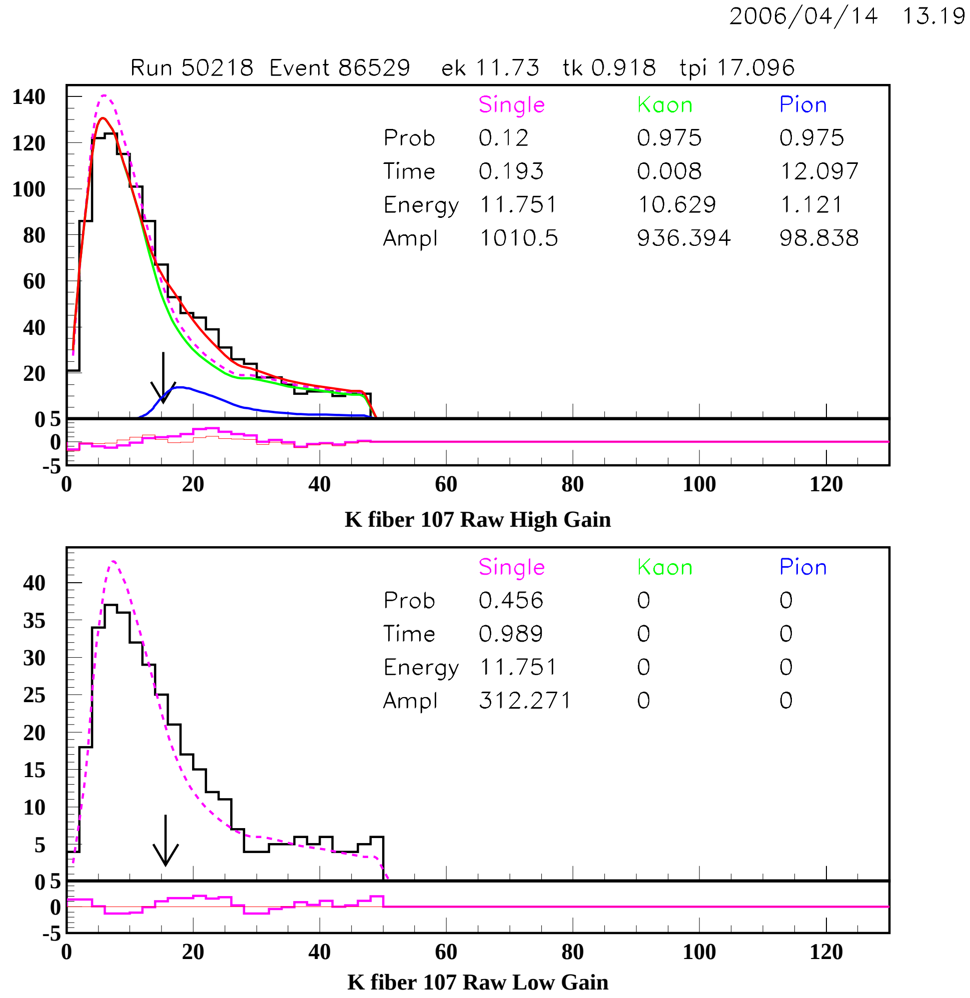

	Single	Kaon	Pion
Prob	0.12	0.975	0.975
Time	0.193	0.008	12.097
Energy	11.751	10.629	1.121
Ampl	1010.5	936.394	98.838

	Single	Kaon	Pion
Prob	0.456	0	0
Time	0.989	0	0
Energy	11.751	0	0
Ampl	312.271	0	0

Figure 2.24: Double-pulse fit to the CCD pulse shape in the Kaon decay-vertex fiber for the high (top) and low (bottom) gain read out. The energy of the second pulse is a typical one for the energy deposit of a decay pion heading directly towards the detector acceptance.

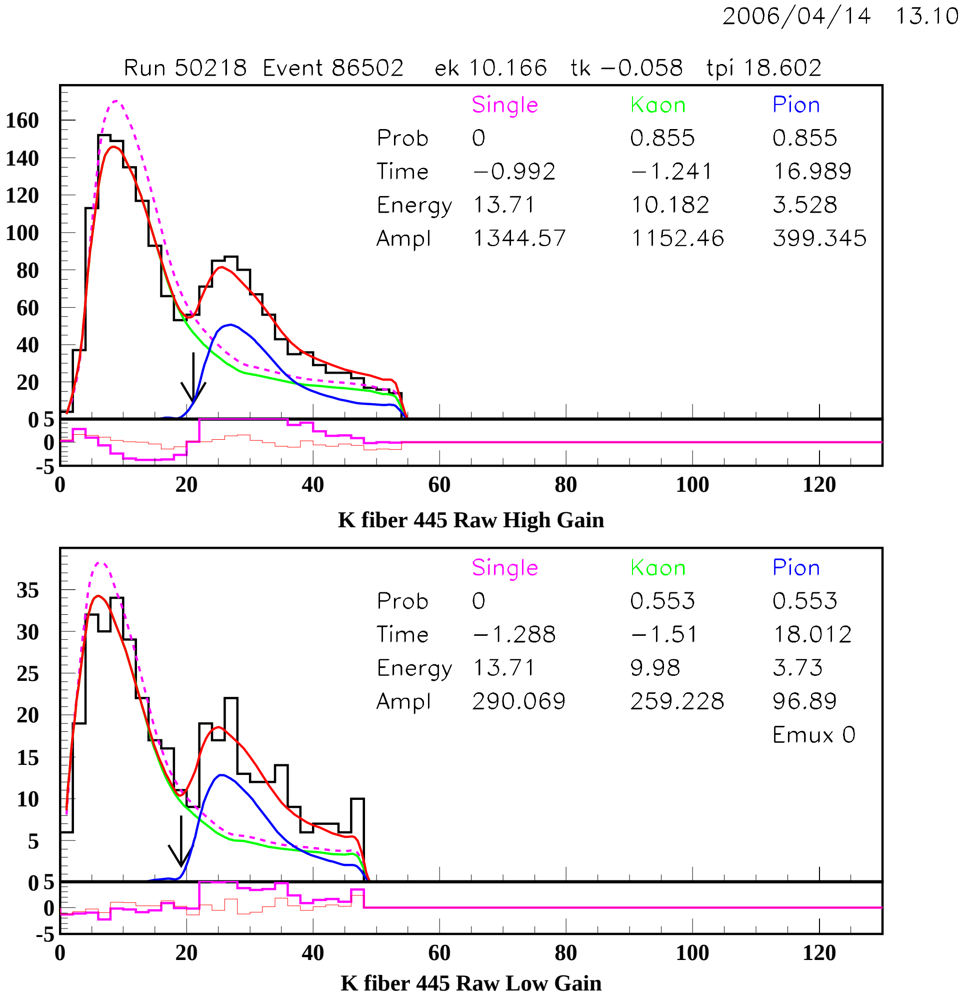

Figure 2.25: Double-pulse fit to the CCD pulse shape in the Kaon decay vertex fiber for the high (top) and low (bottom) gain read out. The energy of the second pulse is significantly higher than the typical energy deposit of a decay pion heading directly towards the detector acceptance, and may signify a scatter (see Section 3.2).

The energy deposit of the charged track in the Range Stack is calculated next. The energy deposit in each track counter is primarily obtained from the ADC energy, which is the area of a pulse within an ADC gate of 100 ns. If an accidental hit deposits energy in one of the track counters within the ADC gate, the track energy could be overestimated, which would result in loss of signal acceptance. To avoid this, the energy obtained from the TD pulse height information is used instead of the ADC energy, if the ADC energy is much greater than the the one expected from the TD pulse height, because the pulse height of the track hit is less disturbed by the existence of an accidental pulse. The total energy deposit of the track in the RS is obtained by summing up the energies in the track counters, and subtracting the muon energy in the stopping counter measured by the TD pulse fitting. This visible energy in each track counter is corrected to the true energy deposit by Birk's formula [55],

$$\frac{dL}{dX} = \frac{dE/dX}{1 + k_B \cdot dE/dX}, \tag{2.4}$$

where L is the luminescence in a plastic scintillator and $k_B = 0.01$ is called Birk's constant.

The range of the charged track in the RS is derived from a fitted track, calculated separately in the x-y and r-z planes. A fit is performed only in the x-y plane, by propagating a track in the RS that looses kinetic energy with the Bethe-Bloch formula with assumption that the charged track is due to a π^+, and is being bent in a 1-Tesla magnetic field. The incident momentum and angle (in the x-y plane) at the entrance of the RS are the fit parameters, and the track is required to match the measured positions of the sector crossings and RSSC hits and the measured energy in the stopping counter. In the r-z plane, the path of the track is obtained by extrapolating the UTC track to the stopping position of the track. The χ^2s for the r-z track are calculated from the residuals between the extrapolated UTC track and the z measurements based on the RSSCs and the end-to-end time differences in the individual counters. The range in the RS is calculated from the path length of the fitted track, and is then corrected to the total range, *rtot*, by summing the target range, the range in the I-Counter, and the ranges in the dead materials using the extrapolated UTC track. Finally, the total energy, *etot*, is calculated by adding the RS, TG, and IC energy, and energy loss in the UTC material (based upon *ptot*).

In the Kaon and Pion Čerenkov Counters, coincident TDC or CCD hits are clustered from 14 PMTs in each. The average time and the multiplicity of those hits are calculated for each cluster. In the BW Chambers, beam particle hits are reconstructed when two or three planes have coincident TDC hits. The TDC values of the wire hits are averaged to obtain the time of the incoming particle. In the B4 Hodoscope, two perpendicular counters in different layers are clustered when they have coincident TDC or CCD hits. The time and x-y position of the cluster are obtained from the energy-weighted average of the TDC or CCD hits. The measured energy deposits are used to separate K^+'s and π^+'s, which leave different energies in the B4 Hodoscope. The times of hits in any of the above beam detectors are used to remove double-beam events (see Section 3.2.4) by checking extra activities at t_{RS}.

In the photon detectors, the time and energy of each module in the detector subsystems are calculated. The hits that are coincident with the track time are searched for to veto the backgrounds that include photons.

2.14 Monte Carlo Simulation (UMC)

The detector and the physics processes in E949 are modeled by a Monte Carlo (MC) simulation program. The MC includes all of the detector elements, except for the beam instrumentation upstream of the Target, therefore the simulation of K^+ decays in the E949 detector starts from a "beam file" with the (x,y,z) positions and energy of K^+ hits in the TG obtained from an analysis of $K^+ \to \mu^+\nu$ decays. The MC generates all data, except for the TD and CCD pulse-shape information.

Multiple coulomb scattering of charged particles with various nuclei in the detector are calculated according to the theory of Moliere [56], with corrections for the spin of the scattered particle and the form factor of the nucleus [57]. Hadronic interactions of positively charged pions in the plastic scintillators are calculated using a combination of data and phenomenological models [58]. Photon and electron interactions are calculated using the EGS4 electromagnetic-shower simulation package [59].

The accuracy and the performance of the MC has been verified by comparing the different kinematic variables from data and MC for $K^+ \to \pi^+\pi^0$ and $K^+ \to \mu^+\nu$ decays [36].

2.15 Summary of 2002 Data Taking

The E949 experiment had the first and only physics run for 12 weeks from March to June in 2002. The data collected in the run period corresponded to $KB_{live} = 1.77 \times 10^{12}$ (K^+ decays in the Target). This number is found by scalers that count the number of KB triggers for every spill, and then is corrected for the amount of data discarded because the detector had some technical flaw during that time (bad runs). Fig. 2.26 shows the number of accumulated K^+ decays as a function of the data-taking days for the various running years of E787 and E949.

The E949 run was performed under a high-intensity beam environment. The proton intensity of the AGS increased to twice as high as in E787. The total exposure of K^+'s available for E949 was 30% that of E787, which recorded 5.94×10^{12} K^+ decays in the Target.

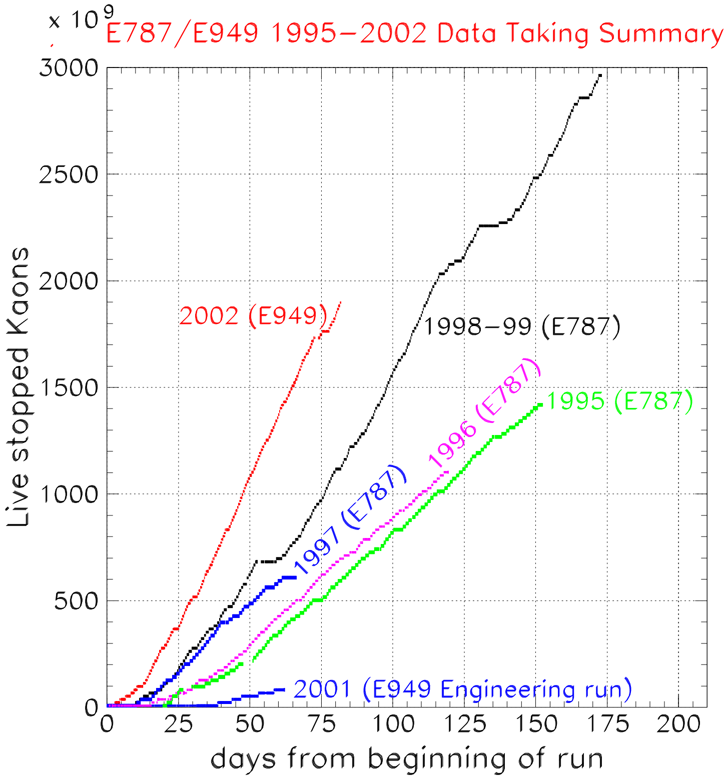

Figure 2.26: Number of K^+ decays in the Target as a function of the data-taking days for E787 and E949.

Chapter 3

Analysis

3.1 Method and Strategy

Disentangling the $K^+ \to \pi^+\nu\bar{\nu}$ decay from background in this experiment was difficult because of the poor kinematic signature and very small expected rate of the $K^+ \to \pi^+\nu\bar{\nu}$ signal ($\mathcal{B}(K^+ \to \pi^+\nu\bar{\nu}) \sim 10^{-10}$). To distinguish $K^+ \to \pi^+\nu\bar{\nu}$ events from a background process, all backgrounds must be suppressed to be less than one event. Therefore, backgrounds need to be suppressed to a rate less than $\sim 10^{-11}$. All measurements (backgrounds and signal acceptance) were measured by triggered events (both monitor and signal) due to limitations in Monte Carlo simulations not taking into account many conditions that the background measurements depend upon, such as running condition and detector effects. As detailed below, care must be taken to limit or avoid bias in background estimates that rely on samples with low statistics.

3.1.1 Blind Analysis Method

A blind analysis method was developed to search for the $K^+ \to \pi^+\nu\bar{\nu}$ signal. In this method, background sources were identified *a priori*, see Section 3.2. The signal region for the $\pi\nu\bar{\nu}(1)$ and $\pi\nu\bar{\nu}(2)$ triggers was "blinded" or hidden until the background and acceptance analysis was completed (i.e. any study using signal triggers required a cut to be inverted). When possible, selection criteria (cuts) were developed using the monitor samples to avoid examining the signal region. If monitor samples were inadequate and the signal trigger sample had to be used, at least one selection criterion used to distinguish signal from backgrounds was inverted (i.e. used to select a background region) to avoid examining the signal region. In addition, the background evaluations were performed such that the final background estimates were obtained from different samples than that used to determine the selection criteria. Each set of three consecutive events of signal data were routed uniformly into "1/3" and "2/3" sample groups. The 1/3 group was used to determine the selection criteria and an unbiased background estimate was obtained from the 2/3 group. The signal region was examined only after the background analysis was completed.

"Loop holes" can occur and become a signal candidate event (even though the event is not a $K^+ \to \pi^+\nu\bar{\nu}$ decay). This can happen if a background process was not considered *a priori*, mostly likely due to a pathology. To identify and remove any possible pathologies not initially considered, a single-cut failure study was performed (see Section 4.10). This single-cut technique will allow a peek at possible problems with the selection criteria and unidentified backgrounds, leading to creation of "safety cuts" to remove these identified pathologies. The idea is that backgrounds which will contribute to measuring $\mathcal{B}(K^+ \to \pi^+\nu\bar{\nu})$ should show up in a sample of events which only fail one cut, see Section 4.10

3.1.2 Bifurcation Method for Evaluating Background

The principle method for evaluation of background relying only on information outside the signal region involved the application of two complementary but uncorrelated cuts. Fig. 3.1 illustrates this bifurcation method showing the parameter space of two cuts, "CUT1" and "CUT2". The number of background events in the signal region (i.e., region "A") is A events. If the two cuts are uncorrelated, that is, if the rejection[1] of a cut does not depend on the rejection of the other cut, the ratio of the number of background events in region "A" to region "B" must be equal to the ratio in region "C" to region "D", i.e., $A/B = C/D$. Background events in the signal region are therefore obtained from the relation $A = BC/D$.

In practice, the bifurcation analysis was done through two branches. A "normalization branch" analysis was used to obtain the number of events in "B" region. A "rejection branch" study was done to get the ratio of D/C. The rejection was defined as $R = 1 + D/C$. The background level was then estimated as $N_{Bkg} = B/(R-1)$ in the signal region. For the case of very small statistics, "CUT1" was subdivided into another two cut categories, and B was estimated in the same way as the "first" bifurcation.

To check if the two bifurcated cuts were uncorrelated, one could loosen both simultaneously. This method thus provided input to the evaluation of systematic uncertainties.

3.1.3 Analysis Strategy

The data analysis used the following key steps to determine the selection criteria, evaluate the background level, investigate the systematic uncertainty, measure the

---

[1] The rejection of a cut on a pure sample of a background is $(\frac{events\ before\ cut}{events\ after\ cut})$.

acceptance[2] and finally obtain the branching ratio.

- During initial offline processing, as detailed in Appendix C, events were reconstructed and subjected to a number of selection criteria to remove obviously bad events. The signal triggers were split into two samples; 1/3 of the events were used to optimize the cuts and 2/3 of the events were used to obtain an unbiased estimate of measurements.

- Blind analysis was adopted in designing, calibrating and tuning the selection criteria. Signal-like and background samples were taken from the monitor trigger samples when applicable. When using the skimmed sub-samples, at least one critical selection criterion was inverted to avoid examining the signal region (see Section 3.3).

- The background level was initially evaluated by applying the bifurcation method to the 1/3 data. For each background, at least two uncorrelated cuts with large background rejections were chosen and then inverted sequentially to create high-statistic background data samples. For example, on the 1/3 sample, after some basic selection criteria, "Cut1" is inverted. Due to Cut1's large rejection of "background-A", inverting "Cut1" creates a high-statistic sample of "background-A." Another sample of "background-A" is created by inverting "Cut2." The expected background numbers (Section 4.1-4.7) were determined via the method described in Section 3.1.2.

- The final cut positions were optimized with respect to the signal-to-noise level estimated from the 1/3 data.

- Correlations between the bifurcated cuts were checked by conducting a series of reevaluations of the background levels outside the signal region (see Fig. 3.2).

---

[2] The efficiency of the cuts on signal events is referred to as *acceptance* $(\frac{events\ after\ cut}{events\ before\ cut})$.

A study of events which fail only one cut was also conducted to investigate possible flaws in the technique. To avoid the potential bias of the 1/3 background study, the final background evaluations were taken from the 2/3 portion. A bias could occur when a cut is optimized in such a way that it targets events in a method similar to a "cookie cutter", warping the cut parameters to remove a small set of events in the sample chosen. This will most likely increase the rejection of the cut in the optimization sample, but may not necessarily increase the rejection on another sample.

- Acceptances were measured, see Chapter 5, with the monitor trigger samples except for the signal phase space, the trigger efficiency, and those that could not be extracted from the monitor trigger data. Both of these two exceptions were obtained from Monte Carlo. Comparison of the measured $K_{\pi 2}$ branching-ratio to the world standard was used to validate the acceptance measurement. Single-event sensitivity was obtained from the inverse product of the total K^+ exposure and the acceptance.
- The signal region will be examined after the final total background level was estimated. Events observed in this region will be considered as signal candidates.
- The branching ratio will be obtained from likelihood analysis incorporating the predicted background rate in the signal region.

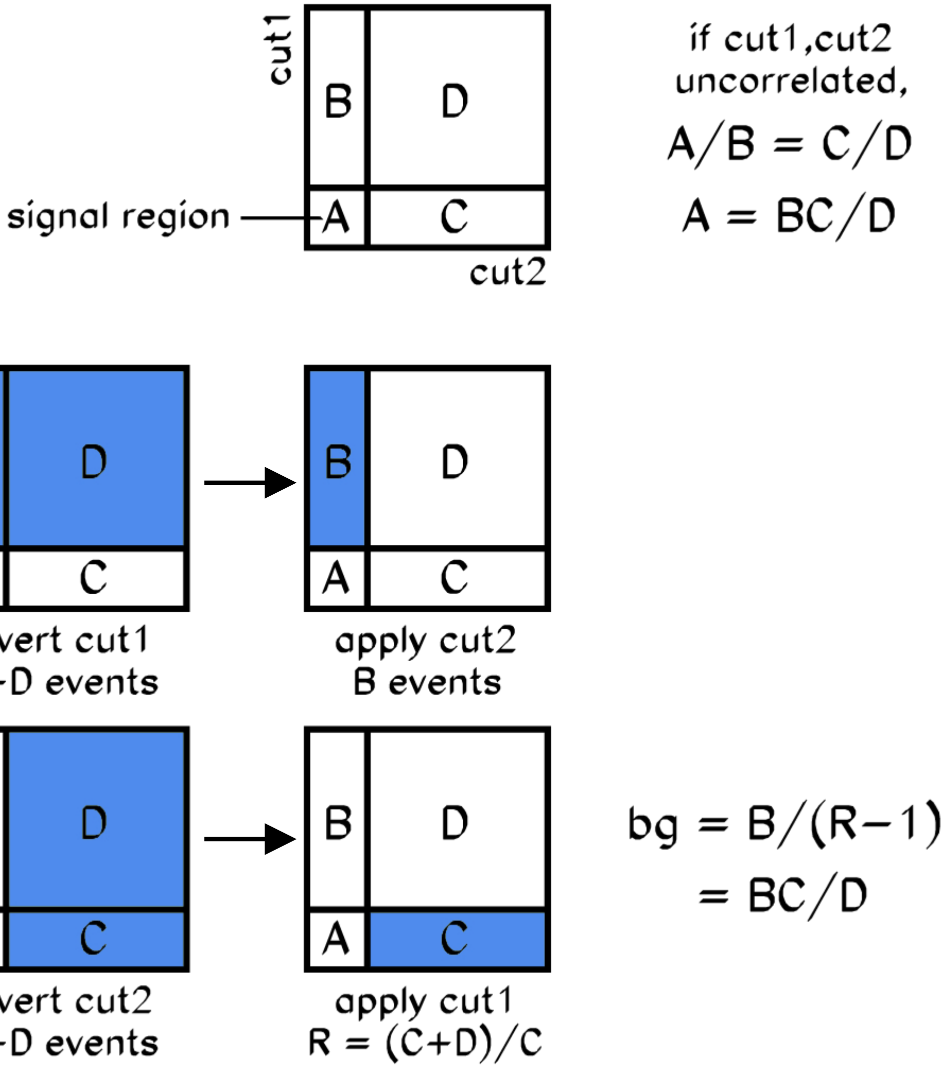

Figure 3.1: A background estimate resulting from a bifurcated analysis. The letters signify both the samples and the number of events in them.
Top: If a certain background is suppressed by cut1 and cut2, then the data sample can be represented in the parameter space of these two cuts as four sub-samples "A", "B", "C", and "D". If these cuts are uncorrelated, then the number of background events in region "A" relative to that in "B" is equal to that in "C" relative to "D".
Middle: Count events that fail cut1 and pass cut2 to get the normalization "B".
Bottom: Select events that fail cut2, and measure the rejection of cut1 via $R = (C + D)/C$. Region "A" is never examined in this procedure. The background estimated to be present in region A is given by $BC/D = B/(R - 1)$.

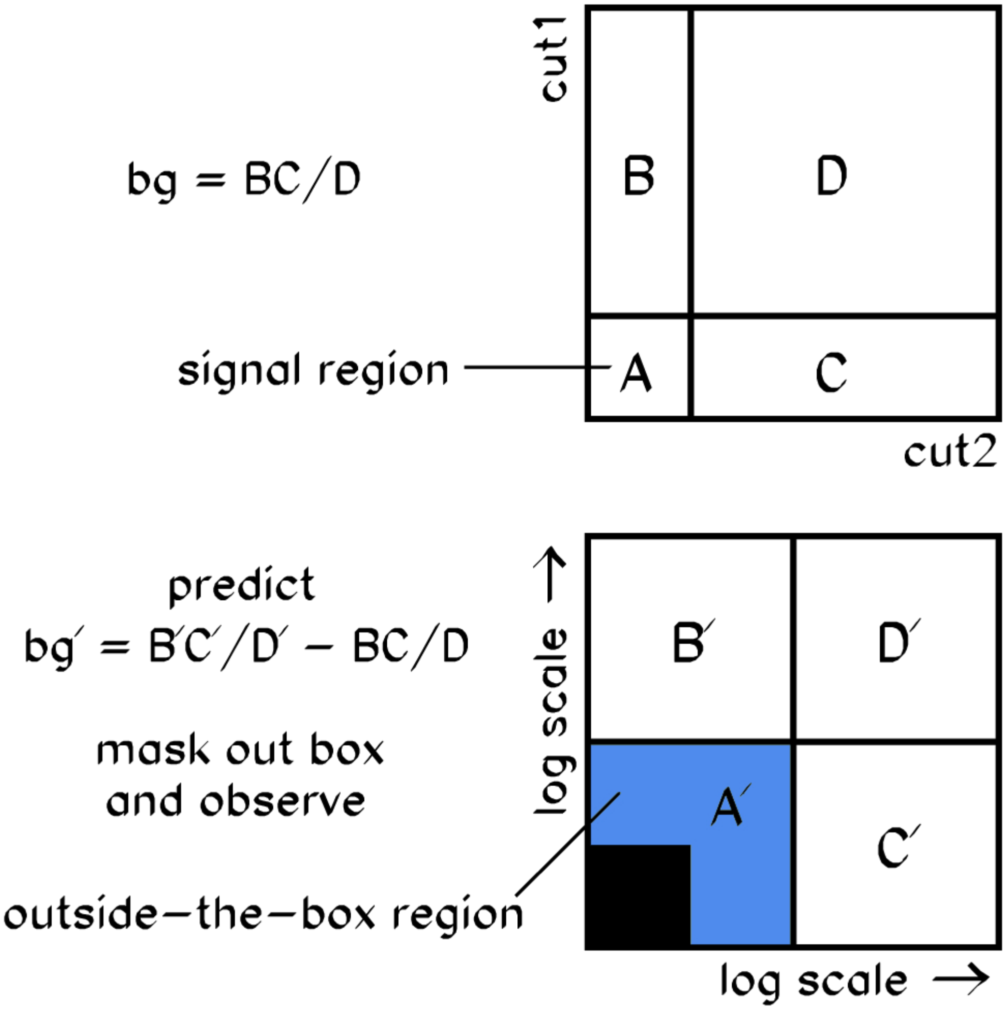

Figure 3.2: Schematic representation of the outside-the-box study.

3.2 Identifying Backgrounds

Experimentally, $K^+ \rightarrow \pi^+\nu\bar{\nu}$ is very similar to other K^+ decays when any of the following occur: (1) particles, especially photons, are not observed due to detector limitations, (2) activity unrelated to a K^+ decay cause a condition that emulates the signal decay, (3) charged-track scatter causing an incorrect reconstruction of the event kinematics, (4) multiple tracks overlap geometrically interfering with kinematic measurements and particle-identification methods. Fig. 3.3 shows the range versus momentum distribution of the charged-track daughter of the K^+ decay, using $\pi\nu\bar{\nu}(1)$ and $\pi\nu\bar{\nu}(2)$ triggers; prominent features are labeled.

Any K^+ decay could become a background if enough things go wrong during the detection of the event. Hence, every possible background needs to be properly investigated to determine multiple methods to identify them. Table 3.1 list K^+ decays in order of branching-ratio magnitude along with qualities which distinguish the process from $K^+ \rightarrow \pi^+\nu\bar{\nu}$; and these qualities will be agressively utilized to removed from consideration. Table 3.2 lists charge-exchange, double-beam, single-beam, and scattering processes which may contribute to the overall PNN2 background.

Kinematically forbidden backgrounds can also be found in the PNN2 kinematic region if the K^+ decayed in flight; In this case delayed-coincidence timing can identify the background. In addition, each of these decays are identified as background by numerous other features, such as photons and particle identification. Therefore, decays with kinematics lower than 140.0 MeV/c do not contribute to the overall PNN2 background.

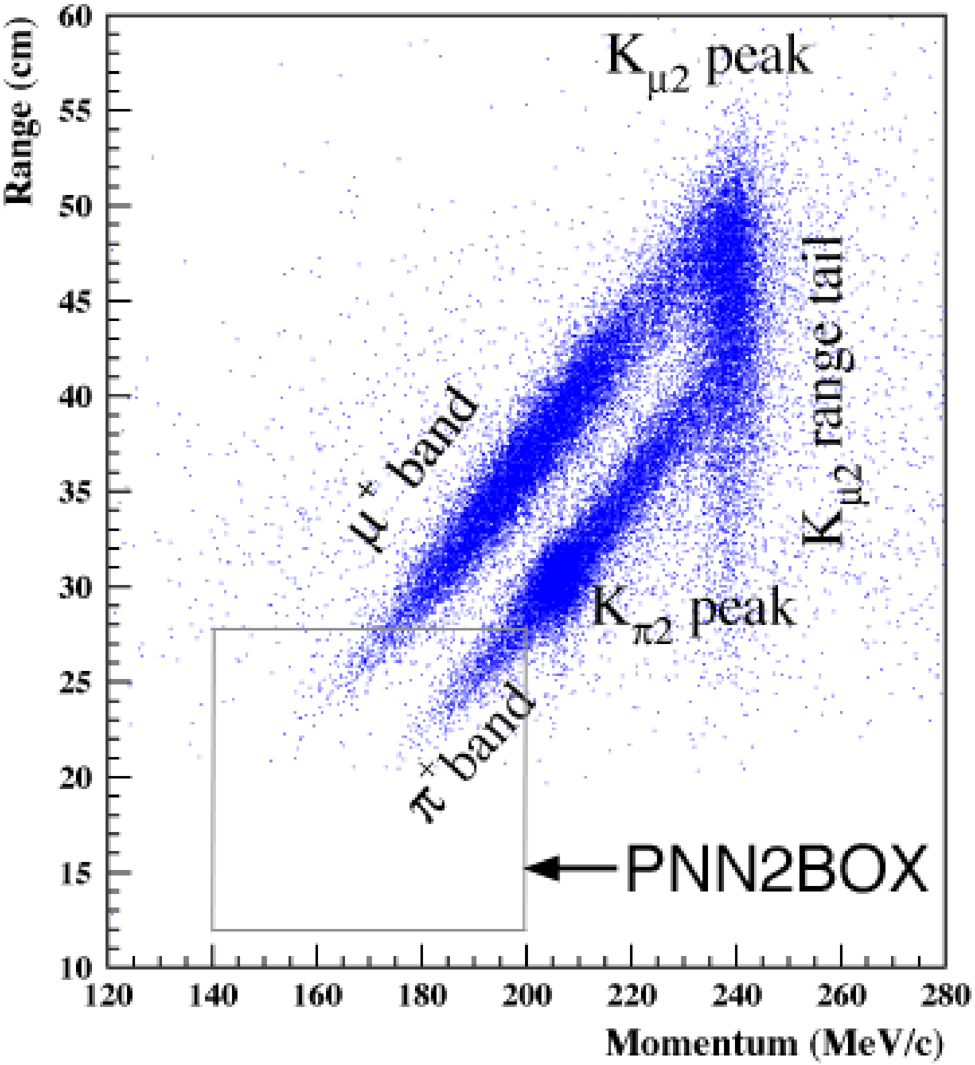

Figure 3.3: The range in plastic scintillator (*rtot*) versus momentum (*ptot*) distribution of the outgoing charged particle (π^+ mass assumed for momentum measurement, even for μ^+) for the events which passed the $\pi\nu\bar{\nu}(1)$ or $\pi\nu\bar{\nu}(2)$ trigger.

Background	Branching Ratio	Track Kin.	Extra Energy	DC	Particle ID	Photons
$K^+ \to \mu^+\nu$	0.6344	X			✓	
$K^+ \to \pi^+\pi^0$	0.2092	X*				✓^{2}
$K^+ \to \pi^+\pi^+\pi^-$	0.05590	X	✓			
$K^+ \to \pi^0 e^+\nu$	0.0498				✓	✓^{2}
$K^+ \to \pi^0\mu^+\nu$	0.0332				✓	✓^{2}
$K^+ \to \pi^+\pi^0\pi^0$	0.01757	X				✓^{4}
$K^+ \to \mu^+\nu\gamma$	0.0062				✓	✓
$K^+ \to \pi^+\pi^0\gamma$	0.000275					✓^{3}
$K^+ \to \pi^0 e^+\nu\gamma$	0.000269				✓	✓^{3}
$K^+ \to \pi^+\pi^+\pi^-\gamma$	0.000104	X	✓			✓
$K^+ \to \pi^+ 3\gamma$	< 0.0001					✓^{3}
$K^+ \to e^+\nu\nu\bar{\nu}$	< 0.00006				✓	
$K^+ \to \pi^+\pi^- e^+\nu$	0.0000409		✓			
$K^+ \to \pi^0\mu^+\nu\gamma$	0.000024				✓	✓^{3}
$K^+ \to \pi^0\pi^0 e^+\nu$	0.000022				✓	✓^{4}
$K^+ \to e^+\nu$	0.0000155	X			✓	
$K^+ \to e^+\nu\gamma$	0.0000152				✓	✓
$K^+ \to \pi^+\pi^-\mu^+\nu$	0.000014		✓			
$K^+ \to \pi^+\pi^0\pi^0\gamma$	0.0000076	X				✓^{5}
$K^+ \to \mu^+\nu\nu\bar{\nu}$	< 0.000006				✓	
$K^+ \to \pi^0\pi^0 e^+\nu\gamma$	< 0.000005				✓	✓^{4}
$K^+ \to \pi^0\pi^0\pi^0 e^+\nu$	< 0.0000035	X			✓	✓^{6}
$K^+ \to \pi^+\gamma\gamma$	0.00000110					✓^{2}
$K^+ \to \mu^+\nu\mu^+\mu^-$	< 0.00000041		✓		✓	
$K^+ \to e^+\nu\mu^+\mu^-$	0.000000017		✓		✓	
$K^+ \to e^+\nu e^+ e^-$	0.000000025		✓		✓	
$K^+ \to \mu^+\nu e^+ e^-$	0.000000071		✓		✓	

Table 3.1: K$^+$ decays with their branching ratios [5]. ✓ denotes a quality which distinguishes the process from the signal. X (X*) identifies the process as kinematically forbidden in PNN2 signal region (, but very close). Kin. = Kinematics, DC = Delayed Coincidence, ID = Identification, ✓^{n} = n photons in product.

Background	Branching Ratio	Track Kin.	Extra Energy	DC	Particle ID		Photons	
					Track	Beam	Fid.	Beam
$K^+n \rightarrow K^0p$	0.000028		✓	✓				
$K^0_L \rightarrow \pi^+\mu^-\bar{\nu}$	0.1350		✓	✓				
$K^0_L \rightarrow \pi^+e^-\bar{\nu}$	0.1940		✓	✓				
π-Beam	-			✓		✓		
K-DIF	-			✓	$\checkmark^{*}$	✓	$\checkmark^{*}$	
KK-Beam	-		✓		$\checkmark^{*}$	✓	$\checkmark^{*}$	
Kπ-Beam	-		✓			✓		
Charged-track scatter in Target								
$K^+ \rightarrow \mu^+\nu$	0.6344				✓			
$K^+ \rightarrow \pi^+\pi^0$	0.2092		✓					$\checkmark^{2}$
$K^+ \rightarrow \pi^+\pi^0\gamma$	0.000275		✓				✓	$\checkmark^{2}$
Charged-track scatter in Range Stack								
$K^+ \rightarrow \mu^+\nu$	0.6344	$\checkmark^{P}$			✓			
$K^+ \rightarrow \pi^+\pi^0$	0.2092	$\checkmark^{P}$	✓				$\checkmark^{2}$	
$K^+ \rightarrow \pi^+\pi^0\gamma$	0.000275		✓				$\checkmark^{3}$	

Table 3.2: Additional background processes with their Branching Ratios [5]. ✓ denotes a quality which distinguishes the process from the signal. X identifies the process as kinematically forbidden in PNN2 signal region. DIF = Delay in Flight, Kin. = Kinematics, DC = Delayed Coincidence, ID = Identification, Fid. = Fiducial region photon detection, $\checkmark^{*}$ = depends on which K$^+$ decay, $\checkmark^{P}$ = distinguished by momentum only. The reported branching ratio of $K^+n \rightarrow K^0p$ is the K_L production rate as found in [36].

3.2.1 Muon Background

As observed in Fig. 3.3 and Table 3.1, the $K^+ \rightarrow \mu^+\nu$ ($K_{\mu2}$) decay mode accounts for the majority of K$^+$ decays and due to the two-body nature of the decay occurs in a kinematic peak in range, energy, and momentum. The $K_{\mu2}$ range-tail, as denoted in Fig. 3.3, occurs when the μ^+ undergoes a inelastic scattering in the RS. The scattering in the RS allows proper momentum measurement; the momentum is measured properly since the UTC is interior of the RS. However, the range is mismeasured due to incorrect RS-range. $K_{\mu2}$ range-tail contribution to background is considered to be negligible due to the large kinematic separation of these events from the PNN2 kinematic signal region; background studies performed validated this claim.

One component of the μ^+ band is μ^+ scatters in the Target, causing a mismeasurement in both momentum and range. For such, a process to become a PNN2 background (or just to get inside the PNN2 kinematic box) the μ^+ must lose a lot of kinetic energy during the decay and the range must be mismeasured by $\sim$ 30 cm. The 6 cm TG radius makes (effective length in z to be $\sim$ 15 cm) scattering of a μ^+ from a $K_{\mu2}$ decay very unlikely. Thus, $K_{\mu2}$scattering background is considered negligible.

The significant background from μ^+ events are from $K^+ \rightarrow \pi^+\pi^0\gamma$ ($K_{\pi2\gamma}$) and radiative μ^+ decays. With a BR of 6%, the μ^+ from this $K_{\pi2\gamma}$ occurs naturally within the PNN2 kinematic region. The best cuts for μ^+ backgrounds are the particle-identification method of observing $\pi^+ \rightarrow \mu^+ \rightarrow e^+$ as well as kinematics.

3.2.2 $K^+ \rightarrow \pi^+\pi^0$ Background

Nominally, events from $K^+ \rightarrow \pi^+\pi^0$ ($K_{\pi2}$) are forbidden to be in the PNN2 signal region by kinematics (even if the photons escaped without converting within the detector). However, when the π^+ scatters within either the TG or RS the kinematics of the π^+ change, as measured by the detectors, resulting in the π^+ kinematics within the kinematic signal region.

The topology of $K_{\pi 2}$ TG-scatters, which is depicted in Fig. 3.4, attack the weakness of E949 detectors. To remove $K_{\pi 2}$ events, kinematics and detection of photons were employed. The π^+ kinematics are not measured correctly in this process and photon coverage is not as reliable as one in the non-scatter case. In a non-scatter $K_{\pi 2}$ event, the π^0 travels within the charged-track fiducial region ($K_{\pi 2}$ being a two-body decay, the π^0 will be back-to-back with the π^+) and thus the two photons will likely convert in the BV-BVL detectors. In a TG-scatter event the π^+ may start off traveling in the z direction with the π^0 traveling in the opposite (z) direction. As shown in Fig. 2.16, E949's photon detection is weakest at larger $\cos\theta$. This mechanism along with the large $K_{\pi 2}$ BR (21%) makes this background the largest in E949-PNN2.

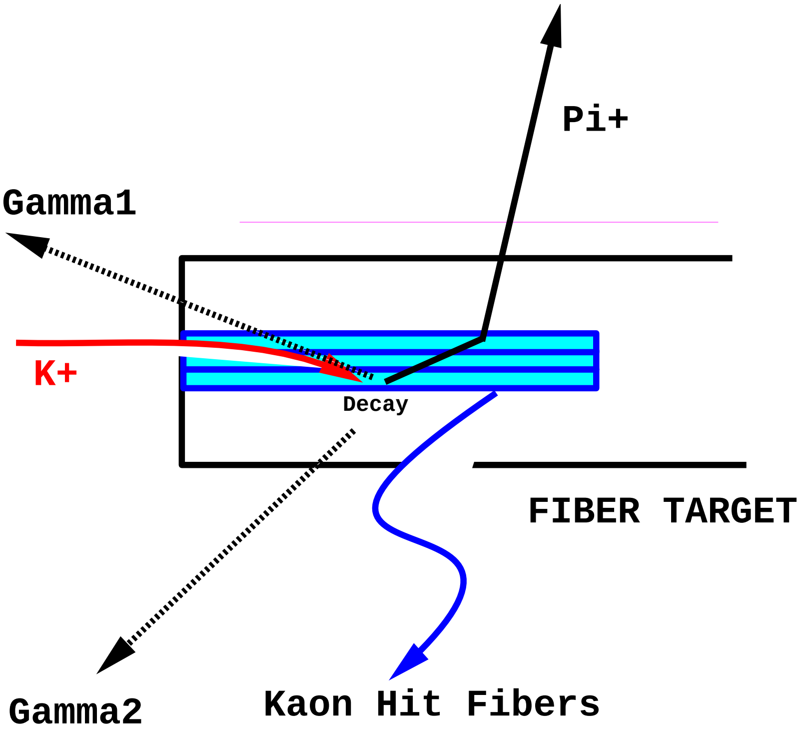

Figure 3.4: Schematic drawing of $K_{\pi 2}$ target-scattering background.

3.2.3 Single-Beam Background

Fig. 3.5 diagrams single-beam background processes. An entering K^+ can decay in flight (K-beam). Decay-in-flight events are subject to the same nature as other K^+ stopped decays. In K^+-beam background, beam systems observe a signal-like K^+ and the TG, UTC, and RS observe an outgoing charged track. Photons in the product will enhance background suppression from K^+-beam events; as will μ^+ identification. $K_{\pi2}$'s will have additional kinematic suppression (over a stopped $K_{\pi2}$) due to a Lorentz boost of the π^+. A requirement on the time difference between the incoming beam particle and the outgoing charged track, delayed coincidence (delco), has the ability to highly suppress this background.

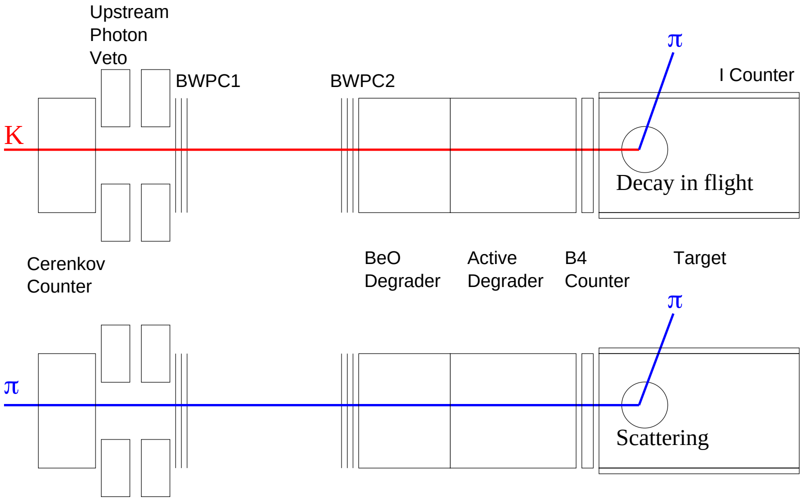

Figure 3.5: Schematic diagrams of the single-beam background: a single-K^+ beam background (top) and a single-π^+ beam background (bottom).

A π^+ existing in the particle beam (K^+:π^+, 3:1) can scatter into our fiducial region and cause another type of single-beam background called π^+ scatters (π_{scat}'s). No photons are produced and the π^+ can have the same character as a signal π^+. The Čerenkov, AD, and B4 beam detectors can suppress π_{scat} background due to their ability to distinguish a K^+ and π^+. π_{scat}'s are similar to K-beam background due to the beam particle and outgoing π^+ having the same time. Hence, delco is an effective means to suppress this background.

3.2.4 Double-Beam Background

An incoming K$^+$ is often followed by a K$^+$ or π^+, see Fig. 3.6, within the window of time between the first entering particle and the decay causing the T•2 trigger. Additional beam particles are of no concern unless the particle enters the detector at the charged-track time (T•2 trigger condition time). When this condition occurs, it is not possible to reliably determine which beam particle ultimately causes the T•2 trigger condition. Therefore, the background must be measured in this case. An event is not considered to be background when the second particle enters sufficiently before the decay time of the first incoming beam particle.

The contribution to background from two π_{scat}'s are negligible.

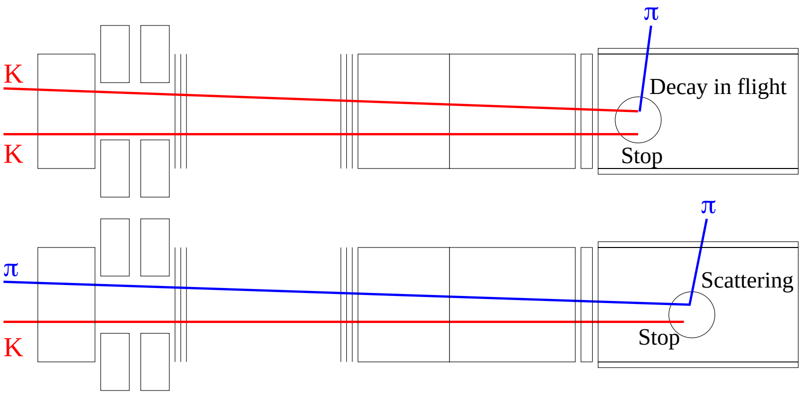

Figure 3.6: Schematic diagrams of the double-beam background: a $K - K$ double-beam background (top) and a $K - \pi$ double-beam background (bottom).

Particles coming from the beam, other than the K$^+$ whose decay products cause the T•2 trigger condition, may cause conditions which can emulate the signal decay. In the K$^+$-π^+ double-beam (Kπ) process the second π^+ can be observed by the $\check{C}_\pi$, BW1, BW2, AD, B4, and TG. The Kπ process becomes a background when the π^+ enters the detector at, or near, the same time as the K$^+$ decays. The K$^+$-K$^+$ double-beam process (KK) becomes a background when the second K$^+$ decays in flight at the, or near, the same time as the initial K$^+$ decays. The second K$^+$ in KK can be detected by $\check{C}_K$, BW1, BW2, AD, B4, and TG. The π^+-π^+ double-beam process is highly suppressed due to multiple entering particles and delco and is therefore not considered to be a background.

3.2.5 Charge-Exchange Background

While interacting with matter (i.e. when being slowed down in the Target), K$^+$'s sometimes produce a neutral Kaon (K^0) via the charge-exchange (CEX) process, see Fig. 3.7. Being a neutral particle, K^0s are not slowed down in the Target. K_s^0, having a very short lifetime (0.1 ns), cause a prompt decay. Therefore, any background from K_s^0 will be included in the single-beam and double-beam background measurements. However, a K_L^0 has a lifetime of $\sim$ 50 ns which is within the time window E949 searches for a decay after a KB trigger. The semileptonic decay modes $K_L^0 \rightarrow \pi^+ e^- \nu_e$ and $K_L^0 \rightarrow \pi^+ \mu^- \nu_\mu$ with BR of 40.53% and 27.02% [5], respectively, can become a background when the e$^-$ or μ^- is not observed in the TG. The non-interacting nature of the K_L^0 can create a gap between the initial K$^+$ hits within the TG and the point where the daughter π^+ emerged from the decay vertex. In addition to geometry separation in the K$^+$/π^+ TG hits, CEX background can be suppressed by detection of excess energy due to the negatively charged lepton (e$^-$ or μ^-) within the TG.

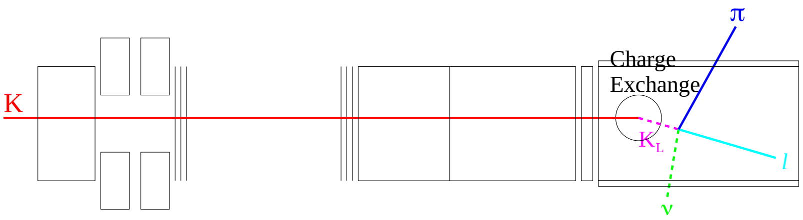

Figure 3.7: Schematic diagram of the charge-exchange interaction background.

3.2.6 Other Backgrounds

Table 3.1 and Table 3.2 contain a very long list of K^+ decays and interactions which could contribute to PNN2 backgrounds. However, all of these decays have already been considered a background or can be discredited as a PNN2 background by the observation of a few key points.

- Decays with a BR less than < 0.00000041 do not contain a π^+ as a product, have multiple charged products, and have very small BRs. The combination of particle identification, extra energy, and small BR eliminate these decays as background processes.
- Many of the decays have three or more photons with no π^+'s in the decay product while having a relatively small (compared to the 21% of $K_{\pi 2}$ decays) branching ratio. E949's photon detection abilities suppress these backgrounds sufficiently well to remove these processes from being a background.
- Decay modes whose charged product's kinematics are below that of the PNN2BOX are nonexistent, except when an event decays in flight. DIF events are included within the single- or double-beam background measurement, so no further measurements are required.
- Events with no π^+ or μ^+ (i.e. events where the e^+ triggers the T•2 condition) are highly suppressed by the $\pi^+ \rightarrow \mu^+ \rightarrow e^+$ criteria along with, the BR value, and dE/dX measurements. Therefore, these decay modes are not expected to contribute as a background to the PNN2 signal.

3.3 Offline Selection Criteria

Initial cuts were created to insure that reconstruction algorithms worked properly to reconstruct an event. When proper reconstruction is assured further cuts to remove background events are employed. Following are descriptions of all cuts used within the analysis.

Each description of the numerous selection criteria (cut) which follow in this section include the acceptance in sequential order as applied in Chapter 5 and, when relevant, the acceptance after all correlated cuts are applied. Some cuts are highly correlated to others which is evident when the two shown acceptance values differ greatly. Also, note that reported time window may have a time offset which is not shown in the description. The time offset is effectively a secondary calibration process and is not necessary in understanding the purpose of the cut.

3.3.1 PASS1 Cuts

Pass1 cuts are the most basic set of cuts which are used to reduce computer processing time and size of data files (ntuples). Pass1 cuts are applied to all signal data throughout this analysis, see Appendix C.

- Trigger Bit (TRBIT)
  The event passes the online trigger bit of $\pi\nu\bar{\nu}(1)$ or $\pi\nu\bar{\nu}(2)$, see Section 2.12.

- Data Taking Quality (BAD_RUN)
  Remove any runs in which the quality of data is in question. Occasionally, sub-detectors have tripped power-supplies, problems arise in electronics, and data acquisition fails leading to unreliable results. Runs with less than 500 events (a typical run had about 200,00 triggered events) were not understood; thus were removed from further analysis. The amount of data in short runs are extremely small.

- Charged Track Reconstruction (RD_TRK)
  Require proper reconstruction of the charged track in the Range Stack. $K_{\mu 2}$

monitors are used to measure an acceptance of 1.0000 and an acceptance of 1.0000 after all correlated cuts are applied.

- Track Time Reconstruction (TRKTIM)

  The average time of the track hits in the Range Stack is obtained. $K_{\mu2}$ monitors are used to measure an acceptance of 0.9999 and an acceptance of 0.9999 after all correlated cuts are applied.

- Consistency between Online and Offline Stopping Counters (STLAY)

  The stopping counter that is found by the online Stopping-Counter Finder (SCF) is required to be the same as the one determined by the offline track finding routine. $\pi_{scatter}$ monitors are used to measure an acceptance of 0.9907 ± 0.00042 and an acceptance of 0.9944 ± 0.00043 after all correlated cuts are applied.

- Stopping-Counter Performance (BAD_STC)

  TD channels for eight sectors of layer 10 in the RS had unreliable signals during specific periods of data collection. Events with stopping counter in the unreliable counters will not be considered for further analysis. $\pi_{scatter}$ monitors are used to measure an acceptance of 0.9984 ± 0.00010 and an acceptance of 0.9984 ± 0.00010 after all correlated cuts are applied.

- UTC Track Fitting (UTC)

  Require charged track to be successfully reconstructed in the UTC. $K_{\mu2}$ monitors are used to measure an acceptance of 0.9435 ± 0.00019 and an acceptance of 0.9435 ± 0.00019 after all correlated cuts are applied.

- Matching Between UTC and RS Tracks (RDUTM)

  The extrapolated UTC track is required to intersect the T•2 sector. $K_{\mu2}$ monitors are used to measure an acceptance of 0.9994 ± 0.00002 and an acceptance of 0.9994 ± 0.00002 after all correlated cuts are applied.

- Target Reconstruction (TARGET)

  Target reconstruction is required to be successful, see Appendix B. $K_{\mu 2}$ monitors are used to measure an acceptance of 1.0000 and an acceptance of 1.0000 after all correlated cuts are applied.

- Momentum in UTC (PDC)

  The momentum measured by the UTC is required to be less than 280.0 MeV/c. This requirement removes failures of UTC pattern recognition.

- Photon Veto around the Stopping Counter (RSHEX)

  Extra hits are not allowed in the counter after the stopping counter and the hextants that do not have track hits. $\pi_{scatter}$ monitors are used to measure an acceptance of 0.9637 ± 0.00082 and an acceptance of 0.9666 ± 0.00103 after all correlated cuts are applied.

- Sector Crossing Cut (RSHEX2)

  A charged track crossing from one sector into another in the stopping layer is not allowed. $\pi_{scatter}$ monitors are used to measure an acceptance of 0.9814 ± 0.00042 and an acceptance of 0.9999 ± 0.00005 after all correlated cuts are applied.

3.3.2 PASS2 Cuts

- PASS2 Photons (PVCUT)

  Detect photons in Barrel Veto (BV), End Cap (EC) and Range Stack (RS) which are coincident in time with the T•2 charged track. Coincident energy is defined within a time window about the charged track time as shown in Table 3.3. The total concident energy must be less than the energy threshold as shown in Table 3.3. $K_{\mu 2}$ monitors are used to measure an acceptance of 0.9622 ± 0.00085 and an acceptance of 0.9888 ± 0.00061 after all correlated cuts are applied.

Subsystem	Time Window	Energy Threshold
Barrel Veto	±2.0 ns	1.5 MeV
End Cap	±1.5 ns	3.5 MeV
Range Stack	±1.5 ns	3.0 MeV

Table 3.3: PASS2 Photon Veto (PVCUT) parameters.

- Target Reconstruction (TGCUT)

  This cut consists of the following requirements:

  - Target reconstruction successful, see Appendix B.
  - Consistency between TG K^+ time and B4 time: $|t_{\mathrm{K}} - t_{b4strob}| \leq 4.0$ ns, such that t_{K} is the average time of K^+ TG-fiber hits and $t_{b4strob}$ is the B4 Hodoscope hit time.
  - Consistency between TG time and RS time: $|t_\pi - t_{RS}| \leq 5.0$ ns
  - Consistency between IC time and RS time: $|t_{IC} - t_{RS} + 0.3| \leq 5.0$ ns.
  - The energy deposit in the IC should be consistent with expected energy deposit due to π^+: $|E_{ICest} - E_{IC}| \leq 4.0$ MeV.

  $K_{\mu 2}$ monitors are used to measure an acceptance of 0.9781 ± 0.00008 and an acceptance of 1.0000 after all correlated cuts are applied.

- Accidentals at Muon Time (TDCUT)

  Search for accidental activity in the RS that is coincident with the second pulse time (muon time) in the stopping counter. Events are rejected if the energy sum of the coincident hits exceeds a threshold. $\pi_{scatter}$ monitors are used to measure an acceptance of 0.9396 ± 0.00090 and an acceptance of 0.9930 ± 0.00034 after all correlated cuts are applied.

- Beam dE/dX & Double-Beam (PSCUT)

  Require that the energy deposit in the B4 Hodoscope is consistent with the energy deposit of a K^+ (> 1.0 MeV). Also, require no extra beam particle coincident, as determined by the B4 and $\check{C}_\pi$, with the time of the T•2 track. $K_{\mu 2}$ monitors are used to measure an acceptance of 0.9485 ± 0.00014 and an acceptance of 1.0000 after all correlated cuts are applied.

- Target Photon Veto (TGPVCUT)

  Remove events with coincident ($|t_\gamma + 0.5| < 1.0$ ns) TG-photon energy greater than 5.0 MeV, see Appendix B for information regarding photon fibers in TG. $K_{\mu 2}$ monitors are used to measure an acceptance of 0.9903 ± 0.00045 and an acceptance of 1.0000 after all correlated cuts are applied.

- Pass1 Loose Delayed Coincidence (DELCO)

  Require that Kaons decay at least 1.0 ns after entering the Target. $K_{\mu 2}$ monitors are used to measure an acceptance of 0.8569 ± 0.00020 and an acceptance of 0.9669 ± 0.00023 after all correlated cuts are applied.

- TG-scatter (GOODKINK)

  Observed a scatter in the TG π^+ track, see Appendix B. Instead of determining the signal region, this cut is employed to flag events for photon cut optimization in x-y scattered events (kinks).

3.3.3 Skims

To reduce the size of resultant data ntuples, as seen in Table 3.4, PASS2 cuts are grouped together to form four sets of events, skims. The cuts for each skim are determined to enhance a given background. The skims are subdivided into the 1/3 and 2/3 analysis samples. The union of skims 1-3 (5-7) gives the 2/3 (1/3) data sample used throughout the analysis. The union of skim 4 and 8 gives the full, three-thirds (3/3) TG-scatter sample used to optimize the photon-veto studies.

skim	Data Sample	Cuts
1 (5)	1/3 (2/3) $K_{\pi 2}$	TGCUT, PSCUT, TDCUT, TGPVCUT
2 (6)	1/3 (2/3) $K_{\mu 2}$	TGCUT, PSCUT, PVCUT, TGPVCUT, DELCO
3 (7)	1/3 (2/3) $\pi_{scatter}$	TGCUT, TDCUT, PVCUT
4 (8)	1/3 (2/3) kinks	GOODKINK

Table 3.4: Definition of skims. Each skim is an enhanced background sample, as denoted in the *Data Sample* column. The union of skim 1-3 (5-7) comprise the 1/3 (2/3) signal sample. "kinks" are TG-scatters in the x-y plane.

3.3.4 Kinematic Cuts

When all cuts in this subsection are joined together it is referred to as KINCUT.

Fiducial Cuts

- Layer-14 Cut (LAYER14)

  No charged track is allowed to come to rest in the second layer of the RSSCs embedded between RS layers 14 and 15. Events are rejected if the stopping layer is 14 and a prompt RSSC hit is found in the same sector or one sector clockwise of the stopping counter.

- Polar-Angle Cut (COS3D)

  Restrict the cosine of the polar angle ($cos3d$), see Fig. 2.3, of the charged track (allow $|\cos\theta| \leq 0.5$).

- Stopping Z-Position Cut (ZFRF)

  Require that the π^+ stopping z position in the Range Stack ($z_{\pi stop}$) is within the fiducial volume as defined in Table 3.5.

Stopping Layer	Cut Condition (cm)
11,12	$-35 \leq z_{\pi stop} \leq 35$
13	$-40 \leq z_{\pi stop} \leq 40$
14	$-30 \leq z_{\pi stop} \leq 30$
15,16,17,18	$-50 \leq z_{\pi stop} \leq 50$

Table 3.5: z position conditions for stopping π^+ for relevant stopping layers.

- Fiducial Cut in UTC (ZUTOUT)

  Demand that the charged track must pass through the active region of the UTC. This is accomplished by requiring the z position of the track exiting point be no further than 25 cm from the UTC center.

Track Reconstruction Cuts

- Track Reconstruction in the UTC (UTCQUAL)

  The necessity of a good UTC track is required to obtain reliable kinematics. Therefore, UTCQUAL reject events with poor fits to the track within the UTC or with an overlapping track. A likelihood condition based upon the number of hits used in the UTC track fit, number of UTC layers hit, and the number of unused hits within 1.5 cm of the fitted track is employed by the analysis to select good fits. Conditions exist for both the x-y plane and the z plane. $\pi_{scatter}$ monitors are used to measure an acceptance of 0.9510 ± 0.00072 and an acceptance of 0.9634 ± 0.00068 after all correlated cuts are applied.

- RS Track Reconstruction and Matching with the UTC Track (PRRF)

  This cut is implemented to remove scattering of the charged track in the RS. It consists of the following criteria:

  - χ^2 Probability Cut for RS Track Reconstruction (PRRF1)

    Reject events if the quality of the RS track fitting in the x-y plane is poor. The RS track fitting is performed using sector crossing positions, RSSC hit positions, and the energy deposit in the π^+ stopping counter. $\pi_{scatter}$ monitors are used to measure an acceptance of 0.9918 ± 0.00033 and an acceptance of 1.0000 after all correlated cuts are applied.

- Track Matching in RSSC Z Measurements (PRRFZ1)
  Reject events if the track reaches the RSSCs and the matching in the r-z plane between the UTC extrapolation and the RSSC hit positions is poor. $\pi_{scatter}$ monitors are used to measure an acceptance of 0.9659 ± 0.00066 and an acceptance of 1.0000 after all correlated cuts are applied.

- Track Matching in RS Z Measurements (PRRFZ2)
  Reject events if the matching in the r-z plane between the UTC extrapolation and the track hit positions derived from end-to-end timing in the RS counters is poor. $\pi_{scatter}$ monitors are used to measure an acceptance of 1.0000 and an acceptance of 1.0000 after all correlated cuts are applied.

dE/dX Cut in the Range Stack (RSDEDX)

- Maximum Energy Deviation in RS (RSDEDXMAX)
  Deviations of energy deposits in the individual track counters are examined.

$$\chi_i \equiv \frac{\log E^i_{exp} - \log E^i_{meas}}{\sigma^i} \tag{3.1}$$

  In Eq. (3.1), E^i_{meas} is the measured energy deposit in the i^{th} track counter and E^i_{exp} is the energy in the i^{th} track counter expected from the measured range. Reject events with the absolute value of the largest χ_i greater than or equal to 4. Additional constraints are based upon fit times and energy determined by *fitpi4* routine [54]. $\pi_{scatter}$ monitors are used to measure an acceptance of 0.9711 ± 0.00058 and an acceptance of 1.0000 after all correlated cuts are applied.

- Confidence Level in RS Energy Measurements (RSDEDXCL)
  The confidence level is calculated from the probability of χ^2 from Eq. (3.1).

Events are cut if the RS confidence-level is less than 0.04 (*cl_rsdedx* < 0.04). $\pi_{scatter}$ monitors are used to measure an acceptance of 0.9550 ± 0.00073 and an acceptance of 1.0000 after all correlated cuts are applied.

- Likelihood Cut for RS Energy Measurements (RSLIKE)

  A likelihood condition is constructed from the energy deposits in the track counters. The likelihood value is required to be between 0 and 10. $\pi_{scatter}$ monitors are used to measure an acceptance of 1.0000 and an acceptance of 1.0000 after all correlated cuts are applied.

π/μ Separation in Range Stack

- Range-Momentum Consistency (RNGMOM)

  π^+'s and μ^+'s occupy different regions of the range-momentum phase-space, see Fig. 3.3. This cut is designed to remove charged tracks within the muon-band, events which do not exhibit π^+ kinematics. The condition in Eq. (3.2) is implemented to fulfill the desired effect.

$$\chi_{RP} \equiv \frac{R_{meas} - R_{exp}}{\sigma_R} \leq 2.2 \tag{3.2}$$

  where R_{exp} is the range expected from the measured momentum with the assumption that the charged track is a π^+. $\pi_{scatter}$ monitors are used to measure an acceptance of 0.9819 ± 0.00046 and an acceptance of 0.9845 ± 0.00045 after all correlated cuts are applied.

Phase Space Cuts

- Kinematic Box for PNN2 region (BOX)

  Define the PNN2 region of phase space by the kinematic constraints in

Eq. (3.3)-Eq. (3.5). BOX is a loosen version of BOX used in E787.

$$140.0\ \text{MeV/c} \leq \ ptot \ \leq 199.0\ \text{MeV/c} \tag{3.3}$$

$$60.0\ \text{MeV} \leq \ etot \ \leq 100.5\ \text{MeV} \tag{3.4}$$

$$12.0cm \leq \ rtot \ \leq 28.0\ \text{cm} \tag{3.5}$$

- Tight Kinematic Box for PNN2 region (TIGHTBOX)

  Define a background-reduced region of phase space by employing the kinematic constraints listed in Eq. (3.6)-Eq. (3.8). This kinematic region was created to effectively removed K_{e4} background. These constraints are identical to previous PNN2 analysis. TIGHTBOX monitors are used to measure an acceptance of 0.0 ± 0.0 and an acceptance of 0.0 ± 0.0 after all correlated cuts are applied.

$$165.0\ \text{MeV/c} \leq \ ptot \ \leq 197.0\ \text{MeV/c} \tag{3.6}$$

$$72.0\ \text{MeV} \leq \ etot \ \leq 100.0\ \text{MeV} \tag{3.7}$$

$$17.0cm \leq \ rtot \ \leq 28.0\ \text{cm} \tag{3.8}$$

3.3.5 Beam Cuts

Single-Beam Cuts

- dE/dX in B4 Hodoscope (B4DEDX)

  Demand a K^+ entering the TG by requiring the energy in the B4 to be $\geq$1.1 MeV. $K_{\mu 2}$ monitors are used to measure an acceptance of 0.9945 ± 0.00005 and an acceptance of 0.9973 ± 0.00007 after all correlated cuts are applied.

- K^+ Stop Requirement: Delayed Coincidence (DELC3)

  Determining that the incoming K^+ stops within the TG is accomplished by observing a delay in the outgoing charged track which is presumed to be a K^+-decay product. This requirement will remove beam-π^+ scattering events and

K^+ decay-in-flight events. DELC3 requires a delay of at least 3.0 ns between the target π^+ time, t_π, and the target K^+ time, t_K,($tpi - tk \geq 3.0$ ns). Additionally, DELC3 requires the constraints defined in the conditional delco function, *delc*, described below. $K_{\mu 2}$ monitors are used to measure an acceptance of 0.8569 ± 0.00020 and an acceptance of 0.9669 ± 0.00023 after all correlated cuts are applied.

- Tight Delayed Coincidence (DELC6)

  A tighter delayed coincidence cut is employed for the use in a signal region with reduced background. This is accomplished by a 6.0 ns delayed concidence requirement ($tpi - tk \geq 6.0$ ns). $K_{\mu 2}$ monitors are used to measure an acceptance of 0.7044 ± 0.00026 and an acceptance of 0.8804 ± 0.00043 after all correlated cuts are applied.

- Delayed Coincidence Function (*delc*)

  This function tightens the delay coincidence when the timing consistency between detectors are degraded. Events are rejected if $t_\pi - t_\mathrm{K} < delc_{thres}$. The cut threshold, $delc_{thres}$ is the maximum of the following conditions ($delc_{thres}$ minimum is 2.0 ns).

  - $delc_{thres} = 5.0$ ns if the discrepancy between the TG K^+ time and B4 hit time is greater than 1.0 ns.
  - $delc_{thres} = 6.0$ ns if the discrepancy between the TG π^+ time and track time is greater than 1.5 ns.
  - $delc_{thres} = 5.0$ ns if t_π is obtained from the time of the I-Counter hit, not from the TG π^+ fiber hits.
  - $delc_{thres} = 4.0$ ns if the energy deposit of a K^+ in the TG is less than or equal to 50 MeV.
  - $delc_{thres} = 3.0$ ns if there are less than four TG π^+ fibers found.

  - $delc_{thres}$ = 3.0 ns if the beam likelihood value is less than 200 (to be explained in the Pathology Cuts section).
  - $delc_{thres}$ = 4.0 ns if the discrepancy between any of the individual K^+ fiber times and the average K^+ time is greater than 2.0 ns.
  - $delc_{thres}$ = 4.0 ns if the discrepancy between any of the individual π^+ fiber times and the average π^+ time is greater than 3.5 ns.

Double-Beam Cuts

The purpose of double-beam cuts are to remove events with beam particles occurring at track time, t_{RS}, due to the possibility of the particle scattering into the fiducial region. Events which scatter into the fiducial region may create conditions that occur in signal candidates.

- Double-Pulse Fitting in B4 Hodoscope (B4CCD)
  Pulses recorded in the B4 CCDs are fitted with a double-pulse assumption. Reject events if hit modules have a signature of double pulses, and the average time of the fitted second pulses is within ±3.5 ns of the track time. The signature of double pulses is a ratio of the single-pulse fit χ^2 to the double-pulse fit χ^2 that is greater than 2.5 and the amplitude of the fitted second pulse exceeds a threshold. $K_{\mu 2}$ monitors are used to measure an acceptance of 0.9865 ± 0.00008 and an acceptance of 0.9902 ± 0.00013 after all correlated cuts are applied.

- Timing in B4 Hodoscope (B4TRS)
  Events are rejected if the average TDC time of hit modules in the B4 Hodoscope is within ±2.5 ns of the track time or the average CCD time of hit modules is within ±1.5 ns of the track time when the energy sum is above 0.7 MeV. $K_{\mu 2}$ monitors are used to measure an acceptance of 0.9744 ± 0.00011 and an acceptance of 0.9757 ± 0.00020 after all correlated cuts are applied.

- Timing in BWPCs (BWTRS)

  Remove events with a beam particle near track time by requiring the time of a hit cluster in any Beam-Wire Chamber be within ±4.5 ns of track time. $K_{\mu 2}$ monitors are used to measure an acceptance of 0.9179 ± 0.00017 and an acceptance of 0.9591 ± 0.00026 after all correlated cuts are applied.

- Timing in K^+ Čerenkov Counter (CKTRS)

  Events are rejected if the average TDC or CCD time of hits in the K^+ Čerenkov Counter is within ±2.0 ns of the track time. $K_{\mu 2}$ monitors are used to measure an acceptance of 0.9936 ± 0.00005 and an acceptance of 0.9981 ± 0.00006 after all correlated cuts are applied.

- Trailing-Edge Timing in K^+ Čerenkov Counter (CKTAIL)

  The average time of hits in the K^+ Čerenkov Counter, $t_{C_k tail}$, obtained from the trailing edge of the pulses, must not be coincident with the track time ($|t_{C_k tail} - t_{RS}| < twindow_{cktail}$). $K_{\mu 2}$ monitors are used to measure an acceptance of 0.9839 ± 0.00008 and an acceptance of 0.9912 ± 0.00012 after all correlated cuts are applied. The timing window, $twindow_{cktail}$, for this cut is defined as follows:

  - $twindow_{cktail} = 3.0$ ns when $t_\pi - t_{\mathrm{K}} < 15.0$ ns.
  - $twindow_{cktail} = 3.5$ ns when $15 \leq t_\pi - t_{\mathrm{K}} < 25.0$ ns.
  - $twindow_{cktail} = 2.0$ ns when $t_\pi - t_{\mathrm{K}} \geq 25.0$ ns.

- Timing in π^+ Čerenkov Counter (CPITRS)

  Events are rejected if the average TDC or CCD time of hits in the π^+ Čerenkov Counter is within ±2.0 ns of the track time. $K_{\mu 2}$ monitors are used to measure an acceptance of 0.9983 ± 0.00003 and an acceptance of 0.9997 ± 0.00002 after all correlated cuts are applied.

- Extra Timing Cut in Pion Čerenkov Counter (CPITAIL)

  The average time of hits in the Pion Čerenkov Counter, obtained from the trailing edge of the pulses (minus the TDC width), is required not be coincident with the track time. The event is rejected if there are any hits within ±2.0 ns of the track time. $K_{\mu 2}$ monitors are used to measure an acceptance of 0.9995 ± 0.00001 and an acceptance of 0.9998 ± 0.00002 after all correlated cuts are applied.

  - $twindow_{cpitail} = 3.0$ ns when $t_\pi - t_{\mathrm{K}} < 15.0$ ns.
  - $twindow_{cpitail} = 3.5$ ns when $15 \leq t_\pi - t_{\mathrm{K}} < 25.0$ ns.
  - $twindow_{cpitail} = 2.0$ ns when $t_\pi - t_{\mathrm{K}} \geq 25.0$ ns.

- Timing in USPV (USPVTRS)

  Events are removed if there is a USPV hit that is coincident with track time. This is implemented by removing events with the following criteria using USPV time from CCDs and TDCs:

$$-3.5 < \quad t_{CCD} - t_{RS} \quad < 2.4 \text{ ns} \tag{3.9}$$

$$-3.75 < \quad t_{TDC} - t_{RS} \quad < 2.5 \text{ ns} \tag{3.10}$$

  $K_{\mu 2}$ monitors are used to measure an acceptance of 0.9836 ± 0.00009 and an acceptance of 0.9847 ± 0.00016 after all correlated cuts are applied.

- Timing in RV (RVTRS)

  Require events have no hits within ±4.0 ns of track time using CCDs and TDCs. $K_{\mu 2}$ monitors are used to measure an acceptance of 0.9990 ± 0.00002 and an acceptance of 0.9993 ± 0.00003 after all correlated cuts are applied.

Pathology Cuts

- Consistency between B4 Hodoscope Analyses (B4ETCON)

  Require consistency between timing and energy within the B4 electronics by demanding the time of the TDC and CCD are within ±2.0 ns of each other.

Also, demand the energy determined from ADC is within 1.5 MeV of energy from CCD. $K_{\mu 2}$ monitors are used to measure an acceptance of 0.9901 ± 0.00005 and an acceptance of 0.9962 ± 0.00008 after all correlated cuts are applied.

- Double-beam in Target (TGGEO)

  Timing information in the IC is used to reject double-beam background with the following signature:

  1. Both particles enter the TG from the target edge or an I-Counter
  2. The first particle or its decay product deposits a large energy pulse in the I-Counter
  3. The first particle enters the TG, decaying downstream or decaying very late (i.e., the decay product is not detected). The second particle is scattered upstream of the beam line and misses some beam counters. Later, by multiple scattering, the product of the second particle enters the TG and intersects the hit fibers of the first beam particle.

  These signatures fool the target reconstruction. $K_{\mu 2}$ monitors are used to measure an acceptance of 0.9599 ± 0.00014 and an acceptance of 0.9860 ± 0.00016 after all correlated cuts are applied.

- Target Reconstruction (TGQUALT)

  The target reconstruction algorithm *swathccd*, see Appendix B, successfully reconstructed the event with at least one TG fiber being classified as a Pion (or Muon). $K_{\mu 2}$ monitors are used to measure an acceptance of 0.9651 ± 0.00010 and an acceptance of 1.0000 after all correlated cuts are applied.

- Timing Consistency between Target and B4 Hodoscope (TIMCON)

  Require consistency between the target K^+ time (t_{K}) and the time of hit in the B4 Hodoscope (t_{B4}). Also, require consistency between the target π^+ time (t_π) and the track time (t_{RS}), as shown in Eq. (3.11). $K_{\mu 2}$ monitors are used to measure an acceptance of 0.9985±0.00002 and an acceptance of 0.9991±0.00004 after all correlated cuts are applied.

$$|t_{\rm K} - t_{B4}| \leq 3.0 \text{ ns} \quad \text{and} \quad -4.5 < t_\pi - t_{RS} < 4.0 \text{ ns} \tag{3.11}$$

- Timing Consistency among Target $\rm K^+$ Fibers (TGTCON)

  Require consistency between the average time of the $\rm K^+$ fiber hits and the times of the individual $\rm K^+$ fiber hits in the Target. For every $\rm K^+$ fiber, i, require $|t_{\rm K} - t^i_{\rm K}| \leq \sigma_{thres}$. σ_{thres} is an energy dependent value with values between 2.05 − 3.68 ns. $K_{\mu 2}$ monitors are used to measure an acceptance of 0.9892 ± 0.00005 and an acceptance of 1.0000 after all correlated cuts are applied.

3.3.6 Target Quality Cuts

When all cuts in this subsection is grouped together they are referred to as TGCUT06.

- Beam Likelihood (B4EKZ)

  The $\rm K^+$ identified in the TG must behave as a beam $\rm K^+$. Using the energy deposited in the B4, energy deposited by the beam particle in the TG, and the stopping position of the beam particle in the TG (determined by UTC track extrapolation) a likelihood value is determined for each event. If the likelihood value ($like_{b4ekz}$) is less than 10.0, the event will be rejected. The threshold is tightened to 20.0 if t_π is based upon the IC time, see Appendix B for further details. $K_{\mu 2}$ monitors are used to measure an acceptance of 0.9116 ± 0.00020 and an acceptance of 0.9474 ± 0.00029 after all correlated cuts are applied.

- Target Fiducial Region (TGZFOOL)

  Demand that the $\rm K^+$-decay vertex (tgx,tgy,tgz) be within the TG fiducial volume. The upstream edge of the TG is at $tgz = -10$ cm, where tgz is the z

position of the decay vertex. The cut is set to be $tgz < -5.0$ cm which is much tighter than PNN1 analysis performed; this is due to possible π^+ scatters in the B4 before entering the UTC and RS. $K_{\mu 2}$ monitors are used to measure an acceptance of 0.9876 ± 0.00008 and an acceptance of 0.9850 ± 0.00016 after all correlated cuts are applied.

- Energy Cut on Target Pion Fiber (EPITG)
  Require that any target π^+ fiber should have an energy of less than or equal to 3.0 MeV. The nominal energy of a π^+ in a fiber is $\sim$1.2 MeV. Large energy within an individual fiber is indicative of a scattering process. $K_{\pi 2}$ monitors are used to measure an acceptance of 0.8965 ± 0.00129 and an acceptance of 0.9665 ± 0.00085 after all correlated cuts are applied.

- Target Gap between K$^+$ and Pion Fibers (TARGF)
  Require the identified K$^+$ cluster to be contiguous with π^+ fibers by rejecting events with the minimum distance between K$^+$ and π^+ fibers greater than 0.6 cm (i.e. more than one fiber). $K_{\mu 2}$ monitors are used to measure an acceptance of 0.9678 ± 0.00013 and an acceptance of 0.9705 ± 0.00022 after all correlated cuts are applied.

- Tag Gaps between K$^+$ and Charged Track (KPIGAP)
  KPIGAP is a specialized function used to tag events where the π^+ track does not emerge from the K$^+$ fibers in the TG. TARGF will do this in ideal situations. However, the *swathccd* algorithm has limitations placed upon the energy of the charged track. This limitation can mask possible K$^+$ decays where the charged track emerges from the K$^+$ identified stopping position. TG π^+ scatters have this quality. *swathccd* will likely reconstruct high-energy scatter pion-fiber hits as photon hits. KPIGAP searches for coincident photon fibers (within 3.0 ns of t_{RS}) that can fill the gap. If the gap between the K$^+$ and π^+ fibers are bridged with coincident photon fibers, then do not tag the event. KPIGAP is used only in the beam and CEX background measurements to tag

a cleaner, compared to previous analyses, sample. In past analysis, $\overline{TARGF}$ was used to tag the background samples used in 2-beam and CEX backgrounds. This cut is not applied in normalization branches of backgrounds or the final signal box, so no acceptance was measured.

- Matching between Target and UTC (DTGTTP)

  Require that the TG and UTC tracks are well matched to each other at the target radius. This cut eliminates events in which the UTC track does not intersect the target edge. $K_{\mu 2}$ monitors are used to measure an acceptance of 1.0000 and an acceptance of 1.0000 after all correlated cuts are applied.

- Quality on Target Path Length Calculation (RTDIF)

  Require a small uncertainty in the calculation of the π^+ path length in the Target. This is equivalent to the π^+ path hidden under the K^+ fibers, and it is required to be less than 1.5 cm. $K_{\mu 2}$ monitors are used to measure an acceptance of 0.9904 ± 0.00007 and an acceptance of 0.9955 ± 0.00009 after all correlated cuts are applied.

- Target Kink (DRP)

  The maximum and minimum distance from the center of the TG π^+ fibers to the center of the circle that is fitted to the track path by the UTC are examined. Reject events if the distribution of the π^+ fibers is broad, namely

  $$\frac{d_{max} - d_{min}}{R_{tg}} > 0.35 \tag{3.12}$$

  where d_{max} and d_{min} are the maximum and minimum distances, respectively, and R_{tg} is the range of the track in the Target. $K_{\pi 2}$ monitors are used to measure an acceptance of 0.9983 ± 0.00019 and an acceptance of 0.9982 ± 0.00020 after all correlated cuts are applied.

- Time Consistency with the B4 (TGKTIM)

  The time in each target K^+ fiber is required to be consistent with the K^+ time in the B4 counter and the track time in the Range Stack. These criteria are established by the following cutting conditions:

$$t^i_{\mathrm{K}} - t_{B4TDC} > \quad 3.5 \text{ ns} \tag{3.13}$$

$$t^i_{\mathrm{K}} - t_{B4TDC} > \quad (t_{RS} - t^i_{\mathrm{K}}) - 1.0 \text{ ns} \tag{3.14}$$

TGKTIM is correlated with TIMCON and TGTCON. $K_{\mu 2}$ monitors are used to measure an acceptance of 0.9901±0.00007 and an acceptance of 0.9980±0.00006 after all correlated cuts are applied.

- Expected I-Counter Energy (EIC)
  Require consistency between the IC measured energy (E_{meas}), as shown in Eq. (3.15), and energy estimated based on the IC path length (E_{est}). $K_{\mu 2}$ monitors are used to measure an acceptance of 0.9732 ± 0.00012 and an acceptance of 0.9732 ± 0.00021 after all correlated cuts are applied.

$$-5.0 \text{ MeV} \leq E_{meas} - E_{est} \leq 1.75 \text{ MeV} \tag{3.15}$$

- Timing Consistency between Range Stack and I-Counter (TIC)
  As shown in Eq. (3.16), Require timing consistency between the track time (t_{RS}) and I-Counter hit time (t_{IC}). $K_{\mu 2}$ monitors are used to measure an acceptance of 1.0000 and an acceptance of 1.0000 after all correlated cuts are applied.

$$|t_{RS} - t_{IC}| \leq 5.0 \text{ ns} \tag{3.16}$$

- Energy in Target Edge Fibers (TGEDGE)
  Reject events with large energy in the TG edge fibers, see Appendix B and Section 2.8. This is done by rejecting events with $E^i_{edge} \geq 4.0$ MeV, such that E^i_{edge} is the total energy in an edge-fiber PMT (edge-fiber PMTs are highly multiplexed), within ±5.0 ns of t_{RS}. $K_{\pi 2}$ monitors are used to measure an acceptance of 0.9945 ± 0.00033 and an acceptance of 0.9946 ± 0.00035 after all correlated cuts are applied.

- Target dE/dX Cut (TGDEDX)

  The dE/dX of π^+'s in the PNN2BOX (140 MeV/c to 195 MeV/c) changes from 3.08 MeV/cm to 2.47 MeV/cm in plastic scintillator. A likelihood function was created by using the total measured momentum (*ptot*), target range (*rtg*) and the target energy (*etg*) of beam-π^+ events. The target range was quantified in five momentum bins and 15 target energy bins. For each bin, the mean target range and sigma was stored and a likelihood function was created assuming a Gaussian distribution. This cut rejects events if this likelihood is small, $tgdedx\_like \leq 0.05$. Details of TGDEDX calibration is available in Appendix D. $K_{\pi 2}$ monitors are used to measure an acceptance of 0.9893 ± 0.00042 and an acceptance of 0.9970 ± 0.00026 after all correlated cuts are applied.

- Extreme Target Pion Energies (TGENR)

  This cut rejects events if the total π^+ energy in the TG is either too large ($E_{tg} > 28$ MeV) or too small ($E_{tg} < 1$ MeV). $K_{\pi 2}$ monitors are used to measure an acceptance of 0.9673 ± 0.00073 and an acceptance of 0.9793 ± 0.00067 after all correlated cuts are applied.

- Gap between TG Pion Fibers (PIGAP)

  Reject events with a gap between target π^+ fibers greater than 1.5 cm. This cut is tightened to 1.0 cm when the cosine of the polar angle is negative and the z position of the track in the I-Counter is less than -7.0 cm. $K_{\mu 2}$ monitors are used to measure an acceptance of 0.9913 ± 0.00007 and an acceptance of 0.9947 ± 0.00010 after all correlated cuts are applied.

- Consistency between B4 and Target K$^+$ Position (DB4TIP)

  Require consistency between the beam particle in the B4 and TG. Implement this cut by removing events that have the position of the beam particle (x_{B4}, y_{B4}) and the closest tip of a K$^+$ cluster, see Appendix B, to be greater than 1.8 cm. $K_{\mu 2}$ monitors are used to measure an acceptance of 0.9949 ± 0.00006 and an acceptance of 1.0000 after all correlated cuts are applied.

- Decay Vertex at Tip (DVXTIP)

  Reject events with a distance between the K$^+$-decay vertex and the nearest tip of the K$^+$ cluster of more than 0.7 cm.; effectively requiring the vertex to be at a tip of the K$^+$'s path in the TG. $K_{\mu 2}$ monitors are used to measure an acceptance of 0.9974 ± 0.00004 and an acceptance of 1.0000 after all correlated cuts are applied.

- Gap between K$^+$ and Pion Fibers in Target (DVXPI)

  Reject events with a distance between the K$^+$-decay vertex and the closest π^+ fiber of more than 1.5 cm. This cut ensures that the π^+ is from the identified K$^+$ cluster. $K_{\mu 2}$ monitors are used to measure an acceptance of 0.9779 ± 0.00012 and an acceptance of 1.0000 after all correlated cuts are applied.

- Back-to-back Track Cut in Target (PHIVTX)

  Reject events with back-to-back tracks in the Target. $K_{\mu 2}$ monitors are used to measure an acceptance of 0.9700 ± 0.00014 and an acceptance of 0.9878 ± 0.00015 after all correlated cuts are applied.

- Opposite-side Pion Fibers (OPSVETO)

  Remove possible multiple-body decays. This is accomplished by requiring the total energy of opposite-side pions within ± 4.0 ns of t_π be less than 1.0 MeV. The energy threshold is reduced to 0.5 MeV when $like_{beam} < 200.0$. Opposite-side pions are hits that exist in fibers on the other side of the K$^+$ cluster (relative to π^+ fibers). $K_{\mu 2}$ monitors are used to measure an acceptance of 0.9742 ± 0.00063 and an acceptance of 0.9742 ± 0.00063 after all correlated cuts are applied.

- Target Likelihood (TGLIKE1)

  Require the π^+ hits within the TG to have characteristics consistent with a clean non-scattered π^+-track (in the TG) by removing events with additional energy from other processes such as photons or pion-scattering. This criteria is accomplished by use of the TG-pion-likelihood function. This likelihood function is employed during TG reconstruction, see Appendix B, as a means of selecting π^+ hits. The likelihood value $like_{TG}$ for each π^+ hit is based upon the following:

- Time difference between the time of the π^+ hit and the energy-weighted time average of all TG-pion hits.
- Distance between the center of the hit fiber and the closest approach of the extrapolated UTC track.
- Expected energy based upon average π^+ energy per fiber, calibrated with $K_{\pi 2}(1)$ monitor triggers.

Remove events when the average $like_{TG}$ is less than $10^{-3.2}$. $K_{\pi 2}$ monitors are used to measure an acceptance of 0.9819 ± 0.00055 and an acceptance of 1.0000 after all correlated cuts are applied.

- Target Trajectory Likelihood (TGLIKE2)
  TGLIKE2 is an additional fiber-position constriction of TGLIKE1 with the likelihood value determined with the time difference defined as 0. ns and the observed energy defined as 1.0 MeV. This results in a value which represents the trajectory of the π^+ track in the TG. The new threshold to removed events is $10^{-2.3}$. $K_{\pi 2}$ monitors are used to measure an acceptance of 0.9840 ± 0.00053 and an acceptance of 1.0000 after all correlated cuts are applied.

- Time, Energy and Position Cut for K$^+$ Fibers (TIMKF)
  Demand consistent information along the path of the K$^+$ in the TG. As the K$^+$ slows down in the TG the times of each subsequent fiber is later than the preceding one. The TG timing accuracy is sufficient to observe this effect in K$^+$ hits. An analogous cut is not applied for the π^+ fibers since, the accuracy of π^+ hit times is lower than K$^+$ hit times due to lower energy per fiber. One intent of TIMKF is to remove high-energy π^+ fibers which were misclassified as

a K^+ hit during the reconstruction process. $K_{\mu 2}$ monitors are used to measure an acceptance of 0.9025 ± 0.00036 and an acceptance of 0.9056 ± 0.00037 after all correlated cuts are applied.

- Minimum Number of Pion Fiber (NPITG)

  Within the TG, require that at least one π^+ hit to exist outside a K^+ fiber. $K_{\mu 2}$ monitors are used to measure an acceptance of 1.0000 and an acceptance of 1.0000 after all correlated cuts are applied.

- CCD Pulse Fits in the K^+ Fibers (ALLKFIT)

  Require the fitting algorithm for target CCD pulses to work properly in all hit fibers. This is only required on fibers with energy greater than 3.0 MeV. $K_{\mu 2}$ monitors are used to measure an acceptance of 0.9874 ± 0.00015 and an acceptance of 0.9874 ± 0.00015 after all correlated cuts are applied.

- Pion Time Distribution Width (TPICS)

  Reject events for which the standard deviation of the pion-fiber time distribution in the TG is greater than 4.0 ns. $K_{\mu 2}$ monitors are used to measure an acceptance of 0.9987 ± 0.00005 and an acceptance of 0.9987 ± 0.00005 after all correlated cuts are applied.

- Pion Energy Under a K^+ Fiber Found by *swathccd* (EPIONK)

  If the target reconstruction routine, *swathccd*, has found a π^+ fiber overlapping a K^+ fiber, then the π^+ fiber is required to have energy less than 1.25 MeV. *swathccd* can find π^+ hits in K^+ fibers for $t_\pi - t_K > 15.0$ ns. The cuts on π^+ fiber energy EPITG and EPIMAXK are at 3 MeV, whereas the cut on π^+ energy under a K^+ fiber (CCDPUL, explained later) is at 1.25 MeV. Therefore, if a fiber is classified as both K^+ and π^+ and is not properly fit by the CCDPUL algorithm, then the π^+ energy cut on these fibers would be 3 MeV. $K_{\mu 2}$ monitors are used to measure an acceptance of 0.9954 ± 0.00008 and an acceptance of 0.9956 ± 0.00009 after all correlated cuts are applied.

- Quality of π^+ track in TG (CHI567)

  Require a good fit to the π^+ hits in the TG. Appendix E describes the TG track fitter in detail and describes the quantities employed CHI567. This cut rejects events where the probability of $\chi^2_5+\chi^2_6+\chi^2_7$ is less than 0.010, where the degree of freedom is the number of fibers used in the fit plus the 2 (decay-vertex position and target radius). $K_{\mu2}$ monitors are used to measure an acceptance of 0.8742 ± 0.00148 and an acceptance of 0.8746 ± 0.00148 after all correlated cuts are applied.

- Maximum Contribution to the Target Fitter χ^2_5 (CHI5MAX)

  If the contribution from any individual fiber to χ^2_5 is more than 35., then the event is rejected. $K_{\mu2}$ monitors are used to measure an acceptance of 1.0000 ± 0.00002 and an acceptance of 1.0000 ± 0.00002 after all correlated cuts are applied.

- Matching Target Track Fit with Vertex Fiber (VERRNG)

  Demand the TG-fitted track intersect the decay-vertex fiber. Measure the range of the fitted track in the decay vertex, *verrng*. Require $verrng \geq 0.005$ cm. $K_{\mu2}$ monitors are used to measure an acceptance of 0.9318 ± 0.00032 and an acceptance of 0.9318 ± 0.00032 after all correlated cuts are applied.

- *swathccd* and UTC Track Fitting Consistency (ANGLI)

  For short TG tracks, require the TG-track fit be consistent with the UTC extrapolated fit. Implement this requirement by rejecting events if the TG charged-track range is less than 2.0 cm and the angle between the TG-fitter track and the UTC extrapolated track in the Target is greater than 0.01 radian. $K_{\mu2}$ monitors are used to measure an acceptance of 0.9994 ± 0.00003 and an acceptance of 0.9994 ± 0.00003 after all correlated cuts are applied.

- K^+ Time in I-Counter (KIC)

  Do not allow the K^+ to be in the IC. Determine if any K^+ fibers exist outside a radius of 4.5 cm in the TG and within 3.7 cm of center of a IC section with a coincident hit. Reject events by defining the a coincident hit as $|t_{IC} - t_{\mathrm{K}}| \leq 3.0$ ns. $K_{\mu 2}$ monitors are used to measure an acceptance of 0.9997 ± 0.00002 and an acceptance of 0.9997 ± 0.00002 after all correlated cuts are applied.

- Target CCD-Pulse Fitting

  Pion Energy from the CCD-Pulse Fitting (CCDPUL)

  Reject events with K^+ fibers whose second pulse found by the CCD fitter has energy more than 1.25 MeV within $-7.5 \leq t_{2^{nd}} - t_{\pi} \leq 10.0$ ns, such that $t_{2^{nd}}$ is the time of the fitted second pulse.

  Bad Fit Results from CCD Fitter (CCDBADFIT)

  Remove events from consideration when the single and double pulse probability from the CCD pulse fit is zero within a hit TG fiber and the energy in this fiber is greater than 1.25 MeV.

  $K_{\mu 2}$ monitors are used to measure an acceptnace of CCDPUL and CCDBADFIT of 0.4526 ± 0.00040 and an acceptance of 0.4976 ± 0.00047 after all correlated cuts are applied.

3.3.7 $\pi^+ \to \mu^+ \to e^+$ Decay Sequence Cuts

The cuts are collectively referred to as TD cuts and TDCUT02.

- Pion-Time Consistency (PIFLG)

  Events in which an accidental hit plus a sequential hit of a muon track fake the $\pi^+ \to \mu^+$ double pulses in the stopping counter should be removed. The first pulse time in the stopping counter, obtained from the TD Double-Pulse Fitting ($t_{\pi,TD}$), is required to be within ±2.5 ns of the track time (t_{RS}), as shown in Eq. (3.17). $\pi_{scatter}$ monitors are used to measure an acceptance of $0.8243 \pm$

0.00107 and an acceptance of 1.0000 after all correlated cuts are applied.

$$|t_{\pi,TD} - t_{RS}| \leq 2.5 \text{ ns} \tag{3.17}$$

- $\mu^+ \to e^+$ Decay Requirement (EV5)

  A signature consistent with the $\mu^+ \to e^+$ decay is required in and around the stopping counter. A cluster of hits coincident with the third pulse time of the stopping counter is searched for around the stopping counter. Reject events if the cluster has hits in counters on both sides of the stopping counter. This cut is only employed within the tight signal region. $\pi_{scatter}$ monitors are used to measure an acceptance of 1.0000 and an acceptance of 1.0000 after all correlated cuts are applied.

- Muon-Time Accidental (ELVETO)

  Events with accidental activity coincident with the second-pulse time in the stopping counter should be removed. The accidental hits are searched for in the Range Stack, Barrel Veto, Barrel Veto Liner, and End Cap. Reject events if the total coincident energy in any subsystem is above the given threshold, as shown in Table 3.6. $\pi_{scatter}$ monitors are used to measure an acceptance of 0.9576 ± 0.00079 and an acceptance of 1.0000 after all correlated cuts are applied.

- Muon-Time Accidental in the Track Counters (TDFOOL)

  Events with accidental activity overlapping the track counters and creating the second pulse in the stopping counter should be removed. TD pulses in the two layers prior to the stopping counter are fitted with a double-pulse assumption. Reject events if the fitted pulses are consistent with double pulses and the fitted time of the second pulse is coincident with the second-pulse time in the stopping counter. $\pi_{scatter}$ monitors are used to measure an acceptance of 0.9965 ± 0.00024 and an acceptance of 1.0000 after all correlated cuts are applied.

Category	Time Window (ns)	Energy Threshold (MeV)
Both-end hit category		
Range Stack (RS)	±3.00	0.20
RS (TD)	±0.25	5.20
Barrel Veto (BV)	±1.25	0.20
Barrel Veto Liner (BVL)	±2.75	0.20
Single-end hit category		
RS single energy, both time	±7.00	0.20
RS both energy, single time	±4.50	9.40
RS single energy, single time	±8.75	6.60
RS no energy, both time	±5.00	-
RS (TD) single energy, single time	±3.00	3.20
BV single energy, both time	±3.00	1.60
BV both energy, single time	±0.25	0.40
BV single energy, single time	±3.00	1.80
BV no energy, both time	±5.75	-
BVL both energy, single time	±0.75	0.10
BVL single energy, single time	±5.00	1.00
BVL no energy, both time	±5.50	-
Other category		
End Cap (EC)	±0.25	22.00

Table 3.6: Time window and energy threshold for each category of the muon-time accidental cut, ELVETO.

- Neural-Net $\pi^+ \rightarrow \mu^+$ Decay Cut (TDNN)

  Tail fluctuations in the TD pulse as well as K^+ decays with μ^+'s should be removed. A neural-net (NN) function with five variables is constructed from the single-pulse fit χ^2's, the ratios of a single-pulse fit χ^2 to that of a double-pulse fit, the energy and time of the fitted second pulse, and the difference of the second pulse times between both ends. The cut position on the NN function is set to 0.30. This value was loosened compared to PNN1 analysis as discussed in Appendix F for the loose signal region. The threshold value is 0.76, same as PNN1 analysis, for the tight signal region. $\pi_{scatter}$ monitors are used to measure an acceptance of 0.9421 ± 0.00094 and an acceptance of 1.0000 after all correlated cuts are applied.

3.3.8 Photon Cut

PVCUTPNN2 removes events with photon activity at track time, t_{RS}, by searching all systems with the ability to detect photons for hits coincident with the track time, but not associated with the charged track. The time window and energy threshold for each category are shown in Table 3.7. BV, BVL, and RS hits are subdivided based upon the quality of the information from the hit. Appendix G for information regarding the optimization of PVCUTPNN2 parameters. The acceptance of PVCUTPNN2 is 0.6391 ± 0.0022 as measured by $K_{\mu2}$ monitor triggers. The tight parameters yield an acceptance of 0.3585 ± 0.0024. Acceptances of the individual photon-detector cuts are listed in Table 5.5. Acceptance values of 30% and 60% were chosen during cut optimization to give appropriate levels of signal to background in the tight and loose signal region.

Category	**60% (Loose)**			**30% (Tight)**		
	Timing (ns)		Energy	Timing (ns)		Energy
	offset	window	(MeV)	offset	window	(MeV)
BV	2.25	7.95	0.20	1.35	8.85	0.70
early BV	-20.70	15.0	30.00	-22.5	15.0	30.0
BVL*	3.15	7.55	0.30	3.15	7.55	0.30
RS	0.05	4.30	0.30	2.25	5.55	0.60
EC	1.80	6.15	0.40	1.75	7.75	0.20
EC inner-ring	0.99	4.64	0.20	-2.45	11.55	0.20
EC 2nd pulse	-1.60	4.07	10.60	-1.51	4.19	1.70
TG	-0.25	2.40	2.00	-2.15	4.40	1.40
IC*	1.25	3.25	5.00	3.20	6.10	5.00
VC	-2.40	4.15	6.80	-0.20	7.25	6.00
CO	2.90	2.95	0.60	2.15	2.95	1.60
μCO	-1.60	3.90	3.00	-0.60	3.90	0.60
AD	3.00	5.00	0.60	3.00	5.00	0.60
DSPV	2.50	7.50	0.00	2.50	7.50	0.00
BV$_{early}$	3.50	1.50	10.00	3.50	1.50	10.00

Single-end hit categories

	hit-ends							
	energy	time						
BV	both	single	3.05	15.95	1.00	0.55	13.05	0.40
BV	single	both	4.80	1.50	1.40	4.00	3.10	0.60
BV	single	single	-8.10	8.50	1.60	-8.30	6.90	1.00
BVL*	both	single	-5.65	11.80	8.19	-5.65	11.80	8.19
RS	both	single	-2.85	0.70	5.20	0.01	5.36	0.20
RS	single	both	6.60	1.35	0.00	3.70	6.10	0.00
RS	single	single	-6.80	1.22	3.40	-11.54	4.53	0.60
RS	no	both	-3.00	5.00	0.40	-3.00	5.00	0.40

Table 3.7: 30% and 60% photon cut parameters. The time window is shown in ns and energy threshold in MeV. The BV, BVL, and RS photon cuts require both ends of the detector obtain a result for time and energy. Additional photon cuts are applied when the both-ends requirement in time and energy are not met. *single* refers to a hit in only one end of the detector observed in either *energy* or *time*. *both* means both ends were hit and *no* means a hit was not observed in either end. $|t - t_{offset}| < t_{window}$ is defined as a coincident hit.

Chapter 4

Background

To give an unbiased result, the cuts in Section 3.3 were optimized on 1/3 of the data. Background values are then measured on the 2/3 sample (results from the 1/3 sample are reported here). All background values were scaled, for comparison purposes, to the full (3/3) sample size. High suppression of backgrounds created low-statistics samples; in cases where the background sample size was reduced to zero events, one event was assumed in the calculations. Calculation of statistical errors is explained in Appendix H.

4.1 $K_{\pi 2}$ Target-Scatter Background

The $K_{\pi 2}$ decay, where the π^+ scatters in the Target, is the dominant background for the PNN2 analysis. As it has been shown with Monte Carlo simulations [60], the photon distribution from the π^0 decay is more uniform in polar angle for events where the π^+ has scattered in the Target, than for unscattered ones. Since E949's photon detection is not uniform with the polar angle, see Fig. 2.16, the PV of $K_{\pi 2}$ peak events will not be the same as $K_{\pi 2}$ which scatter in the TG. Obtaining a sample to measure $K_{\pi 2}$ peak events required inverting kinematics, $\overline{KPI2BOX}$. The scattering process changed the kinematics of the π^+ to be within the PNN2 kinematic box, not the $K_{\pi2}$ box. Therefore, to obtain a sample of events with a π^+ that scatters into the fiducial region after initialing traveling in the z direction (z-π_{scat}'s), for PV rejection measurement, tagging the sample requires inverting non-kinematic cuts.

The target quality cuts (TGCUT06) have the power to suppress the $K_{\pi2}$ TG-scatter background. These cuts eliminate $K_{\pi2}$ TG-scatter events by using information from the target region. A π^+ may scatter in the Target in different ways. A scattering in the x-y plane is referred to as a "kink", since there is a kink in the π^+'s trajectory. A scattering in the rz plane is referred to as a z scatter (z-π_{scat}'s) since the π^+ initially is traveling in the z direction. A z-π_{scat}'s most likely occurs within a fiber identified as a K$^+$, since a π^+ traveling in the z direction is more likely to stay in the fiber the decay occurred. A x-y scatter could occur anywhere along the π^+ track and could have a component in the z direction. The two categories are not mutually exclusive, but some cuts from TGCUT06 have more power against either an x-y or z (i.e. CCDPUL is powerful at identifying z-scatters, while CHI567 is powerful at identifying x-y scatters).

By selectively inverting and applying cuts from TGCUT06, samples with varying mixtures of x-y and z scatters can be created for the rejection branch. These samples were contaminated, to some extent, with K_{e4} and $K_{\pi2\gamma}$ decays and Charge-Exchange background; however, these backgrounds were small compared to $K_{\pi2}$ target-scatters, as shown in the following sections. Thirteen such samples or "classes" were devised and implemented. The classes are described in Table 4.1, and the measured PV rejection of each class, in both the PNN2 and $K_{\pi2}$ kinematic boxes, detailed in Table 4.2. The PV rejections measured for different classes are consistent with each other within statistical uncertainties.

Due to adequate statistics and being more effective in tagging z-scatters, Class 12 was chosen to measure the PV rejection in $K_{\pi2}$ TG-scatter events. Class 12 used the cuts that are most effective against $K_{\pi2}$ TG-scatters. CCDPUL and EPIONK

CLASS	TG Tagging Cuts
1	All cuts, KP2BOX
2	$\overline{CCDPUL}$, $\overline{EPIONK}$
3	$\overline{CCDPUL}$, $\overline{EPIONK}$, all others
4	CCDPUL, EPIONK, TGZFOOL, EIC, OPSVETO, $\overline{OTHERS}$
5	$\overline{CCDPUL}$, $\overline{EPIONK}$, $\overline{CHI567}$, $\overline{VERRNG}$
6	$\overline{CCDPUL}$, $\overline{EPIONK}$, $\overline{CHI567}$, $\overline{VERRNG}$, all others
7	$\overline{CHI567}$, $\overline{VERRNG}$
8	$\overline{CHI567}$, $\overline{VERRNG}$, all others
9	$\overline{CCDPUL}$, $\overline{EPIONK}$, $\overline{CHI567}$, $\overline{VERRNG}$, KIC, PIGAP, TARGF, TPICS
10	$\overline{B4EKZ}$
11	$\overline{B4EKZ}$, all others
12	$\overline{CCDPUL}$, $\overline{EPIONK}$, $\overline{B4EKZ}$
13	$\overline{CCDPUL}$, $\overline{EPIONK}$, $\overline{B4EKZ}$, all others

Table 4.1: Definition of the classes of events (2-13) used to measure the PV rejection in the PNN2 kinematic box. Class-1 events have passed all the TG quality cuts, therefore they are required to be in the $K_{\pi2}$ kinematic box.

cut events with large pulses in the kaon fibers at decay time. B4EKZ rejects events in which the z position of the decay vertex found by the UTC does not agree with the expected z position determined by K$^+$ energy deposit (and thus path length) in the Target. Both signatures are characteristic of a daughter π^+ that started in the beam direction and then scattered into the detector's fiducial region. The second-pulse energy distribution for class 12, $K_{\pi2}$ peak events, and $K_{\mu2}$ events is shown in Fig. 4.1. The difference in PV rejection between different classes with adequate statistics will be used as an estimate for the systematic uncertainty.

In the normalization branch (see Table 4.3), PV was inverted and all other analysis cuts were applied (including TGCUT06). Some contamination from $K_{\pi2}$ RS-scatters and $K_{\pi2\gamma}$ was expected, but these backgrounds were found to be small compared to $K_{\pi2}$ TG-scatters. The momentum (*ptot*) distribution of the events remaining in the normalization branch after the inversion of PVCUTPNN2, after the

	PNN2BOX			KP2BOX	
	bef. (af.) PV	rejection	bg (3/3)	bef. (af.) PV	rejection
1				56196 (35)	1605.6±271.3
2	25828 (10)	2582.8±816.6	0.579±0.183	155269 (134)	1158.7±100.1
3	2547 (3)	849.0±489.9	1.762±1.018	56918 (55)	1034.9±139.5
4	4469 (3)	1489.7±859.8	1.004±0.580	67715 (48)	1410.7±203.5
5	31681 (3)	2437.0±675.8	0.613±0.170	193431 (163)	1186.7±92.9
6	3661 (3)	1220.3±704.3	1.225±0.708	79626 (72)	1105.9±130.3
7	24498 (6)	4083.0±1666.7	0.366±0.150	92462 (65)	1422.5±176.4
8	267 (1)	-	-	11173 (9)	1241.4±413.6
9	25085 (11)	2280.4±687.4	0.655±0.198	181864 (157)	1158.4±92.4
10	10840 (4)	2710.0±1354.8	0.551±0.276	29393 (28)	1049.8±198.3
11	50 (1)	-	-	2853 (3)	951.0±548.8
12	27944 (11)	2540.4±765.8	0.588±0.178	167727 (143)	1172.9±98.0
13	3051 (3)	1017.0±586.9	1.470±0.850	62835 (59)	1065.0±138.6

Table 4.2: The rejection branch for the $K_{\pi2}$ TG-scatter background: PV rejection for the PNN2 and $K_{\pi2}$ boxes, and respective background, for the 12 classes. The classes that are skipped do not have enough statistics for a meaningful measurement. The same setup cuts as in the normalization branch (Table 4.3) are applied.

application of all the TGCUT06 except CCDPUL, and after the application of CCDPUL is shown in Fig. 4.2. In the same figure, the *ptot* distribution of the events in class 12 of the rejection branch is also shown before and after PVCUTPNN2.

Using the numbers from Table 4.2 and Table 4.3, the $K_{\pi2}$ target-scatter background is

$$\begin{aligned} N_{K_{\pi2}-TGscat} &= 3\times\frac{N}{R_{PVclass12}-1} \qquad (4.1)\\ &= 3\times\frac{498}{(2540.4\pm765.8)-1}\\ &= 0.588\pm0.178(stat.)^{+0.067}_{-0.222}(sys.) \qquad (4.2)\end{aligned}$$

The systematic error comes from the difference in background predicted by the class with the highest (Class 7) and lowest (Class 9) PV rejection, with respect to the central value from Class 12. Only classes with adequate statistics were considered.

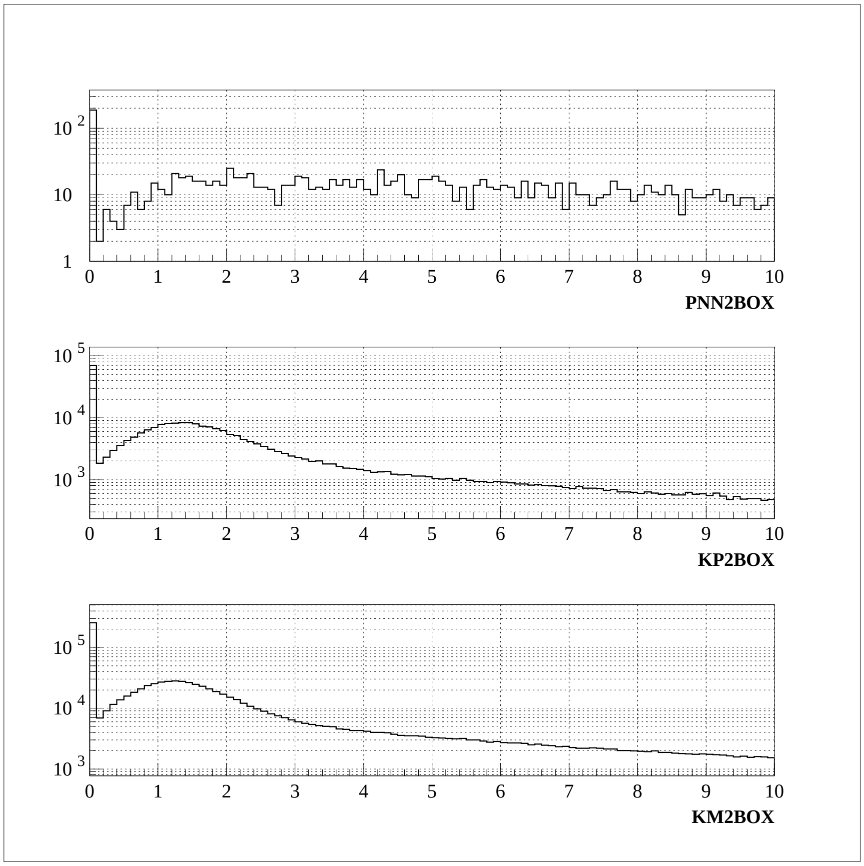

Figure 4.1: Energy distribution of the second-pulse in K^+ fibers for class 12 of the $K_{\pi 2}$ TG-scatter rejection branch (top), for $K_{\pi 2}$ peak events (middle), and for $K_{\mu 2}$ events (bottom).

Further details regarding normalization sample purity are discussed in [61].

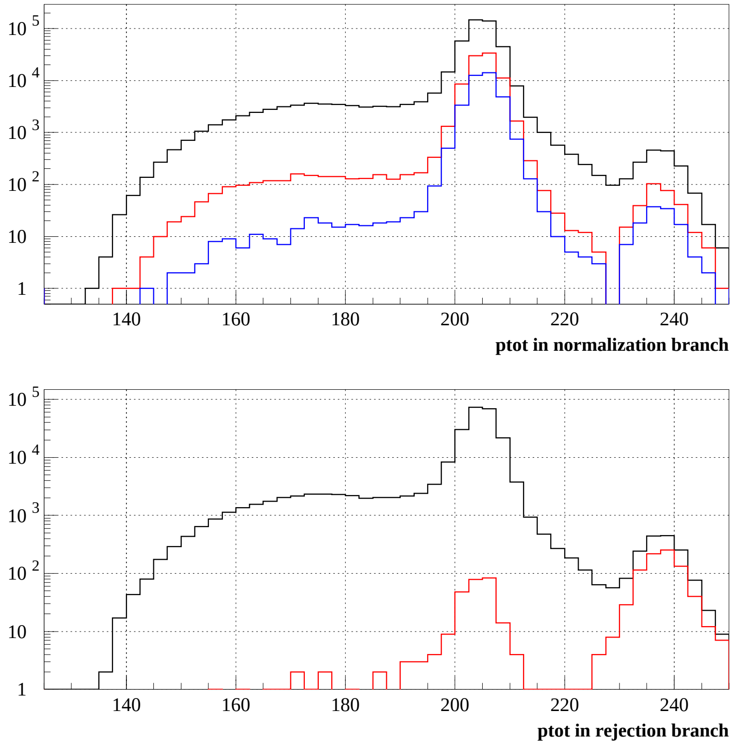

Figure 4.2: Top: *ptot* distribution of the events remaining in the $K_{\pi2}$ TG-scatter normalization branch of the $K_{\pi2}$ TG-scatter study after applying $\overline{PVCUTPNN2}$ (upper black), after all the TGCUT06 cuts except CCDPUL (red), and the remaining events, after CCDPUL (lower blue). Bottom: *ptot* distribution of the events in class 12 of the rejection branch of the $K_{\pi2}$ TG-scatter study before (black) and after (red) PVCUTPNN2.

CUT	No box	PNN2BOX	KP2BOX
BAD_RUN	12525587		
Setup	409159		
$\overline{PVCUT}$		38078	330814
B4EKZ		27242	301449
TGZFOOL		26853	296595
EPITG		16889	260545
EPIMAXK		16889	260545
TARGF		14397	251761
DTGTTP		14397	251753
RTDIF		14287	249613
DRP		14091	248758
TGKTIM		13852	246332
EICCON		13560	242238
TICCON		13560	242237
TGEDGE		13343	239972
TGDEDX		12547	238494
TGENR		12277	232184
PIGAP		12091	230556
TGB4		10860	216849
KIC		10854	216747
PHIVTX		8128	209500
OPSVETO		7100	200239
TGLIKE1,2		6691	193841
TIMKF		5448	172474
ALLKFIT		5202	166539
TPICS		5198	166511
EPIONK		4906	158435
CHI567		4037	135866
VERRNG		3377	127354
CHI5MAX		3150	118701
ANGLI		3142	118633
CCDBADFIT		2860	107477
CCDPUL		**498**	56161

Table 4.3: The normalization branch for the $K_{\pi2}$ TG-scatter background: events after setup cuts and TGCUTS, for PNN2 and $K_{\pi2}$ boxes. *Setup* includes SKIM5, RECON, PSCUT06, DELCO3, TDCUT02, KINCUT06.

4.2 $K_{\pi 2}$ Range-Stack Scatter Background

π^+'s from the $K_{\pi 2}$ decay will sometimes undergo inelastic scattering in the Range Stack and fall into the PNN2 kinematic box by losing energy in the scattering process. However, for a $K_{\pi 2}$ RS-scatter to be a background for PNN2, the π^+ momentum also has to be mis-measured and the photons from the π^0 decay have gone undetected. Therefore, this background was expected to be much smaller than the $K_{\pi 2}$ target-scattered background.

It should be noted that these background events are already included in the normalization branch in Table 4.3[1], but were absent in the TS-scatter photon-veto rejection study in Table 4.1 because the target cuts were reversed to measure this photon-veto rejection. The $K_{\pi 2}$ events which scattered in the RS should be assigned the same Photon Veto rejection as the $K_{\pi 2}$ peak events, since the topology of the π^0 will be identical to non-scattered $K_{\pi 2}$ events.

The most effective cuts against this background are the RS track quality cuts, RSDEDX and PRRF (collectively referred to as RSCT), the momentum-BOX cut (PBOX), and the Photon cut. Table 4.4 summarizes this background measurement. The SETUP cuts are the same as the $K_{\pi 2}$ target-scatter normalization branch. The second and the third columns of the table contain events in the $K_{\pi 2}$ momentum peak. Events with the momentum of the $K_{\pi 2}$ peak events, but lowered in range and energy are assumed to be the result of a scattering in the Range Stack.

The efficiency ϵ_{RSCT} and the rejection R_{RSCT} of these cuts can be measured as

$$\begin{aligned} \epsilon_{RSCT} &= 56196/76030 = 0.739 \pm 0.002 \\ R_{RSCT} &= 602/78 = 7.718 \pm 0.815 \end{aligned} \tag{4.3}$$

The fourth and fifth column of Table 4.4 are for normalization; RSCT was reversed

---

[1] Correcting the normalization of $K_{\pi 2}$ TG-scatters for $K_{\pi 2}$ RS-scatters does not make a significant difference in the background, given the statistical uncertainty.

CUT	Rejection PBOX from KP2BOX		Normalization $\overline{RSDEDX}$ or $\overline{PRRF}$	
	KP2BOX	PNN2 RE BOX	KP2BOX	PNN2BOX
SETUP	86172	681	23249	212
LAYER14	86114	681	23230	212
FIDUCIAL	79180	615	20880	197
UTCQUAL	76665	602	20030	177
RNGMOM	76030	602	19834	154
RSDEDX	66354	106	NA	NA
PRRF	56196	78	NA	NA
PVCUT	35	0	9	0

Table 4.4: Background study for $K_{\pi 2}$ RS-scatters. PBOX is the momentum cut and RE BOX the range and energy cut. "NA" means that the cut is not applied, because the RSCT cuts have been reversed in the normalization branch.

and all other cuts were applied. The various contributions to the total 154 events left in the PNN2BOX before the application of the PV have to be considered in order to calculate the background of interest. The largest component of this sample comes from scattering in the TG that contaminated the RSCT-reversed sample because of the inefficiency of the RSCT cuts. On the other hand, the total 498 events in the $K_{\pi 2}$ target-scatter normalization branch (Table 4.3) have a target-scattered (N_{tg}) and a RS-scattered (N_{rs}) component. Therefore

$$\begin{aligned} N_{tg} + N_{rs} &= 498 \\ (1-\epsilon_{RSCT}) \times N_{tg} + (R_{RSCT}-1) \times N_{rs} &= 154 \end{aligned} \tag{4.4}$$

Solving this system of equations, the real $K_{\pi 2}$ RS-scatter normalization is obtained, $N_{rs} = 3.730 \pm 0.494$. As shown in Eq. (4.6), the final background due to RS-scattered events can be measured by applying the $K_{\pi 2}$-peak photon-veto rejection to N_{rs} from the second column of Table 4.4, $R_{PV-K_{\pi 2}peak} = 56196/35 = 1605.6 \pm 271.3$.

$$\begin{aligned} N_{K_{\pi 2}-RSscat} &= 3 \times \frac{N_{rs}}{R_{PV-K_{\pi 2}peak} - 1} \qquad (4.5) \\ &= 0.007 \pm 0.002 \qquad (4.6) \end{aligned}$$

4.3 Beam Background

4.3.1 Single-Beam Background

The two cuts that highly suppress this background are delco (either DELC3 or DELC6) and B4DEDX. In the rejection branch, after some basic setup cuts, B4DEDX is inverted, requiring B4 energy consistent with a pion ($b4abm\_atc < 1.0 MeV$), and the rejection of delco was measured on this sample. The $t_\pi - t_{\mathrm{K}}$ distribution before and after the inversion of B4DEDX is shown in Fig. 4.3. The branch is divided into three sub-branches of varying purity before delco is applied. It is assumed that the delco rejection is the same for beam π^+'s and K^+'s. In the normalization branch, delco is inverted and all other relevant cuts are applied. The schematic of the two branches, together with the number of events that survive after every (set of) cut(s), is shown in Fig. 4.4. Using these numbers, the single-beam background in the 3/3 sample is

$$\begin{aligned} N_{1bm} &= 3 \times \frac{A_{PV_{pnn2}}}{A_{PV_{beam}}} \times \frac{Norm_{1bm}}{R_{DELCO} - 1} \qquad (4.7) \\ N_{1bm} &= 3 \times \frac{0.58}{0.95} \times \frac{1.0 \pm 1.0}{(4532.0 \pm 4531.5) - 1} \\ &= (0.45 \pm 0.64) \times 10^{-3} \qquad (4.8) \end{aligned}$$

where $\frac{A_{PV_{pnn2}}}{A_{PV_{beam}}} = \frac{0.58}{0.85}$ is the ratio of the acceptance of the nominal PNN2 photon-veto and the looser PV cut used to produce the beam-background samples. For

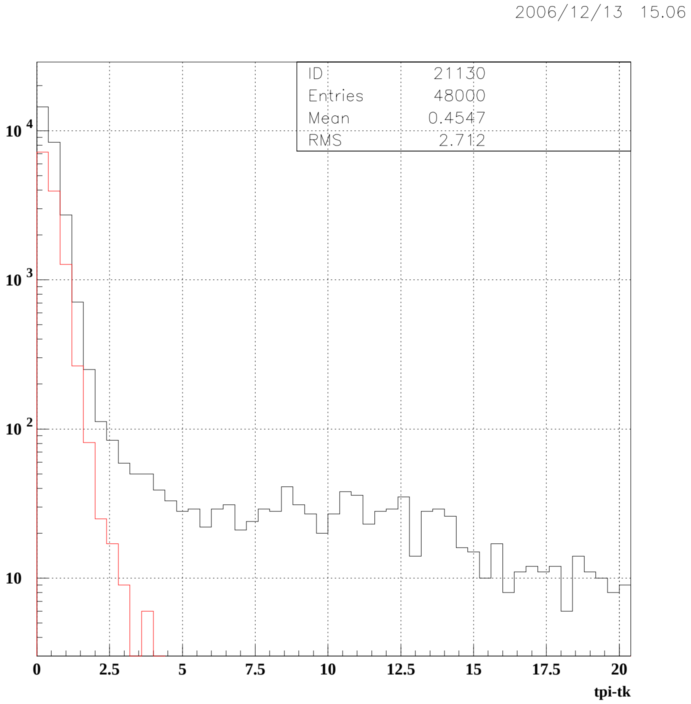

Figure 4.3: $t_\pi - t_\mathrm{K}$ distribution of events in the single-beam-background rejection branch before (black) and after (red) the inversion of B4DEDX.

a conservative estimate of the background, the smallest value of R_{DELCO} from the three rejection sub-branches was used.

4.3.2 Double-Beam Background

In order to calculate this background, it is assumed that the Čerenkov counter and the Beam Wire Chambers are uncorrelated with the B4 and the Target, since the Degraders, where the beam particles undergo multiple scattering, are located between them. Double-beam events are tagged by requiring a hit in the B4 at RS time, and the rejection of the BWPCs and the $\check{\mathrm{C}}_K$ and $\check{\mathrm{C}}_\pi$ was measured with this sample. In the normalization branch, either the BWPCs, or $\check{\mathrm{C}}_K$ or $\check{\mathrm{C}}_\pi$ are required to have

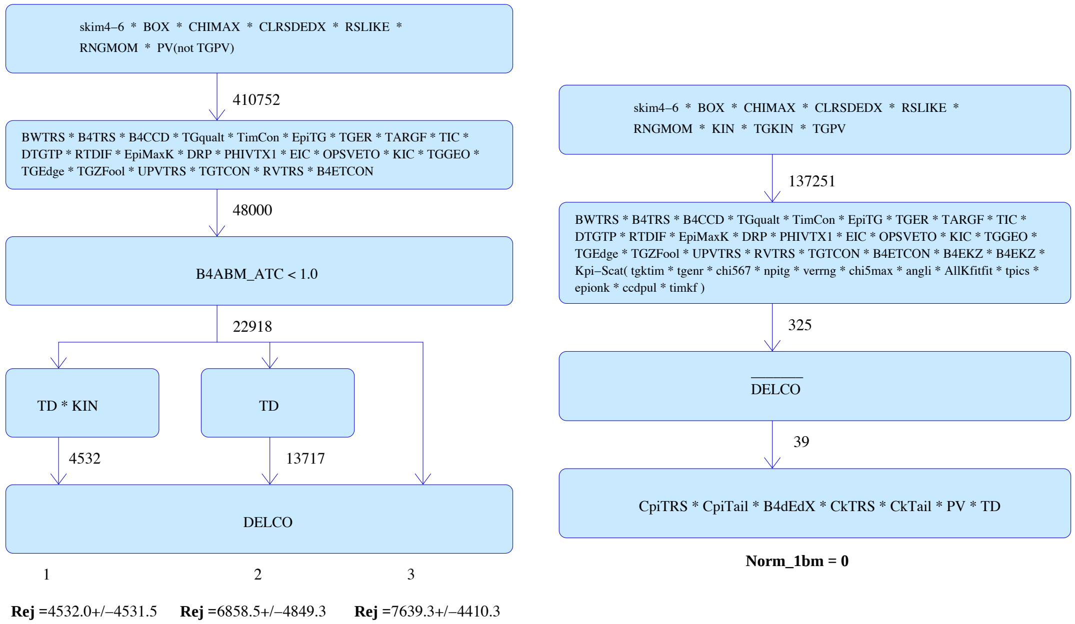

(a) Rejection (b) Normalization

Figure 4.4: Single-beam bifurcations: (a) rejection branch, with the values of the DELCO3 rejection obtained for the three sub-branches, and (b) normalization branch. Numbers under the boxes are the number of events remaining after the cuts were applied. TD is the TDCUT02 cut, KIN the KINCUT cut, and DELCO is DELC3.

a hit at RS time and all other cuts are applied. A schematic of the double-beam bifurcation study is shown in Fig. 4.5.

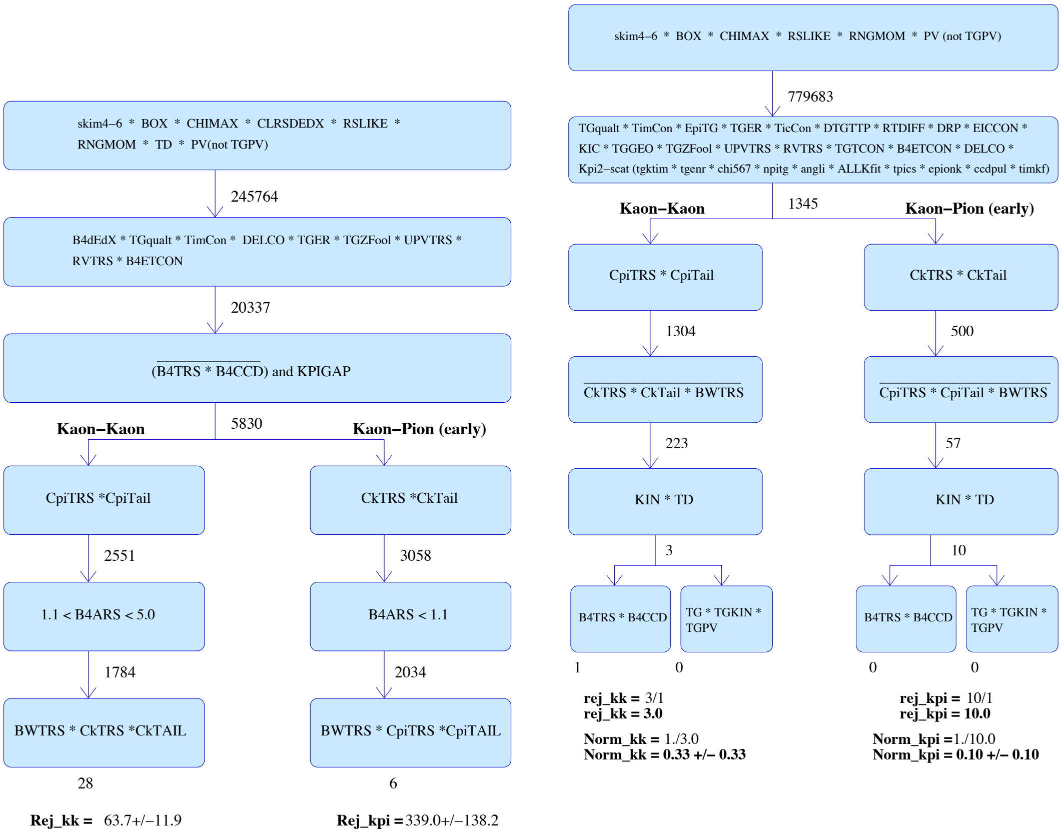

(a) Rejection (b) Normalization

Figure 4.5: Double-beam Bifurcations: (a) rejection branch, and (b) normalization branch, for both K-K and K-π. Numbers under the boxes are the number of events remaining after the cuts were applied. The K-π numbers are for the early runs (before the change in trigger) and the K-K numbers are from all runs.

In addition to the B4-tag, KPIGAP is also applied in the rejection branch, which requires the K^+ and π^+ cluster in the Target to be disconnected in x-y. This is done to remove K-decay contamination from the double-beam sample: either a photon from $K_{\pi 2}$ or a charged particle from a multibody decay, both relevant in the PNN2 kinematic region, can give a signal in the B4 at t_{RS}, faking a second beam particle in the B4. Such events are not expected to have any BWPC or Čerenkov rejection, and should be removed, in order to measure the BWPC and Čerenkov rejection correctly. On the other hand, the rejection of the beam counters does not depend significantly on the proximity of the two beam particles, therefore such a subset of events with spatially disconnected beam particles, can be used to measure the rejection.

Both the rejection and normalization branches bifurcate into K-K and K-π sub-branches, requiring a $\check{C}_\pi$ or $\check{C}_K$ veto respectively, before either inverting $\check{C}_K$ or $\check{C}_\pi$ (in the normalization branch), or measuring the $\check{C}_K$ or $\check{C}_\pi$ rejection (in the rejection branch). The normalization branch bifurcates further at the bottom, in order to handle the small statistics, therefore the KK (Kπ) normalization numbers are given by Eq. (4.9).

$$Norm_{KK(K\pi)} = \frac{n_{KK(K\pi)}}{r_{KK(K\pi)}} \tag{4.9}$$

where $n_{KK(K\pi)}$ is the number of events remaining in the ADPV*B4TRS*B4CCD sub-branch, and $r_{KK(K\pi)}$ the rejection of TG*TGKIN*TGPV.

K-K background

Using the method described above, and the results from Fig. 4.5, the K-K double-beam background is

$$N_{KK} = 3 \times \frac{A_{PV_{pnn2}}}{A_{PV_{beam}}} \times \frac{Norm_{KK}}{R_{KK} - 1} \tag{4.10}$$

and, using Eq. (4.9),

$$N_{KK} = 3 \times \frac{0.58}{0.95} \times \frac{\frac{1.0\pm1.0}{3.0\pm2.4}}{(63.7 \pm 11.9) - 1} \tag{4.11}$$

$$= 0.0107 \pm 0.0141 \tag{4.12}$$

K-π background

A complication arises when the Kπ double-beam background is to be calculated, due to the addition of the $\check{C}_\pi$ veto to the online trigger in the middle of the run (see section Section 2.12). The offline $\check{C}_\pi$ rejection is very low for the late part of the run, and the normalization branch runs out of statistics, producing an unnaturally high background estimate with large uncertainty. Therefore it is impossible to just add the K-π background for the early and late part of the run. Instead, the background calculated for the set of runs before the trigger change was scaled by the ratio of KB_{live} of the two parts of the run $f_{KB_{live}} = \frac{0.606}{0.394} = 1.54$. This approach is justified by the fact that the K-π background measured for the early and late part of the run for $\pi\nu\bar{\nu}(1)$ triggers agree with each other. The K-K background calculated for the early and late runs for $\pi\nu\bar{\nu}(2)$ is also consistent [62]. Everything indicates that there was no increase in beam background after the trigger change occurred, therefore scaling by $f_{KB_{live}}$ is valid. The K-π background is thus

$$N_{K\pi} = 3 \times \frac{A_{PV_{pnn2}}}{A_{PV_{beam}}} \times (1 + f_{KB_{live}}) \times \frac{Norm_{K\pi}}{R_{K\pi} - 1} \tag{4.13}$$

$$N_{K\pi} = 3 \times \frac{0.58}{0.85} \times (1 + 1.54) \times \frac{\frac{1.0\pm1.0}{10.0\pm9.5}}{(339.0 \pm 138.2) - 1}$$

$$= (1.54 \pm 2.24) \times 10^{-3} \tag{4.14}$$

4.3.3 Total Beam-Background

Summarizing the previous results, the total beam background expected in the signal region for the 3/3 sample is

$$\begin{aligned} N_{beam} &= N_{1bm} + N_{KK} + N_{K\pi} && (4.15) \\ &= (12.7 \pm 14.3) \times 10^{-3} && (4.16) \end{aligned}$$

This expected background is an improvement of about a factor of 10 compared to the E787 result [63], and is consistent with the PNN1 background, given the difference in phase space of the two kinematic regions.

4.4 Muon Background

The muon background is expected to come mainly from $K^+ \to \mu^+\nu\gamma$ and $K^+ \to \pi^0\mu^+\nu$ decays ($K_{\mu 2\gamma}$) in the PNN2 kinematic region. This background is expected to be small, because for these processes to be confused with signal, both the muon has to be misidentified as a π^+ and the photon(s) have to be missed. The cuts used to suppress the muon background are the $\pi^+ \to \mu^+ \to e^+$ decay sequence cuts (TDCUT02) and the pion-muon kinematic separation cut, RNGMOM.

After some setup cuts that remove $K_{\pi 2}$ decays and beam backgrounds, in the normalization branch (Table 4.5) TDCUT02 is inverted. When the remaining cuts are applied (KCUTS and PVPNN2), one event remains in the normalization branch, therefore N=1 will be used for the background estimation. In the rejection branch (Table 4.6), RNGMOM is inverted and the rejection of the TDCUT02 is measured on this sample. Using these values, the muon background is

$$\begin{aligned} N_{\mu} &= 3 \times \frac{N}{R_{TD} - 1} = 3 \times \frac{1 \pm 1}{(421.0 \pm 148.7) - 1} && (4.17) \\ &= 0.0071 \pm 0.0076 && (4.18) \end{aligned}$$

CUT	events
PNN2BOX	4649482
PSCUT06	550771
TGCUT06	15622
$\overline{TDCUT02}$	2941
KCUTS	0
PVCUTPNN2	0

Table 4.5: Normalization branch for the muon background.

CUT	events
PSCUT06	5971094
TGCUT06	652242
$\overline{RNGMOM}$	485160
other KCUTS	24294
PVCUTPNN2	3368
EV5	1707
ELVETO	988
TDFOOL	986
TDVARNN	8
Total $R_{TD} = 3368/8 = 421.0 \pm 148.7$	

Table 4.6: Rejection branch for the muon background.

4.5 $K^+ \rightarrow \pi^+\pi^-e^+\nu$ Background

The K_{e4} decay with a BR of $(4.08 \pm 0.09) \times 10^{-5}$ and with the π^+ maximum momentum at 203 MeV/c could be a serious background in the PNN2 region because this decay contains no photon in the final state to veto on and the π^- and the e^+ could be undetectable in the TG. Fig. 4.6 shows the total kinetic energy (T_2) of the π^- and the e^+ versus the momentum of the π^+ (*ptot*) for Monte Carlo events that passed

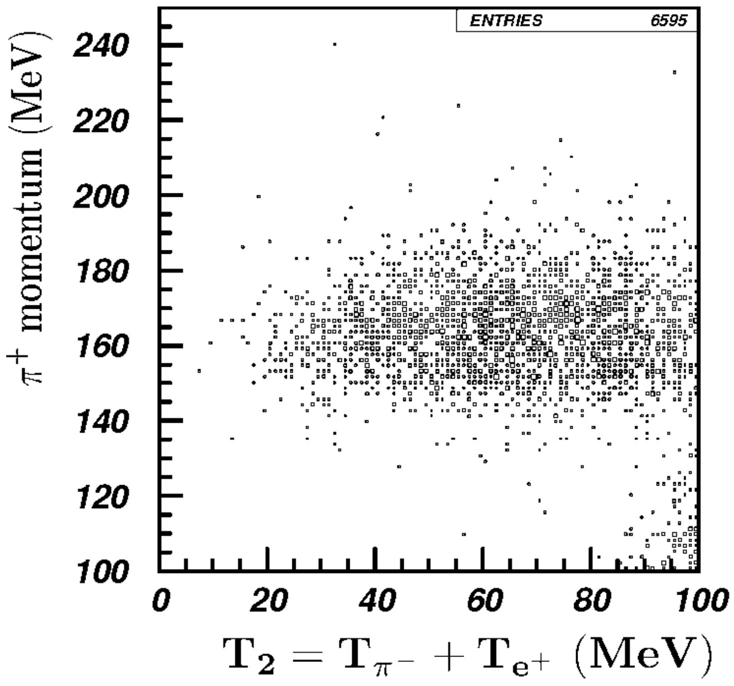

Figure 4.6: Total kinetic energy (T_2) of the π^- and the e^+ versus the momentum of the π^+ (*ptot*) for $K^+ \rightarrow e^+\nu$ Monte Carlo events that pass the $\pi\nu\bar{\nu}(2)$ trigger.

$\pi\nu\bar{\nu}(2)$ trigger. When T_2 is very low, the π^- and the e^+ can not escape the TG and may avoid detection if they deposit all their energy in some inactive material or if their path overlaps with kaon fibers. For these low-T_2 events the distribution of P_{tot} concentrates around 160 MeV, the middle of the PNN2 kinematic box.

4.5.1 K_{e4} Background using Data

The two cuts that are most effective against this background are TGPV* OPSVETO and CCDPUL. TGPV*OPSVETO removes events with energy deposits outside the kaon and pion fibers (classified as "photon" and "opposite side pion" fibers respectively), and CCDPUL removes events with extra energy deposit in the kaon fibers.

Two K_{e4} background branches from data are selected in from skim5 by applying

$\overline{TGPV} \cdot \overline{OPSVETO}$ or $\overline{CCDPUL}$. The number of events remaining after every cut in these branches are listed in Table 4.7. Some cuts have been loosened in this measurement, in order to avoid revealing part of the signal box, therefore a background estimate using the results of this table will be an overestimation, provided that the background distribution does not change drastically when these cuts are tightened. For instance, the photon-veto is at a loose setting (85% acceptance and 146.1 ± 9.9 rejection for class 12 of Table 4.1, see plots in Appendix G), the time window and energy threshold of TGPV and OPSVETO have been loosened from their nominal values to 1.3 ns and 5 MeV and 3 ns and 2 MeV respectively, and the CCDPUL energy threshold is set to 2 MeV.

The events that remain at the end of each branch were scanned manually to understand their nature, and a significant contamination of $K_{\pi2}$ scatters, $K^+ \to \pi^+\mu^+\mu^-$ and other decays was found, among the K_{e4} events. Therefore, the trigger data is insufficient to calculate this background, because a clean sample of K_{e4} cannot be isolated. The $\overline{TGPV \cdot OPSVETO}$ branch from data will be used for normalization, and the TGPV*OPSVETO rejection will be calculated with Monte Carlo, in order to get a conservative background prediction.

Eventhough the sample was contaminated with $K_{\pi2}$ TG-scatters, the effect of the tighter final PV cut can be determined. Using the PV rejection of class 12 for the loose and nominal PV parameters, the normalization is shown in Eq. (4.20).

$$\begin{aligned} Norm_{ke4} &= \frac{R_{PV_{ke4}}}{R_{PV_{pnn2}}} \times N = \frac{146.1}{1753.8} \times 15 \qquad (4.19) \\ &= 1.25 \pm 0.31 \qquad (4.20) \end{aligned}$$

Cut	$\overline{TGPV \cdot OPSVETO}$	$\overline{CCDPUL}$
TRIGGER	30995248	30995248
PNN2BOX	1201592	1201592
PSCUT06	423959	423959
TDCUT02	179203	179203
KCUTS	112435	112432
PRESEL	8593	8594
RCUT	7346	5923
PVICVC	3303	2901
TGCUT06	95	122
FINALCUT	15	42

Table 4.7: The K_{e4} normalization branches of data, using $\overline{TGPV \cdot OPSVETO}$ and $\overline{CCDPUL}$. PRESEL contains DELCO6, B4TIM, TGZFOOL and all Photon cuts except that for IC and VC. RCUT means $\overline{TGPV \cdot OPSVETO}$ in the $\overline{TGPV \cdot OPSVETO}$ branch and $\overline{CCDPUL}$ in the $\overline{CCDPUL}$ branch. FINALCUT means $CCDPUL$ in the $\overline{TGPV \cdot OPSVETO}$ branch and $TGPV \cdot OPSVETO$ in the $\overline{CCDPUL}$ branch.

4.5.2 K_{e4} Background with UMC

In order to understand the rejection of TGPV·OPSVETO and CCDPUL, Monte Carlo is used to simulate the energy deposit of charged tracks in the TG. The main source of uncertainty in simulation comes from the absorption of π^- in the TG. The π^- absorption is modeled with an experimental measurement of stopped π^- in the Range Stack [64]. Fig. 4.7 shows the absorption-energy distribution of stopped π^- from that experiment (measured energy deposit - kinetic energy). In simulation, the absorption energy is sampled according to this distribution. If the energy is sampled to be negative, then the last fiber on the π^- trajectory is assigned 0 energy. This model, however, assumes that all the observable energy is deposited locally and promptly, in a single fiber, where the π^- stopped. Possible energy deposit in neighboring fibers from the relatively energetic photons that are produced in π^--Carbon absorption as well as deposits from neutrons outside the TG are not simulated.

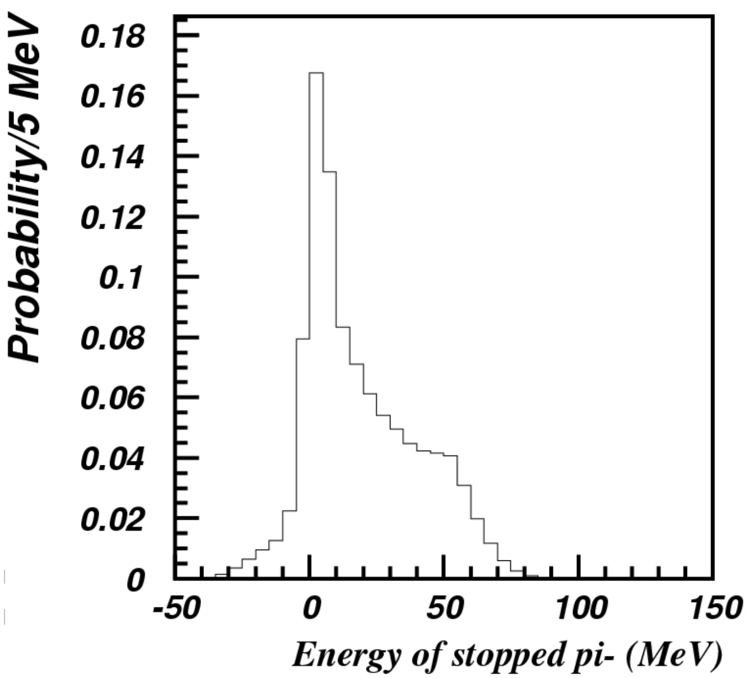

Figure 4.7: Observable absorption energy of π^- stopped in the Target.

About 2×10^8 events were simulated using this model, with an additional cut at $T_2 < 50 MeV$, in order to enhance the phase-space region most responsible for the background. To study the correlation between TGPV·OPSVETO and CCDPUL, two variables were used: the energy deposit in target fibers outside of kaon and pion fibers T_{xtg}, corresponding to the energy deposits available to TGPV·OPSVETO, and the total energy deposit of pions and electrons in kaon fibers E_{hide}, corresponding to the energy deposit that would be found by the CCDPUL.

Table 4.8 shows the number of events left after the application of all possible cuts to MC data, and Fig. 4.8 the relation between E_{hide} and T_{xtg} for the surviving events. In Table 4.9 the rejection of TGPV·OPSVETO is calculated as a function of the cut on E_{hide}, which simulates the effect of CCDPUL. Since the matching of the energy between MC and data is uncertain, the cut on E_{hide} is varied between 1.5 and 10 MeV,

Cut	Events (Acceptance)
Kstops	199998880
TRIGGER	10691979
PNN2BOX	9928203
KCUTS	7697728
PRESEL	3894473
PVICVC	2316910
TGCUT06	63425

Table 4.8: The number of events remaining after all possible PASS2 cuts in $K^+ \rightarrow e^+\nu$ Monte Carlo. PRESEL cut means DELCO6, TGZFOOL, and all photon cuts except that for IC and VC.

and the cut on T_{xtg} between 0.6 and 1.8 MeV. The rejection of TGPV·OPSVETO does not change much with the value of the threshold, but it shows a correlation with the cut in E_{hide}. The mean value for the rejection $R_{TGPV \cdot OPSVETO} = 73$ is used in the evaluation of the background, and the variation with the E_{hide} cut position from $R^{min}_{TGPV \cdot OPSVETO} = 13.6$ to $R^{max}_{TGPV \cdot OPSVETO} = 132.4$ is included in the asymmetric systematic error.

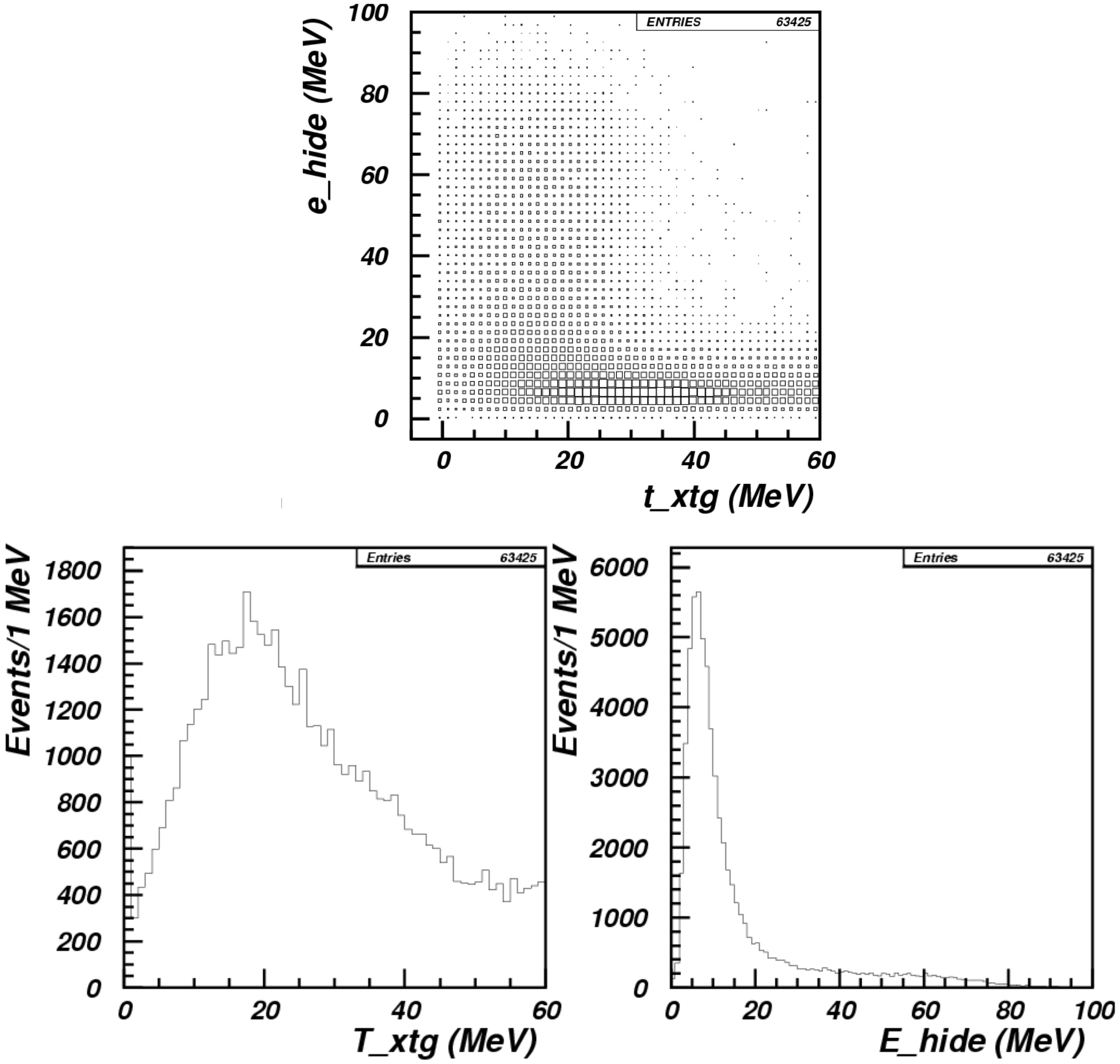

Figure 4.8: E_{hide} versus T_{xtg} (top) and projections on T_{xtg} (bottom left) and E_{hide} (bottom right) for the $K^+ \to e^+\nu$ Monte Carlo events that survive all analysis cuts applicable in UMC.

	$T_{xtg} < 0.6$	$T_{xtg} < 1.2$	$T_{xtg} < 1.8$
$E_{hide} < 1.5$	245/12=20.4	245/18=13.6	245/18=13.6
$E_{hide} < 2.5$	1104/27=40.9	1104/34=32.5	1104/36=30.7
$E_{hide} < 4.0$	5609/61=92.0	5609/70=80.1	5609/78=71.9
$E_{hide} < 10.0$	34943/264=132.4	34943/313=111.6	34943/354=98.7

Table 4.9: Rejection of cuts on T_{xtg} with different cuts on E_{hide} on $K^+ \rightarrow e^+\nu$ Monte Carlo events.

Using the results of Table 4.9 and Eq. (4.20), the K_{e4} background is found to be

$$\begin{aligned} N_{ke4} &= 3 \times \frac{Norm_{ke4}}{R_{TGPV \cdot OPSVETO} - 1} && (4.21) \\ &= 0.052 \pm 0.013(stat.)^{+0.246}_{-0.023}(syst.) && (4.22) \end{aligned}$$

4.6 $K^+ \rightarrow \pi^+\pi^0\gamma$ Background

The background due to radiative $K_{\pi 2}$ is expected to be small, due to the small branching ratio of this decay compared to $K_{\pi 2}$ and the existence of the third photon available to veto on. From the two processes through which this decay proceeds, direct emission with $\mathcal{B}(DE) = (4.4 \pm 0.7) \times 10^{-6}$ and inner Bremsstrahlung with $\mathcal{B}(IB, 55MeV < T_{\pi^+} < 90MeV) = (2.75 \pm 0.15) \times 10^{-4}$ [5], the latter is only of interest, due to its higher branching ratio.

Since it is difficult to separate this background sample from the $K_{\pi 2}$-scatter background sample, both Monte Carlo and data were used to measure it. The method consisted of determining the expected number of $K_{\pi 2\gamma}$ events in the PNN2 kinematic region as a function of the number of $K_{\pi 2}$-peak events observed outside the search region. In order to normalize the number of $K_{\pi 2\gamma}$ events to the number of $K_{\pi 2}$-peak events, it is necessary to know the branching ratio and the rejection of both the online and offline cuts for each decay. This information was calculated using MC.

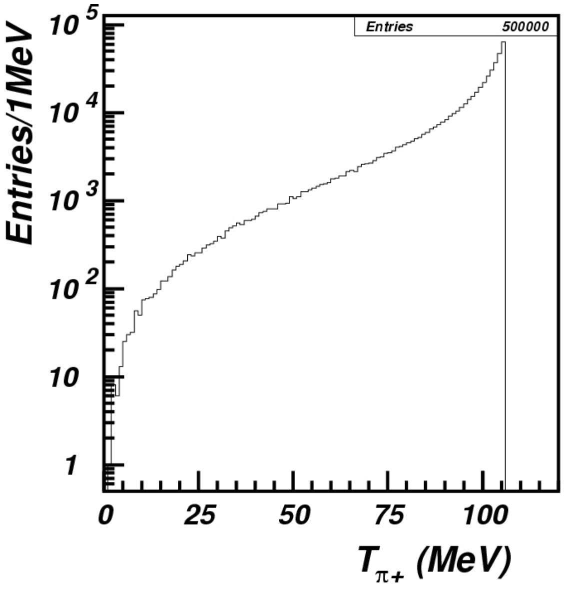

Figure 4.9: π^+ energy spectrum from $K_{\pi 2\gamma}$ generated by MC, using only the inner Bremsstrahlung process.

About 2×10^5 $K_{\pi 2}$ and 5×10^5 $K_{\pi 2\gamma}$ events were generated with MC. Fig. 4.9 shows the π^+ kinetic-energy spectrum of the $K_{\pi 2\gamma}$ events produced. The BR in the whole phase space of the decay (0 MeV $< T_{\pi^+} <$ 106 MeV) can be calculated from this distribution as:

$$\begin{aligned} \mathcal{B}(K_{\pi 2\gamma}) &= \frac{\int_0^{106} dN}{\int_{55}^{90} dN} \times (2.75 \pm 0.15) \times 10^{-4} \qquad (4.23) \\ &= (1.11 \pm 0.06) \times 10^{-3} \qquad (4.24) \end{aligned}$$

Then the online $\pi\nu\bar{\nu}(2)$ trigger and the offline cuts were applied to the simulated samples (Table 4.10). From the number of events remaining and the branching ratio of each decay, the ratio of $K_{\pi 2}$ events in the kinematic peak over the $K_{\pi 2\gamma}$ events in the PNN2 region can be determined as:

Requirement	$K_{\pi 2}$	$K_{\pi 2\gamma}$
K^+ decays ($N^{UMC}_{K_{\pi 2(\gamma)}}$)	199992	499968
$\pi\nu\bar{\nu}(2)$ trigger	20455	49355
offline cuts ($N_{K_{\pi 2(\gamma)}}$)	4950	6907

Table 4.10: Trigger simulation and offline cuts effect on $K_{\pi 2}$ and $K_{\pi 2\gamma}$ simulated samples.

$$\begin{aligned} \kappa &= \frac{N_{K_{\pi 2}}}{N_{K_{\pi 2\gamma}}} \times \frac{\mathcal{B}(K_{\pi 2})}{\mathcal{B}(K_{\pi 2\gamma})} \times \frac{N^{UMC}_{K_{\pi 2\gamma}}}{N^{UMC}_{K_{\pi 2}}} && (4.25) \\ &= \frac{4950}{6907} \times \frac{0.2113 \pm 0.0014}{(1.11 \pm 0.06) \times 10^{-3}} \times \frac{499968}{199992} \\ &= 341 \pm 17 && (4.26) \end{aligned}$$

The rejection due to the photons from the π^0 for both $K_{\pi 2}$ and $K_{\pi 2\gamma}$ decay can be expected to be roughly equal. However, due the presence of the extra photon, the total photon-veto rejection for the $K_{\pi 2\gamma}$ decay is expected to be higher than for $K_{\pi 2}$. The single-photon detection inefficiency of the detector has been measured as a function of the energy and angle of the additional photon in [65]. Using these measurements and the energy and angular distribution of the additional photon for the 6907 events which passed all the analysis cuts (Fig. 4.10), the rejection due to the additional photon was measured to be

$$R_\gamma = \frac{1}{\epsilon_\gamma} = 5.40 \qquad (4.27)$$

where ϵ_γ is the total single-photon detection inefficiency from the convolution of the distribution in Fig. 4.10 and the map in [65]. Using the ratio of $K_{\pi 2}$ events in the kinematic peak over the $K_{\pi 2\gamma}$ events in the PNN2BOX from the MC study, and the additional photon-veto rejection due to the presence of the extra photon in the $K_{\pi 2\gamma}$

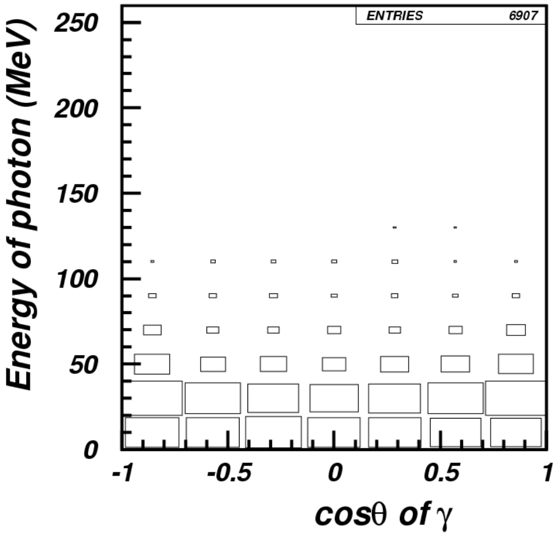

Figure 4.10: Energy vs polar angle of the non-π^0 photon from $K_{\pi 2\gamma}$ MC events that passed all the cuts.

decay, the radiative-$K_{\pi 2}$ background can be measured as

$$\begin{aligned} N_{K_{\pi 2\gamma}} &= 3 \times \frac{N^{data}_{K_{\pi 2}}}{\kappa R_\gamma} && (4.28) \\ &= 3 \times \frac{27 \pm 5.2}{(341 \pm 17) \cdot 5.4} && (4.29) \\ &= 0.044 \pm 0.009 && (4.30) \end{aligned}$$

where $N^{data}_{K_{\pi 2}}$ is the number of events in the $K_{\pi 2}$ kinematic peak which survived all the analysis cuts, used to generate Class 1 of Table 4.1.

4.7 Charge-Exchange Background

The charge-exchange background is expected to come from $K^0_L \to \pi^+ \mu^- \bar{\nu}$ and $K^0_L \to \pi^+ e^- \bar{\nu}$ decays. The DELCO3 cut suppresses the contribution from K^0_S decays, but a slow K^0_L can travel away from the CEX position and decay to a lepton that could

CUT	events
SETUP	1402
KPIGAP	41
TGCUT06	3

Table 4.11: Normalization branch for CEX from data. The cuts mentioned in the text are skipped from the SETUP and the TGCUT06.

be missed and a signal-like pion. Such a topology is suppressed by the cut TARGF, which requires that the kaon and pion clusters be connected.

The normalization branch for this background comes from data, with KPIGAP (a tighter version of $\overline{TARGF}$, see Section 3.3.6) and all other cuts applied, except for DELCO3, B4EKZ, TGPV, OPSVETO, CCDPUL, CHI567, VERRNG, CHI5MAX and ALLKFIT. These excluded cuts also have rejection against CEX, as they would cut events with prompt K^0 decay, ambiguous decay-vertex assignment, or visible e^- energy in the Target, but they are skipped in order to retain statistics. The final normalization number will be corrected for their rejection (R_{excl}). The normalization branch is shown in Table 4.11. SETUP includes PNN2BOX, KCUT, PSCUT06, TDCUT02 and PVCUTPNN2.

Since a pure CEX sample cannot be isolated from data by inverting any other cuts apart from TARGF, the effect of this cut on the background and the rejection of the cuts excluded in the normalization branch on CEX events was measured with Monte Carlo. About 3.42×10^8 $K^0_L \to \pi^+\mu^-\bar{\nu}$ events were generated, using the production point and K^0_L momentum distributions derived from $K^0_S \to \pi^+\pi^-$ data [66]. The $K^0_L \to \pi^+e^-\bar{\nu}$ events are already included in the normalization branch, and the cuts used to suppress $K^0_L \to \pi^+\mu^-\bar{\nu}$ are expected to have the same rejection on $K^0_L \to \pi^+e^-\bar{\nu}$, therefore it is adequate to use only the muon mode. As shown in Fig. 4.11, the expected CEX background in the signal region is determined by

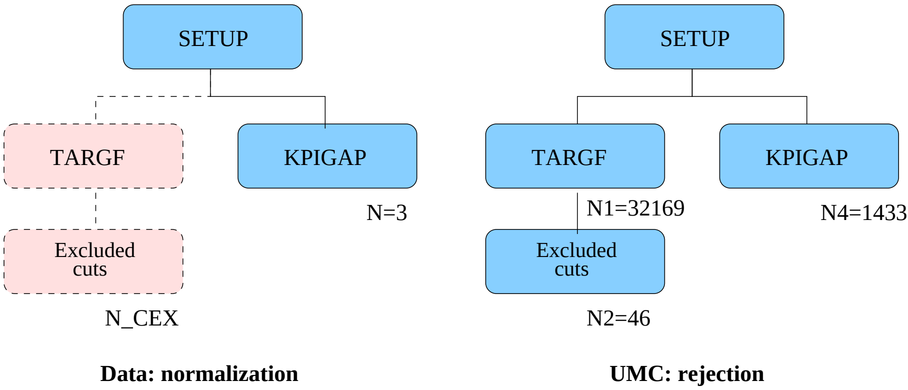

Figure 4.11: The method used to calculate the expected CEX background. The dotted outlined boxes are not accessible in data, since they are the signal region. However, UMC events can be in the signal region without biasing the result.

Eq. (4.31).

$$\frac{N_{CEX}}{N} = \frac{N_2}{N_4} \tag{4.31}$$

where N is the normalization from data and N_2 and N_4 are from MC. But

$$R_{excl} = \frac{N_1}{N_2} \tag{4.32}$$

therefore

$$N_{CEX} = 3 \times N \times \frac{N_1}{N_4} \times \frac{1}{R_{excl}} \tag{4.33}$$

for the whole sample. Therefore,

$$N_{CEX} = 3 \times (3 \pm 1.7) \times \frac{32169}{14336} \times \frac{1}{32169/46} \times 0.62 \tag{4.34}$$

$$= 0.018 \pm 0.010(stat.)^{+0.005}_{-0.003} \tag{4.35}$$

where 0.62 is the acceptance of CHI567, VERRNG, CHI5MAX and ALLKFIT, which was taken from data (see Section 5). The systematic error comes from the variation of the rejection of the excluded cuts with the chosen T_{xtg} and E_{hide} threshold. When they vary from $T_{xtg} < 1.$, $E_{hide} < 1.25$ to $T_{xtg} < 3.$, $E_{hide} < 2.75$, the rejection changes from 32169/38 to 32169/58.

Background	Events in the 3/3 sample
$K_{\pi 2}$TG-scatter	$0.479 \pm 0.116(\text{stat.})^{+0.029}_{-0.123}(\text{sys.})$
$K_{\pi 2}$RS-scatter	0.015±0.004
Beam	0.013±0.014
Muon	0.0071±0.0076
K_{e4}	$0.052 \pm 0.013(\text{stat.})^{+0.246}_{-0.023}(\text{syst.})$
$K_{\pi 2\gamma}$	0.044± 0.009
CEX	$0.018 \pm 0.010(\text{stat.})^{+0.005}_{-0.003}(\text{syst.})$
TOTAL	$0.630 \pm 0.119(\text{stat.})^{+0.248}_{-0.125}(\text{syst.})$

Table 4.12: Total-Background Estimation.

4.8 Background Summary

The total background expected in the signal region based on the 1/3 sample analysis is summarized in Table 4.12

The expected background in the E787 analysis was 1.216±0.239 [63] for comparable KB_{live}, therefore the current result is about a factor of two improvement. Especially the dominant $K_{\pi 2}$ target-scatter background has been drastically reduced, thanks to the upgraded photon-veto systems. The beam background is better understood and consistent with the PNN1 beam-background. Finally, the new method developed to estimate the CEX background is more reliable than the one used in E787, which depended only on Monte Carlo.

4.9 Outside-the-Box Study

In order to verify that the bifurcation cuts are uncorrelated, the outside-the-box (OTB) study was performed on the major ($K_{\pi 2}$ TG-scatter) background. Photon veto was loosened to its loosest parameters (at 85% acceptance) and the CCDPUL and EPIONK cuts to a threshold of 2 MeV pion energy, and the background study

Normalization	424
Events before PV	26360
Events after PV	183
PV rejection	144.0±10.6
Background	2.965±0.220

Table 4.13: The quantities used in the calculation of the expected $K_{\pi 2}$ TG-scatter background in the large signal region, for the outside-the-box study. The background value has not been scaled to the 3/3 sample.

was repeated. The normalization, rejection and number of $K_{\pi 2}$ TG-scatter background events expected in the large signal region for class 2, which has the CCDPUL and EPIONK inverted, are listed in Table 4.13. The expected $K_{\pi 2\gamma}$ background in this region has to be added to this value, because the $K_{\pi 2\gamma}$ backgroung level changes as well when the PV is loosened. Substituting the number of $K_{\pi 2}$ peak events that survive the loose PV $N^{data}_{K_{\pi 2}} = 182$ in Eq. (4.28), the expected $K_{\pi 2\gamma}$ background in the large box is 0.099±0.007, not scaled to the 3/3 sample. Given that the $K_{\pi 2\gamma}$ background is increased by only a factor of two in the large box, the CEX background, which is less sensitive to the PV tightness since it has no photons in the final state, is expected to contribute even less.

Therefore, the expected background in the OTB region is

$$\begin{aligned} N_{OTB} &= N^{large}_{kp2-TGscat} + N^{large}_{kp2g} - N^{small}_{kp2-TGscat}/3 + N^{small}_{kp2g}/3 \qquad (4.36) \\ &= 2.965 + 0.099 - 0.508/3 - 0.044/3 \\ &= 2.880 \pm 0.224 \qquad (4.37) \end{aligned}$$

When this region was examined, 3 events were found, which is consistent with the expectation.

4.10 Single-Cut Failures

A single-cut failure study helps to determine if there are any backgrounds which were not included *a priori* or if there are loop-holes for background processes to pass E949 cuts and become a candidate event. A single-cut failure study was performed by grouping correlated cuts together. By construction, each background process is suppressed by two independent methods; grouping correlated cuts would be the only method to determine if the two independent methods were working properly. Thirteen groups were created and are listed as follows:

- Seven non-grouped cuts include the following:

  BOX, Photon-Veto not including ADPV or TGPV, ADPV, DELC3, B4EKZ, TGZFOOL.

- *Extra Target Energy* Cuts:

  TGPV, OPSVETO.

- π^+ *Energy in* K^+ *Fibers* Cuts:

  CCDPUL, CCDBADFIT, CCDBADTIM, CCD31FIB, EPIONK, TIMKF.

- *Target/IC geometry* Cuts:

  TGGEO, KIC.

- *TD* Cuts:

  PIFLG, ELVETO, TDFOOL, TDNN, RSHEX, RSHEX2.

- *Kinematics* Cuts:

  COS3D, ZFRF, ZUTOUT, UTCQUAL, TICCON, EICCON, RNGMOM, PRRF1, PRRFZ, RSDEDXMAX, RSDEDXCL, RSLIKE, LAYER14.

- *Beam* Cuts:

  BWTRS, CKTRS, CKTAIL, CPITRS, CPITAIL, B4DEDX, B4TRS, B4CCD, TIMCON, UPVTRS, RVTRS.

- *Other* Cuts:

  TGQUALT, NPITG, EPITG, EPIMAXK, TGER, TARGF, DTGTTP, RTDIF, DRP, TGKTIM, TGEDGE, TGDEDX, TGENR, PIGAP, TGLIKE1, TGLIKE2, TBDB4, TGDB4TIP, TGDVXTIP, TGDVXPI, PHIVTX, CHI567, CHI5MAX, ALLKFIT, TPICS, TGTCON, B4ETCON.

Group	number of events	"true" single-cut failures
BOX	36	0
PV(no AD, no TG)	190	20
ADPV	0	0
DELC3	0	0
B4EKZ	0	0
TGZFOOL	0	0
Extra TG Energy	1	0
π^+ energy in K^+ fiber	3	2
TG/IC	1	1
TD	0	0
Kinematics	2	1
Beam	0	0
Other	3	1
Total	236	25

Table 4.14: Number of single-cut failures listed by grouped-cuts. "true" single-cut failures refer to events which only fail one individual cut within the cut group.

For an event to become a single-cut failure, it must fail cuts only in one group. The event can fail multiple cuts in the group and still be considered a single-cut failure. Events are of additional interest if they only fail one cut within a cut group category (“true” single-cut failures). The results of the single-cut failure study are shown in Table 4.14.

Events of interest were visually inspected; these included all single-cut events except for the events which failed multiple PV cuts (66 events in total). The 20 events which failed only one cut within the PV category were very far away from the cut threshold; 16 of the 20 failed ECouter. The reconstruction of these events leads to the conclusion that one or two very energetic photons ($>$ 60 MeV) from a $K_{\pi 2}$ decay were converted and contained solely within one photon detector. All other events are consistent with expectation due to cut efficiencies.

4.10.1 Safety Cuts

An initial single-cut failure study yielded 240 events. The four additional events (compared to Table 4.14) included one ADPV event, one BOX event, and two PV events.

Analysis of the ADPV lead to the creation of CCDBADTIM. The reconstruction of the event showed a $K_{\pi 2}$ TG-scatter event where a photon was detected within the AD. The scatter in the TG was reconstructed in the TG-CCD-pulse fitting. However, the fit was erroneous due to the extremely large second pulse ($\sim$ 8 MeV). CCDBADTIM requires that the times of the single and double pulse are consistent with the times of the TG reconstruction. This cut removed three events from the initial single-cut failure study (the ADPV event and two from the PV group).

Analysis of the “true” single-cut PV failure events yielded a possible loop-hole process. This occurred when the two photons from a π^0 converts in the same BVL element. This pathological process causes the timing to be mismeasured, possibly allowing the π^0 to go undetected. The cut which was devised against this process was named EARLY$_{BVL}$. EARLY$_{BVL}$ removes events when the mean time of the hit in a

BVL element is between -5.0 ns and -2.0 ns, the time difference between the hits on each end is less than 4.0 ns, and the energy of the hit is greater than 10.0 MeV. This additional cut removed one event from the BOX group in the initial single-cut failure study. EARLY_{BVL} also effected at least two other PV single-cut failure events.

Chapter 5

Signal Acceptance

Each criteria imposed to reduce backgrounds will also remove signal. Acceptance loss is the measure of the fraction of signal events removed ($acceptance\ loss = 1 - acceptance$) from consideration; $acceptance_{cut} = \frac{number\ of\ events\ before\ cut}{number\ of\ events\ after\ cut}$ where the sample is composed of signal (or signal like events). To obtain an accurate measure of the BR, the acceptances of all selection criteria must be carefully measured. This is accomplished by carefully selecting a subset of monitor triggers, whenever possible, which emulate qualities of a $K^+ \rightarrow \pi^+ \nu\bar{\nu}$ event; Monte Carlo samples were used for criteria which were not possible to obtain through the use of monitor trigger samples. Acceptance measurements using triggers taken in tandem with the signal triggers allows the running conditions, such as beam rate, to be automatically taken into account. Monte Carlo simulation was unable to reproduce the run-to-run dependences which occurred during data collection.

Acceptance values of cuts, described in Section 3.3, are shown in the tables that follow. The first row labeled 'Setup' shows the number of initial events after obtaining a sample by applying appropriate cuts. To achieve an unbiased acceptance measurement, setup cuts must be uncorrelated with the cuts whose acceptance were measured. The setup cuts were devised to create a PNN2-like sample with respect to the measured cuts (within the given table). The ability to create events similar (in various aspects) to $K^+ \rightarrow \pi^+\nu\bar{\nu}$ events allowed E949 to reduce the dependence on Monte Carlo. In the following tables, TRIGGER refers to the respective online-monitor-trigger bit for the given sample.

A listed cut may have no acceptance loss (i.e. acceptance = 1.0). This is not of concern and does not imply the cut does nothing. This may be due to the cut being correlated with another cut which was previously applied (cuts are applied in sequential order). For example, highly correlated cuts occur when a background process effects multiple detectors such as a photon conversion in the BVL which cascades into the BV. Some cuts have no acceptance loss after all correlated cuts are applied; applying such cuts give the analysis redundancy to prevent backgrounds from 'sneaking' into the signal region. Another possibility, as in the case for the early-BVL cut, is that the process that is being selectively removed can not occur in a measured $K^+ \rightarrow \pi^+\nu\bar{\nu}$ decay and will only reject background. If these no-acceptance-loss cuts have rejection against backgrounds, they provide a benefit without detracting the analysis; as opposed to most cuts which do detract by having acceptance loss, but provides a net benefit by rejecting background(s) (i.e. $acceptance \times rejection > 1$).

5.1 Acceptance Factors from $K_{\mu 2}$ Events

$K_{\mu 2}$ events which have an incoming K$^+$, one charged track entering the fiducial region, and no photons products are ideal in emulating signal event criteria for beam conditions, target reconstruction, tracking, and photons. To obtain appropriate samples for these aspects of the $K^+ \rightarrow \pi^+\nu\bar{\nu}$ decay, setup cuts listed in Table 5.1 were employed.

To measure event reconstruction in the RS, see Table 5.2, the setup cuts chosen, $Setup_{Recon}$, created a sample with good tracks by requiring that the TG and

$K_{\mu 2}$ **Setups**	**Component cuts**
$Setup_{RS\ track}$	TRIGGER, ICBIT, $t_{IC} - t_{Ck} > 5$ ns, B4DEDX, UTC, UTC_QUAL
$Setup_{recon}$	TRIGGER, ICBIT, $t_{IC} - t_{Ck} > 5$ ns, B4DEDX, CPITRS, CPITAIL, CKTRS, CKTAIL, BWTRS, RDTRK, TRKTIM, $\lvert t_{IC} - t_{RS}\rvert < 5$ ns, PVCUTPNN2(noBV+BVL)
$Setup_{beam}$	TRIGGER, ICBIT, RDTRK, TRKTIM, RDUTM, KM2PBOX, COS3D
$Setup_{PV}$	$Setup_{beam}$, A_{beam} cuts, stopping layer< 19

Table 5.1: Setup cuts used for the $K_{\mu 2}$-based acceptance measurements. "A_{beam} cuts" are the cuts whose acceptance is measured in "beam" category. ICBIT is the online-IC-trigger bit, KM2PBOX selects events with 226 MeV/c < *ptot* < 246 MeV/c.

UTC, which are independent of the RS, have a valid reconstruction, a delayed-coincidence style cut using Č$_K$ and IC, K$^+$ entering the TG (B4DEDX). Measuring the reconstruction efficiency of the TG and UTC, see Table 5.3, requires a sample with a single K$^+$ (B4DEDX) and no beam π^+'s entering the detector (CPITRS, CPITAIL, CKTRS, CKTAIL, BWTRS). A requirement that insures a delayed coincidence using Č$_K$ and IC[1] ($t_{IC} - t_{Ck} > 5$ ns), a good charged track traversing the UTC detector ($|t_{IC} - t_{RS}| < 5$ ns, RD_TRK, TRKTIM), and no photons (PVCUTPNN2(noBV+BVL)). BV and BVL photon-vetoing criteria is not used for the

Cut	Loose Box		Tight Box	
	Events	**Acceptance**	**Events**	**Acceptance**
$Setup_{RS\ track}$	2925784		2925784	
RD_TRK	2925784	1.0000	2925784	1.0000
TRKTIM	2925591	0.9999	2925591	0.9999
A_{RS}	0.99993 ± 0.000005		0.99993 ± 0.000005	

Table 5.2: RS reconstruction acceptance using $K_{\mu 2}(1)$ monitor events.

---

[1] DELCO could not be used in here because DELCO requires a TG reconstruction which in turn requires a reconstructed track from the UTC and RS.

A_{RS} sample, so that the sample will not remove events with μ^+'s traversing the entire RS and entering the BVL and BV.

Cut	Loose Box		Tight Box	
	Events	**Acceptance**	**Events**	**Acceptance**
$Setup_{recon}$	1520985		748449	
RDUTM	1520125	0.9994 ± 0.00002	748183	0.9996 ± 0.00002
TARGET	1520125	1.0000	748183	1.0000
A_{recon}	0.99943 ± 0.000019		0.99965 ± 0.000022	

Table 5.3: TG and UTC reconstruction acceptance using $K_{\mu 2}(1)$ monitor events.

The acceptances associated with the beam and target-region cuts require a sample which is definitely a single K$^+$ decay with no photons. So the $K_{\mu 2}$ decay was chosen with requirements on the track momentum (KM2PBOX), on the quality of the track (RD_TRK, TRKTIM, RDUTM), and on the fiducial region (COS3D). The cuts in Table 5.4 were ordered in a way that would allow for a more meaningful acceptance value for each cut (e.g. TGQUALT was placed at the beginning because many of the following cuts require a successful TG reconstruction before they work properly.)

Cut	Loose Box		Tight Box	
	Events	**Acceptance**	**Events**	**Acceptance**
$Setup_{beam}$	3771613		3771613	
TGCUT	3689137	0.9781 ± 0.00008	3689137	0.9781 ± 0.00008
TGQUALT	3560525	0.9651 ± 0.00010	3560525	0.9651 ± 0.00010
NPITG	3560525	1.0000	3560525	1.0000
TIMCON	3555328	0.9985 ± 0.00002	3555328	0.9985 ± 0.00002
TGTCON	3516829	0.9892 ± 0.00005	3516829	0.9892 ± 0.00005
B4ETCON	3481951	0.9901 ± 0.00005	3481951	0.9901 ± 0.00005
DCBIT	3067147	0.8809 ± 0.00017	3067147	0.8809 ± 0.00017

Table 5.4 continued on next page

Table 5.4 continued from previous page

Cut	Loose Box		Tight Box	
	Events	**Acceptance**	**Events**	**Acceptance**
DELCO	2628388	0.8569 ± 0.00020	2160585	0.7044 ± 0.00026
PSCUT	2493148	0.9485 ± 0.00014	2045546	0.9468 ± 0.00015
B4DEDX	2479504	0.9945 ± 0.00005	2034267	0.9945 ± 0.00005
BWTRS	2275862	0.9179 ± 0.00017	1865809	0.9172 ± 0.00019
CPITRS	2272021	0.9983 ± 0.00003	1862726	0.9983 ± 0.00003
CPITAIL	2270965	0.9995 ± 0.00001	1861874	0.9995 ± 0.00002
CKTRS	2256478	0.9936 ± 0.00005	1852681	0.9951 ± 0.00005
CKTAIL	2220172	0.9839 ± 0.00008	1841678	0.9941 ± 0.00006
B4TRS	2163250	0.9744 ± 0.00011	1792894	0.9735 ± 0.00012
B4CCD	2134064	0.9865 ± 0.00008	1773887	0.9894 ± 0.00008
UPVTRS	2099003	0.9836 ± 0.00009	1745815	0.9842 ± 0.00009
RVTRS	2097001	0.9990 ± 0.00002	1744246	0.9991 ± 0.00002
TGGEO	2012822	0.9599 ± 0.00014	1672775	0.9590 ± 0.00015
B4EKZ	1834958	0.9116 ± 0.00020	1522582	0.9102 ± 0.00022
TGZFOOL	1812291	0.9876 ± 0.00008	1503775	0.9876 ± 0.00009
TARGF	1754010	0.9678 ± 0.00013	1455287	0.9678 ± 0.00014
DTGTTP	1754003	1.0000	1455280	1.0000
RTDIF	1737206	0.9904 ± 0.00007	1441269	0.9904 ± 0.00008
TGKTIM	1720074	0.9901 ± 0.00007	1436006	0.9963 ± 0.00005
EICCON	1673926	0.9732 ± 0.00012	1397533	0.9732 ± 0.00013
TICCON	1673922	1.0000	1397530	1.0000
PIGAP	1659315	0.9913 ± 0.00007	1385358	0.9913 ± 0.00008
TBDB4	1614464	0.9730 ± 0.00013	1347219	0.9725 ± 0.00014
TGDB4TIP	1606252	0.9949 ± 0.00006	1340136	0.9947 ± 0.00006
TGDVXTIP	1602025	0.9974 ± 0.00004	1336547	0.9973 ± 0.00004
TGDVXPI	1566607	0.9779 ± 0.00012	1309007	0.9794 ± 0.00012
PHIVTX	1519604	0.9700 ± 0.00014	1265387	0.9667 ± 0.00016

Table 5.4 continued on next page

Table 5.4 continued from previous page

Cut	Loose Box		Tight Box	
	Events	**Acceptance**	**Events**	**Acceptance**
CCDPUL	687795	0.4526 ± 0.00040	627481	0.4959 ± 0.00044
EPIONK	684627	0.9954 ± 0.00008	624313	0.9950 ± 0.00009
CCDBADTIM	679562	0.9926 ± 0.00010	619649	0.9925 ± 0.00011
CCD31FIB	679553	1.0000	619640	1.0000
TIMKF	613292	0.9025 ± 0.00036	558769	0.9018 ± 0.00038
VERRNG	571441	0.9318 ± 0.00032	520584	0.9317 ± 0.00034
ANGLI	571092	0.9994 ± 0.00003	520260	0.9994 ± 0.00003
ALLKFIT	563903	0.9874 ± 0.00015	513528	0.9871 ± 0.00016
TPICS	563178	0.9987 ± 0.00005	512822	0.9986 ± 0.00005
KIC	563015	0.9997 ± 0.00002	512669	0.9997 ± 0.00002
A_{beam}	0.14928 ± 0.000183		0.13593 ± 0.000176	

Table 5.4: Target and Beam acceptance based on $K_{\mu 2}(1)$ events

Cut	Loose Box		Tight Box	
	Events	**Acceptance**	**Events**	**Acceptance**
$Setup_{PV}$	61031		54888	
LHEX	56983	0.9337 ± 0.00101	51233	0.9334 ± 0.00106
HEXAFTER	54888	0.9632 ± 0.00079	49374	0.9637 ± 0.00083
PVONLINE	52544	0.9573 ± 0.00086	47265	0.9573 ± 0.00091
LAY20or21	52129	0.9921 ± 0.00039	46891	0.9921 ± 0.00041
STLAY	51643	0.9907 ± 0.00042	46450	0.9906 ± 0.00045
RSHEX	49767	0.9637 ± 0.00082	44737	0.9631 ± 0.00087
PVCUT	47888	0.9622 ± 0.00085	43045	0.9622 ± 0.00090
TGPVCUT	47425	0.9903 ± 0.00045	42630	0.9904 ± 0.00047
TGPVTR	47425	1.0000	42630	1.0000

Table 5.5 continued on next page

Table 5.5 continued from previous page

Cut	Loose Box		Tight Box	
	Events	**Acceptance**	**Events**	**Acceptance**
TGPV	45969	0.9693 ± 0.00079	39225	0.9201 ± 0.00131
ICPV	45923	0.9990 ± 0.00015	39108	0.9970 ± 0.00028
VCPV	45894	0.9994 ± 0.00012	39033	0.9981 ± 0.00022
COPV	45639	0.9944 ± 0.00035	38884	0.9962 ± 0.00031
MCPV	45634	0.9999 ± 0.00005	38873	0.9997 ± 0.00009
ECinner	42180	0.9243 ± 0.00124	30927	0.7956 ± 0.00205
ECouter	36778	0.8719 ± 0.00163	24669	0.7977 ± 0.00228
EC 2nd	36522	0.9930 ± 0.00043	22849	0.9262 ± 0.00166
RSPV	33844	0.9267 ± 0.00136	16253	0.7113 ± 0.00300
BVPV	31413	0.9282 ± 0.00140	14921	0.9180 ± 0.00215
BVLPV	30914	0.9841 ± 0.00071	14719	0.9865 ± 0.00095
ADPV	29410	0.9513 ± 0.00122	14069	0.9558 ± 0.00169
EARLY$_{BV}$	29385	0.9991 ± 0.00017	14063	0.9996 ± 0.00017
DSPV	29381	0.9999 ± 0.00007	14061	0.9999 ± 0.00010
EARLY$_{BVL}$	29381	1.0000	14061	1.0000
PV_{PNN2}	0.6391 ± 0.0022		0.3585 ± 0.0024	
A_{PV}	0.48141 ± 0.002023		0.25618 ± 0.001863	

Table 5.5: Online and offline photon-veto acceptance using $K_{\mu 2}(1)$ monitor events. PV$_{PNN2}$ is the total acceptance of all offline PV cuts; it is composed of TGPV through EARLY$_{BVL}$. PV$_{PNN2}$ is not an additional cut.

Measuring the photon-veto criteria required a valid decay and successfully reconstructed $K_{\mu 2}$ event without any additional secondary beam particles at decay time ($Setup_{beam}$, A_{beam}). Since a μ^+ from a $K_{\mu 2}$ decay could penetrate the whole RS and reach the BVL or BV photon detector, a requirement of *stopping layer* < 19 was imposed. Both the online and offline PV cuts are measured with $K_{\mu 2}(1)$ since there was no online PV requirement in the trigger. The total acceptance measured using $K_{\mu 2}$-monitor events is calculated via Eq. (5.1) and is summarized in Table 5.6.

$$A_{K_{\mu 2}} = A_{RS} \times A_{recon} \times A_{beam} \times A_{PV} \tag{5.1}$$

	Loose Box	Tight Box
A_{RS}	0.99993 ± 0.000005	0.99993 ± 0.000005
A_{recon}	0.99943 ± 0.000019	0.99965 ± 0.000022
A_{beam}	0.14928 ± 0.000183	0.13593 ± 0.000176
A_{PV}	0.48141 ± 0.002023	0.25618 ± 0.001863
$A_{K_{\mu 2}}$	0.0718 ± 0.0044	0.0348 ± 0.0074

Table 5.6: $K_{\mu 2}$ acceptance summary.

5.2 Acceptance Factors from $\pi_{scatter}$ Events

Since the π^+ from $K^+ \rightarrow \pi^+ \nu \bar{\nu}$ events has a spectrum of energy and range values, unlike π^+'s from $K_{\pi 2}$, π_{scat}'s are ideal to measure acceptances dealing with RS kinematics. The π^+ from π_{scat} events have a continuous stopping-layer distribution, as is expected with $K^+ \rightarrow \pi^+ \nu \bar{\nu}$ events, which is advantageous in considering possible layer dependences within the RS (such as the TD cuts). The setup cuts used to create these samples are listed in Table 5.7.

Creating a sample of single-beam π^+'s which scatter in the TG required removing events with K$^+$ particles in the beam ($b4abm2 < 1.3$ MeV, CKTRS, CKTAIL); the requirement $|t_\pi - t_{RS}| < 5$ ns requires a scattering of the incoming particle and $|t_{IC} - t_{RS}| < 5$ ns requires that the track in the RS and TG are from the same particle. The RS photon-vetoing requirements are applied so as to remove coincident activity within the RS that would otherwise artificially lower the acceptance. PVPNN2 was not applied due to the photon cuts removing events with additional activity

$\pi_{scatter}$ **Setups**	**Component cuts**
$Setup_{bad\_stc}$	RD_TRK, TRKTIM, STLAY, UTC, RDUTM, PDC, ICBIT, $b4abm2 < 1.3$ MeV, $\lvert t_\pi - t_{RS}\rvert < 5$ ns, $\lvert t_{IC} - t_{RS}\rvert < 5$ ns, TARGF, DTGTTP, RTDIF, TGQUALT, TGZFOOL, CKTRS, CKTAIL, PVCUTPNN2(only RS), COS3D, LAYV4, PNN2BOX
$Setup_{RSkin}$	$Setup_{bad\_stc}$, BAD_STC, TDCUT02
$Setup_{\pi\to\mu\to e}$	$Setup_{bad\_stc}$, BAD_STC, RNGMOM, ZFRF, ZUTOUT, LAYER14, UTC_QUAL, EIC

Table 5.7: Setup cuts used for the $\pi_{scatter}$ based acceptance measurements. $b4abm2$ is the energy of the B4 hit near beam time.

at decay time; since a decay does not occur, timing used by the photon cuts are not as meaningful. The remaining cuts which make up $Setup_{bad\_stc}$ require a nicely reconstructed track.

BADSTC, as discussed in Section 3.3.1, removes events when the TD in the determined stopping counter was not working properly.

Cut	Loose Box		Tight Box	
	Events	**Acceptance**	**Events**	**Acceptance**
$Setup_{bad\_stc}$	153716		73145	
BADSTC	153474	0.9984 ± 0.00010	73089	0.9992 ± 0.00010
A_{badstc}	0.99843 ± 0.000101		0.99923 ± 0.000102	

Table 5.8: BADSTC acceptance using $\pi_{scatter}$ monitor events.

5.2.1 Range-Stack-Kinematic Acceptance

Measuring the kinematic acceptance in the RS (A_{RSkin}) required further refinements to the sample employed by the A_{badstc} measurement. The particle-identification cuts TDCUT02 were utilized, requiring a stopped π^+ in the RS. Without the TDCUT02 requirement a π^+, after entering the RS, could decay in flight yielding kinematics similar to a μ^+ or e^+. A sample with decay-in-flight π^+'s included would artificially lower A_{RSkin}.

Cut	Loose Box		Tight Box	
	Events	**Acceptance**	**Events**	**Acceptance**
$Setup_{RSkin}$	88719		31525	
UTCQUAL	84373	0.9510 ± 0.00072	30038	0.9528 ± 0.00119
RNGMOM	82845	0.9819 ± 0.00046	29506	0.9823 ± 0.00076
RSDEDXMAX	80449	0.9711 ± 0.00058	28764	0.9749 ± 0.00091
RSDEDXCL	76828	0.9550 ± 0.00073	27586	0.9590 ± 0.00117
RSLIKE	76828	1.0000	27586	1.0000
PRRF1	76196	0.9918 ± 0.00033	27433	0.9945 ± 0.00045
PRRFZ	73596	0.9659 ± 0.00066	26577	0.9688 ± 0.00105
A_{RSkin}	0.82954 ± 0.001262		0.84305 ± 0.002049	

Table 5.9: RS-kinematic acceptance using $\pi_{scatter}$ monitor events.

In order to account for the systematics associated with poor target reconstruction of the π_{scat} events, which is a function of the kinematics, the kinematic box cut was varied. The PNN2BOX was the nominal box cut. The size of the smaller and larger box cut was a shrunken or expanded PNN2BOX.

The difference in reconstruction quality for $\pi_{scatter}$ events and $K_{\pi 2}$ events was evaluated from the resolution of the reconstructed π^+ mass, $m_\pi = \frac{ptot^2 - etot^2}{2 \cdot etot}$, of the two samples. The distributions from π_{scat} and $K_{\mu 2}$ samples, shown in Fig. 5.1, have resolutions of 13.8 and 8.4 respectively. The fractional uncertainty in $\pi_{scatter}$-target-track reconstruction is therefore $\sqrt{13.8^2 - 8.4^2}/140.0 \simeq 7.8\%$.

Since *ptot* and *etot* contribute roughly equally to the resolution, their uncertainties are $7.8\%/\sqrt{2} = 5.5\%$. *rtot* scales approximately linearly with *etot*, so its uncertainty is also 5.5%. The boundaries of the nominal PNN2 kinematic box were varied by

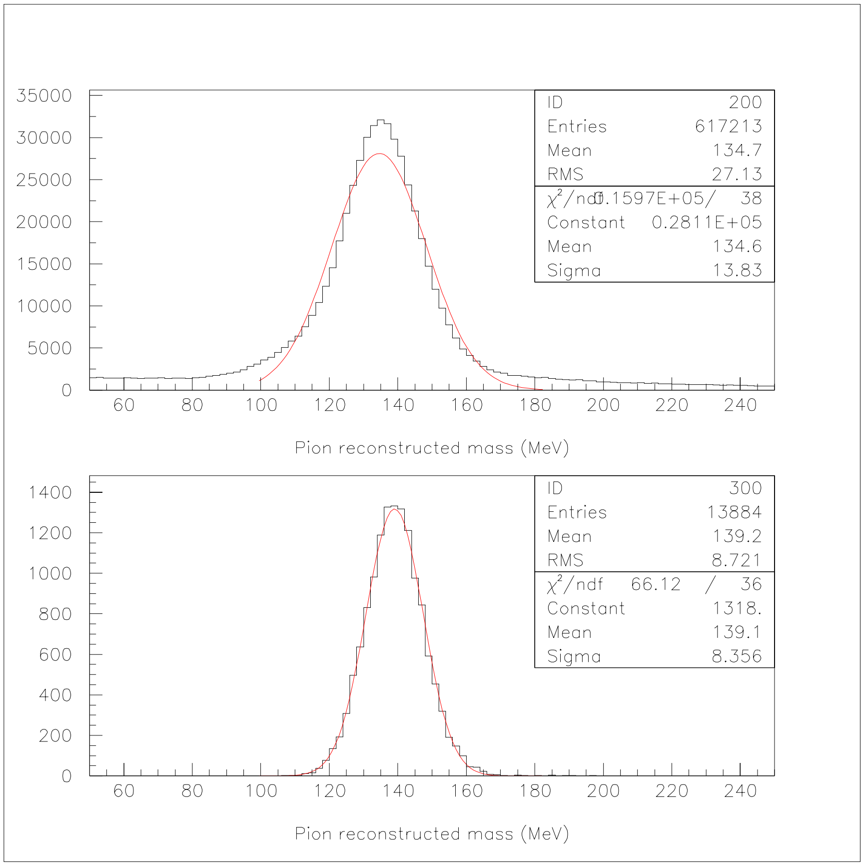

Figure 5.1: Distributions of the reconstructed π^+ mass from $\pi_{scatter}$ (top) and $K_{\pi 2}$ events (bottom).

5.5% yielding the following small and large boxes:

Small box :

147.7 MeV/c $< ptot <$ 188.1 MeV/c

12.7 cm $< rtot <$ 26.5 cm

63.3 MeV $< etot <$ 95.0 MeV

Large box :

132.3 MeV/c $< ptot <$ 209.9 MeV/c

11.3 cm $< rtot <$ 29.5 cm

56.7 MeV $< etot <$ 106.0 MeV

Cut	Loose Box		Tight Box	
	Events	**Acceptance**	**Events**	**Acceptance**
$Setup_{RSkin}^{small}$	63400		29195	
UTCQUAL	60350	0.9519 ± 0.00085	27906	0.9558 ± 0.00120
RNGMOM	59251	0.9818 ± 0.00054	27396	0.9817 ± 0.00080
RSDEDXMAX	57778	0.9751 ± 0.00064	26746	0.9763 ± 0.00092
RSDEDXCL	55375	0.9584 ± 0.00083	25685	0.9603 ± 0.00119
RSLIKE	55375	1.0000	25685	1.0000
PRRF1	55017	0.9935 ± 0.00034	25548	0.9947 ± 0.00045
PRRFZ	53324	0.9692 ± 0.00074	24778	0.9699 ± 0.00107
LAYER14	53324	1.0000	24778	1.0000
$A_{RSkin}^{small\ box}$	0.84107 ± 0.001452		0.84871 ± 0.002097	

Table 5.10: RS kinematic acceptance using $\pi_{scatter}$ monitor events.

Cut	Loose Box		Tight Box	
	Events	**Acceptance**	**Events**	**Acceptance**
$Setup_{RSkin}^{large}$	110317		51078	
UTCQUAL	104830	0.9503 ± 0.00065	48730	0.9540 ± 0.00093
RNGMOM	102909	0.9817 ± 0.00041	47846	0.9819 ± 0.00060
RSDEDXMAX	99517	0.9670 ± 0.00056	46347	0.9687 ± 0.00080
RSDEDXCL	94726	0.9519 ± 0.00068	44201	0.9537 ± 0.00098
RSLIKE	94726	1.0000	44201	1.0000
PRRF1	93737	0.9896 ± 0.00033	43806	0.9911 ± 0.00045
PRRFZ	90176	0.9620 ± 0.00062	42205	0.9635 ± 0.00090
LAYER14	90176	1.0000	42205	1.0000
$A_{RSkin}^{large\ box}$	0.81743 ± 0.001163		0.82629 ± 0.001676	

Table 5.11: RS kinematic acceptance using $\pi_{scatter}$ monitor events.

The variation in the kinematic box determines the systemic error associated with the RS-kinematic cuts, as determined in Eq. (5.2).

$$A_{RSkin}^{sys} = \frac{A_{RSkin}^{large\ box} - A_{RSkin}^{small\ box}}{2} \tag{5.2}$$

Eq. (5.2) is valid when the systematic error is symmetric; this was not the case for the tight signal region. Therefore, the systemic error for the tight region was determined by the difference in the small and large box compared to the nominal box.

Hence, the RS-kinematic acceptance is

$$A^{loose}_{RSkin} = 0.82954 \pm 0.001262(stat.) \pm 0.012(sys.) \tag{5.3}$$

$$A^{tight}_{RSkin} = 0.84305 \pm 0.002049(stat.)^{+0.006}_{-0.017}(sys.) \tag{5.4}$$

5.2.2 $\pi^+ \rightarrow \mu^+ \rightarrow e^+$ Identification Acceptance

In an analogous way as the RS-kinematic-acceptance sample was created, the $\pi^+ \rightarrow \mu^+ \rightarrow e^+$ acceptance ($A_{\pi\rightarrow\mu\rightarrow e}$) requires the sample to be purified via cuts which are uncorrelated to the $\pi \rightarrow \mu \rightarrow e$ criteria (or simply TD cuts) being measured. RS-kinematic requirements were used to insure that the track was from a π^+. Since the $\pi_{scatter}$ did not include the online LEV1.1 and LEV1.2, the acceptances of these online requirements on the $\pi\nu\bar{\nu}(1)$ and $\pi\nu\bar{\nu}(2)$ could also be measured.

RSDEDX is correlated with EV5 due to μ^+ accidentals along the track causing EV5 to reject the event along with RSDEDX rejecting the event due to incorrect dE/dX value. PRRF1's dependence on the stopping-counter energy correlates it to the TD-pulse fitting utilized by TDNN. Tables 5.12 and 5.13 show the measured acceptances without and with RSDEDX and PRRF1,PRRFZ included in the setup cuts (A_{TD1}, A_{TD2}), respectively.

$A_{\pi\rightarrow\mu\rightarrow e}$ will be determined by the average of A_{TD1} and A_{TD2} and the systematic error is calculated from the difference. A 1.014% correction for π^+ decay-in-flight and π^+ absorption in the stopping counter, estimated from Monte Carlo, was applied to A_{TD2}.

Cut	Loose Box		Tight Box	
	Events	**Acceptance**	**Events**	**Acceptance**
$Setup_{\pi\to\mu\to e}$	126239		60258	
PIFLG	104055	0.8243 ± 0.00107	49850	0.8273 ± 0.00154
RSHEX2	102123	0.9814 ± 0.00042	48999	0.9829 ± 0.00058
LEV1.1	82659	0.8094 ± 0.00123	39953	0.8154 ± 0.00175
LEV1.2	69374	0.8393 ± 0.00128	35850	0.8973 ± 0.00152
TDCUT	65186	0.9396 ± 0.00090	33754	0.9415 ± 0.00124
ELVETO	62425	0.9576 ± 0.00079	32471	0.9620 ± 0.00104
TDFOOL	62208	0.9965 ± 0.00024	32365	0.9967 ± 0.00032
TDNN	58607	0.9421 ± 0.00094	27401	0.8466 ± 0.00200
EV5	58607	1.0000	22794	0.8319 ± 0.00226
A_{TD1}	0.46425 ± 0.001404		0.37827 ± 0.001976	

Table 5.12: $\pi^+ \to \mu^+ \to e^+$ acceptance using $\pi_{scatter}$ monitor events.

Hence, the RS kinematic acceptance is

$$A_{\pi\to\mu\to e} = 0.4805 \pm 0.0015(stat.) \pm 0.016(sys.) \tag{5.5}$$

The total acceptance measured using $\pi_{scatter}$-monitor events is calculated via Eq. (5.6) and is summarized in Table 5.14 and Table 5.15

$$A_{\pi_{scat}} = A_{badstc} \times A_{RSkin} \times A_{\pi\to\mu\to e} \tag{5.6}$$

Cut	Loose Box		Tight Box	
	Events	**Acceptance**	**Events**	**Acceptance**
$Setup_{\pi\rightarrow\mu\rightarrow e}$	126239		60258	
RSDEDXMAX				
RSDEDXCL				
RSLIKE				
PRRF1				
PRRFZ	107124		51828	
PIFLG	90161	0.8417 ± 0.00112	43749	0.8441 ± 0.00159
RSHEX2	88616	0.9829 ± 0.00043	43045	0.9839 ± 0.00060
LEV1.1	72545	0.8186 ± 0.00129	35471	0.8240 ± 0.00184
LEV1.2	61913	0.8534 ± 0.00131	32333	0.9115 ± 0.00151
TDCUT	58288	0.9415 ± 0.00094	30492	0.9431 ± 0.00129
ELVETO	55833	0.9579 ± 0.00083	29339	0.9622 ± 0.00109
TDFOOL	55655	0.9968 ± 0.00024	29255	0.9971 ± 0.00031
TDNN	52472	0.9428 ± 0.00098	24807	0.8480 ± 0.00210
EV5	52472	1.0000	20673	0.8334 ± 0.00237
$A_{uncorr\ TD2}$	0.48983 ± 0.001527		0.39888 ± 0.002151	
π^+ DIF/abs	$\times 1.014$			
A_{TD2}	0.4967 ± 0.0015		0.4045 ± 0.0022	

Table 5.13: $\pi^+ \rightarrow \mu^+ \rightarrow e^+$ acceptance using $\pi_{scatter}$ monitor events. $A_{uncorr\ TD2}$ is the acceptance before the correction factor for decay-in-flight (DIF) and π^+ absorption (abs) in the stopping counter (π^+ DIF/abs).

	Loose Box
A_{badstc}	0.99843 ± 0.000101
A_{RSkin}	$0.82954 \pm 0.001262(stat.) \pm 0.012(sys.)$
$A_{\pi\rightarrow\mu\rightarrow e}$	$0.4805 \pm 0.0015(stat.) \pm 0.016(sys.)$
$A_{\pi_{scat}}$	0.3980±0.0014(stat.)±0.014(sys.)

Table 5.14: $\pi_{scatter}$ acceptance summary for loose region.

	Tight Box
A_{badstc}	0.99923 ± 0.000102
A_{RSkin}	$0.84305 \pm 0.002049(stat.)^{+0.006}_{-0.017}(sys.)$
$A_{\pi\rightarrow\mu\rightarrow e}$	$0.3914 \pm 0.0022(stat.) \pm 0.013(sys.)$
$A_{\pi_{scat}}$	$0.3297 \pm 0.0020(\mathrm{stat.})^{+0.011}_{-0.013}(\mathrm{sys.})$

Table 5.15: $\pi_{scatter}$ acceptance summary for tight region.

5.3 Acceptance Factors from $K_{\pi2}$ Events

Within the E949 analysis, events from $K_{\pi2}(1)$ monitors are similar to $K^+ \rightarrow \pi^+\nu\bar{\nu}$ events in a few aspects: (1) They both have a single π^+ track emerging from a single incoming K^+. (2) The π^+ within the TG is minimum ionizing. Condition (1) allows for a valid target reconstruction with a good decay-vertex determination. These properties allow acceptances to be measured for target kinematics.

$K_{\pi2}$ **Setups**	**Component cuts**
$Setup_{utc}$	TRIGGER, RD_TRK, TRKTIM, STLAY, BAD_STC
$Setup_{ops}$	$Setup_{utc}$, UTC, RDUTM, PDC, PSCUT06, KCUTS, TGCUT06 without the ones measured, TDCUT02, KP2BOX
$Setup_{TGkin}$	$Setup_{ops}$, OPSVETO, TGPVCUT

Table 5.16: Setup cuts used for the $K_{\pi2}$-based acceptance measurements.

To obtain a sample of PNN2 signal-like events, setup cut in Table 5.16 were utilized on $K_{\pi2}(1)$ triggers. Measuring the acceptance of the PASS1 UTC cuts required reconstructing the TG and RS.

Cut	Loose Box		Tight Box	
	Events	**Acceptance**	**Events**	**Acceptance**
$Setup_{utc}$	1502895		1502895	
UTC	1417906	0.9435 ± 0.00019	1417906	0.9435 ± 0.00019
A_{utc}	0.94345 ± 0.000188		0.94345 ± 0.000188	

Table 5.17: UTC acceptance using $K_{\pi2}(1)$ monitor events.

The acceptance measurement of OPSVETO, Table 5.18, requires a sample with valid reconstruction within the TG and RS along with the requirement that there are no secondary beam particles (PSCUT06). Applying KP2BOX and TDCUT02 further purifies the sample to be valid $K_{\pi 2}$ decays.

Cut	Loose Box		Tight Box	
	Events	**Acceptance**	**Events**	**Acceptance**
$Setup_{ops}$	62989		38135	
OPSVETO	61365	0.9742 ± 0.00063	37127	0.9736 ± 0.00082
$A_{opsveto}$	0.97422 ± 0.000631		0.97357 ± 0.000821	

Table 5.18: OPSVETO acceptance using $K_{\pi 2}(1)$ monitor events.

Obtaining the best sample to measure acceptance of target kinematics is a combination of (1) good TG reconstruction, which is not available in a $\pi_{scatter}$ sample due to poor reconstruction of the TG at very small delayed-coincidence, and (2) π^+'s with kinetic energies spread throughout the PNN2 signal region (60.0 MeV $\leq E_{\pi^+} \leq$ 100.5 MeV), which is not available in a $K_{\pi 2}(1)$ sample. That is, E949 montior samples do not satisfy both (1) and (2). In the $\pi_{scatter}$ sample, TG fiber hits may be identified as a π^+-fiber near the scattering point (ideally reconstructed as the decay vertex) could have energy much greater than a normal π^+ from a $K^+ \rightarrow \pi^+ \nu \bar{\nu}$ decay. Thus, using a $\pi_{scatter}$ sample would yield a TG kinematic acceptance systematically lower than the true value.

Measuring the acceptance of TGDEDX with the sample used for calibration, $\pi_{scatter}$, would bias the acceptance measurement (see Appendix D). Therefore, the clean $K_{\pi 2}$ sample obtained by applying $Setup_{TGkin}$ is employed. The rest of the cuts in Table 5.19 employed the $K_{\pi 2}$ sample due to their dependence on good determination of the decay vertex and assuming no π^+ energy dependence.

The total acceptance of cuts measured using $K_{\pi 2}$-monitor events, as shown in Eq. (5.7), is summarized in Table 5.20.

$$A_{K_{\pi 2}} = A_{utc} \times A_{opsveto} \times A_{TGkin} \tag{5.7}$$

Cut	Loose Box		Tight Box	
	Events	**Acceptance**	**Events**	**Acceptance**
$Setup_{TGkin}$	60696		36719	
TGDEDX	60044	0.9893 ± 0.00042	36319	0.9891 ± 0.00054
TGER	60029	0.9998 ± 0.00006	36310	0.9998 ± 0.00008
TGENR	58065	0.9673 ± 0.00073	35058	0.9655 ± 0.00096
TGLIKE1	57014	0.9819 ± 0.00055	34413	0.9816 ± 0.00072
TGLIKE2	56103	0.9840 ± 0.00053	33858	0.9839 ± 0.00068
EPITG	50297	0.8965 ± 0.00129	30427	0.8987 ± 0.00164
EPIMAXK	50297	1.0000	30427	1.0000
TGEDGE	50018	0.9945 ± 0.00033	30271	0.9949 ± 0.00041
DRP	49932	0.9983 ± 0.00019	30214	0.9981 ± 0.00025
CHI567	43649	0.8742 ± 0.00148	26432	0.8748 ± 0.00190
CHI5MAX	43648	1.0000 ± 0.00002	26431	1.0000 ± 0.00004
A_{TGkin}	0.71913 ± 0.001824		0.71982 ± 0.002344	

Table 5.19: TG kinematic acceptance using $K_{\pi 2}(1)$ monitor events.

5.4 Acceptance Factors from Monte Carlo Simulation

The acceptance of the online trigger, phase space, solid angle, and the acceptance loss due to π^+ decay-in-flight and π^+ nuclear interactions ("NIDIF") are calculated with $K^+ \rightarrow \pi^+ \nu \bar{\nu}$ Monte Carlo simulated events. About 10^5 signal events were generated with NIDIF on and another 10^5 with NIDIF off. The trigger acceptance ($A_{trigger}$) and the phase space acceptance (A_{ps}) are measured with the NIDIF-off sample. $A_{trigger}$ and A_{ps} are corrected for NIDIF by comparing with the NIDIF-on sample (A_{NIDIF}). The results are shown in Table 5.21, where UFATE, USTMED and USTOP_HEX are cuts based on UMC truth variables. UFATE requires that the π^+ stop without decaying or interacting; this is why it has no acceptance loss for the NIDIF-off case. USTMED requires that the π^+ stop in the RS scintillator, and USTOP_HEX requires that the offline reconstructed stopping-counter agrees with

	Loose Box	Tight Box
A_{utc}	0.94345 ± 0.000188	0.94345 ± 0.000188
$A_{opsveto}$	0.97422 ± 0.000631	0.97357 ± 0.000821
A_{TGkin}	0.71913 ± 0.001824	0.71982 ± 0.002344
$A_{K_{\pi 2}}$	0.6610±0.0017	0.6612±0.0022

Table 5.20: $K_{\pi 2}$ acceptance summary.

the real one. Note that LAYER14 has some phase-space-acceptance loss, due to the small but non-zero number of $\pi\nu\bar{\nu}(2)$ events that reach layer 14 of the RS. The setup cut is $ptot < 300$ MeV/c.

Cut	NIDIF$_{ON}$	NIDIF$_{OFF}$
	99999	100000
T•2	39227	41036
$3_{ct} \cdot 4_{ct} \cdot 5_{ct} \cdot 6_{ct}$	27575	33742
$\pi\nu\bar{\nu}(1)$ or (2)	26288	32914
$A_{trigger}$	0.2629±0.0014	0.3291±0.0015
Setup	25793	32887
UFATE	22688	32887
USTMED	22517	32620
USTOP_HEX	21743	32500
COS3D	20870	31294
LAYER14	20838	31282
ZFRF	20175	30083
ZUTOUT	20148	30063
PNN2BOX	9552	13334
A_{ps}^{loose}	0.3703±0.0030	0.4054±0.0027
TIGHTBOX	7758	10812
A_{ps}^{tight}	0.3008±0.0029	0.3288±0.0026

Table 5.21: Summary of the acceptances obtained from the Monte Carlo events. The errors are statistical. The integer values listed are the number of events remaining after the application of the cut in sequential order.

Using the numbers in Table 5.21,

$$
\begin{aligned}
A_{trigger} &= 0.3291 \pm 0.0015(stat.) \pm 0.0165(sys.) && (5.8)\\
A_{ps} &= 0.4054 \pm 0.0027(stat.) \pm 0.0203(sys.) && (5.9)
\end{aligned}
$$

$$
A_{NIDIF} = \frac{A_{trigger}(NIDIF_{ON})}{A_{trigger}(NIDIF_{OFF})} \times \frac{A_{ps}(NIDIF_{ON})}{A_{ps}(NIDIF_{OFF})} \quad (5.10)
$$

$$
\begin{aligned}
A_{NIDIF}^{loose} &= 0.7297 \pm 0.0092(stat.) \pm 0.0516(sys.) && (5.11)\\
A_{NIDIF}^{tight} &= 0.7308 \pm 0.010(stat.) \pm 0.0517(sys.) && (5.12)
\end{aligned}
$$

The 5% systematic error was due to the small discrepancies between the kinematic quantities of UMC and real events. Since the phase-space acceptance exclusively depends on the momentum, range and energy, these kinematic quantities of the UMC events are adjusted by comparing with those of the real data. The comparison for $K_{\pi 2}$ events is shown in Table 5.22. The values between data and UMC agree within error.

Quantity	Monte Carlo	Real Data
Momentum (MeV/c)	205.1	$204.94 \pm 0.02 \pm 0.02$
Range (cm)	30.4	$30.254 \pm 0.004 \pm 0.010$
Energy (MeV)	108.5	$108.77 \pm 0.01 \pm 0.01$
Momentum Resolution (MeV/c)	2.34	$2.29 \pm 0.01^{+0.0}_{-0.04}$
Range Resolution (cm)	1.02	$0.901 \pm 0.005 \pm 0.002$
Energy Resolution (MeV)	3.02	$3.03 \pm 0.02 \pm 0.02$

Table 5.22: Comparison of the $K_{\pi 2}$ kinematic quantities between Monte Carlo and real data.

Therefore,

$$
\begin{aligned}
A_{UMC} &= A_{trigger}^{NIDIF_{ON}} \times A_{ps}^{NIDIF_{ON}} \times A_{NIDIF} &(5.13)\\
A_{UMC}^{loose} &= 0.0974 \pm 0.0021(stat.) \pm 0.0097(sys.) &(5.14)\\
A_{UMC}^{tight} &= 0.0791 \pm 0.016(stat.) \pm 0.0079(sys.) &(5.15)
\end{aligned}
$$

5.5 T•2 Efficiency

The T•2 efficiency calculated in this section accounts for the acceptance loss due to the geometrical and counter inefficiencies of the T-counters, which cannot be measured with UMC. As seen in Fig. 2.21, the geometrical inefficiency is due to the track passing through an azimuthal gap between two adjacent T-counters. The counter inefficiency occurs if the scintillation light induced by the charged track is not detected by the PMTs. Therefore, the efficiency is shown in Eq. (5.16)

$$
\begin{aligned}
\epsilon_{T\bullet 2} &= 1 - \epsilon(geometrical) - \epsilon(counter)\\
&= 1 - \epsilon(geometrical) - e^{-kE} &(5.16)
\end{aligned}
$$

$\epsilon(geometrical) = 0.02855$ and $\epsilon(counter)$ represent the geometrical and counter inefficiencies respectively, k is the number of photoelectrons per MeV, and E is the mean energy deposit in the T-counters. The value for $\epsilon(geometrical)$ was calculated in [66], where k was also found to be 1.741 p.e./MeV for all sectors apart from two sectors that had hardware problems, for which k was 1.616 p.e./MeV. These values, that were calculated with $K_{\pi 2}$ events, will be used for the evaluation of $A_{T\bullet 2}$ in the PNN2 region, because π^+'s from $K_{\pi 2}$ decays are more similar to the $\pi\nu\bar{\nu}(2)$ signal than μ^+'s from $K_{\mu 2}$ decays.

Using the mean-energy deposit in the T-counters as a function of momentum $E_{dep}(p_\pi)$ and the momentum distribution $f(p_\pi)$ for Monte Carlo simulated $\pi\nu\bar{\nu}$ events in the PNN2 kinematic box, the inefficiency due to photostatistics is

$$\epsilon(counter) = \frac{\int dp_\pi f(p_\pi) e^{-kE_{dep}(p_\pi)}}{\int dp_\pi f(p_\pi)} = 0.02095 \tag{5.17}$$

which is a weighted average of the values in the good and bad sectors. Then the T•2 efficiency for $\pi\nu\bar{\nu}(2)$ is calculated with Eq. (5.16):

$$\epsilon_{T\bullet 2} = 0.9505 \pm 0.0012(stat.) \pm 0.0143(sys.) \tag{5.18}$$

where the 1.5% systematic uncertainty accounts for constraining the z position of the charged track to be in the middle of the T-counters for the study done in [66]. In order to ensure that the track passed through the T-counters, the charged track extrapolated by the UTC was required to have z position within ±20 cm from the middle of the T-counters (z Fiducial Cut). This fiducial requirement increases the T•2 efficiency because events with the track pointing at the z-edge of the T-counters are removed.

5.6 K$^+$-Stopping Efficiency

The acceptances of the $K_{\pi 2}$ selection cuts used in the calculation of the K$^+$-stopping efficiency are measured with $K_{\pi 2}$ events in the real and Monte Carlo data. The acceptances measured using the Monte Carlo $K_{\pi 2}$ events are tabulated in Table 5.23 and Table 5.24. The acceptances of the trigger ($A_{trigger}$), the polar angle cut ($A_{polar\ angle}$), and the range requirement (A_{range}) are taken from the Monte Carlo acceptance measurement.

The other acceptances ($A_{bad\ run}$, A_{recon}, $A_{beam\&target}$ and $A_{photon\ veto}$) are measured with the $K_{\pi 2}$ monitor trigger data, as tabulated in Table 5.25. In this measurement, the same cuts as used to measure the acceptance factors from $K_{\pi 2}$ ($A_{K_{\mu 2}}$) are adopted. By using the same cuts, the uncertainty in the $A_{K_{\mu 2}}$ is canceled when the K$^+$-stopping efficiency is multiplied by the $A_{K_{\mu 2}}$ to get the total acceptance.

Cut	# Events	Acceptance
Setup	50000	-
T$\bullet$2	22721	0.45442
$17_{ct} + 18_{ct} + 19_{ct}$	22077	0.97166
$A_{trigger}$(UMC)	0.44154±0.00222	
UTC/RANGE	22064	0.99941
UTC_QUAL	20427	0.92581
TARGET	20389	0.99814
A_{recon}(UMC)	0.92354±0.00179	
COS3D	20116	0.98661
$A_{polar\ angle}$(UMC)	0.98661±0.00080	
$R > 40$ cm	19869	0.98772
A_{range}(UMC)	0.98772±0.00078	
$A_{K_{\mu 2}}$(UMC)	**0.3974±0.0022**	

Table 5.23: Acceptance factors for the K$^+$-stopping efficiency calculation, obtained from the Monte Carlo $K_{\pi 2}$ events. The symbolic names of the cuts in the table are described in Section 3.3. The errors are statistical.

Cut	# Events	Acceptance
Setup for A_{RD}	648394	
RD_TRK	648394	1.00000
TRKTIM	648347	0.99993
A_{RD}	0.99993±0.00001	
Setup for A_{UTCTG}	487336	
UTC/RANGE	487336	1.00000
UTC_QUAL	410597	0.84253
TARGET	408821	0.99567
A_{UTCTG}	0.83889±0.00053	
A_{recon}	**0.83883±0.00053**	

Table 5.24: Acceptance factors for the K$^+$-stopping efficiency calculation, obtained from the $K_{\pi 2}$-monitor data. The errors are statistical.

Cut	# Events	Acceptance
$Setup_{fs\ beam}$	600807	
ICBIT	600807	1.00000
TIC	599650	0.99807
TIMCON	597618	0.99661
TGTCON	593163	0.99255
DCBIT	523290	0.88220
DELCO	452473	0.86467
CKTRS	444871	0.98320
CKTAIL	433702	0.99940
B4DEDX	426932	0.98439
CPITRS	424939	0.99533
CPITAIL	424685	0.99940
TARGF	406779	0.95784
DTGTTP	406704	0.99982
RTDIF	402318	0.98922
TGQUALT	402318	1.00000
PIGAP	398978	0.99170
TGB4	376730	0.94424
KIC	371264	0.98549
TGGEO	366882	0.98820
B4EKZ	355998	0.97033
B4ETCON	354089	0.99464
TGZFOOL	354089	1.00000
BWTRS	341320	0.96394
U/RPVTRS	335566	0.98314
$A_{beam\&target}$	0.55853±0.00064	
Setup for $A_{photon\ veto}$	361027	-
PV w/o BV	335566	0.92948
$A_{photon\ veto}$	0.92948±0.00043	
Setup for $A_{bad\ run}$	1010411	-
BAD_RUN	1009954	0.99955
BAD_STC	1009805	0.99985
TRIGGER	1009805	1.00000
$A_{bad\ run}$	0.99940±0.00002	
$A_{K_{\mu 2}}$	**0.4352±0.0006**	

Table 5.25: Acceptance factors for the K$^+$-stopping efficiency calculation, obtained from the $K_{\pi 2}$ monitor trigger data. The errors are statistical.

5.7 Confirmation of the $K_{\pi 2}$ Branching Ratio

The acceptances of the $K_{\pi 2}$ selection cuts used in the calculation of the $K_{\pi 2}$ branching ratio are measured with both the $K_{\pi 2}$-monitor data and the $K_{\pi 2}$ data generated by the Monte Carlo simulation. The acceptances of the trigger ($A_{trigger}$), the phase-space cut ($A_{phase\ space}$), the polar angle cut ($A_{polar\ angle}$), and the stopping layer cut ($A_{stopping\ layer}$) are taken from the Monte Carlo acceptance measurement, as tabulated in Table 5.26. The other acceptances (A_{recon}, $A_{beam\&target}$, $A_{bad\ run}$ and $A_{\pi \to \mu \to e}$) are obtained from the measurement with the $K_{\pi 2}$-trigger data, as tabulated in Table 5.27-Table 5.28 and summarized in Table 5.29.

$$\mathcal{B}(K_{\pi 2}) \quad = \quad \frac{N_{K_{\pi 2}}}{\epsilon T \bullet 2 \cdot IC(K_{\pi 2}) \cdot (KB_{live})_{K_{\pi 2}} \cdot A_{K_{\pi 2},Br} \cdot A^{UMC}_{K_{\pi 2},kin} \cdot f_S \cdot A^{UMC}_{K_{\pi 2},trig}} \tag{5.19}$$

where

$$A_{K_{\pi 2},Br} = A_{RD,Br} \times A_{RECO,Br} \times A_{REST,Br} \times A_{IPIFLG} \times A^{acc}_{\mu} \tag{5.20}$$

Cut	# Events	Acceptance
Setup	49997	-
T•2	22697	0.45397
$6_{ct} + 7_{ct}$	19090	0.84108
$\overline{19_{ct}}$	18797	0.98465
UFATE	15910	0.84641
USTMED	15568	0.97850
USTOP_HEX	13909	0.89344
$A_{trigger}$(UMC)	0.2782±0.0020	
UTC/RANGE	13909	1.00000
UTC_QUAL	12660	0.91020
TARGET	12532	0.98989
A_{recon}(UMC)	0.9010±0.0025	
Stopping Layer	12072	0.96329
$A_{stopping\ layer}$(UMC)	0.96329±0.00168	
COS3D	11878	0.98393
$A_{polar\ angle}$(UMC)	0.98393±0.00114	
Phase Space	10840	0.91261
$A_{phase\ space}$(UMC)	0.91261±0.00259	
$A_{K_{\pi2}}$	**0.2168±0.0018**	

Table 5.26: Acceptance factors for the $K_{\pi2}$ branching-ratio calculation, obtained from the Monte Carlo $K_{\pi2}$ events. The errors are statistical.

Cut	# Events	Acceptance
Setup for $A_{bad\ run}$	84793	-
BAD_RUN	84752	0.99952
BAD_STC	84338	0.99512
TRIGGER	84338	1.00000
$A_{bad\ run}$	0.99463±0.00025	
Setup for A_{RD}	51416	-
RD_TRK	51416	1.00000
TRKTIM	51416	1.00000
A_{RD}	1.00000±0.00000	
Setup for A_{UTCTG}	32980	-
UTC/RANGE	32980	1.00000
UTC_QUAL	28117	0.85255
TARGET	27831	0.98983
A_{UTCTG}	0.84388±0.00200	
A_{recon}	**0.84388±0.00200**	

Table 5.27: Reconstruction acceptance factors for the $K_{\pi 2}$ branching-ratio calculation, obtained from the $K_{\pi 2}$ monitor trigger data. The errors are statistical.

Cut	# Events	Acceptance
Setup for $A_{beam\&target}$	32055	-
ICBIT	32055	1.00000
TIC	32055	1.00000
TIMCON	31970	0.99735
TGTCON	31847	0.99615
DCBIT	31542	0.99042
DELCO	27898	0.88447
CKTRS	24368	0.87347
CKTAIL	23710	0.97300
B4DEDX	23032	0.97140
CPITRS	22657	0.98372
CPITAIL	22442	0.99051
TARGF	22431	0.99951
DTGTTP	21467	0.95702
RTDIF	21462	0.99977
TGQUALT	21277	0.99138
PIGAP	21277	1.00000
TGB4	21098	0.99916
KIC	20002	0.94805
TGGEO	19855	0.99265
B4EKZ	16358	0.82387
B4ETCON	15886	0.97115
TGZFOOL	15806	0.99496
BWTRS	15806	1.00000
U/RPVTRS	15096	0.95508
$A_{beam\&target}$	**0.46224±0.00278**	

Table 5.28: Beam and TG acceptance factors for the $K_{\pi 2}$ branching-ratio calculation, obtained from the $K_{\pi 2}$ monitor trigger data. The errors are statistical.

$A_{bad\ run}$	0.99463±0.00025
A_{recon}	0.84388±0.00200
$A_{beam\&target}$	0.46224±0.00278
$A_{\pi\to\mu\to e}$	0.83498±0.00542
$A_{K_{\pi 2}}$	**0.3240±0.0029**

Table 5.29: Summary of acceptance factors for the $K_{\pi 2}$ branching ratio calculation, obtained from the $K_{\pi 2}$ monitor trigger data. See Tables 5.27-5.28. The errors are statistical.

5.8 Total Acceptance

The total acceptance is summarized in Table 5.30.

	Loose Box	Tight Box
$A_{K_{\mu 2}}$	0.0718 ± 0.0044	0.0348 ± 0.0074
$A_{\pi_{scat}}$	$0.3980 \pm 0.0014(\text{stat.}) \pm 0.014(\text{sys.})$	$0.3297 \pm 0.0020(\text{stat.})^{+0.011}_{-0.013}(\text{sys.})$
$A_{K_{\pi 2}}$	0.6610 ± 0.0017	0.6612 ± 0.0022
A_{UMC}	$0.0974 \pm 0.0021(stat.) \pm 0.0097(sys.)$	$0.0791 \pm 0.016(stat.) \pm 0.0079(sys.)$
A_{tot}	$\mathbf{(1.840 \pm 0.120 \pm 0.194) \times 10^{-3}}$	$\mathbf{(0.600 \pm 0.176 \pm 0.0600) \times 10^{-3}}$

Table 5.30: Total acceptance for PNN2.

5.9 Single-Event Sensitivity

The total acceptance for the $\pi\nu\bar{\nu}(2)$ study and the rest of the factors used to calculate the Single-Event Sensitivity

$$S.E.S. = A_{tot} \times \epsilon_{T\bullet 2} \times f_s \times KB_{live} \tag{5.21}$$

are summarized in Table 5.31. A_{tot} is the total acceptance of the online and offline cuts, $\epsilon_{T\bullet 2}$ is the $T \bullet 2$ efficiency, f_s is the fraction of K$^+$'s stopping in the Target and KB_{live} the total number of K$^+$ decays in the detector during the data taking.

In the absence of background, the (S.E.S.)$^{-1}$ is the lowest branching ratio that could be measured by this analysis, which is at the same level with the one in E787's $\pi\nu\bar{\nu}(2)$ analysis ($(S.E.S._{E787})^{-1} = 0.687 \times 10^{-9}$, combined for the 1996 and 1997 data sets).

	Loose Box	Tight Box
A_{tot}	$(1.840 \pm 0.120 \pm 0.194) \times 10^{-3}$	$(0.600 \pm 0.176 \pm 0.0600) \times 10^{-3}$
$\epsilon_{T\bullet 2}$	$0.9505 \pm 0.0012(stat.) \pm 0.0143(sys.)$	
f_s	0.7740 ± 0.0011	
KB_{live}	1.77×10^{12}	
$(S.E.S.)^{-1}$	$\mathbf{0.417 \times 10^{-9}}$	$\mathbf{1.28 \times 10^{-9}}$

Table 5.31: The PNN2 single-event sensitivity.

Chapter 6

Conclusion

The study of the 1/3 sample has been completed. The photon and target reconstruction cuts have been tightened and optimized, in order to suppress the major $K_{\pi2}$ target-scatter background, which has been reduced by a factor of two, compared to E787-PNN2. As a result, the total expected background level has been shown to be $1.069 \pm 0.222^{+0.31}_{-0.26}$ events, less than was measured in E787 1.216 ± 0.239 events [63]. Therefore, the upgrade of the E787-era photon-veto system performed as expected with improved detection efficiency.

The beam background was reduced by a factor of two compared to E787-PNN2, such that current beam backgrounds are consistent with PNN1, after phase-space considerations. E949-PNN2 also implemented a new method of incorporating trigger data into the charge-exchange background, where previously this measurement relied solely on Monte Carlo events. E949-PNN2 also devised a tighter signal region which is much cleaner and will provide better determination of the BR through a likelihood analysis.

This analysis improved the signal acceptance of cuts to a value of $(1.50 \pm 0.05) \times 10^{-3}$, compared to E787-PNN2 ($(1.323 \pm 0.135) \times 10^{-3}$), while also reducing the background in a high-rate environment (double E787 intensity).

Appendices

Appendix A

K^+ Beam

The K^+ beam is produced by a high-intensity proton beam from the Alternating Gradient Synchrotron (AGS) at BNL. A schematic view of the AGS accelerator complex is shown in Fig. A.1.

Protons are accelerated to a momentum of 21.5 GeV/c. 65×10^{12} protons are extracted in a 2.2-second long "spill" once every 5.4 seconds from the AGS. The slow-extracted beam is transported to the K^+ production target for E949. The platinum production target extends 6 cm in the beam direction, and is located on a water-cooled copper base. Under typical AGS running conditions, 65 Tp hit the production target every 2.2 seconds spill at 21.5 GeV/c.

As shown in Fig. A.2, the Low-Energy Separated Beam-Line III (LESBIII) [37] collects and focuses K^+'s produced at the production target. The beam emitted toward 0° contains about 500 π^+'s and 500 protons for every K^+, and is momentum-selected by a dipole magnet (D1 in Fig. A.2). Two electrostatic separators (Separators 1 and 2 in Fig. A.2) sweep π^+'s and protons out of the beam. The resulting beam is further selected by a second dipole magnet (D2 in Fig. A.2). LESBIII contains a number of focusing quadrupole (Q1-10), sextupole (S1-3), and octupole (O1) magnets and collimating slits, and has a total length of 19.6 m from the production

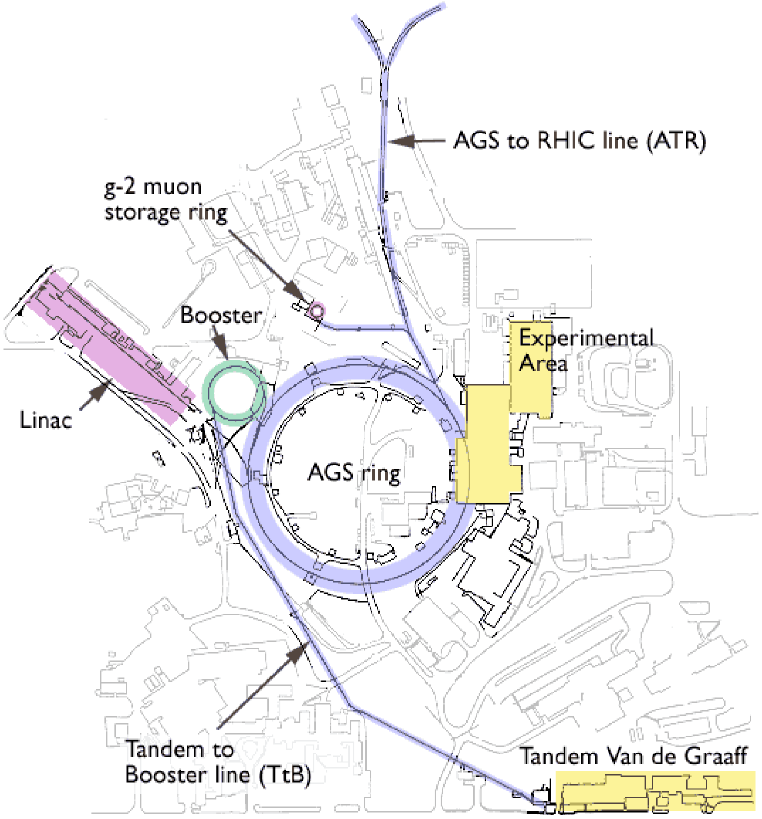

Figure A.1: Schematic view of the AGS complex, which consists of a 200 MeV LINAC, a booster and a synchrotron. The secondary beam lines are located in the experimental area.

target to the E949 target. The resulting K$^+$'s with 710 MeV/c momentum were transported down this beamline.

The angular acceptance of LESBIII is 12 msr and the momentum acceptance is 4.5% FWHM. LESBIII provides the world's highest-intensity K$^+$ beam of 710 MeV/c with a flux of about 5×10^5 K$^+$'s per Tp on the production target. The K$^+$:π^+ ratio in the beam is about 3:1. Proton contamination is negligible due to a large deflection of protons by the separators. Under the typical AGS running condition of 65 Tp (maximum of 76.4 Tp) on the production target per spill, 1.3×10^7 K$^+$'s emerge from LESBIII.

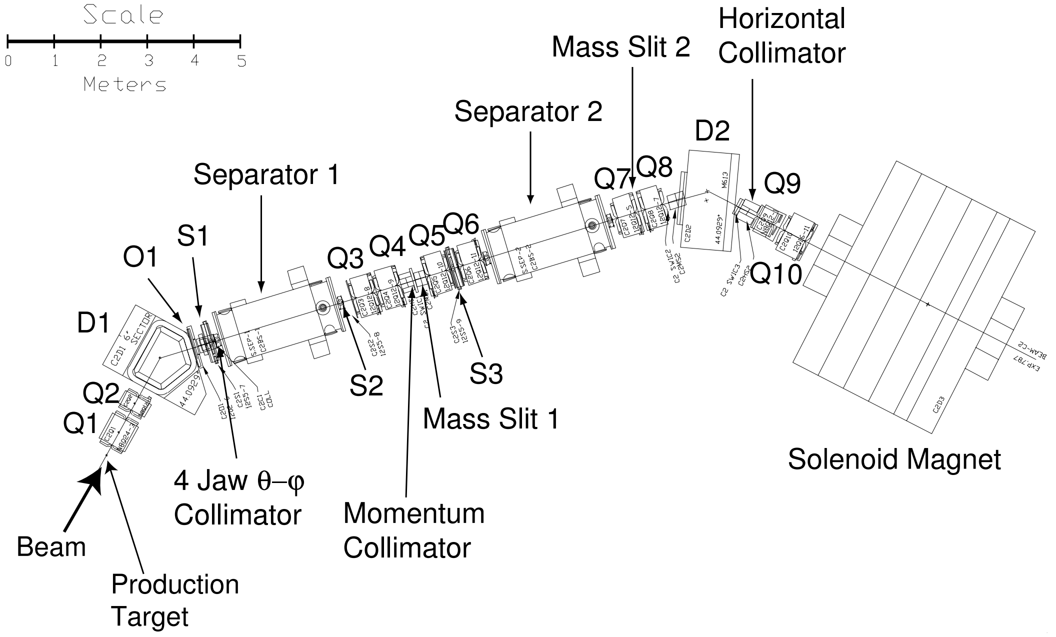

Figure A.2: Low-Energy Separated Beam-Line III at BNL

Appendix B

Target Reconstruction Algorithms

B.1 *swathccd*

swathccd is the aptly named TG reconstruction algorithm due to the dependence on identifying hits along the UTC extrapolated track. The algorithm follows the following basic design:

- External inputs are

  TG fiber geometry,

  List of hits with energy, time, and fiber number,

  Incoming K^+ position (as determined by the B4),

  External track trajectory (determined by UTC and RS), and

  Outgoing charged-track time (t_{RS}).

- Sort hits using timing and information as listed in Table B.1

- Hits are clustered together based upon geometry information.

Hit Catagory	Energy (MeV)	Time (ns)
Kaon	> 4.0	$-8.0 \leq t \leq 8.0$
KaonLate	> 4.0	$8.0 \leq t \leq 50.0$
Pion	$0.1 < E < 10.0$	$\mid t - t_{RS} \mid \leq 8.0$
Gamma	> 0.1	$-999. \leq t \leq 75.0$

Table B.1: Candidate hit list. Candidate hits are not joined by geometry, only by energy and time.

K^+ fibers are grouped together in the manner demonstrated in 'Cluster 1' of Fig. B.1.

π^+ hits uses a swath about the UTC track, Fig. B.2. The width of the swath varies to aid in π^+-fiber identification where the UTC track is not ideal.

- Geometrical matching of K^+ and π^+ clusters (determine if a K^+ cluster and π^+ cluster are adjacent in the x-y plane).

- The K^+/π^+-matched cluster are subjected to additional constrains.

  The chosen π^+'s must satisfy a likelihood value based upon energy, time, and distance from the UTC track. π^+ hits not meeting the standard were assigned to the 'Gamma' list.

  Determine if K^+ and π^+ hits were assigned to the incorrect group. This was done by looking at K^+ fibers not in-time with the remaining K^+ cluster.

- Mending of 'Gamma' hits into the K^+ and π^+ cluster, see Fig. B.1.

  π^+ mended hits must pass the π^+-likelihood function.

  Coincident low-energy 'Gamma' hits were mended if adjacent to the current K^+ cluster.

- "Opposite-side Pions" were hits in TG fibers which appear to be π^+'s (passed the π^+-likelihood function), but were located on the opposite side of the decay

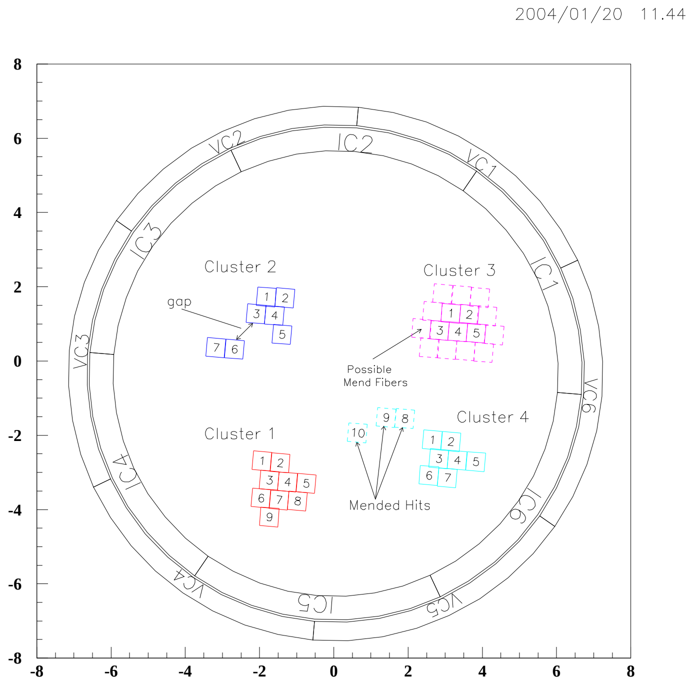

Figure B.1: Cluster 1 is a cluster with no gaps. Cluster 2 is a cluster with gaps. Cluster 3 shows the fibers that *swathccd* and *TGrecon* are allowed to mend. Cluster 4 shows how mending could occur if gaps are allowed in the mending process

vertex (K^+ fibers) with respect to the out-going track. These hits were possibility due to tracks from decays with multiple charged-track products or a converting in the TG.

- Hits not classified as kaon, pion, or opposite-side pions were considered possible photon hits. The time windows in the TG PV cut, determined by the PV optimization (see Appendix G), ultimately decided if a hit in this category would be consider resulting from a photon.

- *swathccd* determined TG reconstructed information is calculated, such as:

  K^+ decay-vertex position (*tgx*, *tgy*, *tgz*)

  The position of the track exit from the TG

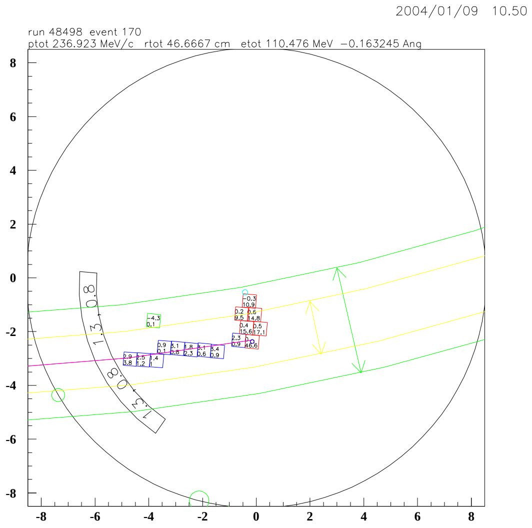

Figure B.2: The large green arrow is the size of a 2.0 cm swath. The smaller yellow arrow points to a typical sized swath of 1.0 cm. Note that the π^+'s are easily contained with the 1.0 cm swath

t_π was the energy weighted average time of the pion fibers. If the standard deviation of t_π is greater than 2.0 ns, then t_π was instead determined by the IC time.

This reconstruction process was done as much as three times per event. There was interplay of the B4 reconstruction algorithm with *swathccd*, in such a way that *swathccd* would construct the event with no B4 information and determine the expected K^+ position. B4 would then use *swathccd*'s position information as input. After B4 information was reconstructed, *swathccd* was called again with a likely B4 value. This allowed for overall improvement in reconstruction efficiency by gradually building upon known information.

B.1.1 Omitted Information

Edge fibers were omitted during reconstruction. This was due to edge fibers being highly multiplexed and lack of precise geometry calibration. The resulting gain from incorporating edge fibers was expected to be small compared to the programing and calibration effort needed to extract those gains.

B.2 *TGrecon*

TGrecon is a TG reconstruction algorithm which removes the dependence on the UTC track to identify the outgoing charged track; the UTC track was only used in the final stages of *TGrecon* (*swathccd* utilized the UTC to select the initial set of π^+'s). The original purpose of *TGrecon* was to successfully construct x-y TG scatters; a sample of x-y TG scatters was important in creating a independent sample for PNN2 photon-veto optimization. z scatters in the TG are difficult to tag, except with CCDPUL and B4DEDX. Further information regarding *TGrecon* and the companion algorithm, *KinkFinder*, was detailed in [71]. The overall design of *TGrecon* was identical to *swathccd*, however, the implementation allowed for greater flexibility in determining how to determine a π^+ fiber from a K$^+$ fiber.

TGrecon was not employed by E949 for signal analysis. Events reconstructed by *TGrecon* were utilized only by the $K_{\pi 2}$-scatter background study, see Section 4.1. *swathccd* was found more than sufficient in reconstructing non-pathological events. However, it is worthy to note that *TGrecon* would be capable, with the correct implementation, of reconstructing multitrack decays and double-beam events, if future analysis requires such tools.

B.3 *KinkFinder* Algorithm Structure

The algorithm *KinkFinder* was created to find charged tracks that scatter in the TG. Since the π^+ is primarily the charged particle that will scatter in the Target, any references to the π^+ track implies the charged decay product of the K^+ which cause the T•2 trigger. *KinkFinder* was made to be independent of *swathccd* and *TGrecon*. *KinkFinder*'s ability to find a kink in the track, i.e. x-y scatter, first assumes a good fit from the UTC. That is, *KinkFinder* looks for a deviation from the expected track and uses the UTC track as the baseline to check for a deviation in the match between the TG-track and UTC-track.

B.3.1 Inputs

KinkFinder uses a list of TG fibers (presumably reconstructed by *TGrecon*), the UTC track parameters, and the reconstructed K^+ decay vertex to determine if an event should be tagged as a 'kink.' Note that only geometry information is used by *KinkFinder*; time and energy of the TG fiber hits are not considered.

B.3.2 Defining Kinked Fibers

As seen in Fig. B.3, kinked fibers are the fibers that occur after the π^+ has scattered. As such, *nonkinked* fibers are the pion fibers from the decay vertex to the scattered point. The fiber in which the scatter occurs is initially defined as part of the kinked fibers since the fiber should lie on the UTC track. The *KinkFinder* algorithm determines the kinked fibers as the fibers that are within a swath of the UTC track; The swath-width used was 0.8 cm.

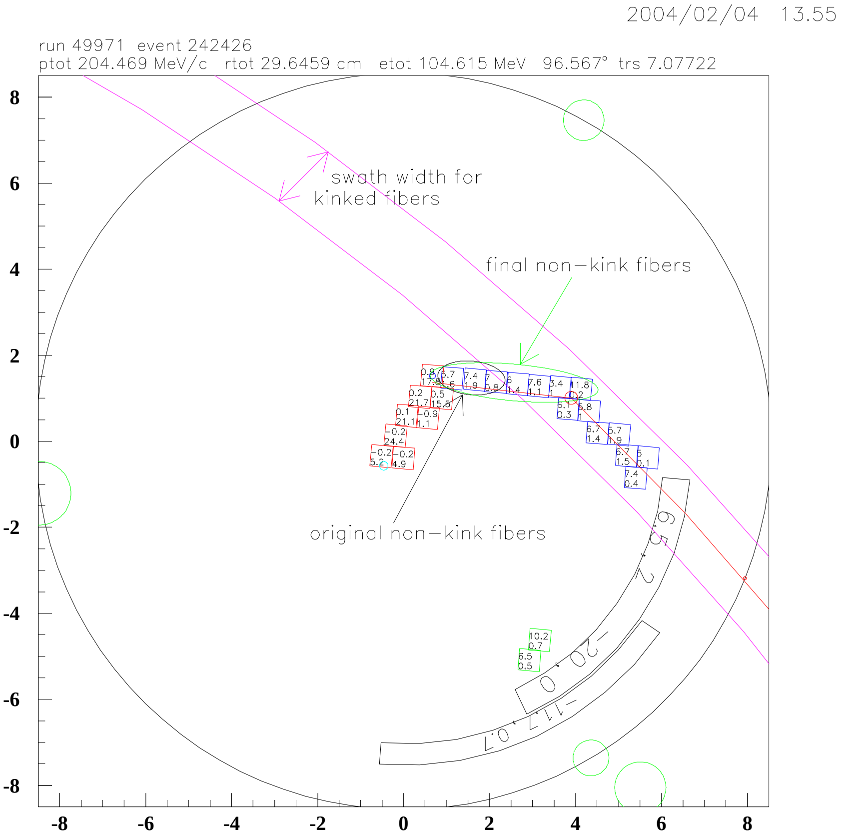

Figure B.3: *KinkFinder* Technique. Blue fiber (fibers with ∼ 7 ns (top number)) are the initial list of TG-fibers given to *KinkFinder* to consider.

B.3.3 Minimum Criteria

To remove possible false positives (identified as a scattered event by the algorithm, but is in fact a non-scattered event), criteria were placed on the suitability of the event as a kink; these criteria are:

(1) There must be at least one fiber near the exit point of the Target.

(2) There must be at least 2 *nonkinked* fibers.

B.3.4 Minimum Track-Deviation

Track deviation was calculated based upon (1) the distance of the arc length along the UTC track to the *nonkinked* fiber, and (2) the distance of closest approach from the *nonkinked* fiber to the UTC track. A least-squares fit was performed using the determined (1) and (2) values for each *nonkinked* fibers. To be considered a kink the slope of the least-squares fit must be ≥ 0.1.

B.3.5 Determining the Nonkinked Trajectory

Only the identified *nonkinked* hits are sent into a modified version of *Target Fitter*, see Section E. The determined track circle (*radius and center point*) from *Target Fitter* was further utilized by *KinkFinder* to give better results by iteration. After *Target Fitter* returns parameters for a track, the fitted track determines if other hits exist which lie within a swath around the fitted track. Additional hit-fibers are added one at a time and must be within one fiber distance of the previous *nonkinked* section of the track. With the newly added hit included *Target Fitter* was applied again. This process was repeated three times. A fiber is added one at a time to construct the *nonkinked* portion of the track in a predictable and precise way. The three added fiber limit is to prevent the nonkink track “absorbing” all the kinked hits in a small-angle-scatter situation. In small-angle scatters, *KinkFinder* will be less efficient in determining the *nonkinked* from the *kinked* fibers, see [62].

Appendix C

Data Acquisition, Storage, and Processing

C.1 Data Acquisition

Signals from the various detector systems, including analog and discriminated signals, were converted to digital signals by analog-to-digital converter (ADC), time-to-digital converter (TDC), transient digitizer (TD) and charged-couple device (CCD) systems; a summary is in Table C.1. The TD and CCD systems were E949 custom built. Data from a triggered event would be digitized and stored to a buffer at the local crate. After each spill, the buffered data would be sent to the DAQ computer.

For the Fastbus systems, SLAC Scanner Processor (SSP) modules [67, 68] served as crate controllers and to read out, reformat, and buffer the data from the front-end after each trigger accepted. The CAMAC ADCs were read out by the FERA bus by a Struck 370 QDP DSP (Fastbus) module. The CAMAC TDCs were read out by custom-built DYC3 modules [69] which pushed the data into VME memory boards. The readout time per event (as determined by the slowest crate) was typically 850 μs.

Type	Model	Standard	Resolution	Subsystems
ADC	LRS 4300B	CAMAC	10 bits	RS,BV,BVL,EC,Beam
	LRS 1881	Fastbus	13 bits	TG,UTC
TDC	LRS 3377	CAMAC	0.5 ns	RS, BVL
	LRS 1879	Fastbus	2 ns	UTC,BV,TG
	LRS 1876	Fastbus	1 ns	EC,RSSC,Beam
WFD	TD	Fastbus	500 MHz sampling 8 bits, 10 μs depth	RS,BVL,IC
	CCD	Fastbus	500 MHz sampling 8 bits, 256 ns depth	Beam,TG,EC

Table C.1: Digitizing electronics for E949. Waveform digitizers (WFD) were custom built, hence, no model numbers.

At the end of each spill, the data from the Fastbus buffer memories were read out via the cable segment (12-15 MB/sec) by Struck 340 SFI modules, each controlled by a MVME 2604 single-board computer (SBC) running VxWorks. The VME memory boards were read out by a separate SBC. Data were transferred from the SBCs to the DAQ computer (SGI Origin 200, designated *bnlku*9) via Ethernet. Event fragments from the readout segments were combined by Event Builder processes running on the DAQ computer. The $K^+ \to \pi^+\nu\bar{\nu}$ triggers, $\pi\nu\bar{\nu}(1)$ and $\pi\nu\bar{\nu}(2)$, were written via two DLT-7000 drives at 5 MB/sec per drive to 35 GB DLT tapes, such that the storage to each tape alternated between spills; a third DLT drive was employed to store monitor triggers.

MIDAS [70], a control system, ran independently on a Linux workstation and was used to monitor a variety of experiment conditions, including crate voltages and temperatures.

Under typical running conditions, ~300 events per spill were stored to tape with a typical event size of ~80 kB. This was well within the maximum throughput of the system of about 50 MB/spill. The DAQ dead time was due entirely to the speed of the event-by-event readout of the front-end electronics at the crate level. The total dead time introduced by the trigger and DAQ was typically 26%.

C.2 PASS-0

After the 7 Tera-bytes of data collection had ended, an initial step to easily manage the monitor triggers was done ("PASS-0"). The trigger types were staged, sorted, and placed onto new DLT tapes (i.e. all $K_{\mu 2}(1)$ monitors were stored together on a set of 22 DLTs, $K_{\pi 2}(1)$ monitors were stored onto separate set of nine $K_{\pi 2}(1)$-only DLTs, and so on.). This PASS-0 processing allowed analyzers as-needed processing of individual monitor trigger samples.

C.3 Processing

The various monitor triggers, $\pi\nu\bar{\nu}(1)$ and $\pi\nu\bar{\nu}(2)$ were analyzed (monitors and signal were done separately). "Unpacking" and reconstruction code took the raw digitized information and determined the physics within each event via E949 Fortran routines. Data processing steps are as follows:

(1) Stage raw data from tape onto hard-drive disks.

(2) Utilizing a cluster of ~ 25 linux-based computers located at TRIUMF the data was unpacked and reconstructed.

  - If processing signal triggers, selective skimming of events would occur, see Section 3.3.3,.

(3) Output files from step (2) were PAW ntuples containing event information, such as momentum of the charged track, for later analysis.

(4) Analysis of the ntuples employed the use of PAW comis functions and PAW kumacs which would read in the ntpules and applied the desired cuts to the events. These functions would store information, such as if the event passed a selection cut, in histograms.

- The cut functions were written in comis-style Fortran so that for a given event a value of 1. or 0. would be returned (passed or failed).

- Cut functions were "checked out" from a standardize cut-function repository, so that analysis could proceed in parallel by multiple analyzers.

Appendix D

Calibration of TGDEDX

D.1 Cut Description

$\frac{dE}{dX}$ (in scintillator) of π^+'s in the PNN2 momentum region, 140 MeV/c $\leq P_{\pi^+} \leq$ 195 MeV/c, changes from 3.08 MeV/cm to 2.47 MeV/cm. Therefore, any cut based upon $\frac{dE}{dX}$ which does not account for the momentum dependence of the outgoing π^+ within the Target will wastefully lose acceptance.

TGDEDX, see Section 3.3, calculates the likelihood that the charged track in the TG was due to a π^+. The $\frac{dE}{dX}$-likelihood ($like_{tgdedx}$), Eq. (D.1), was determined using the measured momentum (*ptot*), target range (*rtg*), target energy, (*etg*[1]), and expected *rtg* (rtg_{exp}) based upon the observed *ptot* and *etg*.

$$like_{tgdedx} = \frac{1}{2} \cdot \left(1 + erf\left(\frac{rtg - rtg_{exp}(etg, ptot)}{\sigma_{exp}(etg, ptot)}\right)\right) \tag{D.1}$$

Over small bands in momentum $\frac{dE}{dX}_{\pi^+}$ will only change slightly. With this assumption, *ptot* was quantized in five momentum "bins" (< 170 MeV/c, 170 − 180,

---

[1] As will be discussed shortly, this was not always the nominal *etg*.

180 – 188, 188 – 199.53, > 199.53) and *etg* was quantized into 15 bins (0 – 2 MeV, 2 – 4,. . . , 26 – 28). The value of the 15^{th} bin was defined equal to the value of the 14^{th} bin; effectively cutting very large energy deposits in the TG, since TGDEDX uses extrapolation of adjacent values to extract the expected *rtg* value for a given *etg* and *ptot*.

Events were cut by TGDEDX if $like_{tgdedx} < 0.05$ (setting the 0.05 threshold value is discussed later). That is, TGDEDX cut events when the measured target range was much smaller than the expected target range of a signal π^+.

D.2 Modifications

In E787-PNN2, *swathccd* does not allow π^+ hits to occur in K^+ flagged fibers; this was allowed in E949 when $t_\pi - t_K > 15$ ns. These K^+/π^+ fibers do not occur in π_{scat} samples, due to the large delayed-coincidence requirement. Since the π_{scat} sample was chosen to calibrate TGDEDX, due to the large π^+-momentum spectrum in π_{scat}'s, TGDEDX was modified to use a corrected *etg* which excluded π^+ energy from a K^+ flagged fiber (this was a local change to *etg*, specific for this cut only). No *rtg* modification was needed, since the decay vertex is not effected in comparing a signal sample to a π_{scat} sample, in this regard. Hence, all references to *etg* in Appendix D refers to the "corrected" π^+ TG energy.

D.3 Calibration

The expected target range, rtg_{exp} requires precise calibration to maximize the efficiency of TGDEDX. A fit of the *rtg* distribution for each *ptot*-*etg* bin (i.e. *ptot*-*etg* spectrum-slice) yielded a mean (rtg_{exp}) and sigma (σ_{exp}) which was utilized by Eq. (D.1). The calibration process used $\pi_{scatter}$ monitors in the π^+-band region (see

Fig. 3.3). The cuts used to determine the final calibration sample are shown in Table D.1. This sample is created by applying cuts which will yield events with only one well reconstructed π^+ track.

$Kpiang > \theta$ selects events which undergo a scatter in the x-y plane; the angle, θ, was determined by the following points: (1) K^+-entering position, (2) "decay vertex" (i.e. scattering vertex), and (3) the position where the π^+ left the TG. The angle θ was set at 35° and 55° in an attempt to construct a clean calibration sample. A π_{scat} event's reconstructed decay vertex would be close to the scattering vertex, but the lack of a delayed coincidence makes the reconstruction process fraught with peril. However, $\pi_{scatter}$ events with a large θ have improved decay-vertex determination by the TG-reconstruction algorithm due to geometrical information available in x-y scattered events (a precise decay-vertex measurement was the key determination to reliable target range). A further sample was created by applying the tighter (30% acceptance) PV cut; to avoid bias the TG photon-veto was excluded. Ultimately these (ideally) better samples contained insufficient statistics for proper calibration. However, studies were performed employing these improved samples to validate the use of the high-statistics sample used to determine all $(2 \times 5 \times 15)$ rtg_{exp} and σ_{exp} parameters. The parameter values are plotted in Figures D.1-D.3.

Cut name	Events remaining (Acc)
BADRUN	5859925 (-)
RDTRK TRKTIM	5856748 (-)
TARGET STLAY	4949979 (-)
UTC PDC RDUTM	2833580 (-)
ICbit,*b4abm2* < 1.3 MeV	1986916 (-)
$\vert t_\pi - t_{RS}\vert \geq 5$	1881543 (-)
$\vert ictime - t_{RS}\vert \geq 5$	1847951 (-)
TGCUT BADSTC	1508139 (-)
tgqualt,*npitg*	1435572 (0.951883)
timcon	1430524 (0.996484)
tgtcon	1390018 (0.971685)
b4etcon	1360826 (0.978999)
targf	1278186 (0.939272)
dtgttp	1278117 (0.999946)
rtdif	1181683 (0.92455)
eiccon	1149627 (0.972873)
ticcon	1149616 (0.99999)
pigap	1034138 (0.899551)
tgdb4	886404 (0.857143)
tgdb4tip	561715 (0.633701)
tgdvxtip	466019 (0.829636)
tgdvxpi	427166 (0.916628)
phivtx1	315481 (0.738544)
pv(*not tg*) 60%	87063 (0.275969)
cos3d	76823 (0.882384)
utcqual	72564 (0.944561)
rngmom	65767 (0.906331)
rsdedxmax,*rsdedxcl*	41896 (0.637037)
rslike	41429 (0.988853)
$tgz > -10.$	41244 (0.995535)
Final E949 calibration used this sample.	
The following are cleaner "decay vertex" samples	
$Kpiang > 35°$	23662 (0.573708)
$Kpiang > 55°$	**14323** (0.605317)

Table D.1: Generated $\pi_{scatter}$ sample for TGDEDX calibration. Numbers in parenthesis are acceptances of that cut.

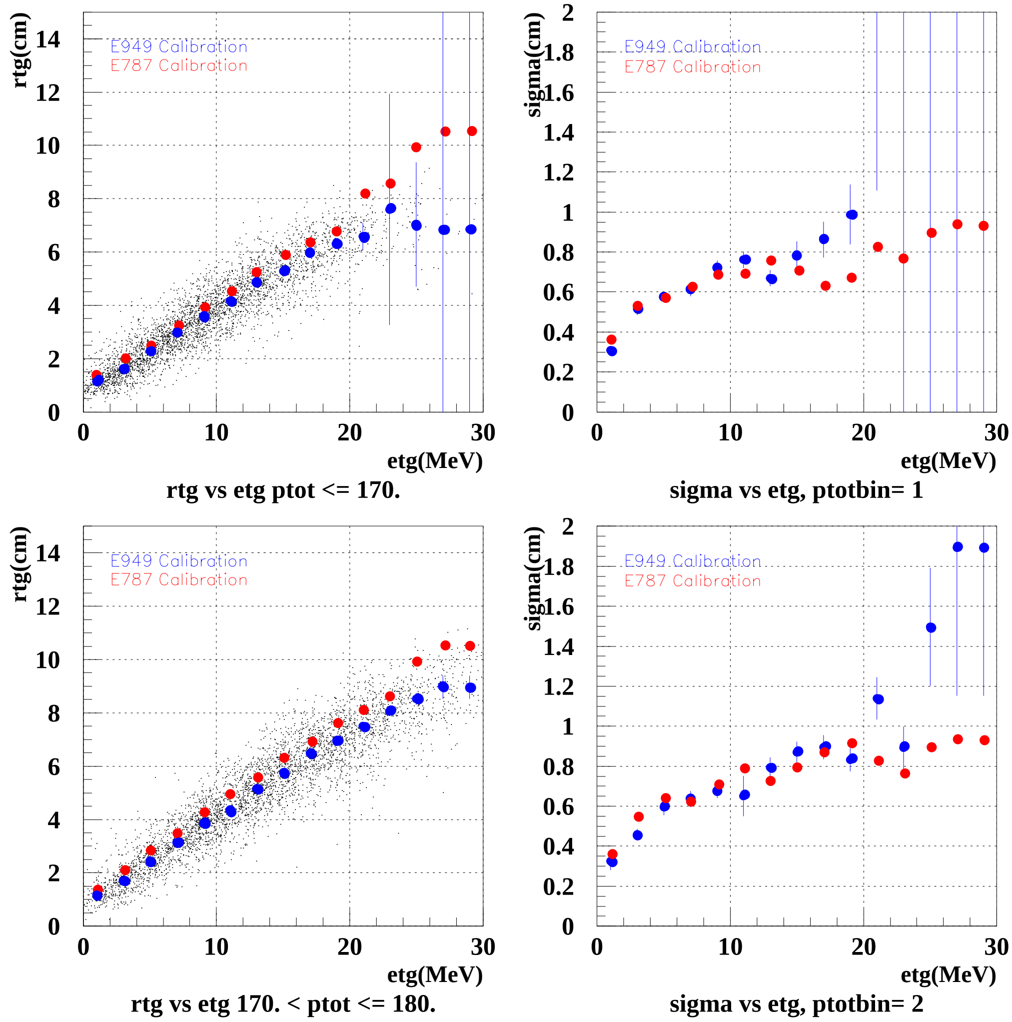

Figure D.1: Calibration of new rtg_{exp} (left) and σ_{exp} (right) values for *ptot* bins 1 (top) and 2 (bottom). Red (blue) points are the E787 (E949) parameter values. The errors shown are the uncertainty on the fitted parameter from a gaussian fit. Black points are the calibration sample.

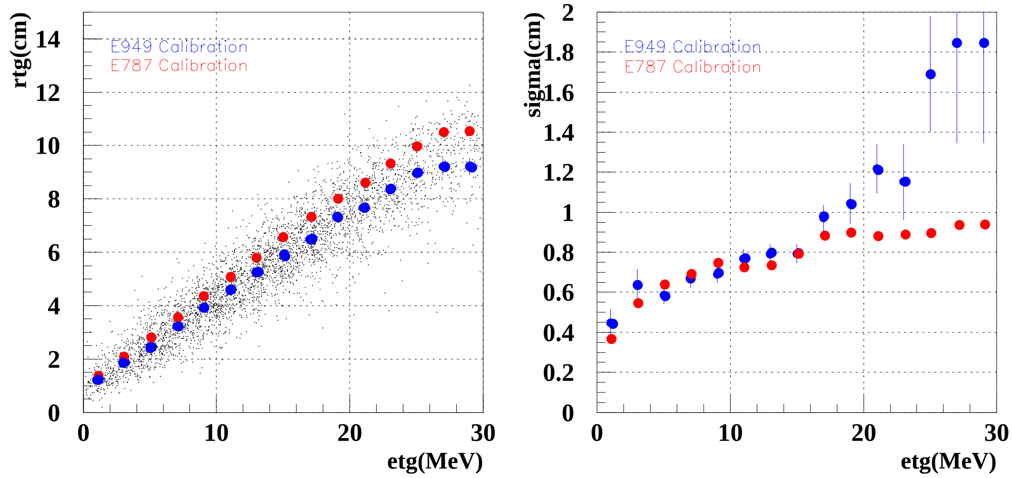

rtg vs etg 180. < ptot <= 188.

sigma vs etg, ptotbin= 3

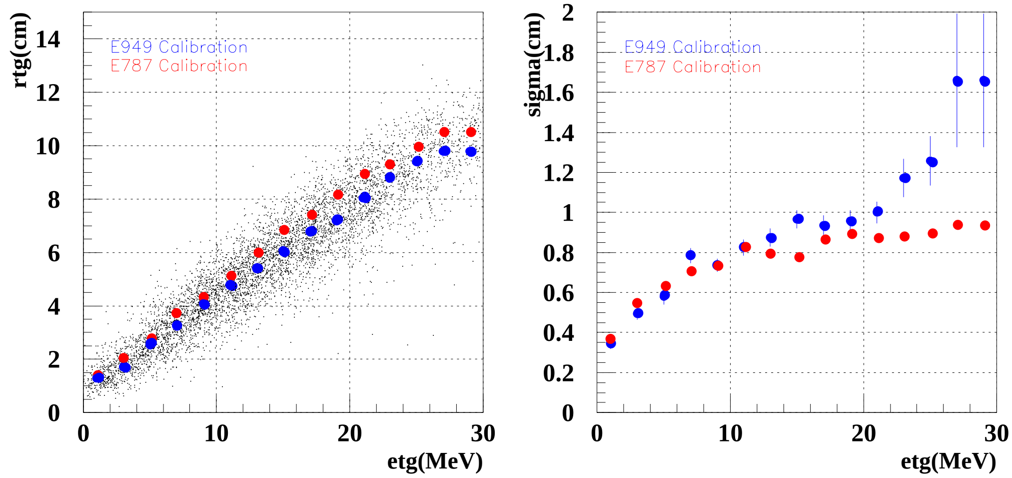

rtg vs etg 188. < ptot <= 199.53

sigma vs etg, ptotbin= 4

Figure D.2: Calibration of new rtg_{exp} (left) and σ_{exp} (right) values for *ptot* bins 3 (top) and 4 (bottom). Red (blue) points are the E787 (E949) parameter values. The errors shown are the uncertainty on the fitted parameter from a gaussian fit. Black points are the calibration sample.

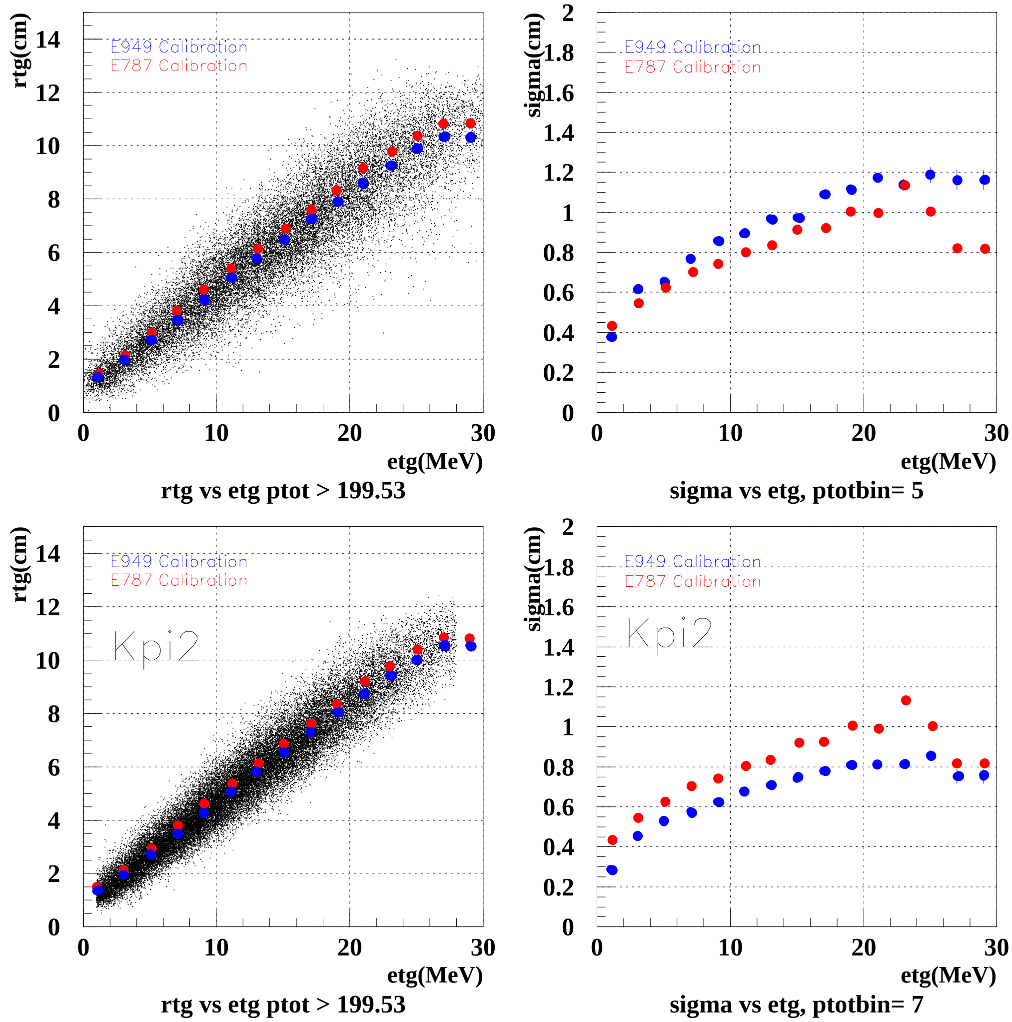

Figure D.3: Calibration of new rtg_{exp} (left) and σ_{exp} (right) for *ptot* bin 5 (top). The bottom plots, labeled "ptotbin = 7", were from the calibration process on $K_{\pi 2}(1)$ monitors; only used as a check. Red (blue) points are the E787 (E949) parameter values. The errors shown are the uncertainty on the fitted parameter from a gaussian fit. Black points are the calibration sample.

D.3.1 Parameters

The rtg_{exp} and σ_{exp} values are listed below in the five $ptot$ bins, rtg^N_{exp}, σ^N_{exp} such that

- $N = 1$: $ptot < 170$ MeV/c
- $N = 2$: 170 MeV/c $< ptot \leq 180$ MeV/c
- $N = 3$: 180 MeV/c $< ptot \leq 188$ MeV/c
- $N = 4$: 188 MeV/c $< ptot \leq 199.53$ MeV/c
- $N = 5$: $ptot > 199.53$ MeV/c

The 15 numbers in each of the following lines are for $etg = 1$ MeV,3 MeV,. . . , 29 MeV.

E787 Parameters

rtg^1_{exp} = 1.41,1.99,2.51,3.28,3.92,4.56,5.23,5.88,6.30,6.77,8.2,8.6,9.95,10.5,10.5
σ^1_{exp} = 0.36,0.53,0.57,0.62,0.69,0.70,0.76,0.71,0.64,0.67,0.83,0.77,0.90,0.93,0.93
rtg^2_{exp} = 1.41,2.09,2.82,3.50,4.29,5.02,5.62,6.31,6.96,7.60,8.17,8.58,9.95,10.5,10.5
σ^2_{exp} = 0.36,0.54,0.64,0.62,0.71,0.79,0.72,0.79,0.88,0.91,0.83,0.77,0.90,0.93,0.93
rtg^3_{exp} = 1.41,2.09,2.82,3.53,4.36,5.05,5.83,6.60,7.29,7.99,8.61,9.33,9.95,10.5,10.5
σ^3_{exp} = 0.36,0.54,0.64,0.70,0.74,0.72,0.73,0.79,0.89,0.90,0.87,0.89,0.90,0.93,0.93
rtg^4_{exp} = 1.41,2.09,2.82,3.72,4.28,5.17,6.06,6.83,7.39,8.17,8.93,9.33,9.95,10.5,10.5
σ^4_{exp} = 0.36,0.54,0.64,0.71,0.73,0.83,0.79,0.78,0.86,0.90,0.87,0.89,0.90,0.93,0.93
rtg^5_{exp} = 1.48,2.15,2.97,3.75,4.58,5.37,6.10,6.84,7.64,8.36,9.16,9.77,10.38,10.83,10.83
σ^5_{exp} = 0.44,0.54,0.62,0.71,0.74,0.80,0.84,0.91,0.92,1.0,0.99,1.14,1.0,0.81,0.81

New E949 Parameters

rtg^1_{exp} = 1.15,1.64,2.27,2.96,3.59,4.16,4.83,5.29,5.95,6.35,6.58,7.,7.5,8.0,8.0
σ^1_{exp} = 0.31,0.52,0.57,0.61,0.72,0.76,0.67,0.79,0.86,0.99,1.04,1.28,1.28,1.28,1.28
rtg^2_{exp} = 1.17,1.69,2.45,3.15,3.86,4.35,5.17,5.77,6.49,6.91,7.50,8.05,8.53,8.96,8.96
σ^2_{exp} = 0.33,0.46,0.60,0.64,0.68,0.65,0.79,0.87,0.90,0.83,1.14,0.89,1.50,1.89,1.89
rtg^3_{exp} = 1.20,1.87,2.46,3.23,3.91,4.59,5.29,5.91,6.50,7.34,7.67,8.35,8.95,9.21,9.21
σ^3_{exp} = 0.45,0.64,0.59,0.67,0.69,0.77,0.79,0.79,0.97,1.04,1.22,1.15,1.69,1.85,1.85
rtg^4_{exp} = 1.29,1.71,2.61,3.29,4.08,4.77,5.43,6.07,6.76,7.27,8.04,8.78,9.40,9.80,9.80
σ^4_{exp} = 0.35,0.49,0.58,0.78,0.74,0.82,0.87,0.97,0.94,0.96,1.00,1.17,1.26,1.66,1.66
rtg^5_{exp} = 1.32,1.96,2.74,3.50,4.27,5.04,5.76,6.47,7.21,7.91,8.59,9.25,9.88,10.30,10.30
σ^5_{exp} = 0.38,0.61,0.66,0.77,0.86,0.89,0.97,0.97,1.09,1.12,1.17,1.14,1.19,1.16,1.16

Manual changes

The fit for $ptot < 170$ MeV/c and $etg > 20$ MeV was very poor due to lack of statistics. Therefore, the rtg_{exp}'s were set by visual inspection of this sample with consideration given to the linear nature of the rtg_{exp} with respect to *etg*. Five bins corresponding to the largest *etg* values were set by this visual inspection method. These last four σ_{exp} values were determined by combining the events from the last four bins, 20 MeV $< etg <$ 30 MeV (to create a sample with sufficient statistics). The σ_{exp} for the $etg = 19$ MeV bin was determined by extending the *etg*-slice to 17 MeV $< etg <$ 21 MeV.

From fits,
rtg^1_{exp} = 1.15,1.64,2.27,2.96,3.59,4.16,4.83,5.29,5.95,6.35,6.58,7.60,7.03,6.84,6.84
σ^1_{exp} = 0.31,0.52,0.57,0.61,0.72,0.76,0.67,0.79,0.86,0.99,2.02,3.64,3.84,12.70,12.70
were changed by visual inspection to the following:
rtg^1_{exp} = 1.15,1.64,2.27,2.96,3.59,4.16,4.83,5.29,5.95,6.35,6.58,7.,7.5,8.0,8.0
σ^1_{exp} = 0.31,0.52,0.57,0.61,0.72,0.76,0.67,0.79,0.86,0.99,1.04,1.28,1.28,1.28,1.28

D.3.2 Calibration Validity

To determine if the calibration removed an observed energy (*etg*) dependence, plots of rtg_{exp} from various samples, such as E787, E949, $kpiang > \theta$, PV_{tight}, were performed. The flat distributions (except for the low momentum bin, "ptot bin 1") in Fig. D.4 indicates that TGDEDX acceptance no longer has an energy dependence. Also, Fig. D.5 shows that there was no noticeable dependence on *etg* for the different calibration samples; most relevant set of points in Fig. D.5 is "*ptot*-bin 5".

Fig. D.6 shows the difference in $like_{tgdedx}$ values before and after calibration. By matching distributions from Fig. D.6 to the different hypothetical samples shown in Fig. D.7 two things are evident:

- The top plot of Fig. D.6 and the "$Mean < 0.0$" (light blue), from Fig. D.7, distribution appear similar in overall shape. Thus, E787 parameters appears to have an offset in the mean, which is also shown in Figures D.1-D.3 as a systematic vertical displacement of the E787 parameters compared to the newly calibrated values.
- The bottom plot of Fig. D.6 and the "$Sigma < 0.0$" (dark blue), from Fig. D.7, distribution appear similar in shape. This implies that the calibration sample (π_{scat}) had worse resolution than the acceptance sample ($K_{\pi 2}$), an expected effect from better determination of the decay vertex in $K_{\pi 2}$ events. A plot of $like_{tgdedx}$ for π_{scat}'s using the updated calibration parameters, not shown, yielded a flat distribution (as it should). Since calibration of TGDEDX employed the entire π_{scat} sample, the acceptance measurement of TGDEDX (Chapter 5) has to be performed on $K_{\pi 2}$ monitors, otherwise a bias would occur.

Obtaining consistent results on an independent sample, such as $K_{\pi 2}$, would validate that the calibration sample used was a proper sample. Thus, distributions associated with TGDEDX were measured on a $K_{\pi 2}$ monitor sample for the (updated) E949 calibration. Fig. D.8 shows no difference discernible between the calibration sample and the cleaner sample with the tight PVPNN2 applied. As shown in Fig. D.8(a), a small difference at large $like_{tgdedx}$ was observed between the calibration sample and the calibration sample with $kpiang > 55°$ requirement. Again, this was expected due to $kpiang > 55°$ having better resolution in rtg due to better decay-vertex finding.

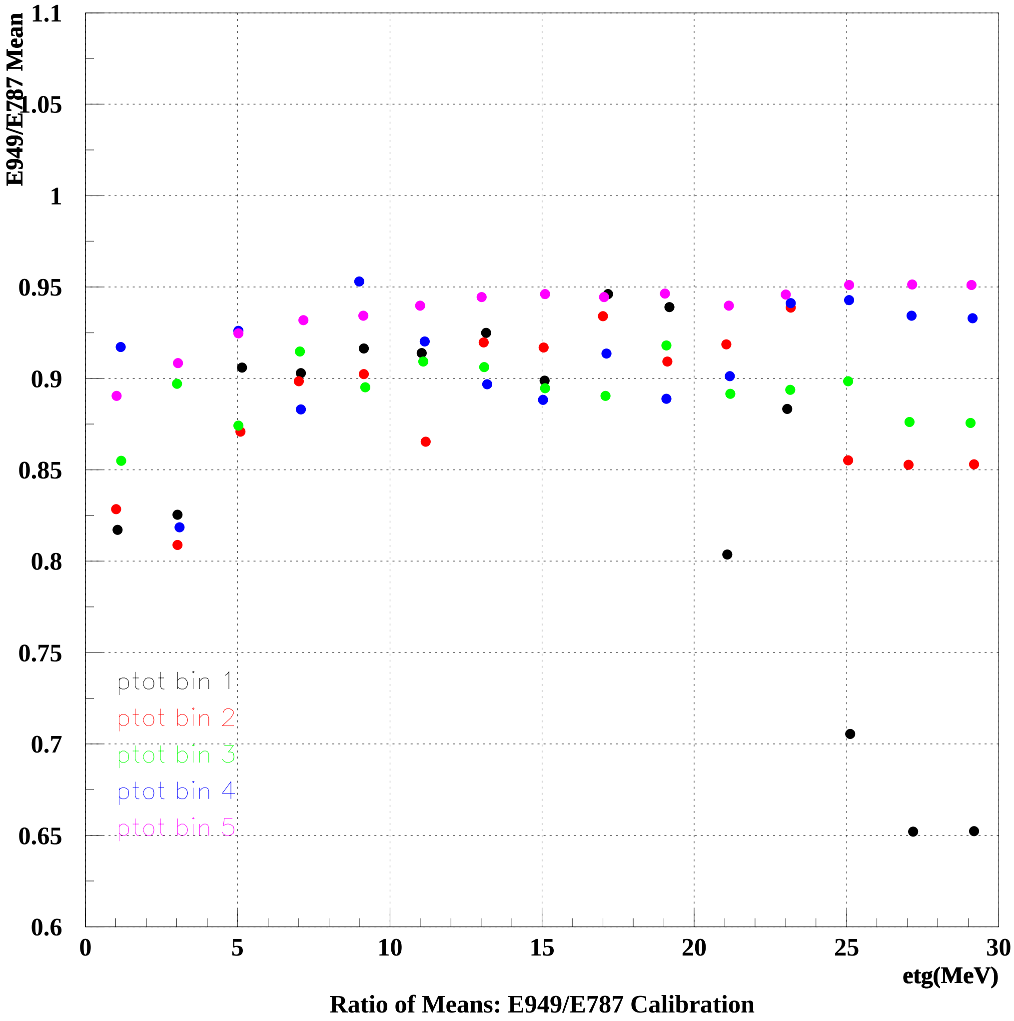

Figure D.4: Ratios of the rtg_{exp} E949 to E787 parameters. The points on the lower right ("ptot bin 1" with large etg) have low statistics and the E949 values for these parameters were later changed by visual inspection.

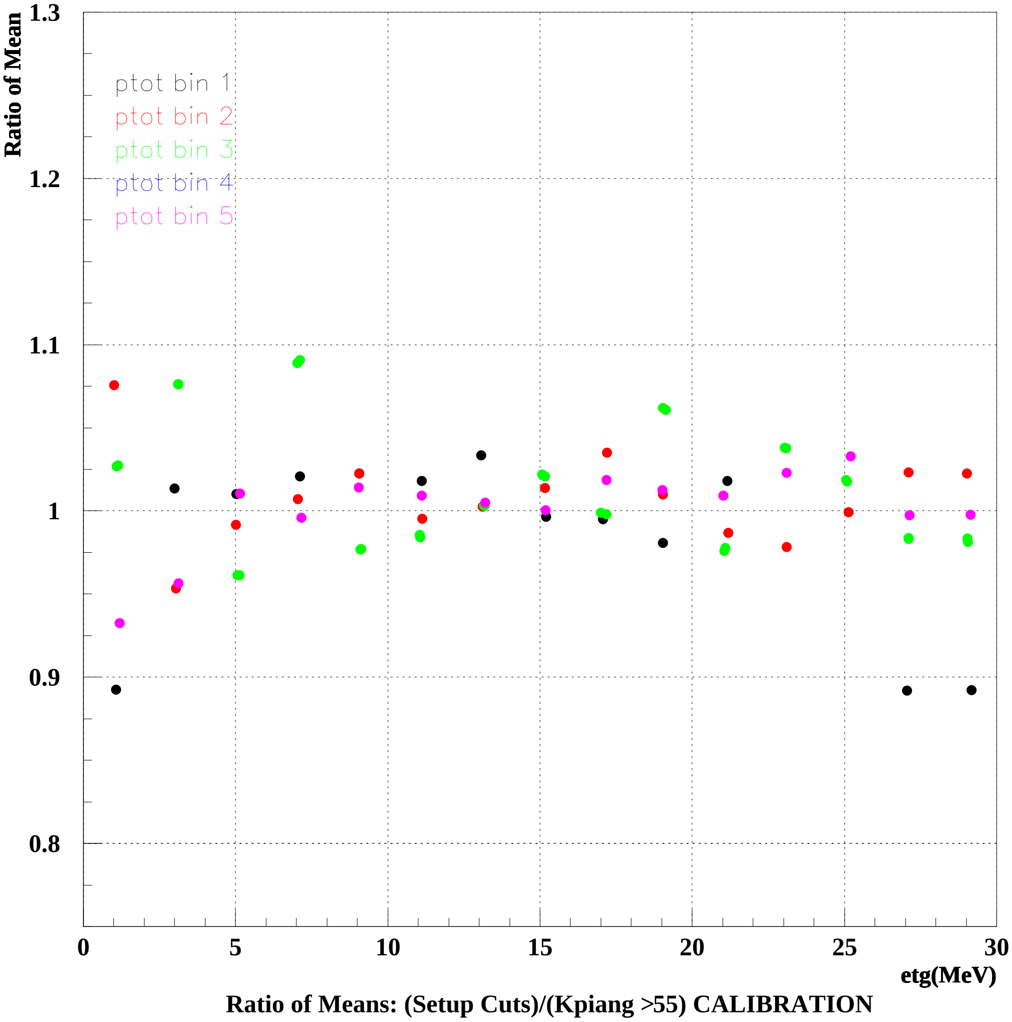

Figure D.5: Ratio of rtg_{exp} (Means) determined by the sample chosen (Setup cuts) and the enhanced decay-vertex sample ($kpiang > 55$).

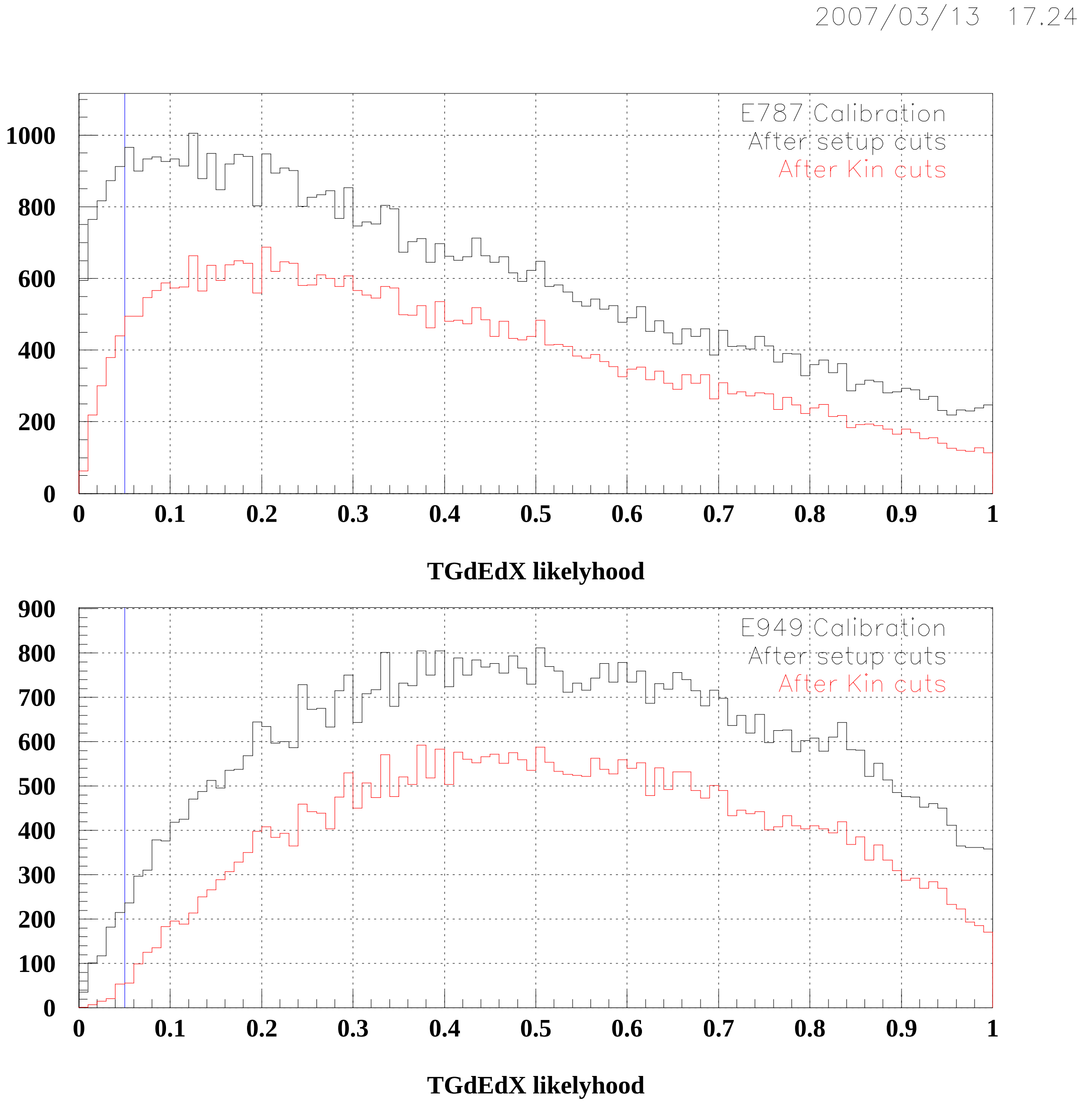

Figure D.6: $like_{tgdedx}$ distributions before and after calibration ("E787 Calibration" means before calibration). "Setup cuts" are cuts applied before TGDEDX cut was applied, as seen in Table 5.19. The "Kin cuts" are all cuts in the acceptance study except for TGDEDX (i.e. TGDEDX applied last). Events left of the blue line (0.05) are removed by TGDEDX.

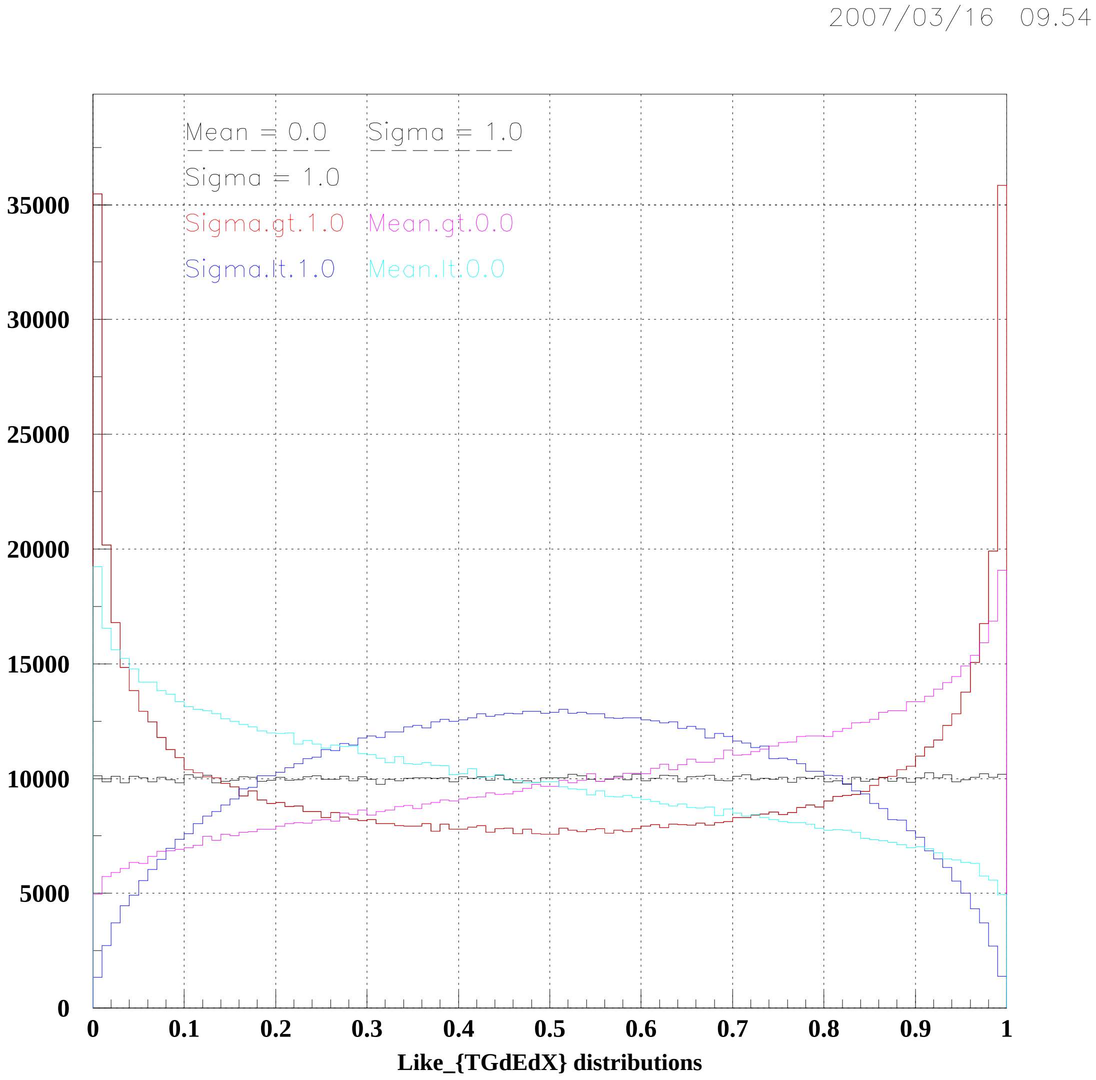

Figure D.7: Expected $like_{tgdedx}$ distributions for different "improperly" calibrated parameters (in colors) and properly calibrated parameters (in black). $Mean = rtg_{measured} - rtg_{exp}$ and $Sigma = \sigma_{exp}/\sigma_{true}$. $Mean = 0$ for the $Sigma = 1$ (black, flat curve), $Sigma > 1$ (red U-shaped), and $Sigma < 1$ (dark blue, upside-down U-shaped) curves. $Sigma = 1.0$ for the $Mean > 0$. (magenta,/-shaped) and $Mean < 0$. (light blue,\-shaped) curves.

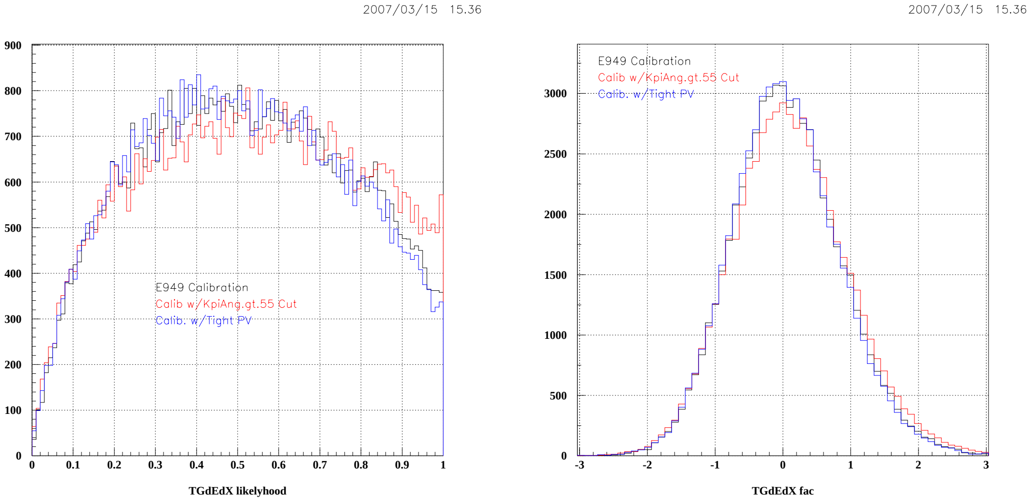

(a) $like_{tgdedx}$

(b) $\frac{rtg-rtg_{exp}(etg,ptot)}{\sigma_{exp}(etg,ptot)}$

Figure D.8: Comparison of the possible calibration samples. Plot (a) is TGDEDX's likelihood value, $like_{tgdedx}$, after different calibration samples were used. Plot (b) is the value given to the error function as indicated in Eq. (D.1). The "E949 Calibration", in black, is the high-statistics sample chosen for the final calibration. The red (blue) distribution is for the better-determined-decay-vertex (tight photon-veto) sample.

D.4 Acceptance

E787-PNN2 measured TGDEDX acceptance of 0.9858. The TGDEDX acceptance measurement employed in this calibration was the same used in Section 5.3. Using E787-PNN2 calibration parameters on E949 data yielded an acceptance of 0.9339. The newly calibrated TGDEDX acceptance was measured to be 0.9893 ± 0.00042 (see Section 5.3), which is consistent with the E787-PNN2 measured value.

D.5 Rejection

E787 tuned the cut to $Rej_{TGDEDX} = 1.44$; however, due to correlation with CHI567, TGDEDX had no rejection after all cuts in E787. Table D.2 shows the sample selection for measuring Rej_{TGDEDX} in E949. $TGDEDX_{uncorr}$, denoted in red, shows a rejection of 1.35 before uncorrelated cuts are applied. After applying the correlated cuts (EPITG, EPIMAXK, CHI567, CHI5MAX), a rejection of 1.07 was measured. The $like_{tgdedx}$ distributions for the acceptance and rejection samples are shown in Fig. D.9.

Cut Applied	Events remaining (Rej)
$BADRUN$	30408052 (0.00)
$TRIGGER$	15232707 (2.00)
$ICbit$	15232564 (1.00)
$lhex$	15232564 (1.00)
DC	15232516 (1.00)
$Lev11$	15232516 (1.00)
RD_TRK	15232515 (1.00)
$TRKTIM$	15232515 (1.00)
$TARGET$	15232515 (1.00)
$STLAY$	15232515 (1.00)
UTC	15232515 (1.00)
$RDUTM$	15232515 (1.00)
BAD_STC	15232515 (1.00)
PDC	15232515 (1.00)
$\overline{PV(not\ tg)60\%}$	12954315 (1.18)
$TGCUT$	7142934 (1.81)
$tgqualt$	6765533 (1.06)
$npitg$	6765533 (1.00)

continued on next page

Cut Applied	Events remaining (Rej)
timcon	6685429 (1.01)
tgtcon	6316877 (1.06)
b4etcon	6184009 (1.02)
DCBIT	6184009 (1.00)
DELCO	4280023 (1.44)
*Delc*3	3595811 (1.19)
PSCUT	2185154 (1.65)
b4dedx	2169877 (1.01)
bwtrs	1799849 (1.21)
cpitrs	1797020 (1.00)
cpitail	1796540 (1.00)
cktrs	1781679 (1.01)
cktail	1762093 (1.01)
b4trs	1674587 (1.05)
b4ccd	1650344 (1.01)
upvtrs	1623531 (1.02)
rvtrs	1615563 (1.00)
tggeo	1060126 (1.52)
b4ekz	886102 (1.20)
tgzfool	870567 (1.02)
targf	826789 (1.05)
dtgttp	826779 (1.00)
rtdif	819240 (1.01)
tgktim	811136 (1.01)
eiccon	792084 (1.02)
ticcon	792075 (1.00)
pigap	774063 (1.02)
*tgdb*4	760772 (1.02)
tgdb4tip	752741 (1.01)
tgdvxtip	746892 (1.01)
tgdvxpi	729199 (1.02)
*phivtx*1	672405 (1.08)
ccdpul	166933 (4.03)
timkf	149649 (1.12)
verrng	135863 (1.10)
angli	135717 (1.00)
ALLKfit	133136 (1.02)
tpics	133047 (1.00)
kic	133004 (1.00)
epionk	132901 (1.00)
BOX Loose	12503 (10.63)
*icodel*14	12503 (1.00)
cos3d	12181 (1.03)
*layv*4	12181 (1.00)
zfrf	12158 (1.00)
zutout	12134 (1.00)
utcqual	11226 (1.08)
*prrf*1	10855 (1.03)
prrfz	9906 (1.10)
rsdedxmax	9406 (1.05)
rsdedxcl	6725 (1.40)
rslike	6725 (1.00)

continued on next page

Cut Applied	Events remaining (Rej)
rngmom	1016 (6.62)
tgdb4	1016 (1.00)
tgdb4tip	1016 (1.00)
tgdvxtip	1016 (1.00)
tgdvxpi	1016 (1.00)
piflg	990 (1.03)
elveto	924 (1.07)
tdfool	920 (1.00)
tdvarnn02 Loose	849 (1.08)
TGDEDX$_{\mathbf{uncorr}}$	**629** (1.35)
epitg	551 (1.54)
epimaxk	551 (1.00)
chi567	415 (1.33)
chi5max	389 (1.07)
TGDEDX	**365** (1.07)

Table D.2: TGDEDX Rejection Table. The red TGDEDX was the value before correlated cuts were applied, and the black TGDEDX(last line) is the rejection after all cuts are applied.

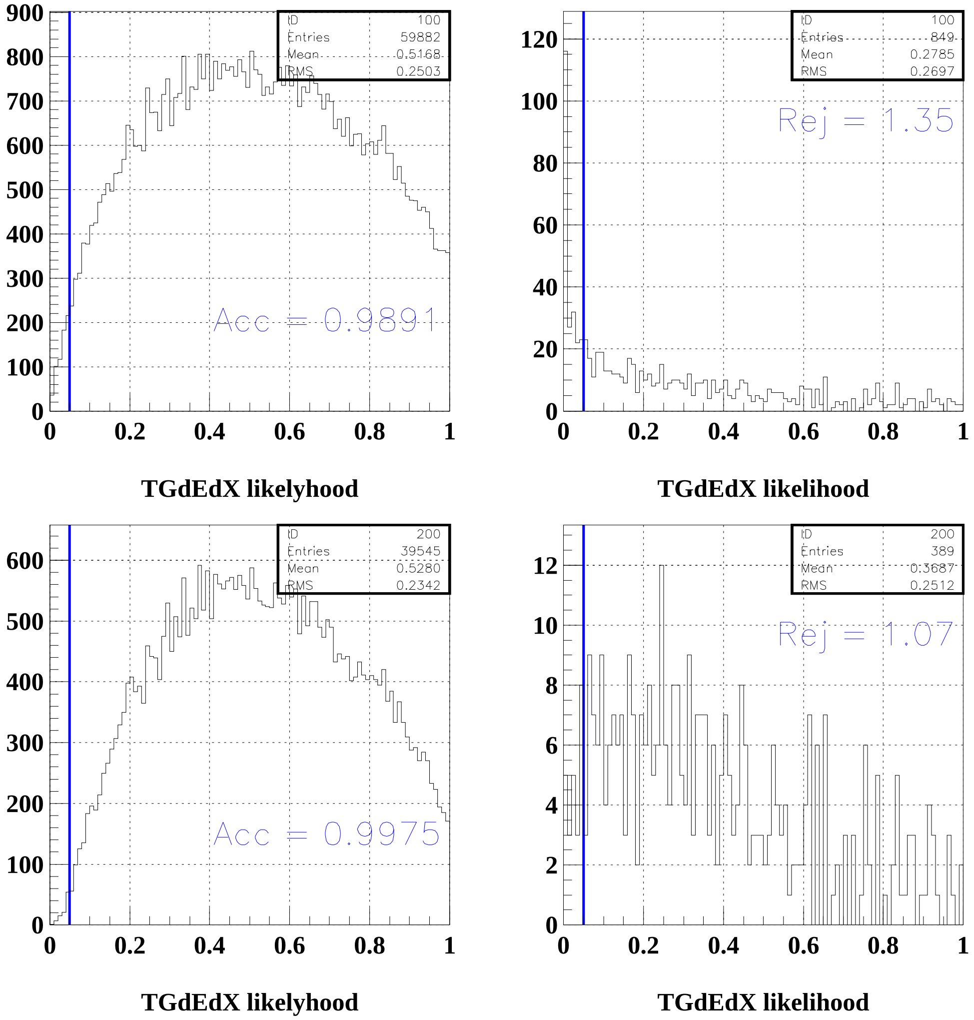

Figure D.9: $like_{tgdedx}$ distributions of the acceptace (left) and rejection (right) samples. The top (bottom) plots are sample without (with) correlated cuts applied. The blue line is the cut threshold value of 0.05 (events on the left of the line are considered possible background). E787 had a acceptance (rejection) of 0.9858 (1.44) and no rejection after all cuts were applied.

D.6 Results

The numbers outlined in Section D.3.1 were officially utilized by the cut due to low statistics limitations in the other samples (*kpiang* $> 55°$, PV(not TG) 30%). Comparisons of the cleaner samples to the high-statistics sample (the sample ultimately chosen) did not show any significant differences in TGDEDX variables, see Figures D.8-D.5. In addition, the *kpiang* $> 55°$, PV(not TG) 30% samples were lacking statistics in the lower-momentum bins. The consistency with E787's measured value indicates the calibration was done successfully. Table D.3 shows that TGDEDX is capable of removing backgrounds after all other cuts are applied; as opposed to E787, in which TGDEDX remained in the analysis as a safety cut.

Experiment	*Acc*	*Rej*	*Acc* × *Rej*
E787	0.9858	1.44	1.42
E949	0.989	1.35	1.34
After all cuts			
E787	0.9858	1.00	0.986
E949	0.989	1.07	1.06

Table D.3: TGDEDX *Acceptance* × *Rejection*. The TGDEDX cut is $like_{tgdedx} < 0.05$.

Determining TGDEDX's cut threshold, or cut value, (nominal value was 0.05) is shown in Fig. D.10. The *acceptance*, *rejection*, and *acceptance* × *rejection* was plotted as a function of the cut value. The lower plot, *acceptance* × *rejection*, indicates that improvement in signal-to-background by tightening this cut (to a larger threshold). However, due to the lack of an inflection point in the *acceptance* × *rejection* versus *cut value* shape leads to the conclusion that setting the threshold to 0.05 gives the benefit of keeping the acceptance loss small. Therefore, the threshold was left at the E787 value of 0.05.

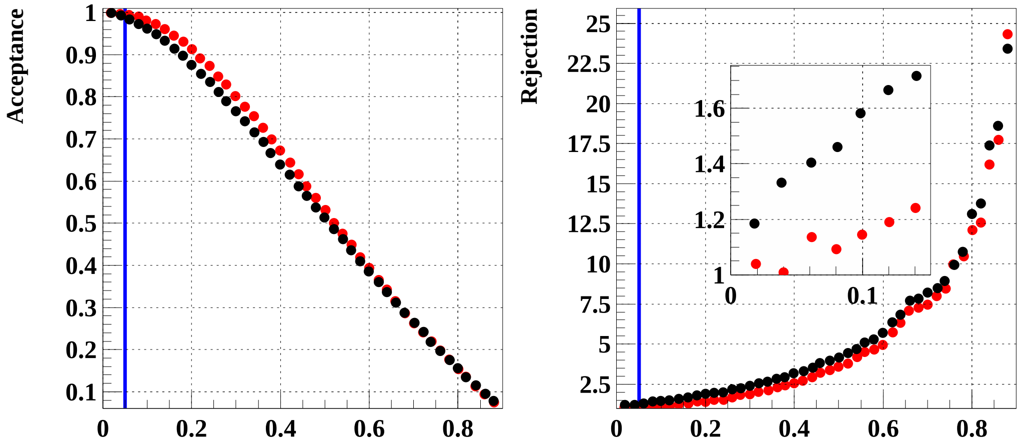

Acc vs TGdEdX cut value - All cuts **Rej vs TGdEdX cut value - All cuts**

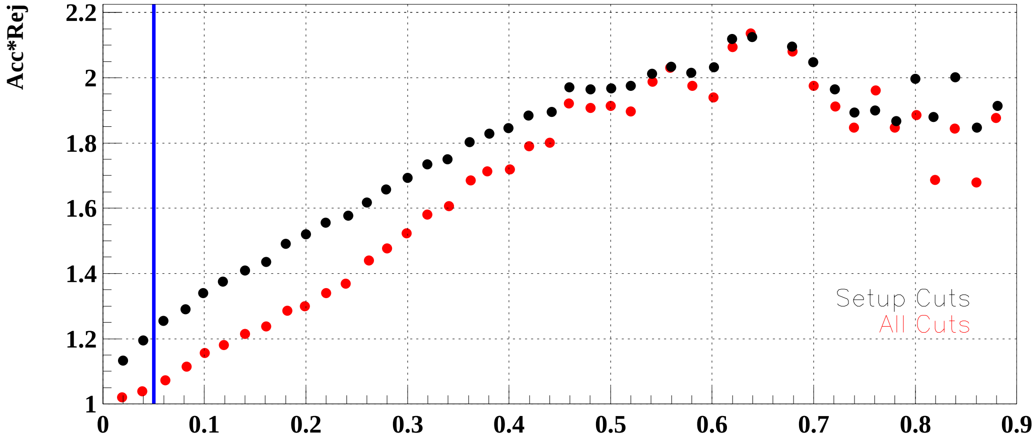

Acc*Rej vs TGdEdX cut value - All cuts

Figure D.10: Acceptance and Rejection versus TGDEDX cut threshold. The TGDEDX cut is $like_{tgdedx} < cut\ value$. The blue line is the nominal cut value of 0.05. The red (black) points are after (before) correlated cuts are applied.

Appendix E

Target π^+-Track Fitter

The charged track within the TG was fit by a χ^2-minimization routine, MINUIT. The fit parameters were the center (X_c and Y_c) and radius (R_c) of a track circle; initial parameters were given by the UTC track fit. The seven components of the χ^2 were composed of the following:

1. Agreement of fitted track with the decay vertex, determined by *swathccd*. Due to TG x-y resolution, the decay vertex was assigned to be at the center of a fiber. With a fiber width of 0.5 cm, $\chi^2_{_1}$ was normalized to uncertainty in the decay-vertex determination of 0.25 cm.

$$\chi^2_{_1} = \left(\frac{\sqrt{(tgx - X_c)^2 + (tgy - Y_c)^2} - R_c}{0.25} \right)^2 \tag{E.1}$$

2. Agreement of fitted track with respect to exit point from the TG; this was measured by UTC extrapolation to the interior surface of the IC. Given the precision of the UTC track, especially at short extrapolated distance, $\chi^2_{_2}$ was normalized to 0.05 cm.

$$\chi^2_{_2} = \left(\frac{\sqrt{(xtgt - X_c)^2 + (ytgt - Y_c)^2} - R_c}{0.05} \right)^2 \tag{E.2}$$

3. χ_3^2 was determined by the difference in the angle between the UTC track and *Target Fitter* track fit ($\Delta\theta_I$) at the target edge. $max(a,b)$ is the mathematical function which chooses the largest of a and b. Again considering the precision of the UTC track, the normalization of χ_3^2 should be small. However, TG tracks with longer range, *rtg*, inheritly have a greater uncertainty which were dependent on *rtg*. Hence, the observed normalization of $max(0.015, 0.0030{\cdot}rtg)$

$$\chi_3^2 = \left(\frac{\Delta\theta_I}{max(0.015, 0.0030 \cdot rtg)}\right)^2 \tag{E.3}$$

4. The fitted radius and the UTC radius should be consistent with each other.

$$\chi_4^2 = \left(\frac{R_{UTC} - R_c}{0.5}\right)^2 \tag{E.4}$$

5. Fibers which are traversed by the fitted track and have observed energies contribute to χ_5^2, such that $\chi_5^2 = \sum_i \chi_{5_i}^2$ where i is the i^{th} fiber satisfying this condition. The minimum uncertainty, σ_E, in the energy measurement was set to be 0.45 MeV.

$$\sigma_E = \sqrt{max(E_{expected}, 0.2)}$$

$$\chi_{5_i}^2 = \left(\frac{ln\left(\frac{E_{observed}}{E_{expected}}\right)}{0.3} \times \sigma_E\right)^2, \; if \; E_{observed} > E_{expected} \tag{E.5}$$

$$\chi_{5_i}^2 = \left(\frac{E_{observed} - E_{expected}}{0.25 \cdot \sigma_E}\right)^2, \; if \; E_{observed} \leq E_{expected} \tag{E.6}$$

6. If the fitted track traverses a fiber with no observed energy, then this discrepancy contributes to χ_6^2. D_{corner} was the distance of the track to the closest corner of fiber i; geometrically the smallest D_{corner} can be is 0.25 cm. The small factor of 0.005 will penalized fitted tracks which attempt to traverse non-hit fibers. $\chi_6^2 = \sum_i \chi_{6_i}^2$

$$\chi_{6_i}^2 = \left|\frac{E_{expected}}{0.005 \cdot min(D_{corner}, 0.3)}\right| \tag{E.7}$$

7. A contribution to χ^2 was made when a fitted track did not traverse a fiber with measured energy. $\chi^2_{7_i}$ scaled with observed energy and distance of the fitted track to the closest corner of fiber i.

$$\chi^2_{7_i} = \left(E_{observed} + 4 \times \frac{min(D_{corner}, 0.2)}{0.2} \right)^2 \tag{E.8}$$

The track which minimized $\chi^2 = \sum_{i=1}^{7} \chi^2_i$ was chosen to be further employed in selection criteria for determining if the π^+ track could be due to a $K^+ \rightarrow \pi^+ \nu\bar{\nu}$ event. The chosen track calculated the projected track path length through the decay vertex fiber, used by ANGLI. See Section 3.3 for other cuts designed based on the TG track fitter, such as CHI567, NPITG, VERRNG, and CHI5MAX. These cuts are highly effective against TG-scattering backgrounds, due to the effect the scattering has on the π^+ track kinematics.

Appendix F

Optimization of PNN2 $\pi^+ \to \mu^+ \to e^+$ Criteria

F.1 Electron Finding

The cut EV5 was scrutinized to determine if it is possible to remove it from the E949 offline cut-list, to gain the observed 17% acceptance loss.

To determine the effect EV5 has on the muon background, the muon background was measured with and without EV5. Table F.1 shows the effect of EV5 on the TD rejection. Table F.2 shows the effect of EV5 on the muon background. Note that the muon tail for the PNN2 energy-range box is very high due to limited statistics in rejection measurement. The total muon background is the sum of the muon-band plus the muon-tail measurements.

The acceptance of EV5, when applied last, is 0.83. When EV5 is removed, a gain of 17% acceptance with an increase of the muon background by a factor of 2.0 is observed. The total background will be 0.0260 ± 0.0260 (band+tail) when EV5 is not applied which is much less than the expected background from TG-scatters of

0.5 events (at the time of this optimization study).

Rej & Norm Measurement	with EV5	without EV5
Band All Rejection	357.89 ± 119.13	140.04 ± 29.10
Band ERbox Rejection	423.00 ± 422.50	211.50 ± 149.20
Tail All Rejection	679.00 ± 678.50	679.00 ± 678.50
Tail ERbox Rejection	9.00 ± 8.49	9.00 ± 8.49
Muon Normalization	1.0 ± 1.0	1.0 ± 1.0

Table F.1: Rejection and Normalization Summary. Band refers to applying $\overline{RNGMOM}$ to the sample and Tail refers to applying $ptot > 229.$, which will tag the muon-band and muon-tail sample respectively. All (ERbox) refer to applying all setup cuts (all setup cuts plus the PNN2 energy range cut).

Background	with EV5	without EV5
Band All	0.00841 ± 0.00841	0.0216 ± 0.0216
Band ERbox	0.00711 ± 0.00711	0.0143 ± 0.0143
Tail All	0.00442 ± 0.00442	0.00442 ± 0.00442
Tail ERbox	0.37500 ± 0.37500	0.3750 ± 0.3750

Table F.2: Muon background summary, scaled to the 3/3 sample. Band refers to applying $\overline{RNGMOM}$ to the sample and Tail refers to applying $ptot > 229$ MeV/c, which will tag the muon-band and muon-tail sample, respectively. All (ERbox) refer to applying all setup cuts (all setup cuts plus the PNN2 energy range cut).

F.2 TD Neural-Net Cut

TD neural-net cut (TDNN), cuts on one parameter. Therefore, loosening was very easily accomplished. The initial cut parameter is 0.76, set in E949-PNN1 analysis. This parameter was varied from 0.05 to 0.8 in 0.05 increments (16 total values) in an attempt to determine the optimal value for PNN2 analysis. The effects of including and excluding EV5 was done in tandem when optimizing TDNN. In Figures F.1-F.4 black (red) points included (omitted) EV5 in the measurement. Figure F.1 shows muon background as a function of the TDNN cut value. Figure F.2 shows muon background as a function of *acceptance*.

The acceptances were measured in the Piscat TD acceptance measurement as in Section 5.2 applying TDNN last in the measurement order. The muon-band background was measured by inverting RNGMOM and the muon-tail background was measured by requiring $ptot > 229$ MeV. At the time this study was performed it was not known if the muon-tail background would be negligible. Therefore, the muon background in this optimization study included band and tail measurements. There was one event remaining in the normalization branch using the nominal TDNN(0.76) cut; the normalization branch was not measured for the TDNN parameter variations to prevent determining possible location of events within the box. Table F.3 lists the background and acceptance values for all TD cut parameter values that were analyzed.

TD cut	with EV5			without EV5		
value	Accept	Band All	Tail All	Accept	Band All	Tail All
0.05	0.9740	0.0470	0.03409	0.9732	0.0689	0.0694
0.10	0.9675	0.0341	0.02545	0.9664	0.0532	0.0516
0.15	0.9612	0.0268	0.02545	0.9602	0.0433	0.0516
0.20	0.9549	0.0220	0.01689	0.9537	0.0366	0.0370
0.25	0.9490	0.0184	0.01123	0.9477	0.0329	0.0312
0.30	**0.9428**	**0.0154**	**0.00560**	**0.9415**	**0.0287**	**0.0255**
0.35	0.9366	0.0130	0.00279	0.9353	0.0262	0.0226
0.40	0.9300	0.0124	0.00279	0.9286	0.0250	0.0197
0.45	0.9224	0.0106	0.00279	0.9211	0.0220	0.0169
0.50	0.9144	0.0106	0.00279	0.9131	0.0214	0.0141
0.55	0.9050	0.00945	0.00279	0.9036	0.0190	0.0141
0.60	0.8939	0.00827	0.00279	0.8928	0.0178	0.0112
0.65	0.8820	0.00590	0.00279	0.8809	0.0154	0.0112
0.70	0.8676	0.00590	0.00279	0.8661	0.0148	0.0084
0.75	0.8511	0.00531	0.00279	0.8495	0.0136	0.00280
0.76	**0.8454**	**0.00531**	**0.00279**	–	**0.0136**	**0.00280**
0.80	0.8270	0.00472	0.00279	0.8253	0.0124	0.00280

Table F.3: Muon background at different TD Neural-Net cut parameters. Value is using the 'All' Setup cuts, i.e. ERBox not applied. The bold 0.76 line is the TD cut parameter set at the PNN1 level. Error is 100% on all values, the normalization branch is 1±1 with one event remaining. Any loosening of the TDNN will only reduce the normalization branch to zero, which for us will be the same as the nominal cut value. Scaled to the 3/3 sample.

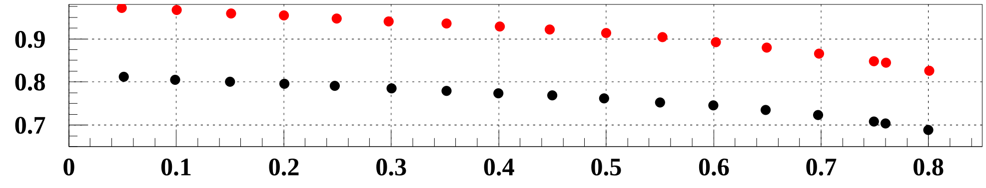

Acceptance vs TD cut value

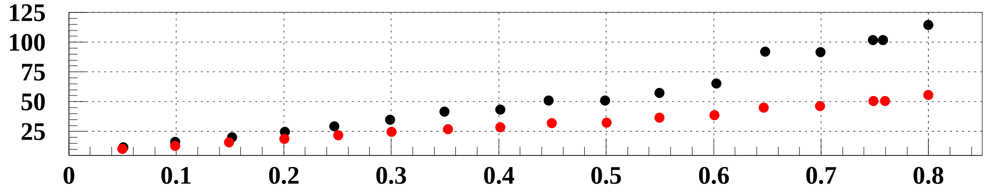

Rejection (Band) vs TD cut value

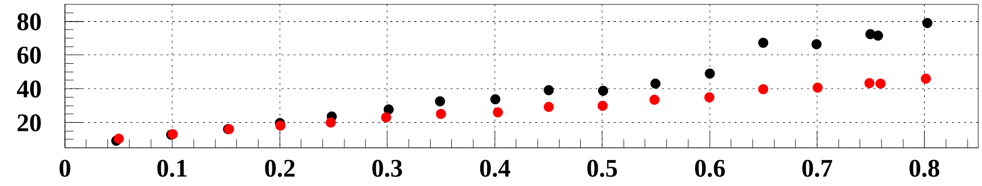

Rej(band)*Acc vs TD cut value

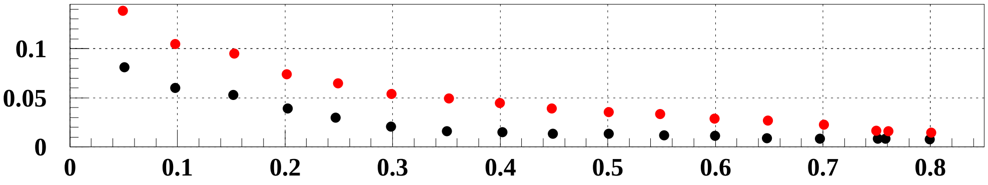

Muon Background vs TD cut value

Figure F.1: Acceptance, Rejection, and Rejection×Rejection versus TD cut parameter. Black points include EV5 in the calculation, red points have excluded EV5 from the analysis.

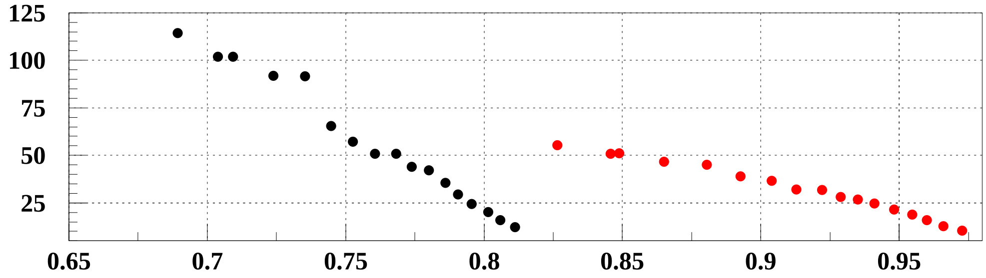

Rejection (Band) vs Acceptance

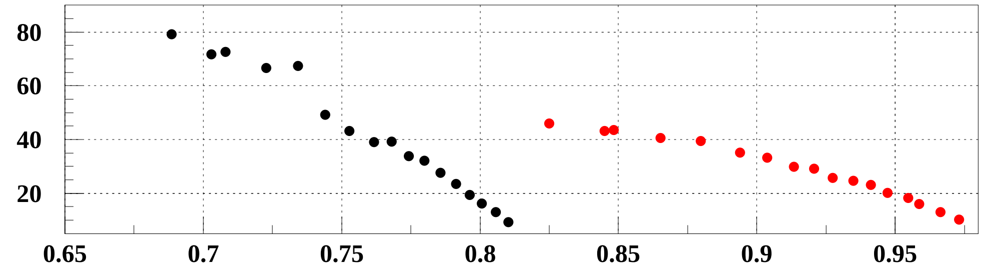

Rej(band)*Acc vs Acceptance

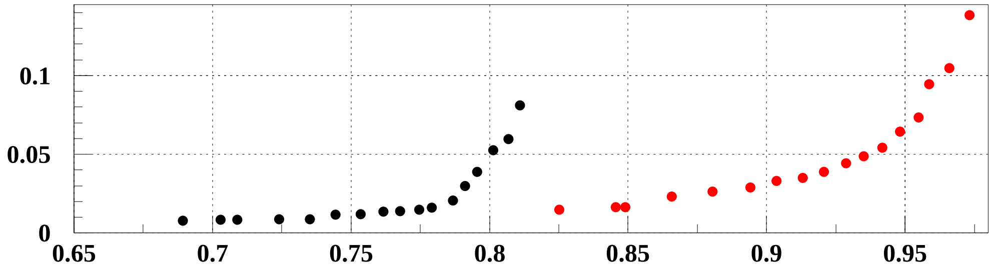

Muon: Background vs Acceptance

Figure F.2: Rejection vs Acceptance with different TDNN cut parameter. Black points include EV5 in the calculation, red points have excluded EV5 from the analysis.

The optimal level for the TDNN's cut parameter can be determined by finding the maximum for the ratio of total acceptance to total background. We assume that all other backgrounds will increase with increased acceptance. All backgrounds (except muon) were measured with EV5 and TDNN(0.76) applied. These backgrounds were scaled with the expected acceptance gain when EV5 and TDNN are loosened. Total background is $N^{*}_{bkg} + N_{muon}$, such that N_{bkg} scales directly with acceptance gain.

Acceptance is normalized to 1.0 when defined as the total acceptance with the TDNN cut parameter being 0.76 and EV5 cut applied (along with all other cuts). The results are plotted in Figure F.3. The maximum for the ratio of total acceptance to total background occurs at the maximum tightness for TDNN. As the cuts were loosen, the gains acceptance occurred. However, the other backgrounds increased with increased acceptance. Sensitivity is lost at a greater rate starting at TDNN value of 0.3. The muon background at 0.3 is 0.0857 (a factor of 3.3 increase) and the TDNN acceptance increases to 0.9415 (9.6%).

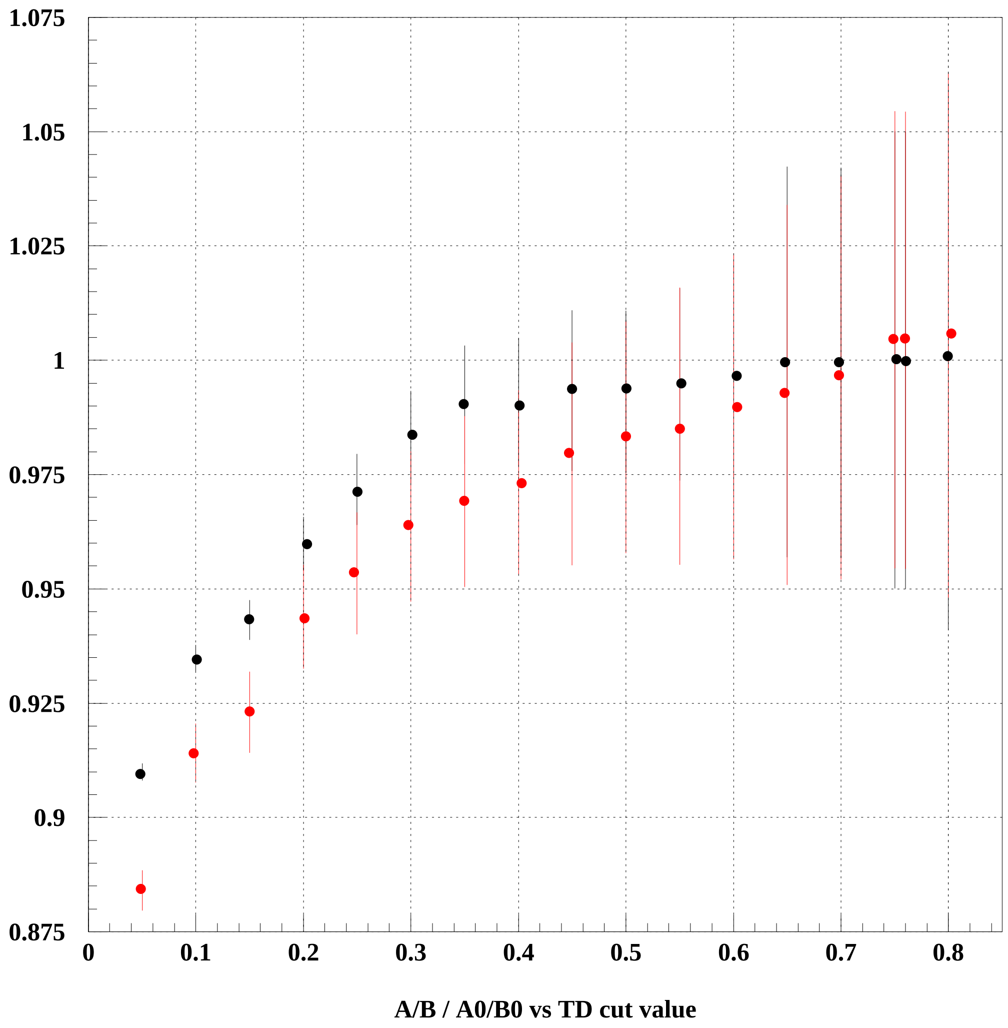

Figure F.3: Total Acceptance/Total Background normalized by A_0/B_0 versus TD cut parameter. Black points include EV5 in the calculation, red points have excluded EV5 from the analysis. Acceptance is normalized to the total acceptance at the tight TD cuts (TDNN(pnn1) and EV5 applied). The total background is approximated from other background + muon background.

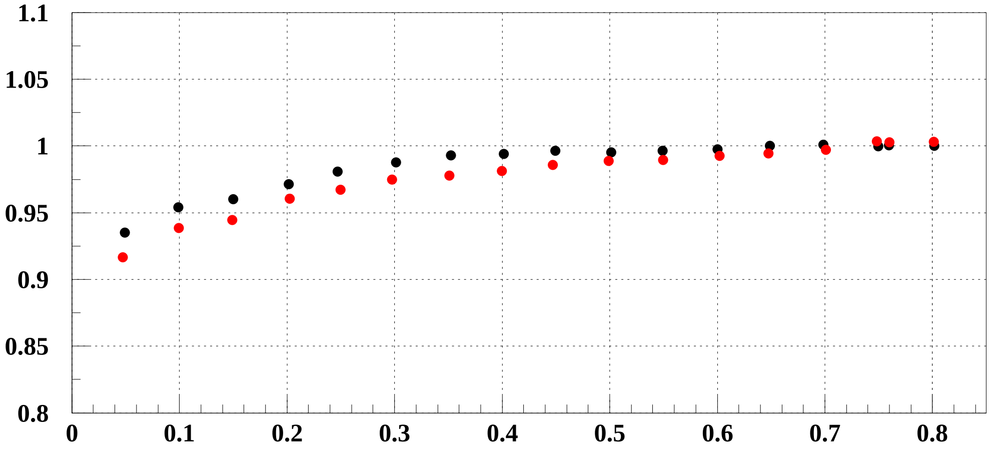

A/(B+1sig) / A0/(B0+1sig) vs TD cut value

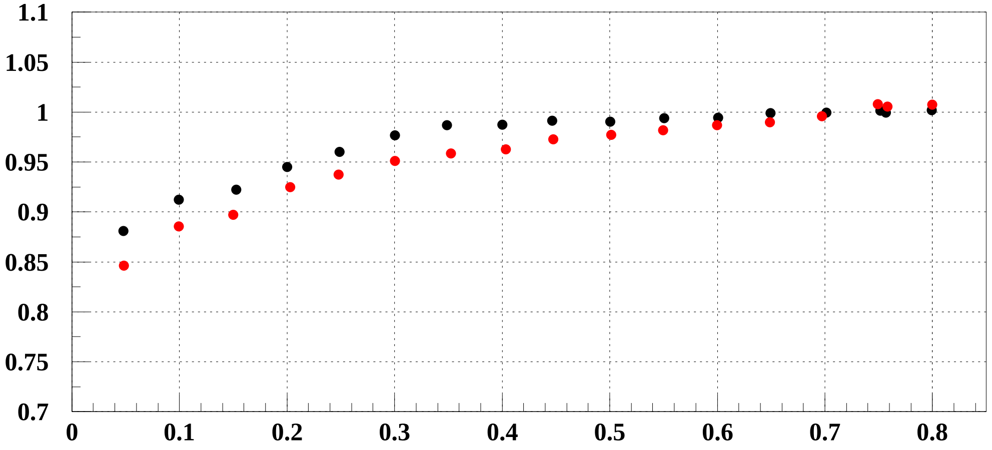

A/(B-1sig) / A0/(B0-1sig) vs TD cut value

Figure F.4: Same as Figure F.3 except the background value has been varied by 1 sigma. Black points include EV5 in the calculation, red points have excluded EV5 from the analysis. Acceptance is normalized to the total acceptance at the tight TD cuts (TDNN(pnn1) and EV5 applied). The total background is approximated from Ilektra's thesis + Muon Background. This assumes no dependence of the TD cuts on other background or acceptances.

F.3 Conclusions

The increase in acceptance from loosening TDNN and EV5 was measured to be $\sim 23\%$ with a muon background at a value much smaller than other backgrounds. Therefore, EV5 should not be applied and TDNN should be loosened to a cut parameter of 0.3. EV5 and the TDNN set at the original 0.76 were used to define a much cleaner PNN2 signal region.

Appendix G

Optimization of PNN2 Photon-Vetoing Parameters

G.1 Choosing the Cuts

The E949-PNN1 analysis optimization was performed without BVL TDC supplemented hits (previously no TDC hits were utilized). Therefore, additional optimization of the photon-veto parameters was required. The goal was to maximize the background rejection, while retaining a reasonable signal acceptance. To search for the best set of parameters for the 19 main PV subsystems (all apart from the BV_{early} and AD), the same optimization process as in the PNN1 analysis was used [65]. Appropriate rejection and acceptance samples were prepared, $K_{\pi 2}$ and $K_{\mu 2}$ monitors, respectively. Given an initial set of parameters (time offsets, time windows and energy thresholds for all the subsystems), the reference rejection and acceptance were measured. Parameters of one subsystem at a time were then changed by given step sizes; after which, the rejection and acceptance were remeasured. A new set of parameters was chosen if it improved both the rejection and acceptance or either of them without decreasing the other. The process was iterated, until no further im-

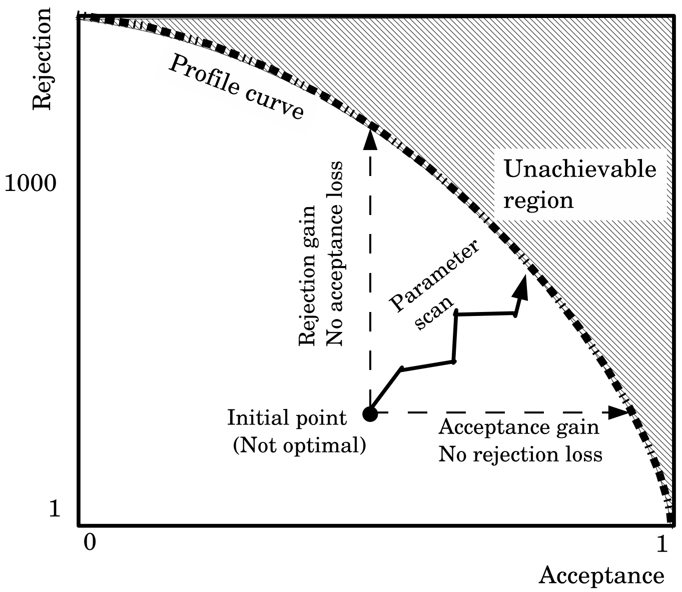

Figure G.1: Schematic of the PV optimization process.

provement could be found. A schematic of the optimization process is shown in Fig. G.1. Due to the large size of the parameter space (3 × 19 free parameters), care was taken to avoid local minimum solutions. Repeating this process for nine different goal acceptances, the optimal set of parameters was found for each of these acceptances, that produced the best rejection-acceptance profile.

Two new PV cut categories were added in the PNN2 analysis, which were not optimized with the previously mentioned procedure:

- Early BV (BV_{early}): It was observed that for a wide time range (around 30 ns) before the prompt peak in the BV at RS time, there were very high energy hits in the $K_{\pi 2}$ sample, but not in the $K_{\mu 2}$ sample. These were most likely due to early accidentals, that blinded the BV TDCs, so that they could not register the photon hits in time with the decay. Since the ADC gates are $\sim$ 50 ns wide, the energy of both the accidental and the photon hit was measured; therefore these blinded BV modules had unusually high energy. Such events were vetoed with an additional BV cut at 30 MeV.

- Active Degrader (AD): To use the AD as a photon detector, care had to be taken not to veto on beam activity at Kaon time. The study and optimization of the AD is described in [72].

Due to the lack of statistics in the 12 rejection classes of $K_{\pi 2}$ TG-scattered events defined in Table 4.1, the optimization was done in the $K_{\pi 2}$ peak. The result in the $K_{\pi 2}$ peak, broken down to each subsystem contribution, is shown in the left plot from Fig. G.2. The same PV cuts were then applied to the 12 TG-scatter classes, the right plot from Fig. G.2 shows class 12. The values at 60% acceptance were chosen, based on the expected background for every set of parameters.

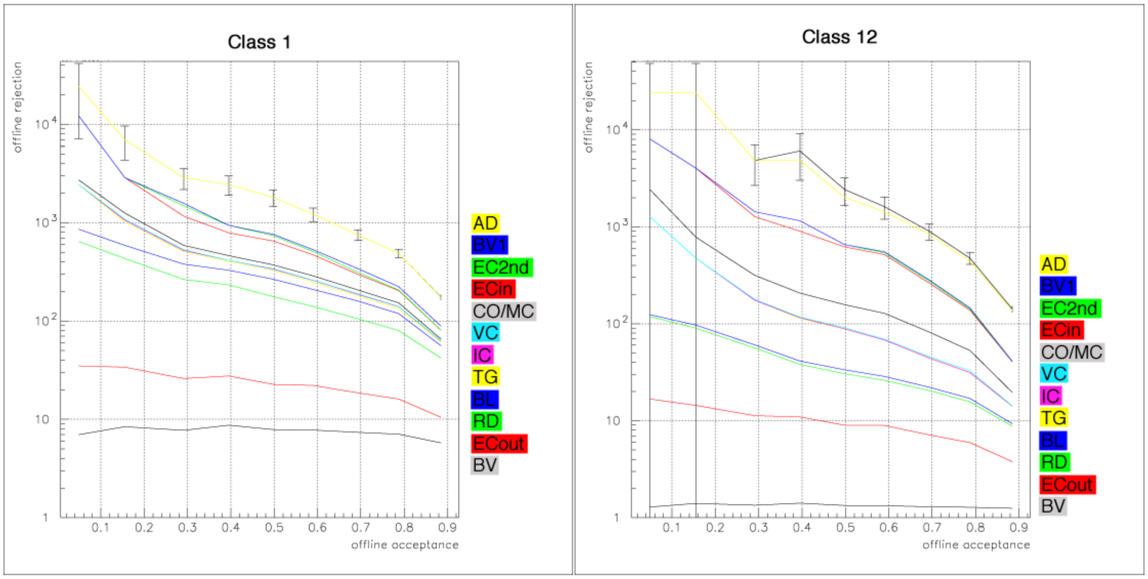

Figure G.2: Offline rejection vs acceptance profile with each subsystem contribution for the $K_{\pi 2}$ peak (left) and Class 12 (right).

G.2 Limits of the Photon-Veto Rejection

There are several factors that cause photon detection inefficiency including lack of radiation length, dead material in the detector, sampling fluctuations, photonuclear interactions, and masking of photon hits due to earlier accidentals (veto blindness).

The weak photon detection areas that existed in the barrel of the E787 detector, seem to have been drastically improved with the addition of the BVL, as shown in Fig. 2.16. Nonetheless, some polar-angle dependence of the PV power of the detector still exists due to dead material of the UTC endplate, and causes position dependent inefficiencies. The area close to the beam is also still more inefficient than the barrel region.

Sampling fluctuations depend on the photon energy. The detection efficiency increases with increased energy and larger detector modules. However, the latter requirement competes with the effect of veto blindness; such that larger PV elements will be more likely to have accidental energy deposits rendering the TDCs unable to register subsequent hits. This inefficiency has been partly compensated by the addition of TDs providing distinguishing information between multiple hits. The BV_{early} cut exploits the fact that accidental hits will deposit energy in the ADC gate, in addition to the photon energy.

Finally, photonuclear interactions can cause photon hits later than the nominal veto time, therefore their energy deposit can go undetected. This mechanism cannot even be reliably simulated, unlike the electromagnetic processes, and limits the photon detection ability of the detector.

Appendix H

E949 Math

The math within the E949 analysis is relativity simple within the standard binomial distributions.

H.1 Normalization Events

The number of events remaining, N, at the end of a normalization study has an error equal to $\sqrt{N}$.

H.2 Acceptance

Acceptance is simply the ratio of events left to the initial number of events within the sample. The acceptance sample employed to measure a cut should have the same properties, pertaining to the cut, of a $K^+ \to \pi^+ \nu \bar{\nu}$ sample. If a sample is not pure, then a systematic error would occur and would need to be measured.

$$acceptance_{cut1} = \frac{number\ of\ events\ after\ cut1}{Number\ of\ initial\ events\ (before\ cut1)} \tag{H.1}$$

$$acc_{cut1} = \frac{n}{N} \tag{H.2}$$

The usual nomenclature to describe a binomial distribution states that the probability of a success (acceptance) in one trial (event) is p (acc).

For a binomial distribution with N trials and ν successes,

$$\bar{\nu} = Np \tag{H.3}$$

$$\sigma_\nu = \sqrt{Np(1-p)} \tag{H.4}$$

such that $\bar{\nu}$ is the mean number of successes and σ_ν is the standard deviation on a measurement of one trial.

Within E949,

$$p = \frac{\bar{\nu}}{N} \implies acc = \frac{n}{N} \tag{H.5}$$

To calculate the error of the acceptance measurement, begin with the error on one trial (event) as shown in Eq. (H.6) and then follow with the error with N initial events shown in Eq. (H.7).

$$\sigma_\nu = \sqrt{Np(1-p)} \tag{H.6}$$

$$\sigma_{acc} = \frac{1}{N} \cdot \sigma_\nu \qquad \text{with N initial events in the sample} \tag{H.7}$$

$$\sigma_{acc} = \frac{1}{N}\sqrt{N \cdot acc \cdot (1-acc)} \tag{H.8}$$

$$= \sqrt{\frac{N \cdot acc(1-acc)}{N^2}}$$

$$= \sqrt{\frac{acc \cdot (1-acc)}{N}} \tag{H.9}$$

H.3 Rejection

Rejection is the measure of how well a cut removes a background. It is the ratio of the number of events in the initial background sample (N) to the remaining number of events (n) after the cut is applied. Rejection is the inverse of acceptance, $R = \frac{N}{n}$. Using the transformation $R = \frac{1}{acceptance}$, the following equations yield the results for the error on the rejection.

$$
\begin{aligned}
\frac{\sigma_R}{R} &= \frac{\sigma_{acc}}{acc} && \text{(H.10)} \\
\sigma_R &= R \cdot \frac{\sigma_{acc}}{acc} \\
&= R^2 \cdot \sigma_{acc} && \text{Substutited acc} = \frac{1}{\text{R}} \\
&= R^2 \cdot \sqrt{\frac{\frac{1}{R} \cdot (1 - \frac{1}{R})}{N}} && \text{Used Eq. (H.9)} \\
&= R \cdot \sqrt{\frac{R \cdot (1 - \frac{1}{R})}{N}} \\
&= R \cdot \sqrt{\frac{R - 1}{N}} && \text{(H.11)}
\end{aligned}
$$

References

[1] D. Griffiths, "Introduction to Elementary Particles", John Wiley & Sons Inc. (1987).

[2] J.H. Christenson, J.W. Cronin, V.L. Fitch and R. Turlay, Phys. Rev. Lett. **13**, 138 (1964).

[3] Collection: M. Gell-Mann and Y. Ne'eman, "The Eightfold Way", New York, Benjamin (1964).

[4] V. E. Barnes *et al.*, Phys. Rev. Lett. **12**, 204 (1964).

[5] Particle Data Group, W.-M. Yao *et al.*, Journal of Physics G **33**, 1 (2006)

[6] M. Kobayashi and T. Maskawa, Prog. Theor. Phys. **49**, 652 (1973).

[7] D. G. Michael *et al.*, Phys. Rev. Lett. **97**, 191801 (2006) .

[8] Z. Maki, M. Nakagawa and S. Sakata, "Remarks on the unified model of elementary particles", Prog. Theor. Phys. **28**, 870 (1962).

[9] S.L. Glashow, J. Iliopoulos, and L. Maiani, Phys. Rev. **D2**, 1285 (1970).

[10] N. Cabibbo, Phys. Rev. Lett. **10**, 531 (1963).

[11] L. Wolfenstein, Phys. Rev. Lett. **51**, 1945 (1983).

[12] CKMfitter Group (J. Charles *et al.*), Eur. Phys. J. **C41**, 1-131 (2005) and http://ckmfitter.in2p3.fr

[13] A.J. Buras, F. Schwab, and S. Uhlig, arXiv:hep-ph/0405132 (2004).

[14] A.J. Buras, M. Gorbahn, U. Haisch and U. Nierste, arXiv:hep-ph/0603079 (2006).

[15] G. Isidori, F. Mescia and C. Smith, Nucl. Phys. B **718**, 319 (2005)

[16] W.J. Marciano and Z. Parsa, Phys. Rev. **D53**, 1 (1996).

[17] Particle Data Group, S. Eidelman *et al.*, Phys. Lett. **B592** (2004) 1, and 2005 partial update for edition 2006 available at http://pdg.lbl.gov.

[18] J.S. Hagelin and L.S. Littenberg, Prog. Part. Nucl. Phys. **23**, 1 (1989);

[19] D. Rein and L.M. Sehgal, Phys. Rev. **D39**, 3325 (1989); M. Lu and M.B. Wise, Phys. Lett. **B324**, 461 (1994); S. Fajfer, arXiv:hep-ph/9602322 (1996); C.Q. Geng, I.J. Hsu, and Y.C. Lin, Phys. Rev. **D54**, 877 (1996).

[20] A. Belyaev *et al.*, Kaon Physics working Group Report "Kaon Physics with a High-intensity Proton Driver", arXiv:hep-ph/0107046 (2001); G. Isidori, arXiv:hep-ph/0110255 (2001); G. Buchalla, arXiv:hep-ph/0110313 (2001).

[21] A.J. Buras, arXiv:hep-ph/0402191 (2004); G. Isidori, arXiv:hep-ph/0301159 (2003).

[22] T. Inami and C.S. Lim, Prog. Theor. Phys. **65**, 297 (1981).

[23] A.J. Buras *et al.*, arXiv:hep-ph/0402112 (2004); A.J. Buras *et al.*, arXiv:hep-ph/0408142 (2004).

[24] Y. Grossman and Y. Nir, Phys. Lett. **B398**, 163 (1997).

[25] V.V. Anisimovsky *et al.*, Phys. Rev. Lett. **93**, 031801 (2004).

[26] S. Adler *et al.*, Phys. Rev. Lett. **64**, 21 (1990).

[27] S. Adler *et al.*, Phys. Rev. Lett. **70**, 2521 (1993).

[28] S. Adler *et al.*, Phys. Rev. Lett. **76**, 1421 (1996).

[29] T. Komatsubara, "Brief Summary of The Status of Upgraded-E787 in 1995", E787 Technical Note **305**, 1995. Unpublished.

[30] S. Adler *et al.*, Phys. Rev. Lett. **79**, 2204 (1997).

[31] S. Adler *et al.*, Phys. Rev. Lett. **84**, 3768 (2000).

[32] S. Adler *et al.*, Phys. Rev. Lett. **88**, 041803 (2002).

[33] M. Atiya *et al.*, Phys. Rev. D **D48**, R1 (1993).

[34] S. Adler *et al.*, Phys. Lett. B **537**, 211 (2002).

[35] S. Adler *et al.*, Phys. Rev. D **D70**, 037102 (2004).

[36] S. Chen *et al.*, "2002 $\pi\nu\bar{\nu}(1)$ Data Analysis", E949 Technical Note **K-034** and **K-038**, 2003. Unpublished.

[37] J. Doornbos *et al.*, Nucl. Instr. Meth. **A444**, 546 (2000).

[38] B. Bhuyan *et al.*, "Summary of the 2002 dataset and Pass0 processing", E949 Technical Note **K-025**, 2004. Unpublished.

[39] D.A. Bryman *et al.*, Nucl. Instr. Meth. **A396**, 394 (1997).

[40] B. Bassalleck *et al.*, "Beam Instrumentation III What Was Built.", E949 Technical Note **K-021**, 2001. Unpublished.

[41] M. Atiya *et al.*, Nucl. Instr. Meth. **A279**, 180 (1989).

[42] E.W. Blackmore *et al.*, Nucl. Instr. Meth. **A404**, 295 (1998).

[43] P. Bergbush, "Range Stack TDC Feasibility", E787 Technical Note **349**, 1998. Unpublished.

[44] D. Jaffe, "FITPI acceptance", E949 Technical Note **K-036**, 2004. Unpublished.

[45] J. Frank *et al.*, "Fiber optic bundles for E949 Range Stack monitoring system", E949 Technical Note **K-017**, 2000. Unpublished.

[46] R.A. McPherson, "Chasing the Rare Decay $K^+ \to \pi^+\nu\bar{\nu}$", Princeton University, Ph.D. Thesis, November, 1995.

[47] M.S. Atiya *et al.*, "A Detector to search for $K^+ \to \pi^+\nu\bar{\nu}$", NIM **A321**, 129 (1992).

[48] P. Meyers, "Barrel Veto Design", E787 Technical Note **72**, 1985. Unpublished.

[49] T.K. Komatsubara *et al.*, Nucl. Instr. Meth. **A404**, 315 (1998).

[50] I.H. Chiang *et al.*, IEEE Trans. Nucl. Sci. **42**, 394 (1995).

[51] N. Yershov, O. Mineev, "Efficiency of T-counters and T•2 trigger signals", E949 Technical Note **K-030**, 2002. Unpublished.

[52] T. Yoshioka *et al.*, IEEE Trans. Nucl. Sci. **51**, 199 (2004).

[53] S. Kettell, T. Yoshioka, "Trigger definitions - (2002)", E949 Technical Note **K-016**, 2002. Unpublished.

[54] D. Jaffe, "FITPI: Triple-pulse fitting and other modifications", E949 Technical Note **K-029**, 2002. Unpublished.

[55] J.B. Birks, Proc. Phys. Soc. **A64**, 874 (1951).

[56] C. Caso *et al.*, European Physical Journal **C3**, 1 (1998).

[57] P. Meyers, "A modified Version of the UMC Multiple Scattering Routine MSCAT1", E787 Technical Note **77**, 1985. Unpublished.

[58] A.J. Stevens, "Nuclear Interactions in CH revisited", E787 Technical Note **140**, 1987. Unpublished.

[59] W.R. Nelson *et al.*, "The EGS4 Code Syatem", SLAC 265, SLAC (1985).

[60] V. Jain, "Simulation of elastic scatters of π^+ in the target from Kp2 decays", E787 Technical Note **375**, 1999. Unpublished.

[61] I. Christidi, "The $K_{\pi 2}$ scatter 1/3 background", E949 Technical Note **K-070**, 2007. Unpublished.

[62] B. Lewis, "PNN2 1/3 Beam Background", E949 Technical Note **K-061**, 2006. Unpublished.

[63] B. Bhuyan, "Search for the Rare Kaon Decay $K^+ \to \pi^+ \nu\bar{\nu}$", Ph.D. thesis, 2003.

[64] C. Witzig, "π^- absorption in the RS", E787 Technical Note **278**, 1994. Unpublished.

[65] K. Mizouchi, "Experimental Search for the Decay $\pi^0 \to \nu\bar{\nu}$", Ph.D. thesis, 2006.

[66] T. Sekiguchi, "Measurement of the $K^+ \to \pi^+ \nu\bar{\nu}$ Branching Ratio", Ph.D. thesis, 2004.

[67] H. Brafman *et al.*, "The SLAC Scanner Processor: A FASTBUS Module for Data Collection and Processing", IEEE Trans. Nucl. Science, **32**, 1, 1985.

[68] H. Brafman *et al.*, IEEE Trans. Nucl. Sci. **32**, 336 (1985).

[69] S. Hansen *et al.*, Description of the DYC+, Fermilab Physics Department Internal Report (1995).

[70] The reference manual can be found in either `http://midas.triumf.ca` or `http://midas.psi.ch`.

[71] B. Lewis, "A new Target Reconstruction and Target Scatter Algorithm", E949 Technical Note **K-063**, 2006. Unpublished.

[72] I. Christidi, "Search for the rare decay $K^+ \to \pi^+ \nu\bar{\nu}$ with $p_{\pi^+} < 199$ MeV/c", Ph.D. thesis, 2006.